

THE ASTROPHYSICAL JOURNAL SUPPLEMENT SERIES, 45:635–725, 1981 April  
 Copyright is not claimed for this article.

## STRUCTURE OF THE SOLAR CHROMOSPHERE. III. MODELS OF THE EUV BRIGHTNESS COMPONENTS OF THE QUIET SUN

J. E. VERNAZZA<sup>1</sup>, E. H. AVRETT, AND R. LOESER

Harvard-Smithsonian Center for Astrophysics

Received 1980 April 7; accepted 1980 October 20

### ABSTRACT

*Skylab* observations of the quiet Sun in the EUV wavelength range 40–140 nm show the inhomogeneous structure of the chromosphere. We use these observations to determine separate chromospheric models for six observed brightness components, ranging from a dark cell center to a very bright network element. In each case we solve the non-LTE radiative transfer, statistical equilibrium, and hydrostatic equilibrium equations to determine the temperature-density stratification that produces a calculated spectrum in best agreement with the observed one. Our hydrogen calculations are carried out with an atomic model consisting of eight explicit levels and supplementary levels 9–12. We account for the effects of partial frequency redistribution in the formation of the hydrogen L $\alpha$  and L $\beta$  lines and the resonance lines of Ca II and Mg II. To obtain the results shown here we carry out non-LTE calculations for H, H $^-$ , C, Si, Fe, Mg, Al, He, He II, Ca II, Mg II, and several other atoms and ions. We obtain good agreement between observed and calculated intensities in the L $\alpha$  and L $\beta$  lines, the Lyman continuum, and other continua in the 40–140 nm range. We base our temperature minimum determination on continuum observations in the 135–168 nm range but obtain minimum temperature values which are lower than implied by the Ca II and Mg II lines and recent microwave observations. In the upper chromosphere our models are in good agreement with those obtained by Basri *et al.* from a study of the observed L $\alpha$  line. However, the temperature reduction in the low chromosphere proposed by Basri *et al.* is a consequence of their assumption of LTE for the carbon continuum which causes a spurious enhancement of the computed intensity in the L $\alpha$  wings. Finally, we compute the net radiative cooling rates for the atoms and ions listed above. We find that the L $\alpha$  cooling rate is the dominant one in the transition region at temperatures between  $2 \times 10^4$  and  $3 \times 10^4$  K. In the chromosphere there is some L $\alpha$  radiative heating but much greater radiative heating by the Balmer continuum which effectively cancels the net cooling by the H $\alpha$  line. We find that the H $^-$  cooling rate is smaller than the rate calculated by Ulmschneider and Kalkofen by a factor of 10. For the average quiet Sun we find that the largest integrated cooling rates in order of decreasing importance are due to the Ca II infrared-triplet and resonance lines, the Mg II resonance lines, H $^-$ , and L $\alpha$ . Contents.—I, Introduction; II, Atomic Data; III, Observational Data; IV, The Model Calculations; V, Properties of the Models; VI, Tables; VII, Comparison with Other Models; VIII, The Temperature Minimum; IX, Energy Balance; Appendix A, The L $\alpha$  Line with Partial Redistribution; Appendix B, Supplementary Levels in the Equations of Statistical Equilibrium; Appendix C, Solution of the Lyman-Continuum Transfer Equation.

*Subject headings:* radiative transfer — Sun: atmosphere — Sun: chromosphere — ultraviolet: spectra

### I. INTRODUCTION

In this paper we solve the non-LTE optically thick transfer equations for hydrogen, carbon, and other constituents to determine semiempirical models for six components of the quiet solar chromosphere. For a given temperature-height distribution we solve the equations of statistical equilibrium, radiative transfer for lines and continua, and hydrostatic equilibrium to find the ionization and excitation conditions for each atomic constituent, and then we calculate the emergent spectrum.

By trial and error we adjust the temperature distribution so that the emergent spectrum is in best agreement with the observed one. The relationship between semiempirical models determined in this way and theoretical models based on radiative equilibrium is discussed by Avrett (1977).

We use Harvard *Skylab* EUV observations to determine models for the following quiet-Sun regions: (A) a dark point within a cell; (B) the average cell center; (C) the average quiet Sun; (D) the average network; (E) a bright network element; (F) a very bright network element. Each of these components is treated separately

<sup>1</sup>Lawrence Livermore Laboratory.

as a plane-parallel atmosphere. The neglect of horizontal interaction between the component models is a reasonable first approximation since these features generally have horizontal dimensions of order  $10''$ , or 7500 km, which greatly exceeds the heights of formation of the lines and continua studied here.

Recent  $L\alpha$  filtergrams of the Sun by Bonnet *et al.* (1980) with a spatial resolution of  $\sim 1''$  show that the network has a highly complex structure at heights where the  $L\alpha$  line is formed. They find in some regions that the network coincides with the bright tops of many individual small loops, that dark absorption loops  $5''$ – $10''$  in length very often cross through the bright network, and that longer dark threads cut across the disk almost everywhere. Brueckner, Bartoe, and Van Hoosier (1977) also have observed highly inhomogeneous structures in EUV transition zone and coronal emission lines.

Despite such complicated observed structure, the present simplified study can be justified on several grounds: (1) it is the first attempt to construct a set of models for the quiet Sun based on the various observed brightness components of the EUV continuum; (2) it can be used to determine the degree of consistency between spatially averaged observations and corresponding calculations, particularly from the viewpoint of understanding the stellar analogs to solar phenomena; and (3) it is the kind of study that must precede those dealing with more complex spatial structures.

The basic procedure we follow to construct each component model is outlined in Papers I and II (Vernazza, Avrett, and Loeser 1973, 1976). The new features incorporated in the present calculations are described in the following paragraphs.

We use a partial redistribution formalism to treat the hydrogen  $L\alpha$  and  $L\beta$  lines and the Ca II and Mg II resonance lines. A complete derivation of the equations we solve is given in Appendix A.

The ratio of the integrated intensity in each of the Lyman lines to the Lyman continuum intensity is accurately known from the *Skylab* observations, but these observed ratios have not been well matched in previous model calculations. We find that good agreement can be obtained by including an adequate number of levels in the model atom used to calculate the excitation and ionization of hydrogen.

The total radiative recombination rate coefficient for hydrogen at a temperature of  $10^4$  K is known to be  $\sim 4.2 \times 10^{-13}$  cm $^3$  s $^{-1}$  (see Osterbrock 1974). To obtain this value we had to include 12 levels in our hydrogen model. For model atoms with eight, five, and three levels we obtain the values  $3.9$ ,  $3.4$ , and  $2.9 \times 10^{-13}$  cm $^3$  s $^{-1}$ , respectively. In Appendix B we show how supplementary levels can be included in the set of statistical equilibrium equations so that correct values of the total radiative recombination rate are obtained. For our hydrogen calculations we use an eight level atomic model with supplementary levels 9 through 12.

In addition to these calculations for hydrogen, we also carry out multilevel non-LTE calculations for 17 other atoms and ions, as described in § IV. In particular, we have solved the non-LTE equations for neutral Fe, Mg, and Al, which we treated in LTE before, in order to see if the results might resolve the conflict between the minimum temperature determined from the UV continuum near 160 nm and that determined from the Ca II and Mg II lines. See § VIII.

Figure 1 shows the average quiet-Sun temperature distribution that we have established and the regions where various spectral features are formed. The spectra indicated are due to H, H $^-$ , C, Si, Fe, Ca II, and Mg II. The hydrogen features are the  $L\alpha$  line at the center and peak intensity and at  $\Delta\lambda=1$  Å and  $\Delta\lambda=5$  Å, the Lyman continuum at 90.7 nm and 70 nm, and the  $H\alpha$  line, core and wing. The continuum intensities at 3 cm, 1 cm, and 3 mm are due mostly to free-free transitions of hydrogen, while the continuum intensities from 1 mm to 50  $\mu$ m are due mostly to free-free transitions of H $^-$ . The ground-state continua of C, Si, and Fe extend over the wavelength regions  $\lambda \leq 109.8$ , 152.4, and 157.5 nm, respectively, and the Si level 2 continuum extends over  $\lambda \leq 168.1$  nm. At 157.5 nm the opacity due to Si is comparable to that of Fe. Here,  $K_1$  refers to the intensity minimum just outside the Ca II K-line centrally reversed emission core,  $K_2$  to the emission peak, and  $K_3$  to the line center, while  $k_1$ ,  $k_2$ , and  $k_3$  are the corresponding designations for the Mg II  $k$  line.

In § II we specify the atomic data used in our radiative transfer and statistical equilibrium calculations for H, C, and Fe. The data consist of energy levels, Einstein  $A$  coefficients for each transition, line broadening parameters, photoionization cross sections, and collision cross sections.

In § III we show the observed values of the central intensity and flux at continuum wavelengths in the EUV range 40–140 nm and the observed microwave and radio brightness temperatures between 0.3 and 20 mm. From *Skylab* spectroheliograms at 42 continuum wavelengths between 42.2 and 131.8 nm we obtain observed intensities corresponding to the six quiet-Sun brightness components A through F listed earlier in this section.

In § IV we show the temperature distributions for six models that we have determined corresponding to the six observed EUV component intensity distributions in § III. We specify a single microvelocity distribution for all six models. Then we show comparisons between the computed and observed continua in the two chromospheric wavelength ranges 40–140 nm and 0.3–20 mm and in the temperature-minimum wavelength ranges 135–168 nm and 33–500  $\mu$ m. Finally, we show comparisons between the computed and observed profiles of the lines Ca K, Mg  $k$ ,  $H\alpha$ ,  $L\alpha$ , and  $L\beta$ .

In § V we compare our results with the integrated  $L\alpha$  and  $L\beta$  intensities and corresponding Lyman continuum intensities observed for the six quiet-Sun components.

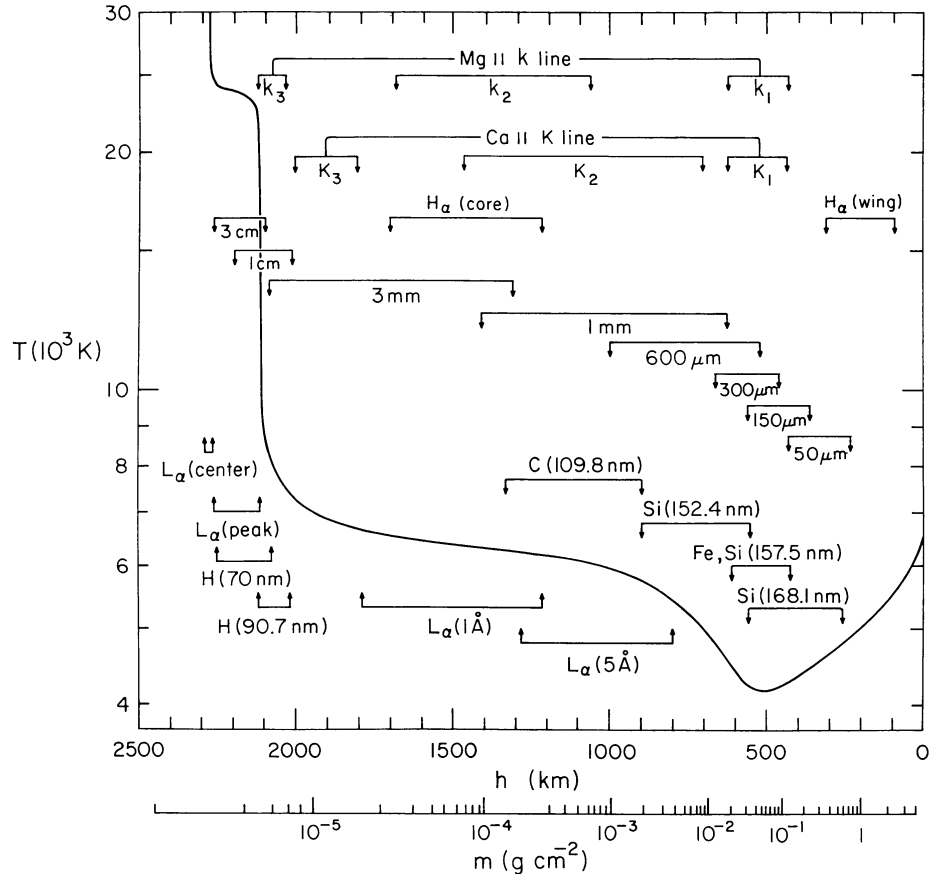


FIG. 1.—The average quiet-Sun temperature distribution derived from the EUV continuum, the  $L\alpha$  line, and other observations. The approximate depths where the various continua and lines originate are indicated.

We find that in order to match the observed Lyman line to Lyman continuum ratios, the calculations should be carried out with (1) a model hydrogen atom which includes the effects of at least five levels and preferably eight or 12 levels, (2) a Lyman line transfer procedure which includes the effects of partial frequency redistribution, and (3) careful attention to the photoionization rates in the  $n=2$ ,  $n=3$ , and higher continua.

We have examined the two procedures which have been used in previous papers to greatly simplify the treatment of Lyman line transfer: (1) assuming radiative detailed balance for the Lyman lines so that effectively each  $A_{nl}=0$ , and (2) assuming complete frequency redistribution in the Doppler core and zero opacity in the wings of each Lyman line. Milkey and Mihalas (1973a) found that the second procedure gave Lyman continuum intensities in close agreement with their partial redistribution results, but we find that in the case of the present models the first procedure is a much better approximation.

In § V we examine the computed non-LTE departure coefficients  $b_n$  for hydrogen and find that there is a region in the middle chromosphere where the  $L\alpha$  radiation heats the gas, in contrast to the radiative cooling

that normally takes place. We explain this effect in terms of the role the  $L\alpha$  line plays in the creation and destruction of Lyman continuum photons. Such  $L\alpha$  heating could be important to the chromospheric energy balance in view of the strong absorption of energy from the gas by  $L\alpha$  in the layers of the transition region which receive energy conductively from the corona.

In § V we also show the computed  $b_n$  coefficients for C, Fe, and Si and a set of graphs indicating how the continuum is formed at selected wavelengths from 3 cm to 40 nm.

Tables of the various model parameters are given in § VI.

In § VII we compare our models with those of Gingerich *et al.* (1971), Ayres and Linsky (1976), Basri *et al.* (1979), Tripp, Athay, and Peterson (1978), and Lites, Shine, and Chipman (1978). We have determined the temperature-minimum portions of our models from observations of the UV continuum in the range 135–168 nm, but we find lower minimum values than have been determined by Ayres and Linsky (1976) from the intensity minima in the Ca II and Mg II resonance line wings. The comparison between calculated minimum brightness temperatures in the 33–500  $\mu\text{m}$  range and those of

Rast, Kneubühl, and Müller (1978) shown in § IV also suggests that our minimum values may be too low. It should be noted, however, that these observed brightness temperatures are higher than some of the earlier measurements, which we have plotted in Figure 11 of Paper II.

In the comparison of our results with those of Basri *et al.* (1979) for the average quiet Sun, there is good agreement in the upper chromosphere between the two temperature distributions, when expressed in terms of column mass. However, we find that their proposed reduction of the temperature in the low chromosphere is due to their assumption of LTE for the carbon continuum which leads to a spurious enhancement of the intensity in the  $\text{L}\alpha$  wings.

We note and provide a correction to an error in the height scales given by Basri *et al.*

In § IX we give the equations for the net radiative losses, or cooling rates, due to the various lines and continua formed in the chromosphere and lower transition region. We show the cooling rates due to the lines

and continua of hydrogen and find that the  $\text{L}\alpha$  cooling rate is the dominant one in our plateau region where  $2 \times 10^4 < T < 3 \times 10^4$  and that there is a moderate amount of  $\text{L}\alpha$  heating in the middle chromosphere. However, the Balmer continuum provides a far larger amount of radiative heating throughout the chromosphere and effectively cancels the cooling due to the  $\text{H}\alpha$  line. This effect has not been recognized before (see, for example, Athay 1976, Table IX-1 where the Balmer continuum is listed as a cooling agent).

We also show in § IX the total hydrogen contribution to the net radiative cooling rate (which is small throughout the chromosphere due to the balance between  $\text{H}\alpha$  and the Balmer continuum) along with the contributions due to the  $\text{Ca II}$  H, K, and infrared triplet lines, the  $\text{Mg II}$  h and k lines, the  $\text{H}^-$  continuum, and other constituents. We find that the integrated net cooling rates  $\int \Phi dh$  of principal importance have values in the following diminishing order: the  $\text{Ca II}$  K, IR triplet, and H lines,  $\text{Mg II}$  k and h,  $\text{L}\alpha$ ,  $\text{H}^-$  bound-free, and  $\text{H}^-$  free-free.

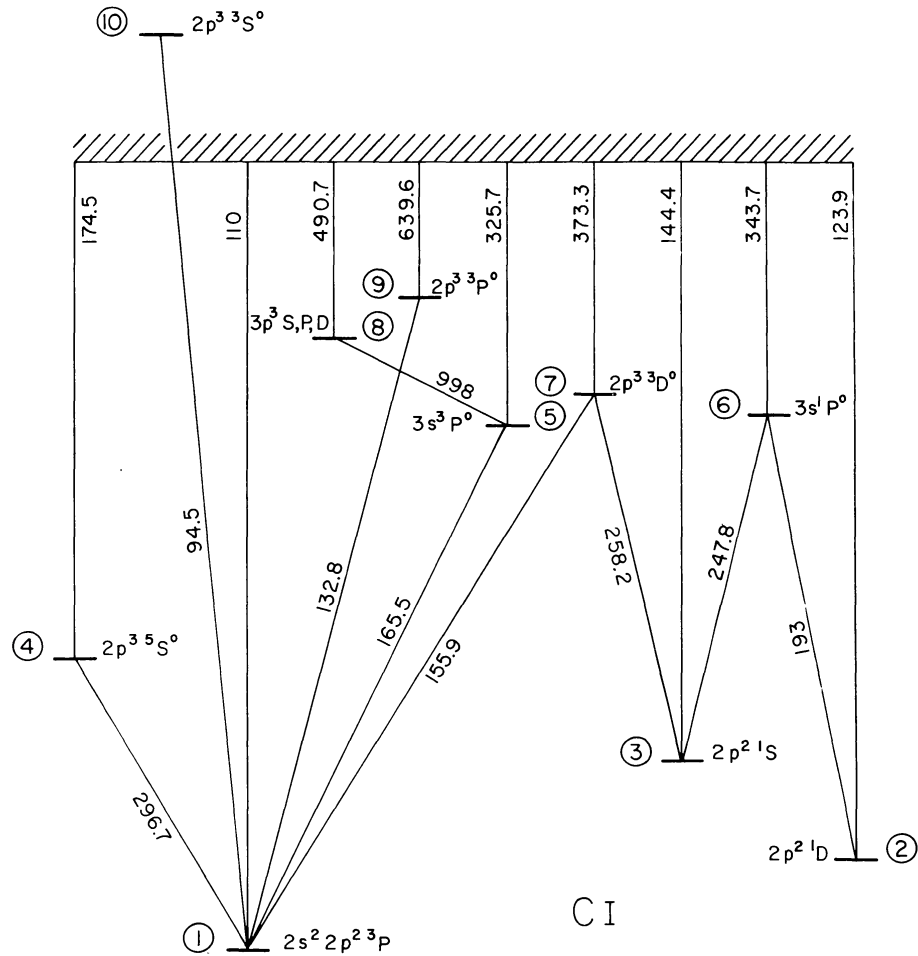


FIG. 2.—The energy level diagram for our model of the C I atom

We also find that in our model of the average quiet Sun, the  $H^-$  bound-free cooling rate never exceeds 0.01 ergs  $cm^{-3} s^{-1}$ , whereas Ulmschneider and Kalkofen (1978) found a maximum value of  $\sim 0.12$  ergs  $cm^{-3} s^{-1}$ . Because of this disagreement we include a detailed discussion of the energy balance equations for  $H^-$ .

## II. ATOMIC DATA

In Paper II we specified the atomic data used in our statistical equilibrium and radiative transfer calculations for Si I. Here we give the corresponding data for C I, Fe I, and hydrogen.

### a) Carbon

Our model for C I consists of 10 levels and a continuum; the adopted energy level diagram appears in Figure 2. The solid lines indicate the radiative transitions which we include in the calculations. We also include all collisional transitions between the indicated levels.

The energy levels consist of the three lowest ones,  $2s^2 2p^2 {}^3P$ ,  $2p^2 {}^1D$ , and  $2p^2 {}^1S$ , and the principal higher levels coupled to these lowest ones by radiative transitions thereby affecting the populations of the three lowest levels. The  $2p^3 {}^3S^0$  level is included because it is coupled to the ground level by the autoionization line at 94.5 nm. We also include  $2p^3 {}^5S^0$  because of its proximity to the three lowest levels. The  $3p$   ${}^3S$ ,  ${}^3P$ , and  ${}^3D$  levels have been combined together since the energy differences between these levels are small, and trial calculations indicate that these levels are in detailed balance with one another.

The photoionization data for levels 1–8 used in the present calculations are given in Table 5 of Paper II.

The photoionization cross section for level 9, in units of  $10^{-18} cm^{-2}$ , is taken to be:

$$a_9(\lambda) = \begin{cases} 0 & \lambda > 639.6 \text{ nm}, \\ 10(\lambda/639.6)^3, & \lambda \leq 639.6 \text{ nm}. \end{cases} \quad (1)$$

No radiative transitions are assumed between the autoionizing level 10 and the continuum. The partition function for C II is chosen to be 6, the statistical weight of the C II ground level, and we adopt a carbon abundance of  $3.55 \times 10^{-4}$  (Withbroe 1971).

We list in Table 1 for each radiative transition indicated in Figure 2 the line wavelength, the Einstein  $A$  coefficient, and the line broadening half-widths  $C_{rad}$ ,  $C_{vdW}$ , and  $C_{Stark}$ . These line broadening parameters are used as follows. The absorption coefficient for each line is assumed to have the frequency dependence of the Voigt function  $\phi(a, y)$  (see eq. (A2) of Appendix A), where  $a = \delta/\Delta\nu_D$  and

$$\delta = C_{rad} + C_{vdW} \left( \frac{n_{H_1}}{10^{16}} \right) \left( \frac{T}{5000} \right)^{0.3} + C_{Stark} \left( \frac{n_e}{10^{12}} \right). \quad (2)$$

The half-widths in Table 1 are expressed in wavelength units (see eq. (5) of Paper II for the corresponding Doppler width expressed in wavelength units).

The Einstein  $A$  values were obtained from the compilation by Wiese, Glennon, and Smith (1969) except those for the 5–1 and 7–1 transitions, which are from measurements by Laurence and Savage (1966). We calculated the van der Waals and Stark half-widths using the formulae given by Griem (1964).

TABLE I  
EINSTEIN  $A$  VALUES AND LINE BROADENING HALF-WIDTHS FOR THE C I ATOMIC MODEL

<i>Transition</i>	$\lambda$ (nm)	$A$ ( $10^8 s^{-1}$ )	$C_{rad}$ ( $10^{-6} nm$ )	$C_{vdW}$ ( $10^{-6} nm$ )	$C_{Stark}$ ( $10^{-6} nm$ )
4–1	296.4	3.0 (-7)	-	-	-
5–1	165.5	3.2	2.49	1.67	.014
5–3	258.2	2.8 (-5)	-	-	-
6–2	193.0	2.4	2.71	1.559	-
6–3	247.8	0.34	4.47	2.56	-
7–1	155.9	2.77	1.79	6.03	-
8–6	998.0	2.2	5.82	57.49	-
9–1	132.8	1.4	0.655	1.782	-
10–1	94.5	61.0	14.0	-	-

TABLE 2  
COLLISIONAL IONIZATION COEFFICIENTS FOR THE C I ATOMIC MODEL

<i>Level</i>	$\Omega_l(T) (10^{-8} \text{ cm}^3 \text{s}^{-1})$				
	3000 K	5000 K	7000 K	9000 K	10000 K
1	0.245	0.352	0.454	0.557	0.868
2	0.374	0.593	0.822	1.06	1.78
3	0.466	0.665	0.868	1.08	1.72
4	0.0742	0.104	0.131	0.154	0.208
5	0.0336	0.0456	0.055	0.0627	0.0787
6	0.294	0.339	0.48	0.546	0.68
7	0.294	0.395	0.474	0.536	0.662
8	0.413	0.545	0.642	0.715	0.858
9	0.8	0.8	0.8	0.8	0.8

The collisional ionization rate per atom in level  $l$  is prescribed by the equation

$$C_{lk} = n_e \Omega_l(T) \exp(-h\nu_{kl}/kT), \quad (3)$$

while the collisional excitation rate per atom in level  $l$  for the  $u-l$  transition,  $u > l$ , is

$$C_{lu} = n_e \Omega_{ul}(T) \exp(-h\nu_{ul}/kT). \quad (4)$$

The values of  $\Omega_l(T)$  and  $\Omega_{ul}(T)$  are listed in Tables 2 and 3 for several temperatures. We use linear interpolation to determine the coefficients at temperatures between the values given in the tables.

The collisional ionization rates for levels 1–3 were computed by means of a Born approximation, using the collisional ionization cross sections of Peach (1968). For levels 4–9 we used Seaton's (1962) approximation to derive collision cross sections from photoionization cross sections.

The collisional excitation coefficients for transitions 2–1, 3–1, and 3–2 are based on the cross sections given by Smith, Henry, and Burke (1967). Those for transitions 5–1, 6–2, 6–3, 7–1, 8–5, 9–1, and 10–1 (the principal radiative transitions) were computed using Van Regemorter's (1962) formula. To each of the remaining transitions we arbitrarily assigned a transition rate roughly equal to one-tenth of that computed using Van Regemorter's formula for radiative transitions from the same level having approximately the same change in energy.

### b) Iron

We include Fe I in the present calculations because it is one of the principal contributors to the electron density at the temperature minimum and an important source of opacity at 157 nm. Our Fe I atomic model is similar to the model of Athay and Lites (1972) and consists of 15 levels and a continuum. We have used the atomic parameters compiled by Athay and Lites except that in our determination of the iron opacity we have divided the first eight levels into sublevels to take account of the fine structure of the Fe I lower levels. The photoionization cross sections for levels 1–8 and the sublevel statistical weights and threshold wavelengths are listed in Table 4. We solve the Fe I statistical equilibrium and radiative transfer equations to determine the composite-level number densities  $n_l$  and then obtain the sublevel number densities  $n_{ls}$  according to

$$n_{ls} = n_l g_{ls} / \sum_{s'} g_{ls'}. \quad (5)$$

### c) Hydrogen

Our hydrogen atom consists of 12 levels and a continuum. These levels correspond to the first 12 principal quantum number levels of hydrogen. We treat only the first eight of these levels explicitly and have added four supplementary levels (principal quantum numbers 9 through 12) in order to obtain a correct value for the total radiative recombination rate. See § V and Appendix B. In Table 5 we give for each of these levels the statistical weight, the threshold ionization wavelength, and the threshold photoionization cross section. For all

TABLE 3  
COLLISIONAL EXCITATION COEFFICIENTS FOR THE C I ATOMIC MODEL

$u-l$	$\Omega_{ul}(T) \quad (10^{-8} \text{ cm}^3 \text{s}^{-1})$				
	3000 K	5000 K	7000 K	9000 K	10000 K
2-1	0.481	0.716	0.924	1.09	1.44
3-1	0.0995	0.138	0.169	0.192	0.229
3-2	0.00331	0.0283	0.0718	0.12	0.247
5-1	0.54	0.54	0.54	0.54	0.56
6-2	0.51	0.51	0.51	0.51	0.61
6-3	0.87	0.87	1.0	1.0	1.08
7-1	0.78	0.78	0.78	0.78	0.84
8-5	92.5	101.	101.	101.	113.

For the following transitions,  $\Omega_{ul}$  does not vary with temperature

$u-l$	$\Omega_{ul}$	$u-l'$	$\Omega_{ul'}$	$u-l''$	$\Omega_{ul''}$
4-1	0.01	7-6	1.0	9-6	0.001
4-2	0.01	8-1	0.5	9-7	0.01
4-3	0.01	8-2	0.05	9-8	0.01
5-2	0.05	8-3	0.05	10-1	0.001
5-3	0.05	8-4	0.01	10-2	0.0001
5-4	0.05	8-6	0.1	10-3	0.0001
6-1	0.01	8-7	1.0	10-4	0.0001
6-4	0.05	9-1	0.135	10-5	0.0001
6-5	1.0	9-2	0.011	10-6	0.0001
7-2	0.01	9-3	0.011	10-7	0.0001
7-3	0.01	9-4	0.011	10-8	0.0001
7-4	0.01	9-6	0.01	10-9	0.0001
7-5	0.01				

levels we use the photoionization cross sections given by Menzel and Pekeris (1935) and the frequency-dependent Gaunt factors of Karzas and Latter (1961).

The Einstein  $A$  values for hydrogen were taken from the compilation of Wiese, Glennon, and Smith (1969), and the radiative broadening coefficients were calculated from these  $A$  values. The resonance and van der Waals broadening coefficients were calculated from the formulae given by Griem (1964). We include resonance broadening by adding the term  $C_{\text{res}}(n_{\text{H}_1}/10^{16})$  to equation (2). In the chromosphere, Stark broadening is smaller than resonance or natural broadening for

most of the members of the Lyman and Balmer series. For this reason, and for simplicity, we did not include Stark broadening in the line source function calculations for hydrogen. However, Stark broadening is included in our determination of the scattering ratio  $\gamma_s$  for the  $L\alpha$  line, as explained in Appendix A.

In Table 6 we give our adopted collisional ionization coefficients for hydrogen. The collisional rate for the ground level was obtained from the collisional ionization cross section measured by Fite, Stebbings, and Brackman (1960) and McGowan, Williams, and Curley (1969). The other ionization rates were calculated using

TABLE 4  
PHOTOIONIZATION DATA FOR THE Fe I ATOMIC MODEL

Level	Term	$\sigma_f$ ( $10^{-18} \text{ cm}^2$ )	Sublevel	$g$	$\lambda(\text{nm})$
$l$			$s$		
1	$a\ 5D$	6.3	1	9	157.53
			2	7	158.57
			3	5	159.30
			4	3	159.77
			5	1	160.00
2	$a\ 5F$	5.0	1	11	176.83
			2	9	178.24
			3	7	179.37
			4	5	180.20
			5	3	180.75
3	$a\ 3F$	3.0	1	9	194.16
			2	7	196.39
4	$a\ 5P$	3.0	3	5	197.97
			1	7	217.72
			2	5	218.56
5	$a\ 3P$	0.44	3	3	219.53
			1	5	221.72
			2	3	227.65
			3	1	230.19
6	$z\ 7D^\circ$	1.7	1	11	226.61
			2	9	227.70
			3	7	228.71
			4	5	229.53
			5	3	230.09
7	$a\ 3H$	1.61	1	13	226.81
			2	11	228.00
8	$b\ 3F$	1.02	3	9	228.88
			1	9	233.43
			2	7	234.71
9	$z\ 7P^\circ-F^\circ$	3.4	3	6	235.62
			70		233.5
			27		252.0
10	$b\ 3G$	1.31	25		266.2
11	$z\ 5D^\circ$	1.76	35		273.3
12	$z\ 5F^\circ$	2.57	15		290.7
13	$z\ 5P^\circ$	1.70	36		335.9
14	$y\ 5F^\circ$	3.28	45		349.8
15	$z\ 5G^\circ$	4.22			

the expressions given by Sampson and Golden (1971). We have compared the Sampson and Golden rates with the ones proposed by Mihalas (1967) and Johnson (1972) and find differences not larger than 20%. Since collisions do not strongly control the hydrogen statistical equilibrium equations, we think that such differences will not alter the hydrogen solution. The collisional excitation rates are given in Table 7. The rate for the 2-1 transition was derived from the experimental photoionization cross sections of Fite and Brackman (1958). For the other transitions, we have used the values of Sampson and Golden (1970). We have compared the semiempirical rates given by Sampson and Golden with

TABLE 5  
PHOTOIONIZATION DATA FOR THE H I ATOMIC MODEL

Level ( $l$ )	$g_l$	$\lambda_f(\text{nm})$	$\sigma_f(10^{-18} \text{ cm}^2)$
1	2	91.19	6.32
2	8	363.6	14.0
3	18	815.5	21.5
4	32	1428	29.0
5	50	2205	36.3
6	72	3127	44.5
7	98	4467	54.7
8	128	5841	63.2
9	162	7433	71.8
10	200	9881	80.8
11	242	10965	88.3
12	288	13417	90.0

those of Mihalas (1967) and Johnson (1972) and again find differences no larger than 20%.

### III. OBSERVATIONAL DATA

The continuum radiation that originates between the temperature minimum and the chromosphere-corona transition region is emitted in two distinct wavelength ranges, between 40 nm and 160 nm in the far ultraviolet and between 0.1 mm and 20 mm in the microwave and radio region. Most of the absolute measurements of the solar ultraviolet radiation have been made from rockets and refer to the flux from the entire solar disk. In the range 40–140 nm the flux from the emission lines is many orders of magnitude larger than the flux from the underlying continuum. The absolutely calibrated instruments flown in rockets generally do not have the dynamic range necessary to measure both lines and continuum; thus, the continuum observations are usually made with satellite-borne instruments which measure continuum-to-line ratios. These observations are then calibrated absolutely from the emission-line absolute intensities measured by rocket instruments.

The ultraviolet data collected here are from observations made at different times during an eight year period. Questions have been raised about possible time variations of the solar ultraviolet flux during the solar cycle (Timothy 1977). However, for the purpose of this investigation we will assume that, in the range 40–140 nm, the continuum flux arising from quiet regions is constant and does not depend on the solar cycle.

We specify the central intensity  $I_\lambda$  in units of  $\text{W cm}^{-2} \text{ sr}^{-1} \mu\text{m}^{-1}$  at the solar surface. The flux  $F_\lambda$  at the

TABLE 6  
COLLISIONAL IONIZATION COEFFICIENTS FOR THE H ATOMIC MODEL

<i>Level</i>	$\Omega_f(T)$	( $\text{cm}^3 \text{s}^{-1}$ )	5000 K	9000 K	15000 K	25000 K	35000 K
1	2.82(-9)	3.92(-9)	5.30(-9)	7.21(-9)	9.01(-9)		
2	5.90(-8)	7.59(-8)	9.44(-8)	1.17(-7)	1.34(-7)		
3	2.87(-7)	3.61(-7)	4.40(-7)	5.23(-7)	5.72(-7)		
4	8.59(-7)	1.06(-6)	1.25(-6)	1.40(-6)	1.47(-6)		
5	1.98(-6)	2.39(-6)	2.69(-6)	2.86(-6)	2.90(-6)		
6	3.80(-6)	4.43(-6)	4.79(-6)	4.90(-6)	4.83(-6)		
7	3.19(-6)	4.47(-6)	5.54(-6)	6.37(-6)	6.68(-6)		
8	4.74(-6)	6.46(-6)	7.83(-6)	8.82(-6)	9.14(-6)		

TABLE 7  
COLLISIONAL EXCITATION COEFFICIENTS FOR THE H ATOMIC MODEL

<i>Transition</i>	$\Omega_{u'}$	( $\text{cm}^3 \text{s}^{-1}$ )	5000 K	9000 K	15000 K	25000 K	35000 K
2-1	2.39(-8)	2.38(-8)	2.31(-8)	2.24(-8)	2.22(-8)		
3-1	6.62(-9)	5.63(-9)	5.31(-9)	5.61(-9)	6.29(-9)		
3-2	4.70(-7)	5.66(-7)	6.46(-7)	7.21(-7)	7.56(-7)		
4-1	2.59(-9)	2.28(-9)	2.08(-9)	2.13(-9)	2.35(-9)		
4-2	8.97(-8)	9.59(-8)	1.06(-7)	1.17(-7)	1.24(-7)		
4-3	3.97(-6)	4.49(-6)	4.80(-6)	4.93(-6)	4.91(-6)		
5-1	1.57(-9)	1.26(-9)	1.11(-9)	1.09(-9)	1.17(-9)		
5-2	3.90(-8)	3.79(-8)	3.98(-8)	4.31(-8)	4.58(-8)		
5-3	5.86(-7)	6.77(-7)	7.44(-7)	7.83(-7)	7.91(-7)		
5-4	1.78(-5)	1.89(-5)	1.90(-5)	1.85(-5)	1.79(-5)		
6-1	9.29(-10)	7.38(-10)	6.42(-10)	6.22(-10)	6.64(-10)		
6-2	2.14(-8)	1.98(-8)	2.01(-8)	2.13(-8)	2.22(-8)		
6-3	2.17(-7)	2.42(-7)	2.64(-7)	2.80(-7)	2.84(-7)		
6-4	2.50(-6)	2.76(-6)	2.86(-6)	2.84(-6)	2.76(-6)		
6-5	5.55(-5)	5.57(-5)	5.43(-5)	5.12(-5)	4.87(-5)		
7-1	5.91(-10)	4.67(-10)	4.04(-10)	3.88(-10)	4.12(-10)		
7-2	1.32(-8)	1.18(-8)	1.17(-8)	1.23(-8)	1.27(-8)		
7-3	1.11(-7)	1.20(-7)	1.29(-7)	1.36(-7)	1.39(-7)		
7-4	8.64(-7)	9.61(-7)	1.00(-6)	1.01(-6)	1.01(-6)		
7-5	7.70(-6)	8.30(-6)	7.92(-6)	7.50(-6)	7.10(-6)		
7-6	1.55(-4)	1.51(-4)	1.44(-4)	1.33(-4)	1.25(-4)		
8-1	3.98(-10)	3.13(-10)	2.70(-10)	2.58(-10)	2.74(-10)		
8-2	8.75(-9)	7.71(-9)	7.54(-9)	7.81(-9)	8.09(-9)		
8-3	6.71(-8)	7.01(-8)	7.48(-8)	7.88(-8)	8.00(-8)		
8-4	4.21(-7)	4.65(-7)	4.89(-7)	4.92(-7)	4.82(-7)		
8-5	2.00(-6)	2.13(-6)	2.15(-6)	2.08(-6)	1.99(-6)		
8-6	1.86(-5)	1.84(-5)	1.75(-5)	1.60(-5)	1.49(-5)		
8-7	2.71(-4)	2.57(-4)	2.40(-4)	2.10(-4)	2.00(-4)		

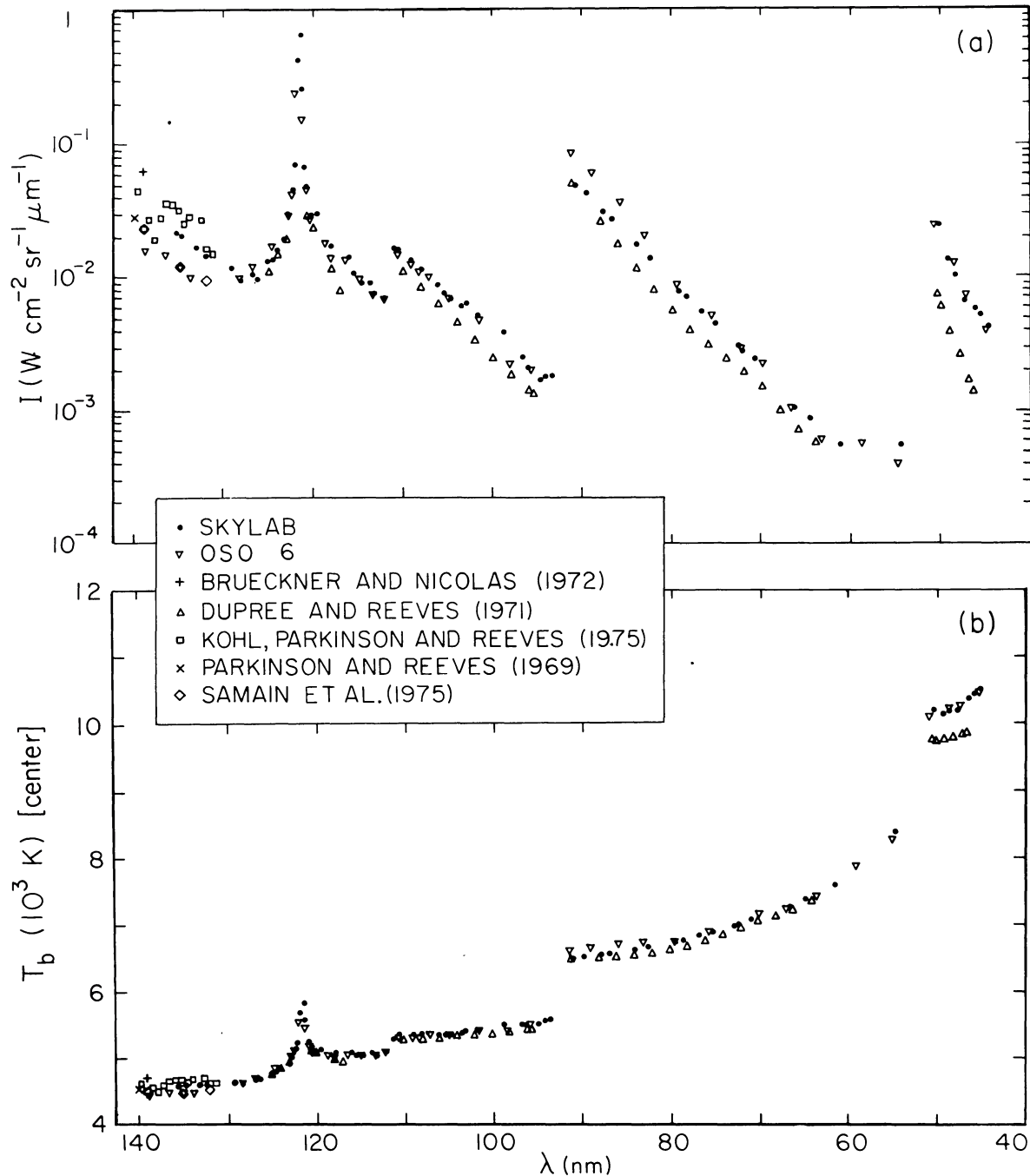


FIG. 3.—Observed values of the disk-center continuum intensity (*upper*) and the corresponding central brightness temperatures (*lower*) in the wavelength range 40–140 nm.

distance 1 AU from the center of the Sun is related to  $I_\lambda$  by

$$F_\lambda = \pi r_\odot^2 F'_\lambda = 6.7997 \times 10^{-5} F'_\lambda, \quad (6)$$

where  $r_\odot$  is the solar radius expressed in AU, and

$$F'_\lambda = 2 \int_0^1 I_\lambda \mu d\mu; \quad (7)$$

$F_\lambda$  and  $F'_\lambda$  have the units  $\text{W cm}^{-2} \mu\text{m}^{-1}$ .

These definitions are such that  $I_\lambda$  and  $F'_\lambda$  are equal to the Planck function  $B_\lambda(T)$  when the radiation emerges from an isothermal atmospheric region with temperature  $T$  under conditions of both pure absorption and LTE such that the source function is equal to  $B_\lambda(T)$ . We use the equations  $I_\lambda = B_\lambda(T_b^{\text{center}})$  and  $F'_\lambda = B_\lambda(T_b^{\text{disk}})$  to define wavelength-dependent brightness temperatures corresponding to given values of intensity and flux. (See eqs. 19 and 20 of Paper II.)

*a) Central Intensity between 40 nm and 140 nm*

All recent central intensity observations, as well as the corresponding disk-center brightness temperatures, in the range 40–140 nm are shown in Figure 3. The observations by Kohl, Parkinson, and Reeves (1975), Samain *et al.* (1975), Brueckner and Nicolas (1972), and Parkinson and Reeves (1969) were shown earlier in Paper II. The observations of Samain *et al.* (1975) are tabulated and discussed in detail by Samain (1978, 1979, 1980). In § IV we compare our results with Samain's data in the wavelength range 135–168 nm.

Figure 3 includes intensities derived from measurements that were made with the Harvard spectroheliometer aboard *Skylab* (Reeves, Huber, and Timothy 1977). These intensities are equivalent to the quiet-region average values reported by Vernazza and Reeves (1978). The observations have a spectral resolution of  $\sim 0.16$  nm (1.6 Å). However, the wings of the instrumental profile extend for several Å, and some contamination of the continuum spectral windows by strong emission lines may occur. Most of the Lyman continuum is free from the effects of emission lines, but the C I and He I continua may be contaminated by such lines. The C I and He I data thus provide upper limits for the continuum intensities. The C I continuum data shortward of 110 nm are contaminated by the 50.4 nm He I continuum which appears in second order at 100 nm. An effort was made to remove this effect, but since the second-order absolute calibration is not well known, the continuum intensities between 90 nm and 100 nm may be uncertain by as much as a factor of 2.

The Harvard *Skylab* data were calibrated on an absolute scale by means of simultaneous observations of the same quiet area made from the satellite and from two sounding rockets (Reeves, Huber, and Timothy 1977). The time dependence of the calibration was established by assuming that the flux emitted by low-chromospheric lines from quiet regions did not change with time. This absolute calibration is believed to have an accuracy of  $\pm 40\%$  except shortward of 50 nm where its accuracy is believed to be  $\pm 70\%$ .

The continuum observations between 40 nm and 130 nm from the *OSO 4* satellite have been published by Dupree and Reeves (1971). Also shown here are the continuum data we derived from *OSO 6* measurements using the same calibration as that described by Dupree *et al.* (1973). These observations have a spectral resolution of 0.32 nm compared with the 0.16 nm resolution of the *Skylab* data. In both cases the instrumental profile extends several Å from the line center, producing contamination of the continuum intensities by strong emission lines. The *OSO 6* data were cross-calibrated with coordinated rocket spectrometer data obtained by H. E. Hinteregger; the *OSO 4* observations were calibrated by comparing them with published values of the solar flux at comparable activity levels. All of the spectrometers

underwent prelaunch laboratory calibrations. The *OSO 4* and *OSO 6* absolute calibrations are probably no better than factors of 2, and the uncertainty in the continuum intensities is about a factor of 3. The uncertainty is larger at wavelengths shorter than 50 nm.

*b) Flux between 40 nm and 140 nm*

All recent flux observations, as well as the corresponding brightness temperatures, in the range 40–140 nm are shown in Figure 4. Since, as mentioned above, emission lines dominate in this part of the solar spectrum, there are few continuum observations of the solar flux. The spectrum from 27 nm to 131 nm was measured by Hall and Hinteregger (1970) from the *OSO 3* satellite. They report continuum observations only between 70 nm and 90 nm in the Lyman continuum. This spectral range is relatively free of emission lines, and there is no need for high-resolution observations. These observations seem to be well calibrated.

Heroux, Cohen, and Higgins (1974) measured the solar flux from 5 nm to 122 nm during a rocket flight on 1972 August 23. They report a few continuum observations in the range 70–90 nm near the head of the Lyman continuum. They estimated an error of  $\pm 30\%$  for these continuum fluxes. We also show the Lyman continuum fluxes obtained by Higgins (1976) from a rocket flight on 1971 November 9, as well as those of Schmidtke *et al.* (1977) obtained in 1973 with the German-U.S. satellite *Aeros A*.

The *OSO 4* satellite was used to obtain full-disk spectroheliograms in addition to central intensities. The solar flux can be derived from these spectroheliograms. The results are given by Reeves and Parkinson (1970). The calibration used is the same as that of Dupree and Reeves (1971) mentioned above, and the same limitations apply. Several observations on different dates were performed at the same wavelength, and in certain cases there were some apparent changes with time; the time averages of these fluxes are shown.

Rottman (1974) measured the flux in the range 116–185 nm averaged over 1 nm intervals during two rocket flights, 1972 December 13 and 1973 August 30. Flux measurements in the range 123–194 nm, also averaged over 1 nm intervals, were made by Heroux and Swirbalus (1976) with a rocket spectrometer flown on 1973 November 2 and 1974 April 23. Their estimated errors are  $\pm 20\%$ . These measurements and Rottman's are shown in Figure 4 for  $\lambda < 140$  nm, and in Figure 5 of Paper II for  $\lambda > 140$  nm.

*c) Brightness Temperature between 0.3 mm and 20 mm*

We show in Figure 5 a selection of the available microwave and radio observations of the Sun in the range 0.3–20 mm; we have plotted these observations as

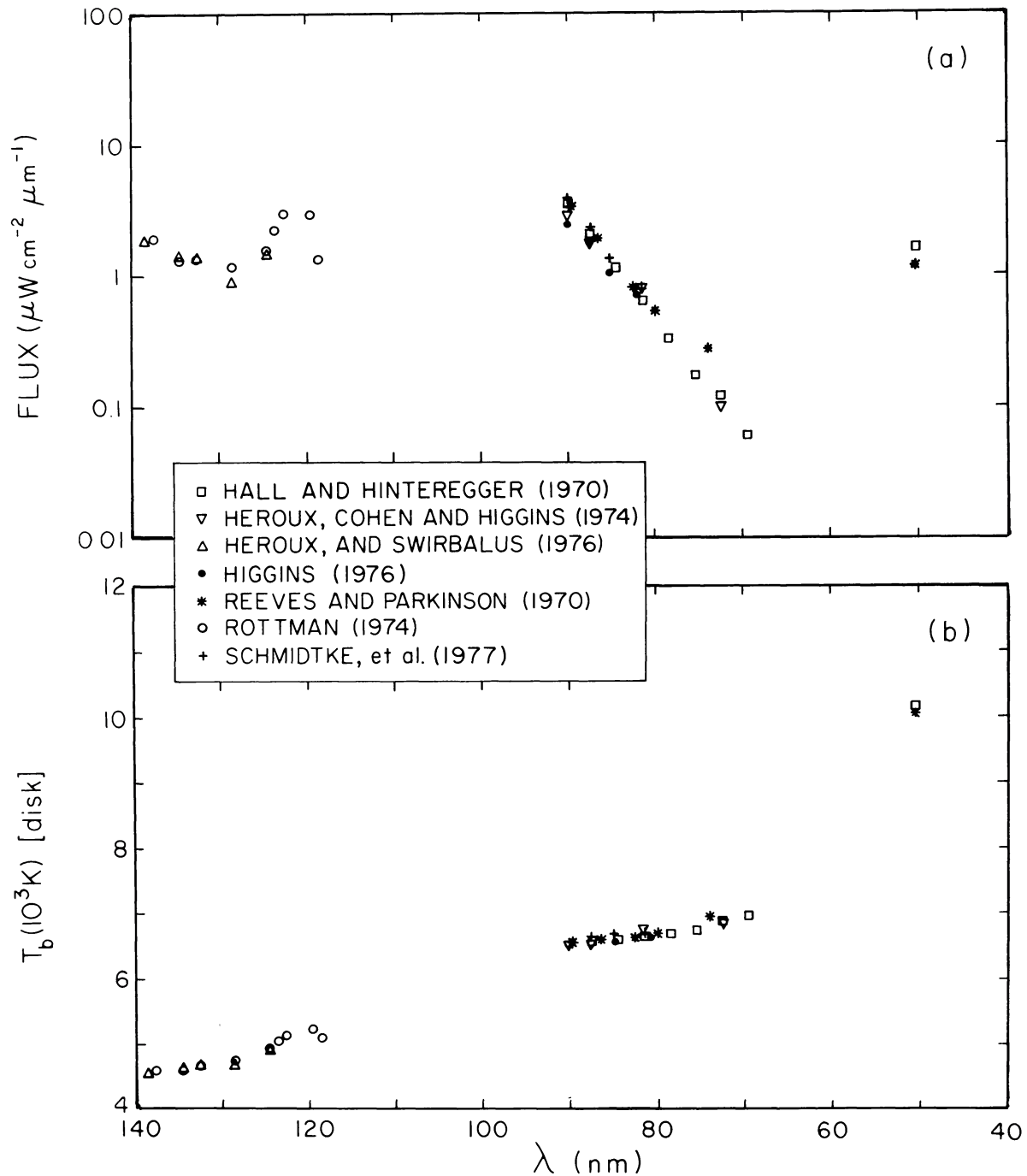


FIG. 4.—Observed values of the full-disk continuum flux, at 1 AU (*upper*) and the corresponding disk brightness temperatures (*lower*) in the wavelength range 40–140 nm.

brightness temperatures (see above, and eqs. 19 and 20 of Paper II). Some of the brightness temperatures are based on fluxes. Because most of the measurements in this spectral range are made with low spatial resolution, and because there is little or no observed center-to-limb variation, a uniform emitting disk is assumed in converting from intensity to flux.

Linsky (1973) used the Moon as a standard to recalibrate solar observations in those cases where ratios between solar and lunar brightness temperatures were available. The original observations in this recalibrated set are those of Bastin *et al.* (1964), Buhl and Tlamicha (1968), Epstein *et al.* (1968), Fedoseev (1963), Low and Davidson (1965), Namov (1963), Reber (1971),

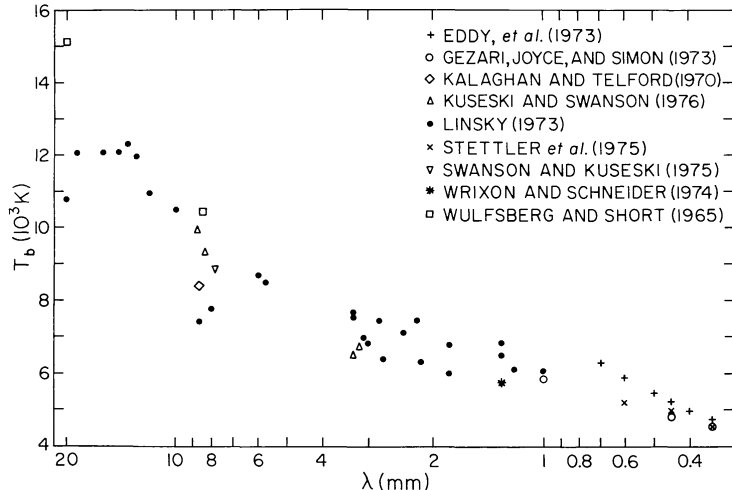


FIG. 5.—Selected brightness temperature observations of the Sun at millimeter wavelengths

Salomonovich (1958), Salomonovich, Koshenko, and Noskova (1959), Staelin *et al.* (1968), Tolbert and Coats (1963), Tolbert and Straiton (1961), Ulich, Cogdell, and Davis (1973), and Wrixon and Hogg (1971).

Figure 5 includes the solar brightness temperatures based on Sun-Moon ratios that have been determined more recently by Wrixon and Schneider (1974), Swanson and Kuseski (1975), and Kuseski and Swanson (1976). We also show the observations at 8.6 mm by Kalaghan and Telford (1970) and at 20 mm by Wulfsburg and Short (1965), and the measurements for  $\lambda < 1$  mm by Eddy *et al.* (1973), Gezari, Joyce, and Simon (1973), and Stettler *et al.* (1975).

The observations in Figure 5 show that the brightness temperature generally increases with wavelength throughout the spectral range  $\lambda > 0.3$  mm.

#### d) Inhomogeneous Structure

High-resolution spectroheliograms in chromospheric lines (Reeves *et al.* 1974; Reeves 1976) show the inhomogeneous structure in the form of a chromospheric network. These structures are also observed at continuum wavelengths as seen in Figure 6 (Plate 28) where we show four spectroheliograms taken by the Harvard spectroheliometer aboard *Skylab*. These spectroheliograms were taken at the wavelengths 104.4, 121.1, 90.7, and 74 nm, corresponding to the C I continuum, the L $\alpha$  wing, and two wavelengths in the Lyman continuum, respectively. The emission at the first three of these wavelengths originates at temperatures between 6000 K and 8500 K in the chromosphere, while the emission at 74 nm originates at higher temperatures (see Fig. 36 of § V). The spatial resolution of these spectroheliograms is 5''  $\times$  5'' and they cover a 5'  $\times$  5' area on the solar surface. Their spectral resolution is 0.16 nm.

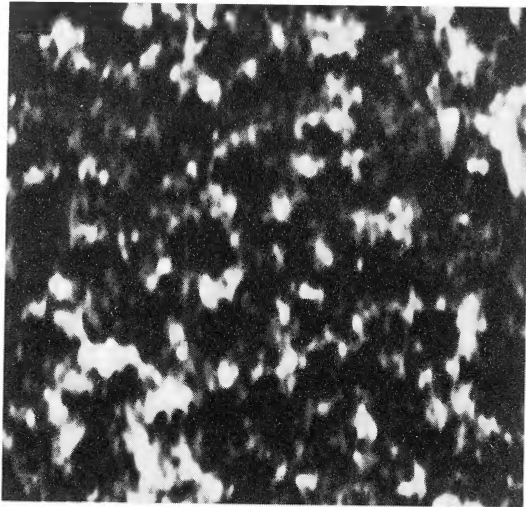
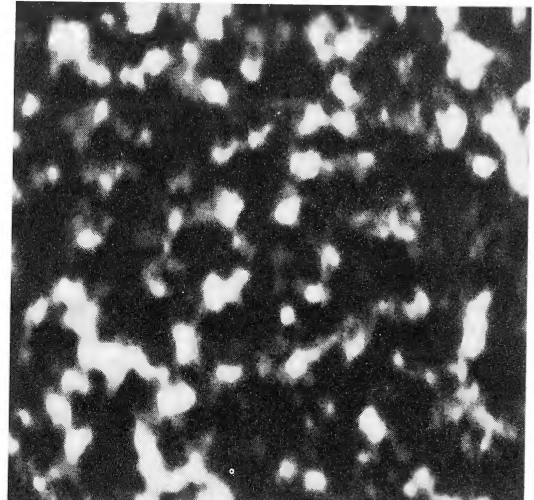
The average contrast in the emission between the network boundaries (bright elements) and the cell centers

(dark elements) is between 1.8 and 2.2, although individual image elements show much greater contrast. This contrast suggests that the temperature and density structure of the network boundaries differs from that of the cell centers.

Reeves (1976) has studied the chromospheric network in detail. He has obtained intensity histograms for average quiet areas and established intensity distributions for the cell centers and the network. Following his work we have obtained histograms of the intensity (expressed in terms of count rates) at several wavelengths in the Lyman continuum, the C I continuum, and the L $\alpha$  wing using spectroheliograms such as those in Figure 6. A typical histogram for a wavelength in the Lyman continuum ( $\lambda = 90$  nm) is shown in Figure 7. This distribution is similar to those derived by Reeves for transition region lines. While such intensity histograms are given in terms of count rates, absolute intensities can be obtained by equating the average count rate to the absolute value given in Figure 3. (The component designations A through F in Fig. 7 will be explained below.)

In Figure 8 we show the intensity at  $\lambda = 104.4$  nm in the C I continuum plotted against the intensity at  $\lambda = 74$  nm in the Lyman continuum and the intensity at 121.1 nm in the L $\alpha$  wing plotted against the Lyman continuum intensity at  $\lambda = 90.7$  nm. Each data point refers to a different location in the observed quiet area. To first approximation, the intensities in the C I continuum and the L $\alpha$  wing are proportional to the intensity in the Lyman continuum. We have verified that such proportional relationships exist between any EUV continuum intensities or line intensities formed in the chromosphere. We assume that the scatter in Figure 8 is due to statistical errors in the measurements, or to temporal fluctuations not significantly affecting the mean temperature structure. Also, we assume that there is a one-to-one correlation between the bright-to-faint intensity

1973 JULY 8

C I Continuum ( $\lambda = 104.4 \text{ nm}$ )Lyman Continuum ( $\lambda = 74.0 \text{ nm}$ )

1973 JULY 9

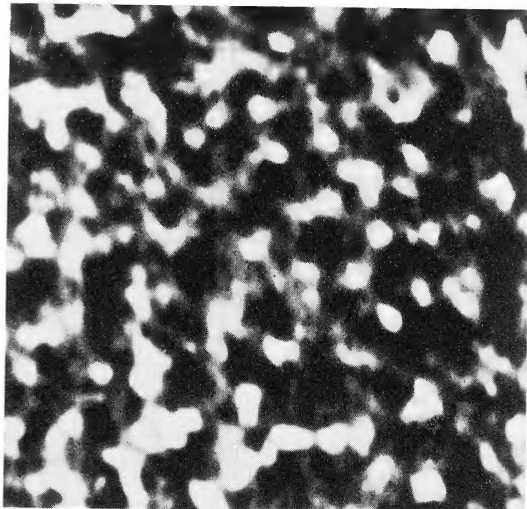
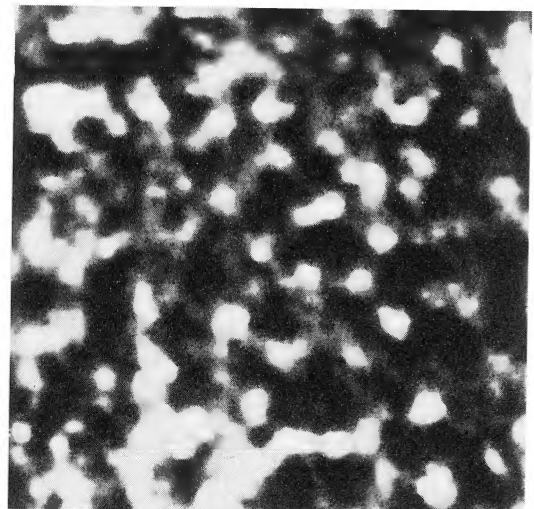
Lyman Alpha Wing ( $\lambda = 121.1 \text{ nm}$ )Lyman Continuum ( $\lambda = 90.7 \text{ nm}$ )

FIG. 6.—*Skylab* spectroheliograms of two 5'  $\times$  5' areas of the solar surface, at wavelengths 104.4 and 74 nm (above) and wavelengths 121.1 and 90.7 nm (below).

VERNAZZA *et al.* (see page 647)

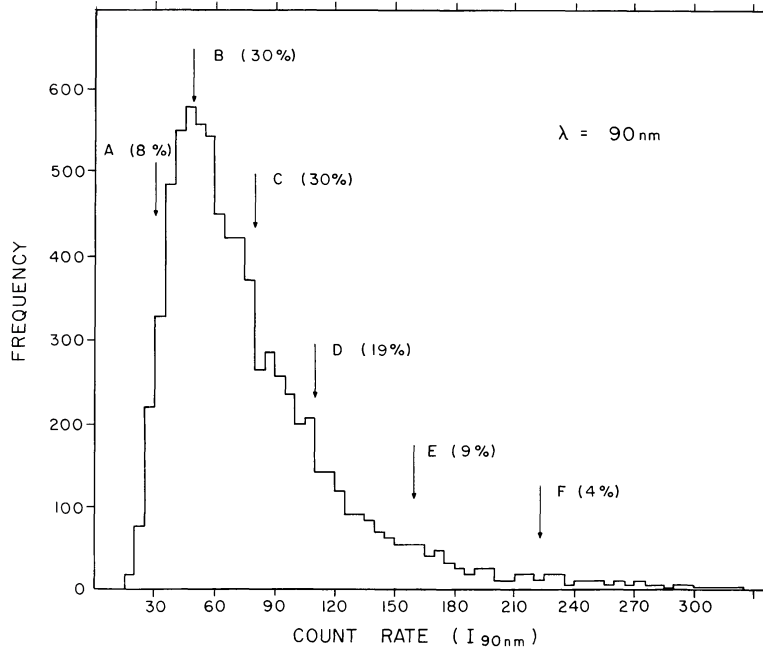


FIG. 7.—Histogram of intensity measurements at  $\lambda=90$  nm showing the frequency of occurrence of a given count rate in an average quiet area (such as in Fig. 6) plotted as a function of the count rate. The component designations A through F are explained in the text.

distribution at one continuum wavelength and that at another continuum wavelength. Then, given the emergent intensity at one wavelength from a given location, we can immediately obtain the intensity from the same location at any other wavelength using graphs similar to Figure 8.

In order to characterize the brightness distribution of the quiet chromosphere we have determined six representative components from the intensity histogram at  $\lambda=90$  nm shown in Figure 7. These six components correspond to the following features in the quiet chromosphere: (A) a dark point within a cell; (B) the average cell center; (C) the average quiet Sun; (D) the average network; (E) a bright network element; (F) a very bright network element. The arrows in Figure 7 are located at the intensity values that we associate with components A through F. The percent of the solar surface that we assume each component covers is indicated in each case.

Once we choose the six intensities from Figure 7 corresponding to the six features of the solar surface at  $\lambda=90$  nm, we can calculate all of the corresponding intensities at other wavelengths using graphs similar to Figure 8. In Table 8 we list the continuum intensities that we obtain for components A through F for 42 wavelengths between 42.2 nm and 131.8 nm. Each value in the table is based on observed relationships between intensities at two wavelengths, as shown in Figure 8. In many cases we used a two-step procedure, involving an intermediate wavelength, to obtain the values at the

listed wavelengths from those at  $\lambda=90$  nm. Such a procedure usually was carried out twice, with intermediate wavelengths larger and smaller than that in the table, and the results averaged. Table 8 includes  $L\alpha$  and  $L\beta$  intensities each integrated over a 0.16 nm bandpass. The continuum values are plotted in Figure 9. These results are consistent with the spectra for the average cell center and the average network obtained by Vernazza and Reeves (1978).

#### IV. THE MODEL CALCULATIONS

We have determined six atmospheric models to match the six EUV intensity distributions given in the previous section. The procedure we follow is the same as that outlined in Papers I and II but with additional features as described in the following paragraphs.

We carry out non-LTE calculations for the atoms and ions in two groups: (1) H,  $H^-$ , C, Si, Fe, Mg, Al, He,  $He\ II$ , and (2) Ca,  $Ca\ II$ ,  $Mg\ II$ ,  $C\ II$ ,  $Si\ II$ , O,  $O\ II$ , Na, and B. The calculations for the first group are interdependent because each atom or ion provides enough opacity to affect the continuum intensity distribution which is used to determine photoionization rates. This group also contains the principal contributors to the electron number density which affects the ionization equilibrium of all constituents. These calculations are carried out iteratively until a converged solution is obtained. The atoms and ions in the second group have little effect on the continuum opacity or on  $n_e$ , and these calculations are performed only once to compare

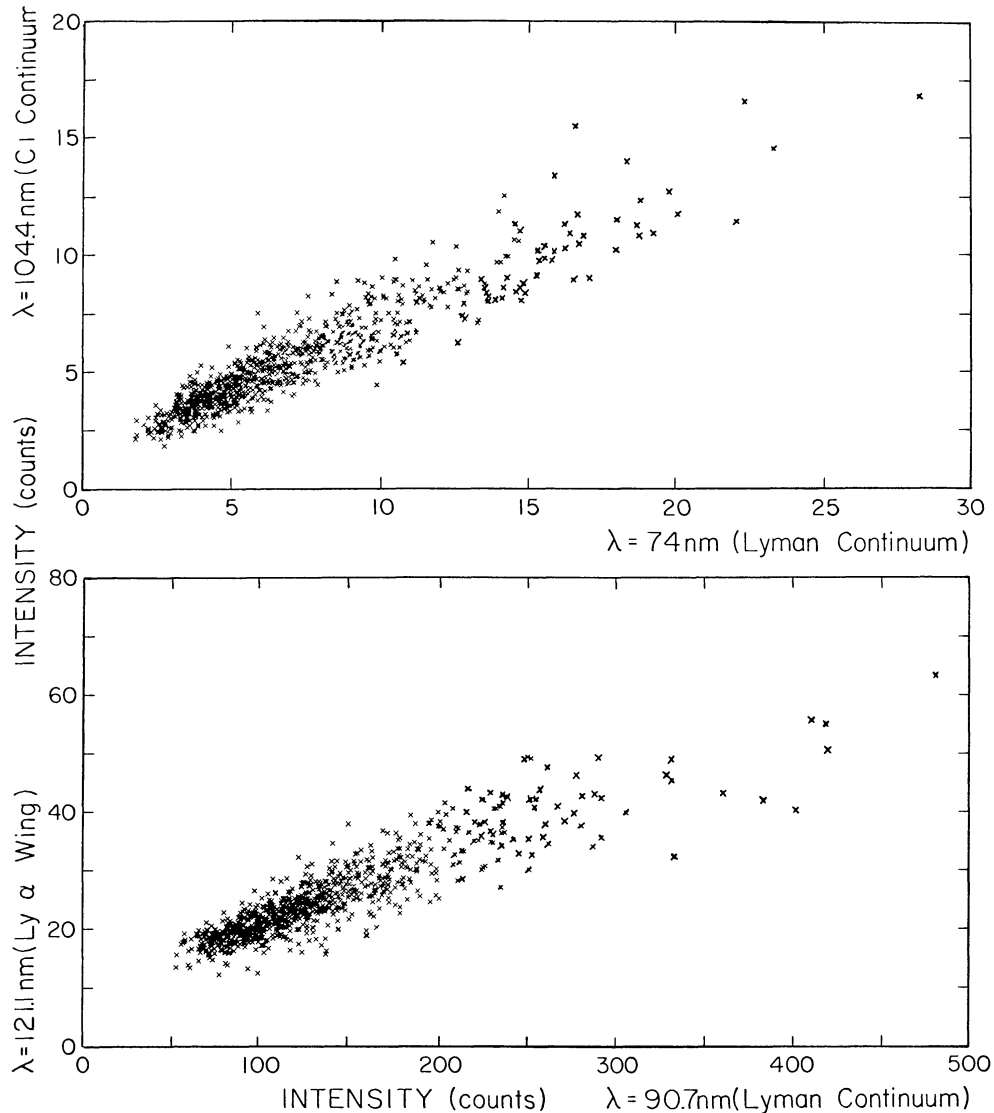


FIG. 8.—Each data point in both graphs represents the intensity from a given location measured at one wavelength plotted against the intensity from the same location at a second wavelength.

computed line spectra with observations. Except for Ca II and Mg II, the calculations we have made for atoms and ions in the second group are preliminary ones, carried out in search of contributions to the net radiative cooling rate considered in § IX.

As explained in § I we calculate the excitation and ionization of hydrogen with an atomic model having eight explicit levels and supplementary levels 9 through 12. In Appendix B we show how we incorporate supplementary levels in the statistical equilibrium equations to derive the Lyman continuum parameters  $\epsilon_1$  and  $\epsilon_2$  and the parameters  $\epsilon$  and  $B^S$  for line transitions.

In Paper I we showed that the wings of the L $\alpha$  line must be formed mostly by coherent scattering. In order to account for the observations we estimated that the

complete redistribution and coherent scattering contributions were 7% and 93%, respectively. Milkey and Mihalas (1973a, b) subsequently investigated the L $\alpha$  partial redistribution problem in detail and obtained results in general agreement with those in Paper I. Their work also led to similar partial redistribution calculations applied to Mg II (Milkey and Mihalas 1974) and Ca II (Shine, Milkey, and Mihalas 1975; Ayres and Linsky 1976) (see also the earlier Ca II results of Vardavas and Cram 1974).

In the present paper we carry out L $\alpha$ , Ca II, and Mg II partial redistribution calculations essentially following the procedure suggested by Heasley and Kneer (1976). A complete derivation of the method we use is given in Appendix A. As explained there, we select the

TABLE 8  
OBSERVED CONTINUUM AND LYMAN LINE INTENSITIES FOR COMPONENTS A-F

$\lambda$ (nm)	$I(10^{-3} \text{ W cm}^{-2} \text{ sr}^{-1} \mu\text{m}^{-1})$						weighted mean	
	A (8%)	B (30%)	C (30%)	D (19%)	E (9%)	F (4%)		
He	42.2	1.30	2.10	3.30	4.40	6.30	9.00	3.49
	47.1	1.47	2.39	3.95	5.29	7.49	10.6	4.12
	47.6	2.06	2.98	5.11	7.31	9.34	13.3	5.36
	49.4	4.80	6.80	10.3	13.3	18.4	26.0	10.7
	50.3	6.97	10.1	15.5	20.5	28.6	39.5	16.3
	74.1	1.08	1.79	3.16	4.22	6.15	8.82	3.09
	75.6	1.18	2.03	3.70	4.80	7.14	10.5	3.79
	77.2	1.78	3.23	5.88	7.96	11.9	17.2	6.16
	78.4	2.48	4.32	7.62	9.90	14.6	21.6	7.84
	79.5	2.99	4.97	8.53	11.3	16.4	23.9	8.87
H	79.6	3.12	5.19	8.90	11.8	17.2	25.0	9.27
	80.6	3.39	5.76	10.5	14.2	20.5	30.0	10.9
	82.3	4.53	8.40	15.0	20.7	30.0	43.0	15.7
	82.7	5.60	8.75	16.0	23.5	30.4	44.0	16.8
	83.8	6.72	11.2	19.1	25.6	37.1	54.1	20.0
	84.5	7.61	12.5	21.4	28.6	41.5	60.5	22.4
	85.1	7.77	12.9	22.2	29.6	43.6	62.7	23.2
	86.4	8.40	14.0	24.0	32.0	46.5	67.7	25.0
	86.4	9.80	17.1	29.3	39.7	56.8	82.8	30.7
	86.8	10.1	17.6	30.3	41.0	58.7	83.6	31.6
C	87.7	11.9	20.8	35.7	48.7	69.3	97.0	37.3
	88.2	14.7	22.9	37.1	50.0	71.0	101	39.1
	88.8	15.9	24.8	40.2	54.2	76.7	108	42.3
	89.0	16.2	25.4	41.2	55.6	78.7	110	43.3
	90.0	18.2	28.4	46.0	62.0	89.0	124	48.5
	90.6	20.1	31.4	50.7	68.4	97.0	136	53.4
	90.7	20.7	32.3	52.2	70.5	100	140	56.0
	100.4	2.29	3.43	4.85	6.26	8.00	10.8	5.01
	101.4	2.60	3.70	5.17	6.92	9.60	12.1	5.61
	105.9	5.61	6.99	9.44	11.1	14.7	20.1	9.61
L $\alpha$	107.5	6.50	8.10	11.9	14.5	20.3	28.2	12.2
	109.8	9.62	12.0	16.0	19.7	27.0	37.3	16.8
	114.1	5.03	6.31	8.28	9.81	12.9	17.7	8.51
	115.4	7.39	8.57	10.6	12.3	15.4	20.0	10.9
	118.1	11.0	13.0	16.0	18.1	22.1	27.8	16.1
	120.5	20.0	23.4	30.5	34.9	43.2	54.1	30.6
	121.0	43.7	53.0	72.0	85.0	110	149	73.0
	121.1	65.0	80.0	102	132	173	230	110
	122.3	37.4	47.5	65.4	81.8	108	146	68.0
	123.2	11.7	14.6	19.5	23.8	30.6	40.8	20.1
C	129.4	5.00	7.10	9.66	12.0	15.4	21.0	9.93
	131.8	5.26	8.18	10.4	12.2	15.4	21.1	10.6
	J L $\alpha$	2.96 <sup>a</sup>	4.23	6.40	8.37	11.6	15.9	6.70
	J L $\beta$	3.78 <sup>b</sup>	5.41	8.19	10.7	14.8	20.3	8.56

<sup>a</sup>( $\times 10^{-3} \text{ W cm}^{-2} \text{ sr}^{-1}$ )  
<sup>b</sup>( $\times 10^{-5} \text{ W cm}^{-2} \text{ sr}^{-1}$ )

values of certain parameters empirically in order to obtain agreement between computed and observed L $\alpha$  profiles.

The *Skylab* EUV data between 40 and 140 nm given in the previous section allow us to determine the six atmospheric models extending from (a) the height in the chromosphere-corona transition region where the center of the L $\alpha$  line is formed to (b) the height in the low chromosphere where the L $\alpha$  wing, the carbon 109.8 nm

continuum, and the silicon 152.4 nm continuum are formed (see Fig. 1). Some preliminary He I and He II calculations were used to extend the model to 10<sup>5</sup> K. As explained later in this section we use rocket data in the range 135–168 nm obtained by Samain (1978), Kohl, Parkinson, and Reeves (1975), and Heroux and Swirbalus (1976) to determine the models in the temperature-minimum region.

Figure 1 indicates other spectral features which are

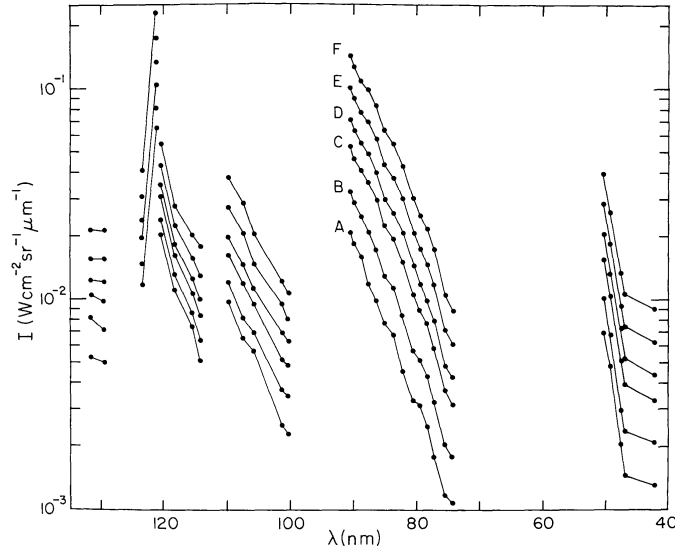


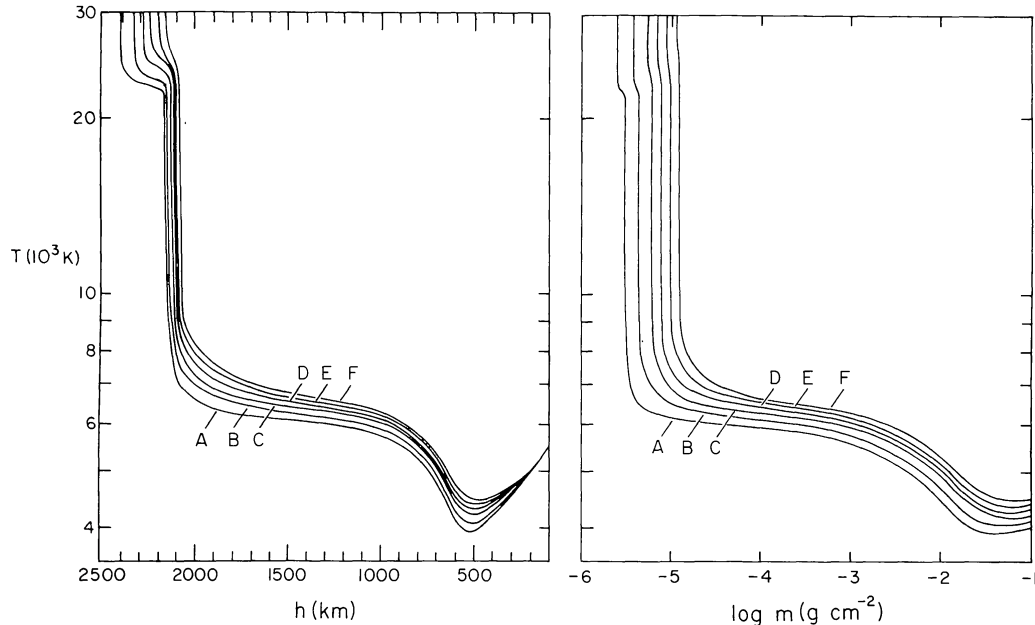
FIG. 9.—Observed EUV continuum intensities for quiet-Sun brightness components A–F

also formed at various heights from the upper photosphere to the chromosphere-corona transition region, namely, the continua from  $50 \mu\text{m}$  to  $3 \text{ cm}$ , the  $\text{H}\alpha$  line, and the  $\text{Ca II}$  and  $\text{Mg II}$  resonance lines. We have not used the  $\text{Ca II}$  and  $\text{Mg II}$  lines to determine the temperature structure of the models, but these lines were used to determine the microvelocity structure (see below). We also show the comparison between our calculations and these observed profiles; as shown later in this section a disagreement occurs at the temperature minimum. We discuss possible causes for this disagreement in § VIII.

Figure 10 shows the temperature as a function of both height and column mass for six models which have been determined empirically to match the observed intensity distributions in Figure 9.

In the model calculations we also specify the microvelocity  $V$  as a function of height, which affects the Doppler width

$$\Delta\nu_D = \frac{v_0}{c} \left( \frac{2kT}{M} + V^2 \right)^{1/2} \quad (8)$$

FIG. 10.—Temperature as a function of height and of  $\log m$  for models A–F

of a line at frequency  $\nu_0$ , where  $M$  is the atomic mass. We also use  $V$  to add a turbulent pressure contribution

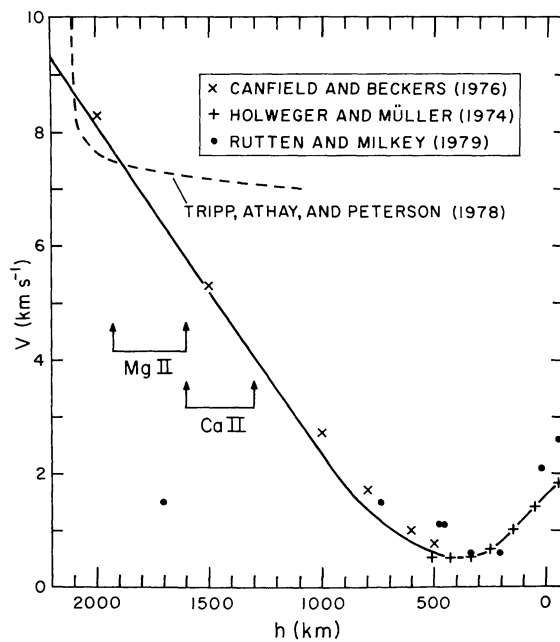


FIG. 11.—The microvelocity distribution adopted for models A–F (solid curve) plotted against the height scale for model C and compared with values given by other authors. We use this velocity distribution for Doppler line broadening and to determine a turbulent pressure contribution in the hydrostatic equilibrium equation.

to the gas pressure  $P_g$  so that the total pressure is  $P = P_g + \frac{1}{2} \rho V^2$ , where  $\rho$  is the gas density. See our discussion of microvelocities and macrovelocities in § IV c of Paper II.

In all our six models A–F we use the same microvelocity  $V(h)$  shown as the solid line in Figure 11. Values of the microvelocity at various heights determined from observed line widths by Holweger and Müller (1974), Canfield and Beckers (1976), and Rutten and Milkey (1979) are indicated in the figure. We also show the relationship  $V = 0.09T^{1/2}$  suggested by Tripp, Athay, and Peterson (1978) for the upper chromosphere (the sound speed is  $V = 0.128T^{1/2}$ ) and the approximate heights at which the outer parts of the Ca II K and Mg II  $k$  Doppler cores are formed. Our choice of  $V(h)$  leads to good agreement between calculated and observed Ca II and Mg II Doppler widths.

Figure 12 shows the continuum intensities in the range 70–135 nm computed from the six temperature distributions in Figure 10. The observed values from Table 8 and Figure 9 are included for comparison. The calculated and observed values in the L $\alpha$  wing (118–125 nm) and the He I continuum (47–50.4 nm) are shown in Figures 13 and 14, respectively. Our He I and He II calculations include ionization by incident coronal line radiation as discussed by Avrett, Vernazza, and Linsky (1976). For simplicity we have used the same incident radiation in all six model calculations. Thus, in Figure 14 our calculated He I intensities for models A–F do

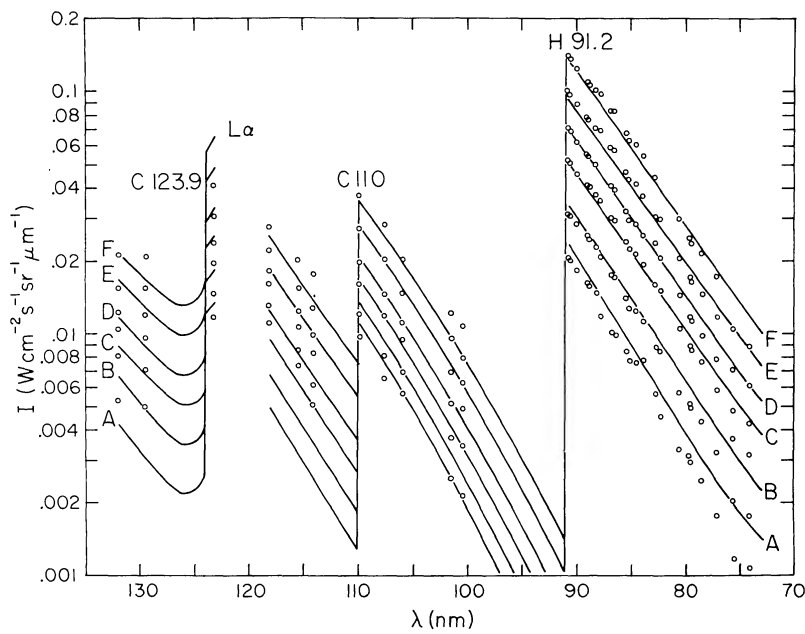


FIG. 12.—Comparison of observed and computed intensities in the range 70–135 nm, exclusive of the L $\alpha$  band (shown in Fig. 13)

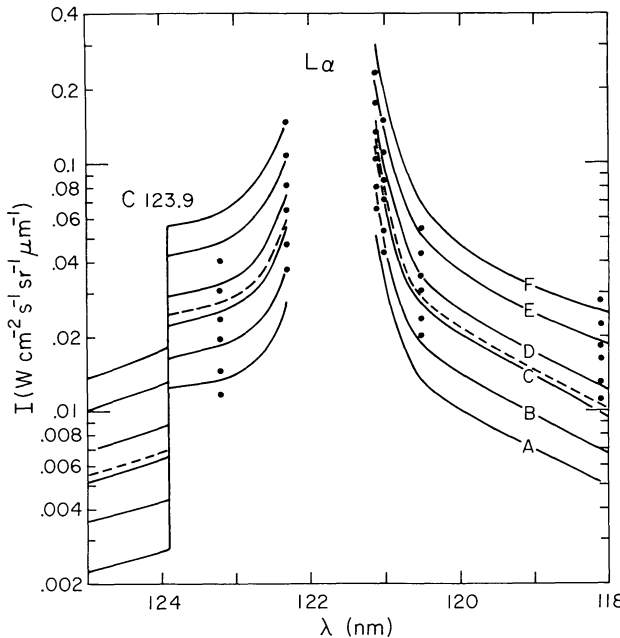


FIG. 13.—Comparison of observed and computed intensities in the wings of  $\text{L}\alpha$ .

not have the brightness range that would be calculated with separate values of the incident coronal radiation appropriate to each model. In § VI we include tables of our He I and He II results, but we will discuss these and other helium calculations in a subsequent paper.

As stated earlier, we have adjusted the temperature distributions by trial and error to obtain agreement between the calculated and observed values. Figures 12–14 show the best correspondence we were able to obtain.

The integrated  $\text{L}\alpha$  and  $\text{L}\beta$  intensities tabulated in Table 8 also were used in these model determinations. The comparison of calculated and observed integrated  $\text{L}\alpha$  and  $\text{L}\beta$  intensities is treated in the next section (Fig. 28).

Table 8 includes values of the spatial-average mean quiet-Sun intensity obtained from the sum of components A–F weighted by the fractions 0.08, 0.3, 0.3, 0.19, 0.09, and 0.04, respectively. In the same way we obtain the mean distribution from the calculated intensity components A–F. These mean calculated intensity values and those for model C are plotted in Figure 15 with the spatial-average observed intensities shown earlier in Figure 3.

In Figure 16 we plot the EUV flux distributions calculated from models A–F, the calculated weighted mean flux, and the observed continuum values shown earlier in Figure 4.

As indicated in Figure 1, the continuum in the wavelength region  $600 \mu\text{m}$  to  $3 \text{ cm}$  is formed at the same

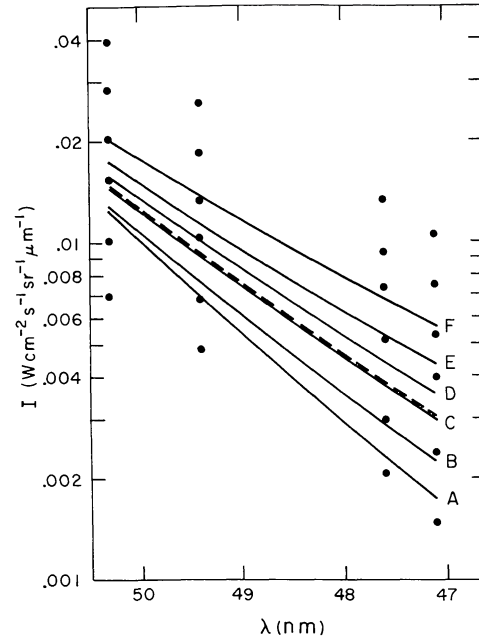


FIG. 14.—Comparison of observed and computed intensities in the He continuum, 47–50.4 nm.

chromospheric heights as the EUV spectrum considered above. In Figure 17 we compare the disk-center brightness temperatures from  $300 \mu\text{m}$  to  $2 \text{ cm}$  calculated for models A–F and the calculated weighted mean, with the observed brightness temperature values shown earlier in Figure 5. As noted in § III we have plotted observed whole-disk and disk-center values together because little center-to-limb variation is observed. Our plane-parallel model calculations predict limb brightening in this region because of the steep outward rise in temperature and because the continuum source function is the Planck function (see Fig. 36 in § V). We assume that inhomogeneities are responsible for reducing the limb brightening predicted by plane-parallel models.

Figure 1 shows that the structure of the temperature minimum region can be determined by the spectra in three wavelength regions: (1) the Si and Fe continua in the UV range 150–168 nm, (2) the  $50$ – $300 \mu\text{m}$  microwave continuum, and (3) the  $K_1$  and  $k_1$  (and the  $H_1$  and  $h_1$ ) minimum features in the wings of the Ca II and Mg II resonance lines. We have chosen to use the UV continuum data to determine the temperature-minimum portions of models A–F because these UV observations appear to be the most reliable ones, and we avoid the uncertainties involved in the Ca II and Mg II partial redistribution calculations.

Figure 18 shows two sets of observations: (1) measurements by Kohl, Parkinson, and Reeves (1975) of the intensity in successive  $0.63 \text{ nm}$  intervals which include all absorption and emission lines, and (2) measurements

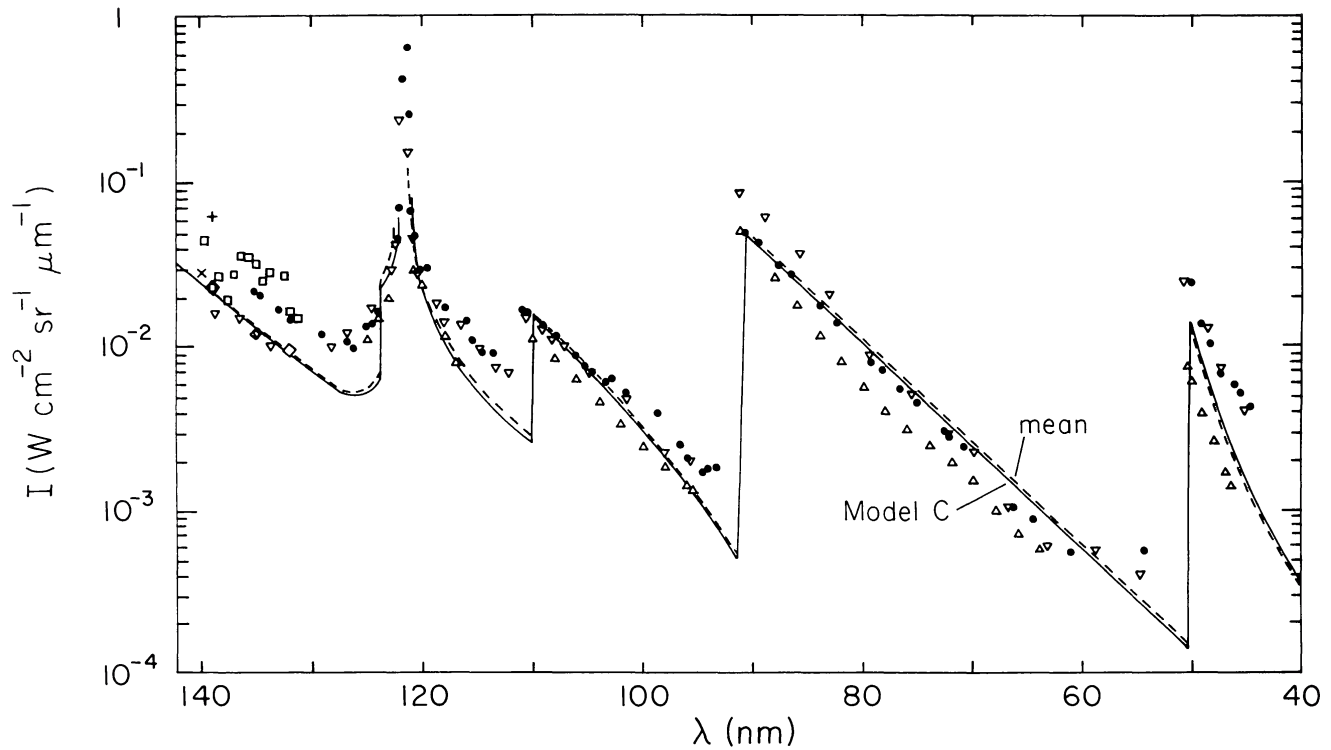


FIG. 15.—Comparison of the observed quiet-Sun EUV intensities from Fig. 3 with those from model C and from the weighted mean of models A–F.

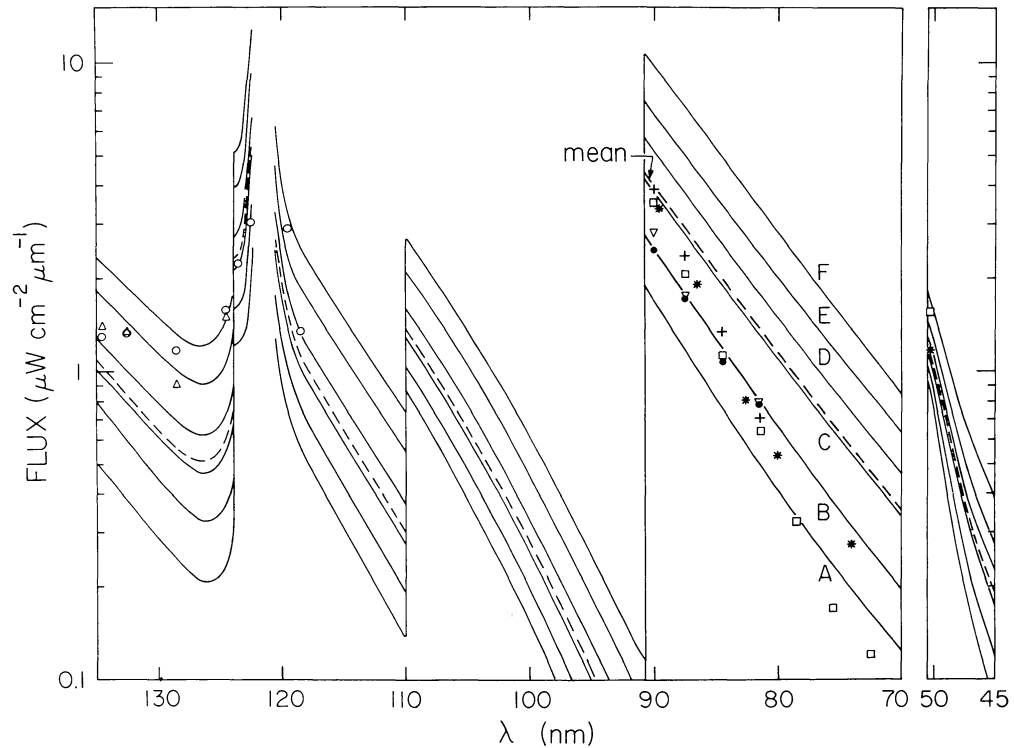


FIG. 16.—Comparison of the quiet-Sun EUV flux observations from Fig. 4 with the flux distributions calculated from models A–F and with the weighted mean of the six flux distributions.

## QUIET SUN EUV BRIGHTNESS COMPONENTS

655

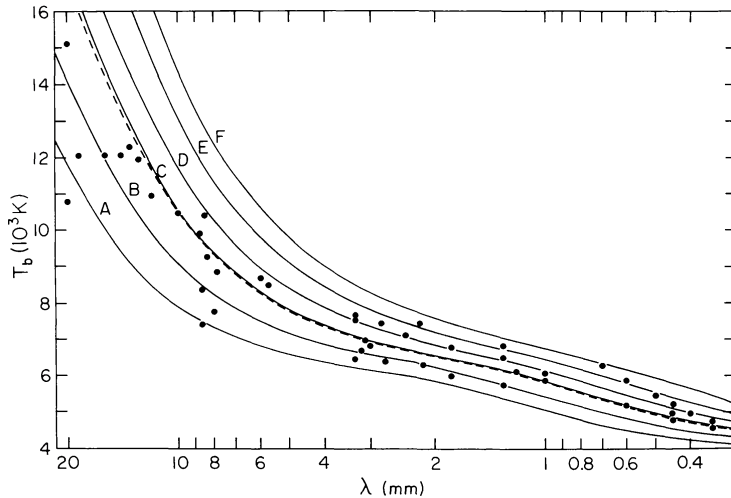


FIG. 17.—Comparison of the observed brightness temperatures at millimeter wavelengths from Fig. 5 with the calculated distributions from models A–F. The weighted mean is shown as a broken line.

by Samain (1978, 1979) of the continuum intensity at selected wavelengths which appear to be free of spectral lines. We extrapolated from the observations plotted in Figure 12 for components A–F to obtain estimates of the component A–F observations relative to the observed mean in Figure 18. We extrapolated on the basis of the heights of formation appropriate to the principal continua in Figures 12 and 18: the ratio of the component F and A intensities is observed to be about 7 and 4 at 90.7 and 109.8 nm, respectively, and we estimate the

ratio to be 3.5 and 2.5 at 152.4 and 168.1 nm. The temperature-minimum distributions plotted in Figure 10 give the component intensities shown in Figure 18.

Figure 19 shows the measurements by Heroux and Swirbalus (1976) of the flux in successive 1 nm intervals and the continuum flux measurements of Samain (1978, 1979) corresponding to the continuum intensities in Figure 18. The computed flux distributions for components A–F and the weighted mean computed flux are shown for comparison.

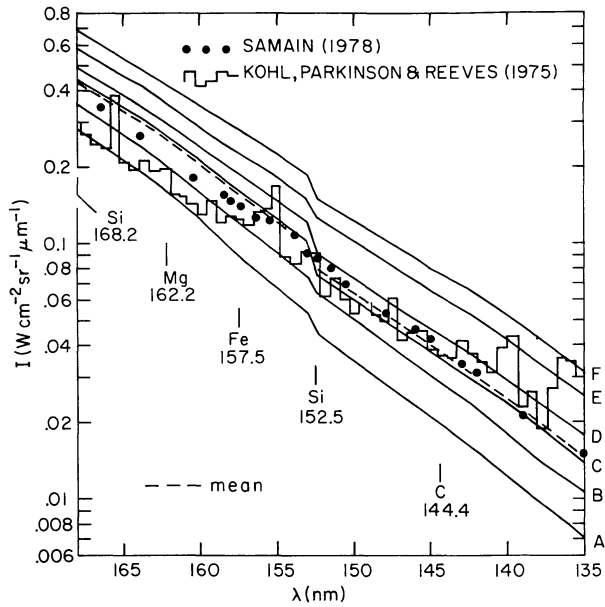


FIG. 18

FIG. 18.—Intensity distributions from models A–F in the range 135–168 nm compared with observations by Samain (1978) and Kohl, Parkinson, and Reeves (1975). The broken line is the weighted mean. Ionization limit wavelengths for C, Si, Fe, and Mg are indicated.

FIG. 19.—Flux distributions from models A–F in the range 135–168 nm compared with observations by Samain (1978) and Heroux and Swirbalus (1976). The broken line is the weighted mean.

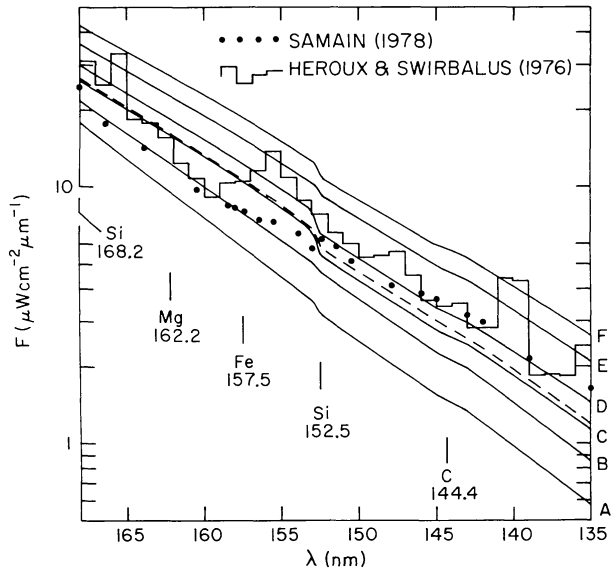


FIG. 19

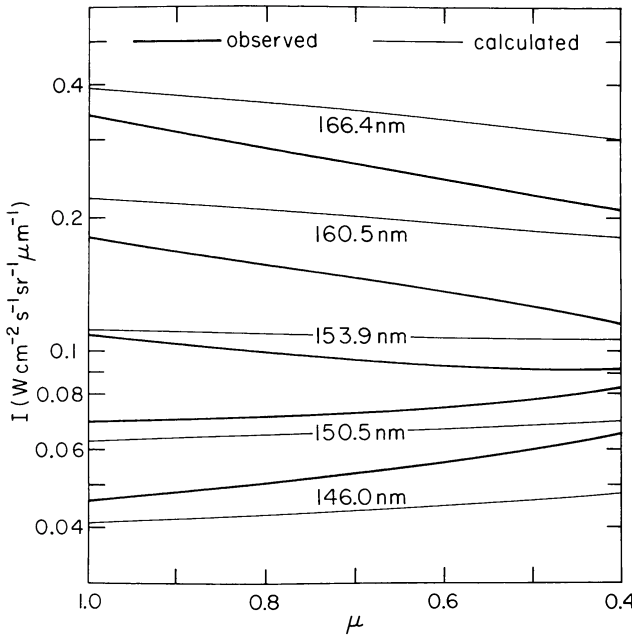


FIG. 20

FIG. 20.—Center-to-limb variation of continuum radiation emerging from the temperature-minimum region, observed by Samain (1978) and calculated from model C.

FIG. 21.—Center-to-limb variation observed by Samain (1978) at 166.4 nm and 146.0 nm, from the photospheric side and the chromospheric side of the temperature minimum, respectively, compared with the variations predicted by models A–F.

At the temperature minimum we expect inhomogeneities to affect the center-to-limb behavior to a smaller extent than in the chromosphere and that a meaningful comparison may be possible between the computed and observed center-to-limb behavior. Figure 20 shows the intensity as a function of  $\mu = \cos \theta$  at wavelengths between 146 and 166.4 nm from the disk center at  $\mu = 1$  to  $\mu = 0.4$ . The observations are those of Samain (1978, 1979), while the calculated values are obtained from model C.

As  $\mu$  decreases there is an increase in the height at which the intensity is formed. The positive slope of the lower curves in Figure 20 indicates that the intensity is formed on the chromospheric side of the temperature minimum, and the negative slope of the upper curves indicates that the intensity is formed on the photospheric side.

Figure 21 shows the observed center-to-limb variation at 146 and 166.4 nm compared with the corresponding variations calculated from models A–F. Figures 20 and 21 show that on the chromospheric side of the temperature minimum the limb brightening we calculate is less than observed, and on the photospheric side of the temperature minimum the limb darkening we calculate is less than observed. This appears to be a discrepancy which is unlikely to be accounted for by the presence of inhomogeneities. See § VIII.

We now consider the other spectra that can be used to determine the structure of the temperature minimum region. Figure 22 shows the brightness temperatures we

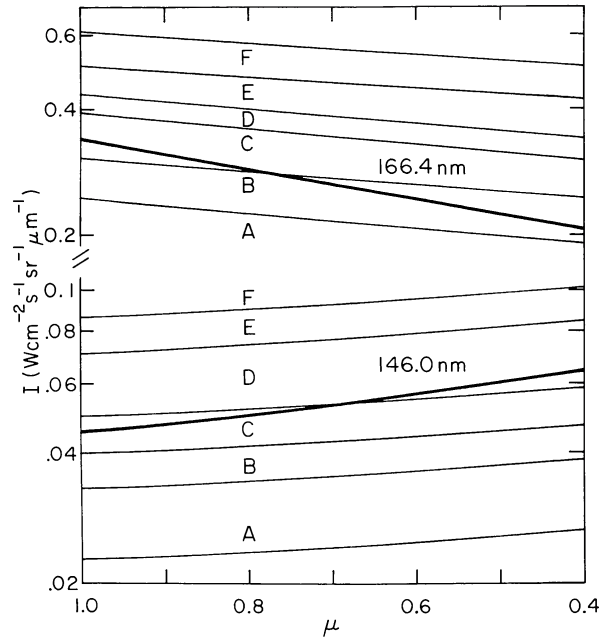


FIG. 21

calculate in the microwave region 33–500  $\mu\text{m}$ , compared with the observations obtained in two rocket flights by Rast, Kneubühl, and Müller (1978). The two sets of observations are plotted as bands of uncertainty. Our calculated mean brightness temperature is systematically lower than these observations, particularly on the photospheric side of the temperature minimum. It should be noted, however, that these observed brightness temperatures are higher than some of the earlier measurements, which we have plotted in a similar figure in Paper II, and for this reason it is not clear that there is a discrepancy between the observed and calculated values.

The profiles we calculate for the Ca II K line are shown in Figure 23. In our Ca II, Mg II, L $\alpha$ , and L $\beta$  calculations we use the partial redistribution method described in Appendix A. In the solution,  $\gamma_s$  is the probability for coherent scattering in the line wing outside the Doppler core. We assume that  $\gamma_s$  is the smaller of  $\Gamma_{\text{rad}} / (\Gamma_{\text{rad}} + \Gamma_E)$  and  $\gamma_{\text{max}}$ , where  $\Gamma_{\text{rad}}$  and  $\Gamma_E$  are the radiative and collisional damping coefficients for which the scattering in the given line is expected to be coherent and noncoherent, respectively, in the atom's frame. The upper limit  $\gamma_{\text{max}}$  is introduced to account for the effect of other redistribution mechanisms in the multilevel atom not included in the derivation of Omont, Smith, and Cooper (1972), e.g., radiative transitions to upper levels and the continuum and various collisional transitions (see Appendix A). We have not attempted to determine  $\gamma_{\text{max}}$  from the atomic transition rates, but

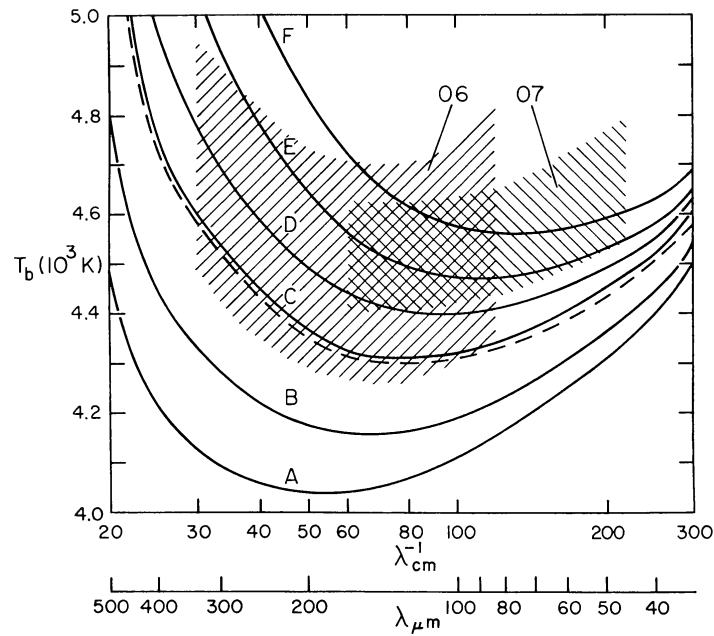


FIG. 22.—Microwave brightness temperatures from the temperature-minimum region. The shaded areas represent the measurement uncertainties in two rocket experiments by Rast, Kneubühl, and Müller (1978), while the curves are the predicted distributions from models A–F.

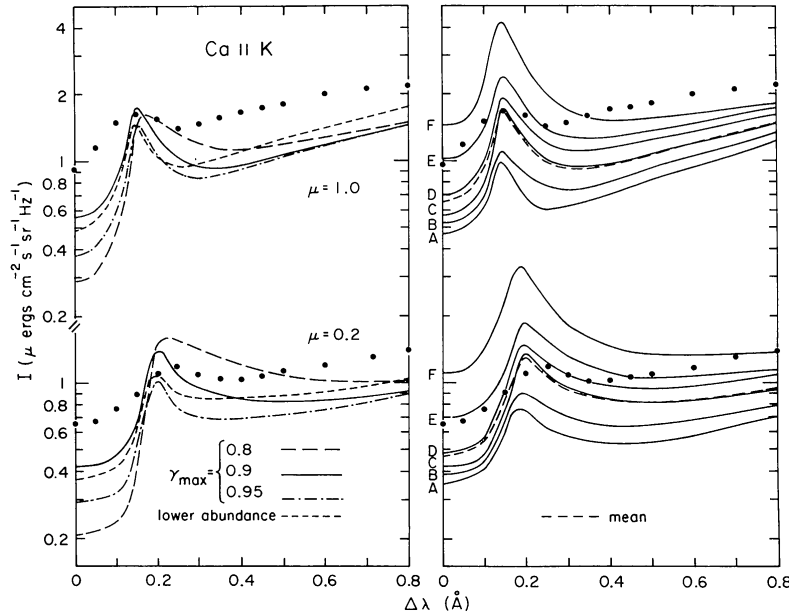


FIG. 23.—Computed Ca II K-line profiles for  $\mu=1.0$  and  $0.2$  compared with observed intensity values (indicated as dots). The left panel shows the profiles computed from model C with the partial redistribution parameters  $\gamma_{\max}=0.8, 0.9$ , and  $0.95$  (see Appendix A). Also shown is the result of lowering the abundance to  $N_{\text{Ca}}/N_{\text{H}}=1.75 \times 10^{-6}$  (with  $\gamma_{\max}=0.9$ ) compared to our standard adopted value of  $N_{\text{Ca}}/N_{\text{H}}=2.82 \times 10^{-6}$ . The right panel shows the profiles computed from models A–F with  $\gamma_{\max}=0.9$ .

instead have selected a value for  $\gamma_{\max}$  which leads to reasonable agreement between calculated and observed profiles. In the atmospheric regions of interest here,  $\gamma_{\max} < \Gamma_{\text{rad}} / (\Gamma_{\text{rad}} + \Gamma_E)$  so that  $\gamma_s = \gamma_{\max}$ .

The left panel of Figure 23 shows the center ( $\mu=1$ ) and limb ( $\mu=0.2$ ) profiles computed with model C and  $\gamma_{\max}=0.8, 0.9$ , and  $0.95$ . When  $\gamma_{\max}=0.8$  there is too much noncoherent scattering in the wings, causing the intensity decrease between the  $K_2$  peak and the  $K_1$  minimum to be too gradual and the  $K_1$  minimum to be located too far in the line wing.

We obtain acceptable line shapes with both  $\gamma_{\max}=0.9$  and  $\gamma_{\max}=0.95$ , but we have adopted  $\gamma_{\max}=0.9$  because the resulting intensities are somewhat higher and closer to the observed values than those with  $\gamma_{\max}=0.95$ . The left panel also shows the profiles computed with  $\gamma_{\max}=0.9$ , but the lower calcium abundance  $N_{\text{Ca}}/N_{\text{H}}=1.76 \times 10^{-6}$ , compared with the value  $N_{\text{Ca}}/N_{\text{H}}=2.82 \times 10^{-6}$  that we have adopted otherwise. The lower Ca abundance gives somewhat better agreement with the observations, but the right panel of Figure 23 shows that the results are more sensitive to changes in the temperature minimum distribution.

The heavy dots in Figure 23 represent spatially averaged and time averaged profiles observed from quiet regions. These observations are the same as those plotted in a similar figure by Ayres and Linsky (1976), which were determined from the *Preliminary Kitt Peak Solar*

*Atlas* (Brault and Testerman 1972), the absolute photometry of Houtgast (1970), and the limb darkening measurements of White and Suemoto (1968).

The right panel of Figure 23 shows the profiles computed from models A–F with  $\gamma_{\max}=0.9$ . As before, the mean computed profile is the sum of components A–F weighted by the area fractions  $0.08, 0.3, 0.3, 0.19, 0.09$ , and  $0.04$ , respectively. These results also suggest higher temperature-minimum values and higher temperatures in the upper photosphere than those we have chosen in order to match UV continuum observations. Ayres and Linsky (1976) show that much closer agreement with the observed profile can be obtained with a model having a temperature minimum value of  $4450$  K, compared with our value of  $4170$  K for model C.

The left panel of Figure 24 shows the center ( $\mu=1$ ) and limb ( $\mu=0.23$ ) profiles of the Mg II  $k$  line for  $\gamma_{\max}=0.95, 0.97$ , and  $0.99$ . The right panel shows the profiles computed from models A–F, and the mean profile, all with  $\gamma_{\max}=0.97$ . We have adopted the magnesium abundance  $N_{\text{Mg}}/N_{\text{H}}=3.9 \times 10^{-5}$ . The heavy dots represent the spatially averaged and time averaged observed profiles from quiet regions and are the same as those plotted in a similar figure by Ayres and Linsky (1976) from observations by Kohl and Parkinson (1976).

These results for Mg II are similar to those for Ca II in suggesting higher minimum temperatures. Ayres and Linsky (1976) found that in order to fit the  $k_1$  minimum

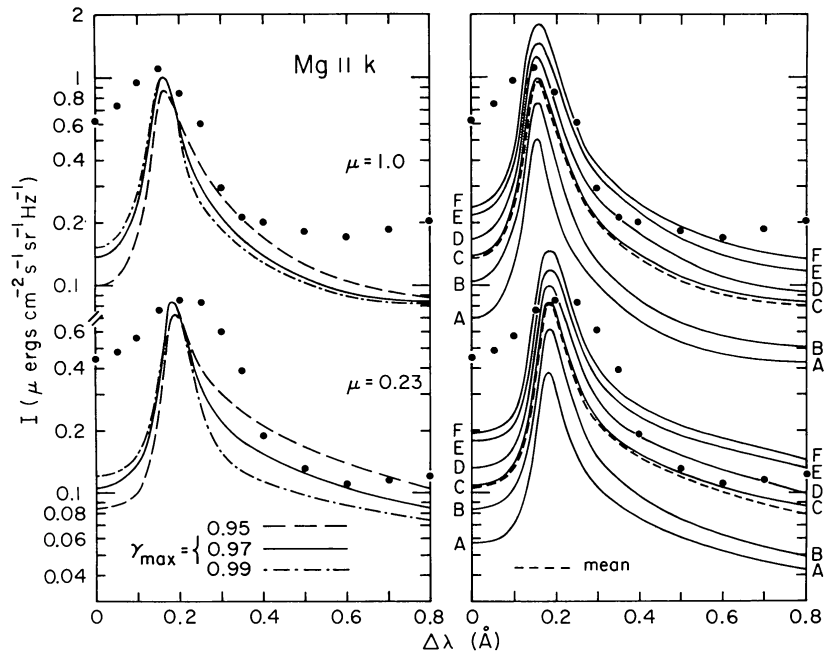


FIG. 24.—Computed Mg II  $k$ -line profiles for  $\mu=1.0$  and  $0.23$  compared with observed intensities (indicated as dots). The left panel shows the profiles computed from model C with the partial redistribution parameters  $\gamma_{\max}=0.95, 0.97$ , and  $0.99$  (see Appendix A). The right panel shows the profiles computed from models A–F with  $\gamma_{\max}=0.97$ .

intensity of the Mg II profile, a somewhat higher minimum temperature is needed,  $4500 (+80, -110)$  K, than is needed for the Ca II K line,  $4450 \pm 130$  K.

It has been suggested that the discrepancy between the higher minimum temperatures determined from the Ca II and Mg II resonance lines and the lower temperatures determined from the UV continuum may be due to different ways in which the cooler and hotter atmospheric components contribute to the spatially averaged intensities in the two cases. Figures 18, 23, and 24 show, however, that the weighted mean intensity is almost the same as determined from model C (our average quiet-Sun component) in both the UV continuum and the resonance lines. Figure 22 shows the same result in the microwave region.

Adopting higher minimum temperatures, however, leads to serious disagreement between the calculated and observed UV continuum intensity and flux values in Figures 18 and 19. We will discuss this problem in § VIII after showing (in Fig. 36) further details of our UV continuum calculations.

It should be noted that even if we have chosen a temperature minimum that is somewhat too low, our models at greater heights in the atmosphere remain valid. The atmospheric parameters as functions of column mass in the chromosphere and chromosphere-corona transition region are unaffected by the adopted structure of the temperature-minimum region. The chromospheric height scale, however, does depend on the temperature structure deeper in the atmosphere.

We conclude this section by showing comparisons of the computed and observed hydrogen H $\alpha$ , L $\alpha$ , and L $\beta$

profiles. The H $\alpha$  profiles from models A and F are plotted in Figure 25. The observed profile is determined from the residual intensities given by White (1964) and the absolute data of Labs and Neckel (1970).

The computed H $\alpha$  profile is sensitive to the adopted atomic model. Figure 26 shows profiles computed from model C and from model hydrogen atoms with three and 12 levels. The change in the H $\alpha$  profile with the increasing number of levels is partly due to the direct effect of the increasing number of transitions and partly due to changes in the ionization of hydrogen. The dependence of hydrogen ionization on the number of levels is discussed in the next section.

We finally show in Figure 27 the comparison between our computed L $\alpha$  and L $\beta$  profiles and the observed profiles of Gouttebroze *et al.* (1978) and Basri *et al.* (1979). The left panel of Figure 27 shows the L $\alpha$  profiles computed with our 12 level atomic model for hydrogen with  $\gamma_{\max} = 0.95, 0.98$ , and  $0.99$ . Also, we show the profile computed with  $\gamma_{\max} = 0.98$  and a five level atomic level.

Our L $\beta$  profiles were determined by partial redistribution calculations with  $\gamma_{\max} = 0.4$ . We have experimented with other values of  $\gamma_{\max}$  for L $\beta$  and have investigated other physical mechanisms, including those proposed by Gouttebroze *et al.* (1978), in attempts to obtain better agreement between calculated and observed L $\beta$  profiles, but so far without success.

The correspondence we obtain in Figure 27 between computed and observed L $\alpha$  profiles is similar to that obtained by Basri *et al.* (1979), but the two calculations differ substantially in two respects: (1) Basri *et al.*

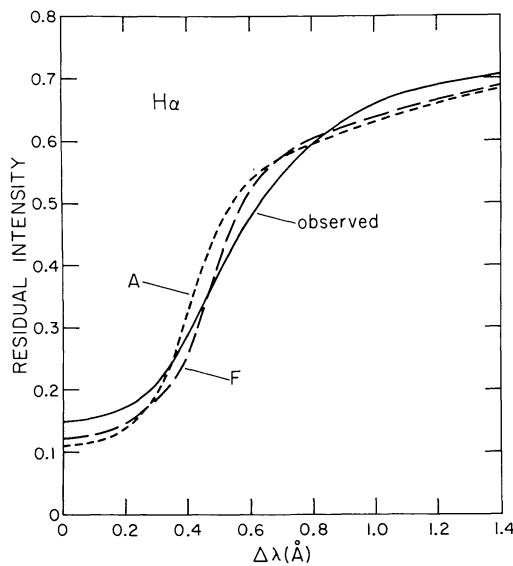


FIG. 25

FIG. 25.—H $\alpha$  profiles computed from models A and F compared with the observed average quiet-Sun profile.

FIG. 26.—H $\alpha$  profiles computed from model C with model hydrogen atoms having 12 and three levels, compared with the observed profile.

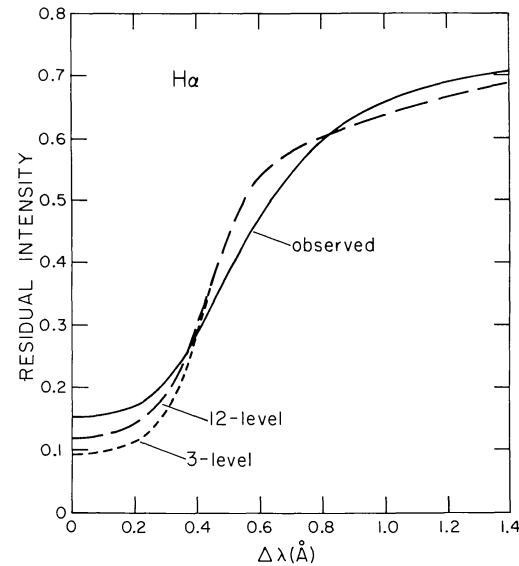


FIG. 26

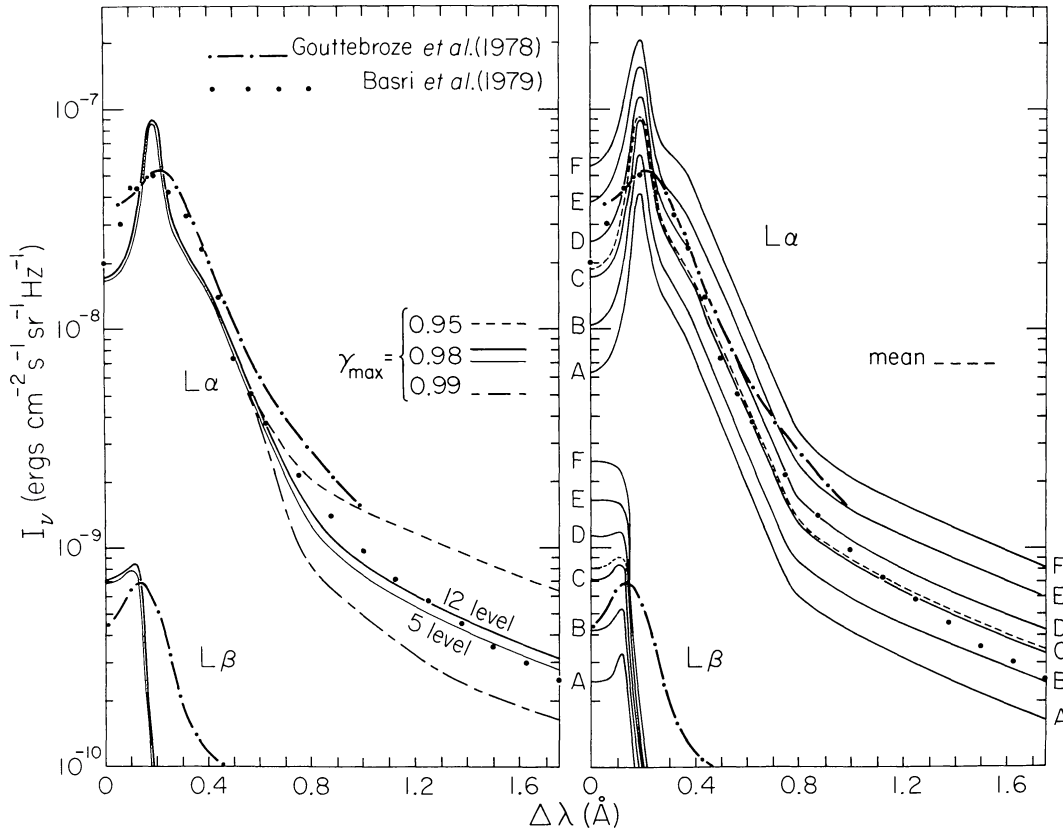


FIG. 27.—Computed profiles for  $L_\alpha$  and  $L_\beta$  at disk center compared with observations by Gouttebroze *et al.* (1978) and Basri *et al.* (1979). The left panel shows profiles computed from model C with the partial redistribution parameters  $\gamma_{\max} = 0.95$ ,  $0.98$ , and  $0.99$ , while the right panel shows the profiles from models A–F with  $\gamma_{\max} = 0.98$ . The left panel also shows the profile computed with a five level model hydrogen atom (and  $\gamma_{\max} = 0.98$ ). All of the other profiles were computed with the 12 level model specified in § II, in which levels 9–12 are treated as supplementary levels (see Appendix B).

determined  $\gamma$  theoretically rather than empirically and their  $\gamma$  exceeds 0.99, and (2) despite such predominant scattering in the wings they found, using a low-chromosphere temperature model such as ours, substantially *higher* intensities in the  $L_\alpha$  wings. Consequently, they proposed a reduction of the temperature distribution in the low chromosphere. As discussed in § VII, however, their higher  $L_\alpha$  wing intensities were caused by the improper use of LTE for the C I continuum in the  $L_\alpha$  wing.

The right panel of Figure 27 shows the  $L_\alpha$  and  $L_\beta$  profiles computed with  $\gamma_{\max} = 0.98$  for  $L_\alpha$  and  $\gamma_{\max} = 0.4$  for  $L_\beta$ , with our 12 level atomic model, and atmospheric models A–F.

##### V. PROPERTIES OF THE MODELS

In Table 8 of § III we have listed not only the various continuum intensities but also the integrated  $L_\alpha$  and  $L_\beta$  intensities for the observed components A–F. In Figure

28 these integrated line intensities are plotted as functions of the Lyman continuum intensity at 90.7 nm for components A–F. The observed values are shown as crosses.

In the two top panels of Figure 28 the heavy dots represent our calculated  $L_\alpha$  and  $L_\beta$  integrated intensities as functions of  $I_{90.7\text{ nm}}$ . The two lower panels show the effects of choosing various atomic models for the hydrogen atom used in the calculation.

The points labeled 3, 5, and 8 indicate the results obtained by using model hydrogen atoms with three, five, and eight levels. The point labeled 8+4 indicates the results using eight levels and the four supplementary levels 9–12 as described in Appendix B. This is the standard atomic model used throughout the present paper. The point labeled 3+9 in Figure 28 indicates the results obtained using a three level atomic model with the nine supplementary levels 4–12. The other results in the lower left panel (3a, 3b, DB, and CRD) will be discussed in subsequent paragraphs.

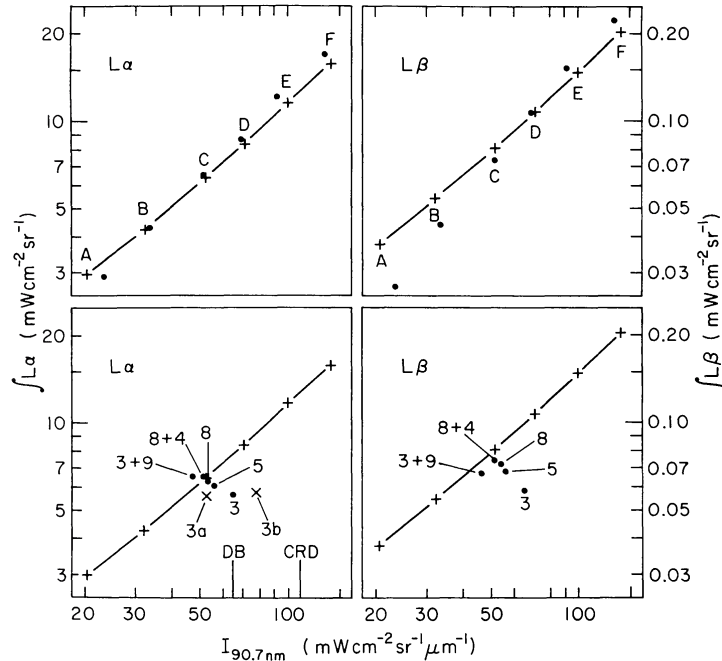


FIG. 28.—Integrated  $L\alpha$  and  $L\beta$  intensities plotted against the intensity near the head of the Lyman continuum. Observed values for components A–F appear as crosses. The upper panels show the computed values for models A–F. The computed values in the lower panels were obtained from model C. See text for details.

The sequence of results labeled 3, 5, 8, and 8+4 in Figure 28 shows that the computed Lyman line-to-Lyman continuum ratio is sensitive to the number of levels in the hydrogen atomic model. In the three level case the computed  $L\alpha$  to Lyman continuum ratio is 0.087 (for intensities measured in the units indicated) compared with the observed value of 0.12. The difficulty appears to be with the computed radiative recombination rates.

We plot as a broken line in Figure 29 the total hydrogen radiative recombination coefficient as a function of temperature tabulated by Osterbrock (1974). We also plot the total radiative recombination coefficients obtained from the sum of our calculated radiative recombination rates for the models having three, five, eight, and 12 levels. At a temperature of  $10^4$  K, the values from the models with eight, five, and three levels are 0.93, 0.81, and 0.69 times the known value, respectively. For comparison the computed  $L\alpha$  to Lyman continuum ratios for the three models are respectively 0.95, 0.88, and 0.71 times the observed ratio.

The point labeled 3+9 in Figure 28 indicates the result we obtain with three levels and supplementary levels 4–12. Since both the 3+9 and 8+4 calculations use the same 12 level set of radiative recombination rates, the differences are due to different numbers of levels treated explicitly.

In the lower left panel of Figure 28 we also show the results of three-level calculations with different values of

the Balmer continuum photoionization rate

$$R_{2\kappa} = 4\pi \int_{\nu_2}^{\infty} (h\nu)^{-1} \alpha_{\nu} J_{\nu} d\nu, \quad (9)$$

where  $\alpha_{\nu}$  is the hydrogen level 2 photoionization cross section and  $J_{\nu}$  is the mean intensity. The frequency range

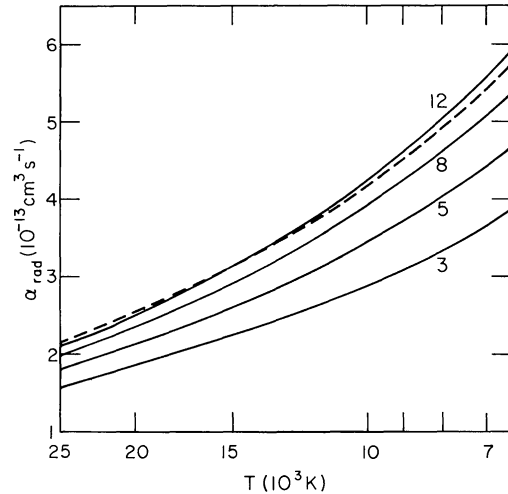


FIG. 29.—Total radiative recombination coefficient as a function of temperature for model hydrogen atoms with three, five, eight, and 12 levels. The broken line represents the theoretical values for hydrogen.

$\nu > \nu_2$  ( $\lambda < 364.7$  nm) is filled with absorption lines, and we use a line opacity distribution function as described in Paper II to account for the lines in our determination of  $J_\nu$ . We have adjusted the opacity function such that our computed central intensity agrees with the observed broad-band intensity distribution. The  $J_\nu$  determined in this way is used in equation (9). In the photosphere  $J_\nu$  varies with depth and eventually approaches the Planck function  $B_\nu$  deep in the atmosphere. In the chromosphere  $J_\nu$  is constant with depth. From equation (9) we obtain the chromospheric value of the photoionization rate  $8.08 \times 10^3$  s $^{-1}$ .

The points labeled 3a and 3b in Figure 28 correspond to solutions in which the above value for  $R_{2\kappa}$  is divided by 1.3 and multiplied by 1.3, respectively. Such changes in  $R_{2\kappa}$  cause the Lyman continuum intensity to decrease and increase by almost the same factor, while the L $\alpha$  intensity remains essentially unchanged.

In previous studies most authors have specified radiation temperatures to determine the photoionization rates  $R_{n\kappa}$  for  $n \geq 2$ . If  $J_\nu$  in equation (9) is written as

$$J_\nu = \frac{2h\nu^3}{c^2} e^{-h\nu/kT_{rn}}, \quad (10)$$

and if

$$\alpha_\nu = \alpha_n (\nu_n/\nu)^3, \quad (11)$$

then

$$R_{n\kappa} = \frac{8\pi}{c^2} \alpha_n \nu_n^3 E_1(h\nu_n/kT_{rn}). \quad (12)$$

The radiation temperature is usually assumed to be the given constant value  $T_{rn}$  above the depth in the photosphere where  $T_{rn} = T$  and equal to  $T$  below this depth. The Balmer continuum radiation temperature corresponding to the value  $R_{2\kappa} = 8.08 \times 10^3$  s $^{-1}$  is  $T_{r2} = 4940$  K. Our chromospheric photoionization rates for the  $n=3, 4$ , and  $5$  continua are  $1.70 \times 10^5$ ,  $3.05 \times 10^5$ , and  $3.07 \times 10^5$  s $^{-1}$ , while the radiation temperatures corresponding to these values are 4810, 4716, and 4738 K, respectively. For completeness we list the chromospheric photoionization rates for levels 6 through 12:  $2.36 \times 10^5$ ,  $2.22 \times 10^5$ ,  $1.41 \times 10^5$ ,  $1.12 \times 10^5$ ,  $7.59 \times 10^4$ ,  $7.55 \times 10^4$ , and  $5.24 \times 10^4$ . Radiation temperatures as defined above are not meaningful for these values of  $\nu_n$  because of the neglect of stimulated emission in equation (12). In § VII we compare these results with the radiation temperatures chosen by other authors in previous studies.

An approximation often used in hydrogen calculations is to assume that the Lyman lines are in radiative detailed balance so that the line absorption and emission terms cancel each other in the equations of statistical equilibrium. We obtain the same result by setting the

Einstein  $A$  coefficients for the Lyman lines equal to zero. We repeated the three level calculation with  $A_{21} = A_{31} = 0$  and obtained the Lyman continuum intensity  $65$  mW cm $^{-2}$  sr $^{-1}$   $\mu\text{m}^{-1}$ , labeled DB in Figure 28. This value is practically identical to that of the three level case in which the Lyman lines were treated explicitly. (A value for the L $\alpha$  intensity is not given since the line was not included in the calculation.) In the exploratory calculations which led to the present results we encountered models for which the assumption of Lyman line detailed balance gave inaccurate results due to a strong radiative interaction between the L $\alpha$  line and the Lyman continuum near  $\tau_{\text{LyC}} = 1$ . In model C, however, detailed balance is an excellent approximation for the purpose of computing Lyman continuum intensities because, as we show later in Figure 30, this radiative interaction between L $\alpha$  and the Lyman continuum takes place at  $\tau_{\text{LyC}}$  of order  $10^2$ , which is too deep to affect the emergent Lyman continuum spectrum.

Another approximation often used in hydrogen calculations is a treatment of only the Doppler core of the Lyman lines, with the wing opacities set equal to zero, using complete redistribution for the absorption and reemission of Lyman line photons instead of a partial redistribution treatment such as the one discussed in Appendix A. We repeated the three level calculation using complete redistribution and only Doppler cores for the Lyman lines and obtained the Lyman continuum intensity  $110$  mW cm $^{-2}$  sr $^{-1}$   $\mu\text{m}^{-1}$ , labeled CRD in Figure 28, which is 1.7 times the partial redistribution value. We repeated our standard 12 level calculation in the same way and obtained a Lyman continuum intensity 1.4 times the partial redistribution value. We conclude that in the case of model C, Doppler core complete redistribution is a poor approximation compared to the much simpler approximation of detailed balance in the Lyman lines. This conclusion appears to conflict with results obtained by Milkey and Mihalas (1973a) who found approximately the same Lyman continuum intensity for detailed balance and for complete redistribution in the Doppler core with the line wings removed. While we have tested the two approximations only in the case of model C, the choice of detailed balance seems generally preferable, given the simplicity of the detailed balance approximation.

We now show graphs of the non-LTE departure coefficients  $b_n$  for hydrogen, carbon, iron, and silicon. In LTE for a given temperature  $T$  and electron number density  $n_e$  the ratio of the number densities of level  $l$  and the continuum is given by

$$n_l^*/n_\kappa^* = n_e \psi_l(T), \quad (13)$$

where

$$\psi_l = \left( \frac{h^2}{2\pi mkT} \right)^{3/2} \frac{g_l}{2U_\kappa} \exp(h\nu_{kl}/kT). \quad (14)$$

In the more general case in which LTE cannot be assumed, the departure coefficient  $b_l$  is defined such that

$$n_l/n_\kappa = b_l n_e \psi_l(T). \quad (15)$$

From equations (13) and (15),  $b_l$  is also given by

$$b_l = (n_l/n_l^*)/(n_\kappa/n_\kappa^*). \quad (16)$$

When the atoms are strongly ionized so that  $n_\kappa \sim n_\kappa^*$ , this equation reduces to

$$b_l \sim n_l/n_l^*. \quad (17)$$

When the atoms are mostly neutral and almost all atoms are in level 1, the departure coefficient for level 1 reduces to

$$b_1 \sim n_\kappa^*/n_\kappa. \quad (18)$$

The values of  $b_l$  for the first five levels of hydrogen that we calculate using model C are shown in Figure 30. Three depth scales are indicated:  $\log m$  and the optical depths at the head of the Lyman continuum and at the center of H $\alpha$ . We make four comments about the behavior of the curves in Figure 30:

1. The values of  $b_l$  generally approach unity with increasing  $l$  according to the enhanced collisional cou-

pling between the higher levels and the continuum and due to the property, from equation (16), that  $b=1$  for the continuum.

2. For  $\tau_{\text{LyC}} > 10^3$ ,  $b_1$  is a measure of the degree of ionization relative to LTE, according to equation (18).

3. The degree of ionization in the chromosphere depends on a ratio of ionization and recombination terms in the Balmer continuum and higher continua. The values of  $b_1$  are less than unity in the temperature-minimum region where  $T$  is below the radiation temperatures in these continua. Above this region  $b_1$  rises rapidly because of the chromospheric temperature increase relative to these radiation temperatures.

4. The substantial reduction of  $b_1$  relative to  $b_2$  above  $\tau_{\text{LyC}} = 10^3$  is due to L $\alpha$  heating. In order to explain this effect we must first consider how Lyman continuum photons are created and destroyed.

In Appendix C we derive the equation

$$\frac{1}{b_1} = \frac{U + \epsilon_2}{1 + \epsilon_1}, \quad (19)$$

where  $U$  is (essentially) the Lyman continuum photoionization rate divided by the corresponding radiative recombination rate, while  $\epsilon_1$  and  $\epsilon_2$  are terms depending on all the indirect transition rates between level 1 and the continuum, i.e., all rates except direct 1- $\kappa$  photoionization and  $\kappa$ -1 radiative recombination. In the present application the collision rates between level 1 and the continuum are negligible. Consequently,  $\epsilon_1$  is proportional to the principal recombination rates to intermediate levels  $L$ , multiplied by a branching ratio of the form  $P_{L1}/(P_{L1} + P_{L\kappa})$ , and  $\epsilon_2$  is proportional to the principal excitation rates from level 1 to the intermediate levels  $L$ , multiplied by  $P_{L\kappa}/(P_{L\kappa} + P_{L1})$ . The parameter  $\epsilon_2$  is a measure of the rate at which Lyman continuum photons are created, apart from the photoionization-recombination resonance process, while  $\epsilon_1$  is the corresponding measure of the rate at which Lyman continuum photons are destroyed. The explicit equations for  $\epsilon_1$  and  $\epsilon_2$  are given in Appendix B.

The principal contribution to the term  $P_{L1}$  in the  $\epsilon_1$  branching ratio  $P_{L1}/(P_{L1} + P_{L\kappa})$  is the L $\alpha$  net radiative cooling rate. Normally this rate is positive so that the number of L $\alpha$  photons emitted by the gas at a given depth exceeds the number of L $\alpha$  photons absorbed by the gas at that depth. At  $\tau_{\text{LyC}}$  of order  $10^2$ , however, the L $\alpha$  net radiative cooling rate is negative due to the enhanced radiation at these depths originating in the higher temperature transition region. Thus, the gas is heated at these depths by net absorption of L $\alpha$  radiation.

As a consequence, the  $\epsilon_1$  photon destruction parameter is reduced in value, even becoming negative at some depths. In turn,  $b_1$  is diminished, and the Lyman con-

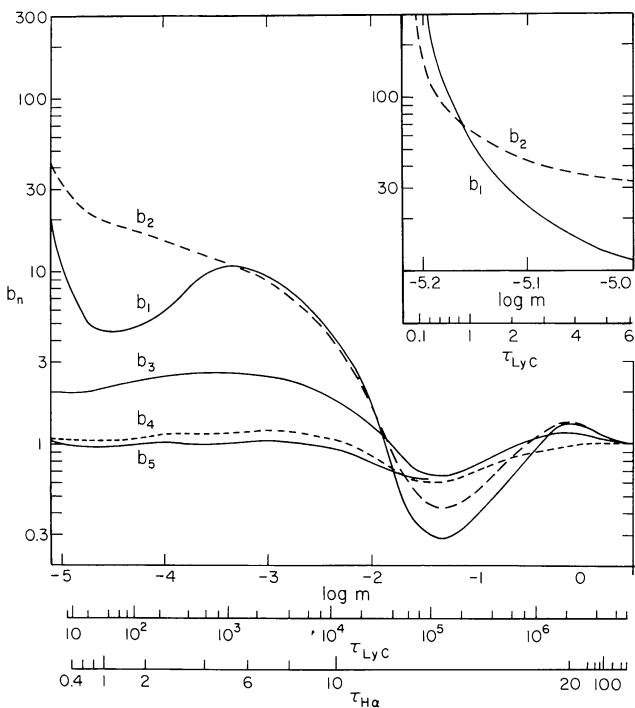


FIG. 30.—Hydrogen departure coefficients  $b_1-b_5$  computed from model C.

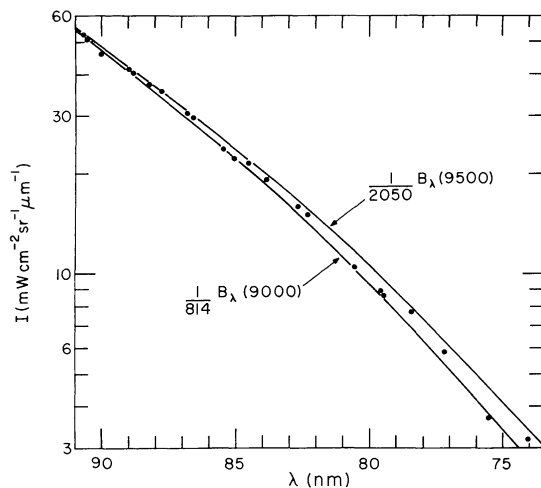


FIG. 31

FIG. 31.—Two Lyman continuum approximations of the form  $b_{1L}^{-1}B_\lambda(T_L)$ .

FIG. 32.—The hydrogen ground-state departure coefficient and the temperature as functions of the optical depth at the head of the Lyman continuum. The values  $b_{1L} = 814$ ,  $T_L = 9000$  K from Fig. 31 are indicated by crosses, while  $b_{1L} = 2053$ ,  $T_L = 9500$  K are indicated by open circles.

tinuum source function  $S_\nu = b_1^{-1}B_\nu$  and the proton and electron number densities are enhanced. Since this occurs at  $\tau_{LyC}$  of order  $10^2$ , the emergent Lyman continuum intensity is largely unaffected (as we found in Fig. 28 when the Lyman lines were put in detailed balance). However, other spectral features formed at these depths such as the 3 mm continuum and the Ca II H and K central intensities (see Fig. 1) could be affected by this  $L\alpha$  heating and additional ionization, which causes an increase in the electron density.

This  $L\alpha$  heating mechanism may play a role in the transfer of energy from the corona to the upper chromosphere. As explained in § IX, thermal conduction from the corona becomes ineffective for transition-region temperatures below  $2.5 \times 10^4$  K in model C. However, the  $L\alpha$  line absorbs energy from the gas in the transition region at temperatures above  $2.5 \times 10^4$  K and returns energy to the gas in the upper chromosphere. This effect is much more pronounced in solar flare models as discussed by Machado *et al.* (1980).

This concludes our attempt to explain why  $b_1$  is much smaller than  $b_2$  in the left portion of Figure 30. Further details on the calculation of  $b_1$  are given at the end of Appendix C.

Noyes and Kalkofen (1970) and others have tried to determine  $b_1$  and  $T$  from observations of the Lyman continuum. Figure 31 shows the observed central intensity in the range 74–91 nm (the component C observations from Table 8) and two empirical curves of the form  $b_{1L}^{-1}B_\lambda(T_L)$ . We have chosen the parameters  $b_{1L}$  and  $T_L$  so that the two curves represent upper and lower

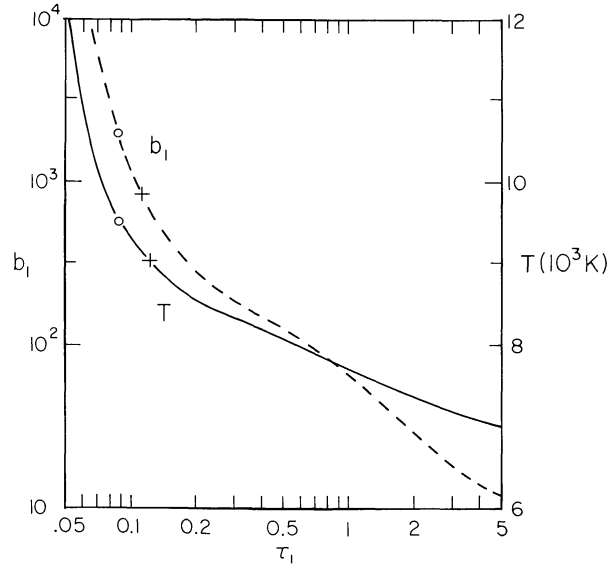


FIG. 32

$b_1^{-1}B_\lambda(T)$  (see Appendix C),  $T_L$  can be identified with the temperature at the depth where the Lyman continuum is formed and  $b_{1L}$  with the value of  $b_1$  at that depth. Noyes and Kalkofen (1970) and subsequent estimates of the observed intensity distribution. Since the Lyman continuum source function is essentially

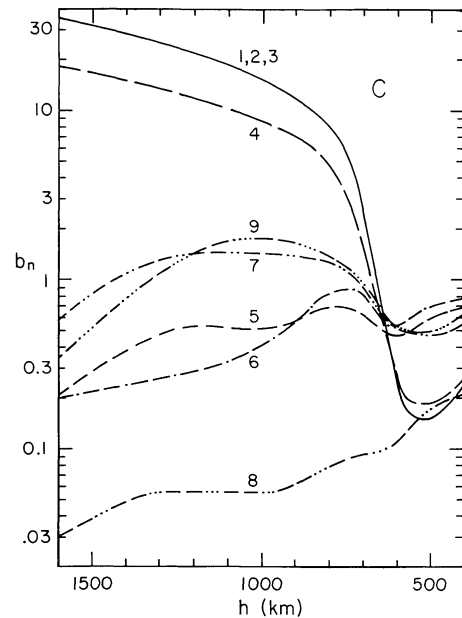


FIG. 33.—Departure coefficients  $b_n$  for carbon computed from model C.

authors have interpreted  $T_L$  as the temperature at unit optical depth at the head of the Lyman continuum.

In Figure 32 we plot  $T$  and  $b_1$  for model C as functions of the optical depth at the head of the Lyman continuum. The values of  $b_{1L}$  and  $T_L$  which determine the upper curve in Figure 31 are shown as open circles, and the crosses indicate  $b_{1L}$  and  $T_L$  for the lower curve. We see that in both cases  $T_L$  and the corresponding  $b_{1L}$  are located at about the same optical depth, but at  $\tau \sim 0.1$  instead of  $\tau \sim 1$ . This method of determining  $T$  and  $b_1$  from Lyman continuum observations does not give useful results for the Sun because the temperature changes very rapidly with depth in the region where the Lyman continuum is formed. In Figure 36 at the end of this section the graphs for  $\lambda = 90.7, 80.6$ , and 70 nm show that the Lyman continuum is formed over a wide range of temperatures, from  $\sim 8000$  K at the head of the Lyman continuum to over  $2 \times 10^4$  K at  $\lambda \sim 70$  nm. We conclude that meaningful values of  $T$  and  $b_1$  cannot be determined from Lyman continuum observations.

In Figure 33 we show the departure coefficients  $b_n$  for our 10 level carbon atom computed with model C. In the figure we show nine departure coefficients; level 10 is an autoionization level for which  $b$  was chosen to be unity. An important feature of these results is that the departure coefficients for the three lowest levels vary from about 10 to 30 in the height range 800 to 1500 km. This is the height range where the continua corresponding to the three levels are formed so that the computed intensities are factors of 10 to 30 lower than they would be in LTE.

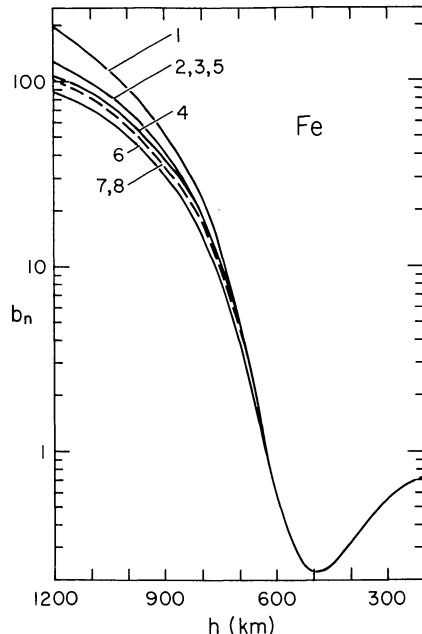


FIG. 34.—Departure coefficients  $b_n$  for iron computed from model C.

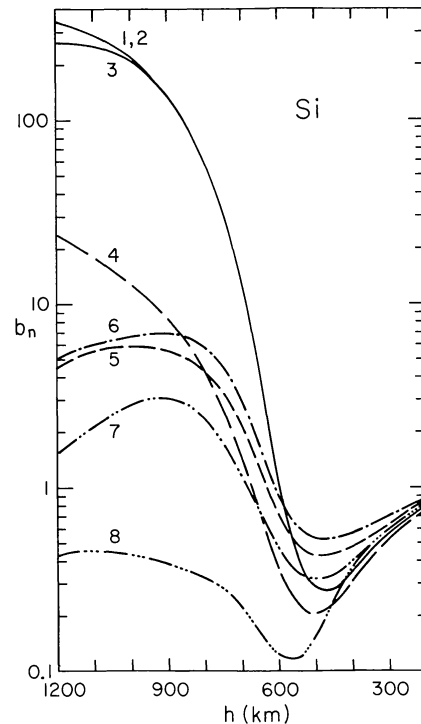


FIG. 35.—Departure coefficients  $b_n$  for silicon computed from model C.

TABLE 9  
WAVELENGTHS FOR FIGURE 36

Absorption Edge	$\lambda$	Absorption Edge	$\lambda$
3	cm	Fe 157.5 nm	
1	cm		157.4
3	mm	Si 152.5	
1	mm		152.4
600	$\mu\text{m}$	C 144.4	
300			143
150			131.8
50		C 123.9	
10			123.2
1.6	$\mu\text{m}$		122.3
500	nm	(L $\alpha$ )	
H 364.7			121
			120.5
Mg 251.4	300		118.1
	250	C 110	
Al 207.6	207.4		109.8
	198.2		105.9
Si 198.6		H 91.2	95
Fe 176.8	176.7		90.7
	168.1		80.6
Si 168.2		He 50.4	70
Mg 162.2	160.5		50.3
			45
			40

The effect of the carbon departure coefficients for the three lowest levels on the monochromatic source functions at various wavelengths can be seen in Figure 36 below. As we discuss in § VII, Basri *et al.* (1979) were led to underestimate the temperature distribution in the low chromosphere because they assumed LTE for the carbon continuum. The departure coefficients for levels 5 to 9 are mostly determined by photospheric radiation which causes the  $b_n$  values to be generally less than unity. Coupling of the upper and lower levels by the resonance lines causes the lower level departure coefficients to be less than unity in the temperature-minimum region.

The departure coefficients we compute for Fe using model C are shown in Figure 34. The indicated levels are the combined ones representing groups of sublevels, as listed in Table 4 of § II. Because of strong collisional coupling, the Fe departure coefficients are all the same throughout the photosphere and the temperature-minimum region. The small values of the Fe departure

coefficients near the temperature minimum indicate that the Fe contribution to the electron density is larger than in LTE. As shown in Figure 47 of § VIII, Fe is the largest contributor to  $n_e$  in this region.

The departure coefficients for Si were shown in Paper II but since there are some differences near the temperature minimum between the results from model C and those from Paper II we plot the newer set of values in Figure 35.

In Table 9 we list 36 wavelengths from 3 cm to 40 nm for the individual graphs composing Figure 36. Table 9 also includes the principal absorption edges for H, Mg, Al, Si, Fe, C, and He.

The individual panels of Figure 36 show  $r_{ab}$  and  $r_{em}$ , the relative contributions to the absorption coefficient and emission coefficient, the Planck function  $B$ , the mean intensity  $J$ , the source function  $S$ , the normalized emergent intensity contribution function  $dI/dh$ , and the emergent intensities for  $\mu = 1.0$  and 0.3. These quantities, which are defined in the same way as in a similar set of

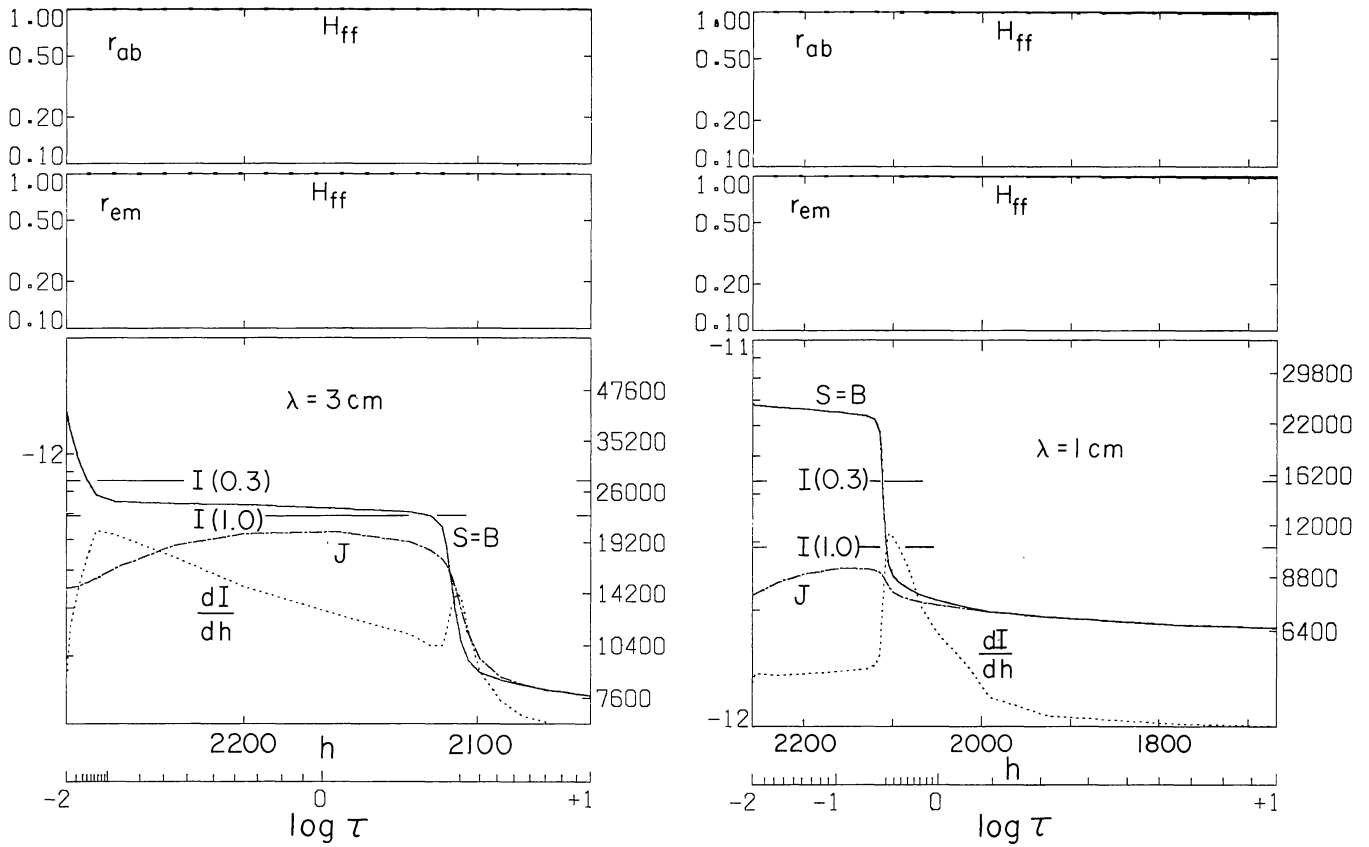


FIG. 36.—( $\lambda = 3$  cm to  $\lambda = 40$  nm). In each panel, the top section (*labeled*  $r_{ab}$ ) shows the relative contributions to the total absorption coefficient at the indicated wavelength, while the section below it (*labeled*  $r_{em}$ ) gives the relative contributions to the total emission coefficient. The bottom section shows the Planck function  $B$ , the absorption source function  $S^{ab}$ , the continuum source function  $S$ , the mean intensity  $J$ , and the contribution per unit height  $dI/dh$  to the emergent intensity at  $\mu = 1$ . See eqs. (21)–(33) of Paper II. These functions are plotted on a linear height scale having limits at selected values of  $\log \tau$ , where  $\tau$  is the monochromatic optical depth. Values of  $I(1.0)$  and  $I(0.3)$ , the emergent intensities at  $\mu = 1.0$  and 0.3, are indicated. The units for  $B$ ,  $S^{ab}$ ,  $S$ ,  $J$ , and  $I$  on the left are  $\text{ergs cm}^{-2} \text{ s}^{-1} \text{ sr}^{-1} \text{ Hz}^{-1}$ . The corresponding brightness temperature scale (in K) is given on the right. Each  $dI/dh$  curve is plotted on a linear scale such that zero is at the bottom and the maximum is at the midpoint of the bottom section.

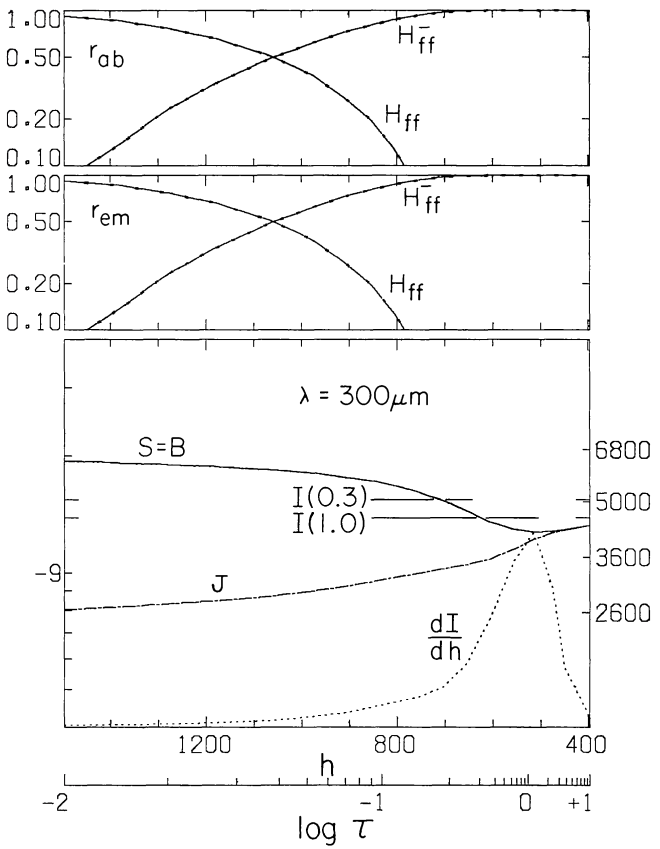
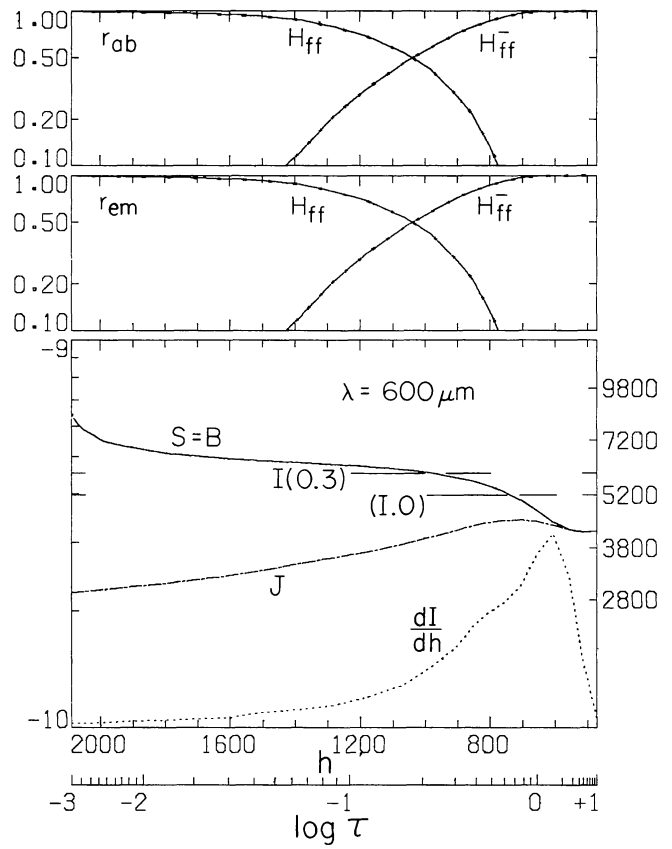
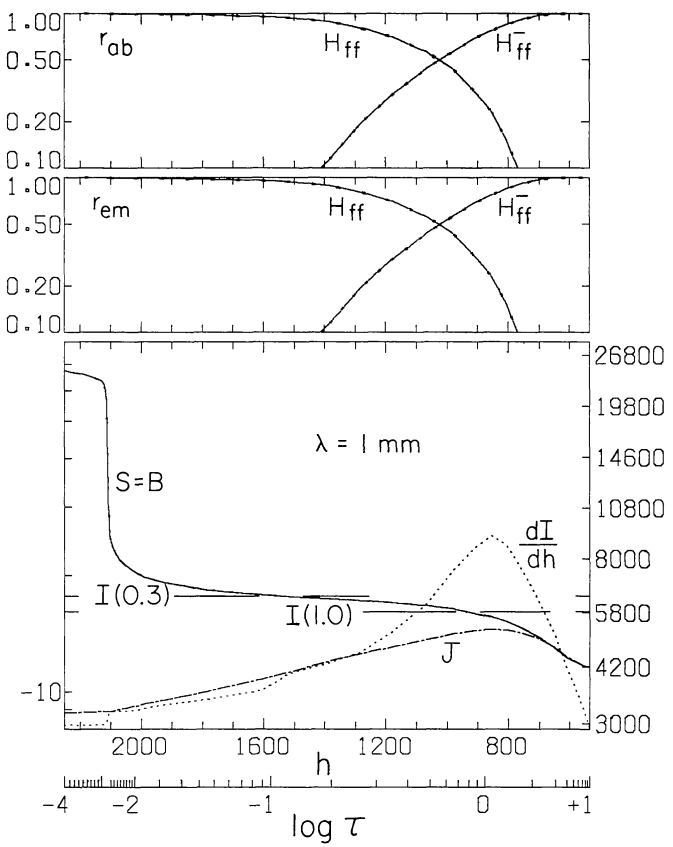
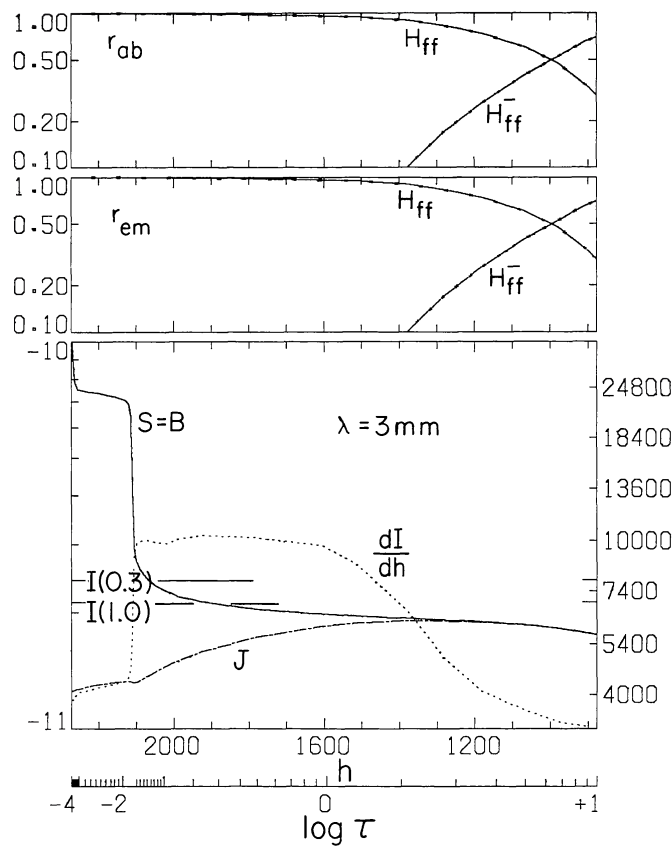


FIG. 36—Continued

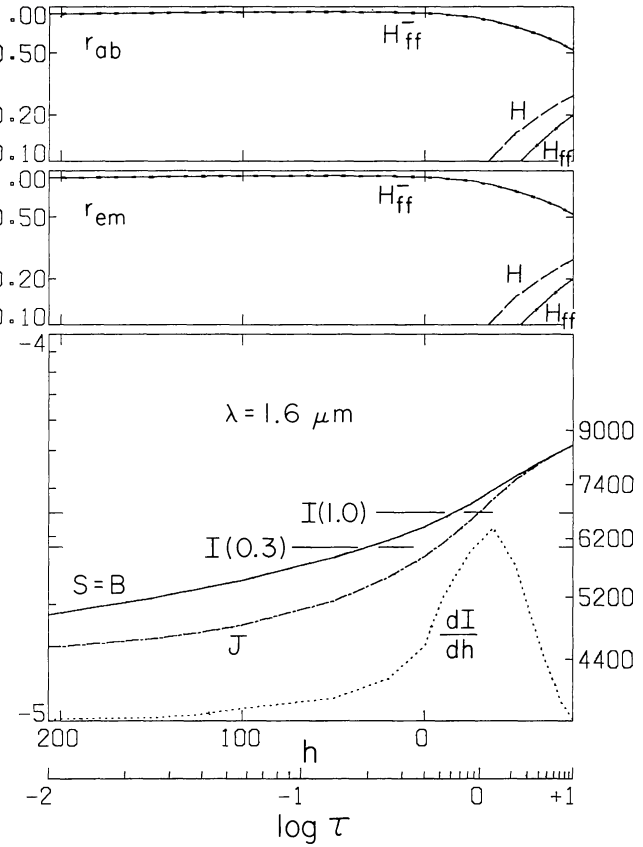
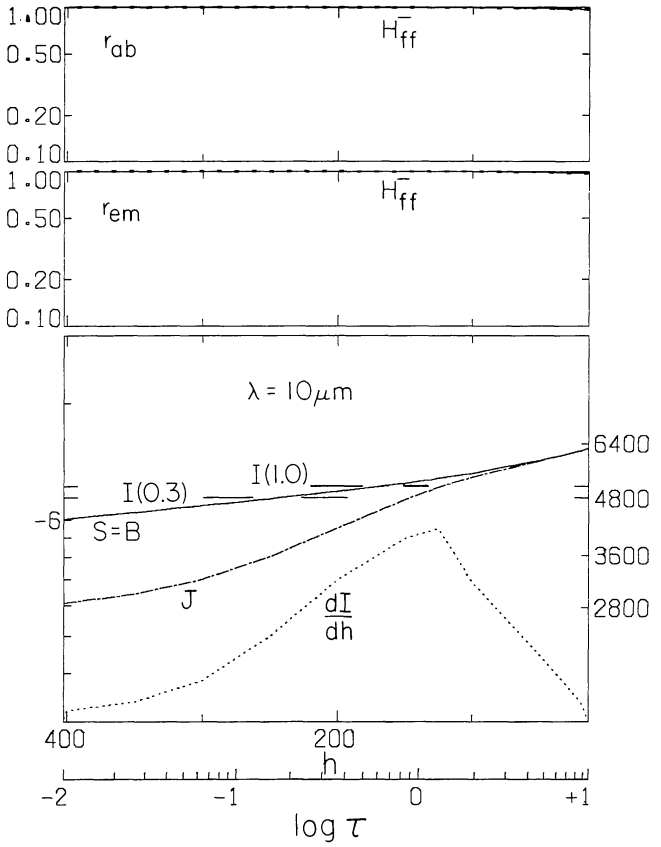
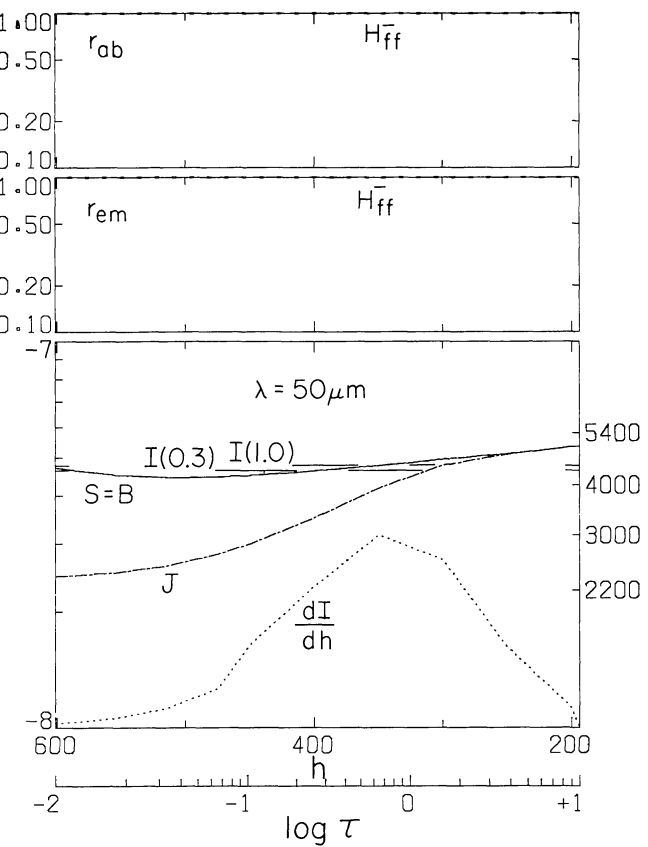
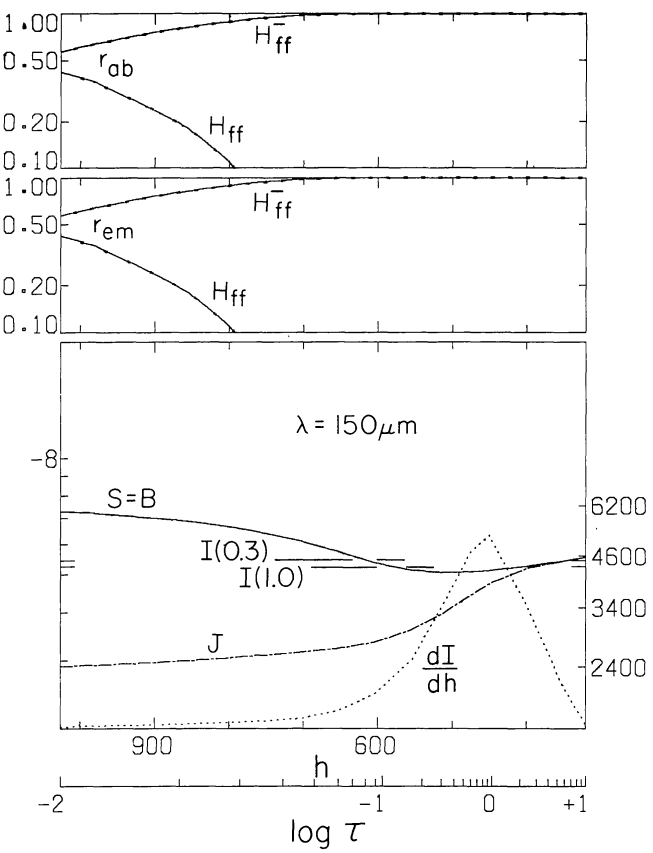


FIG. 36—Continued

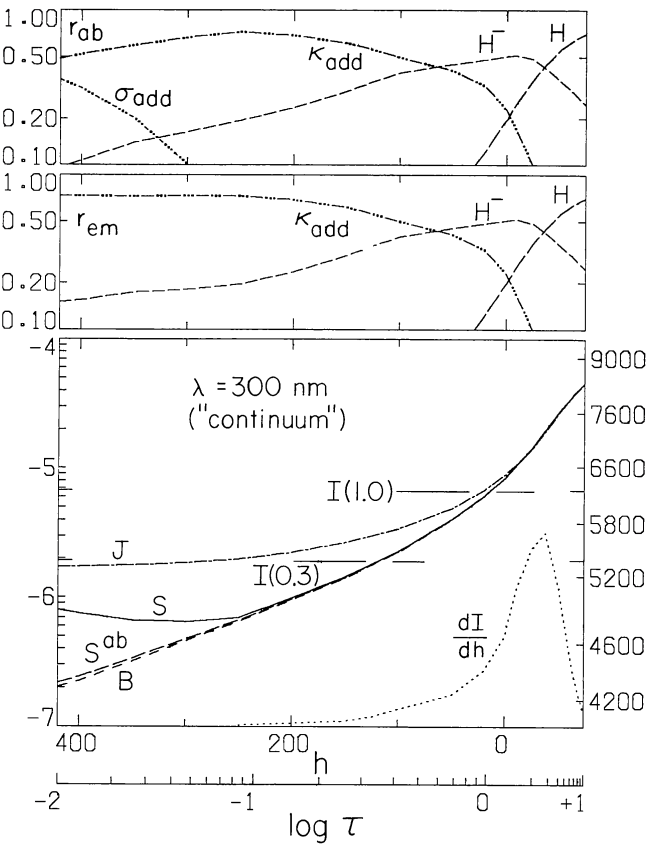
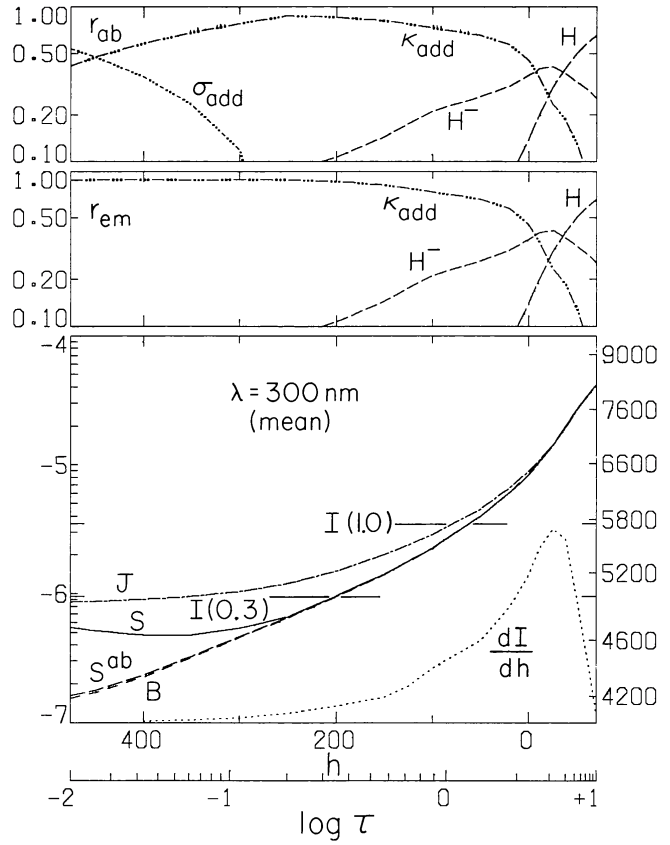
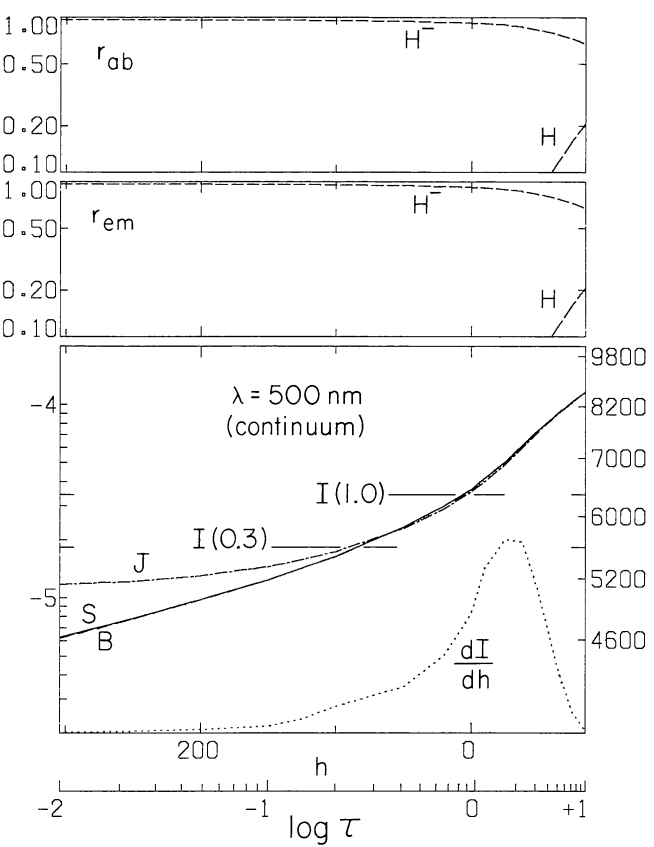
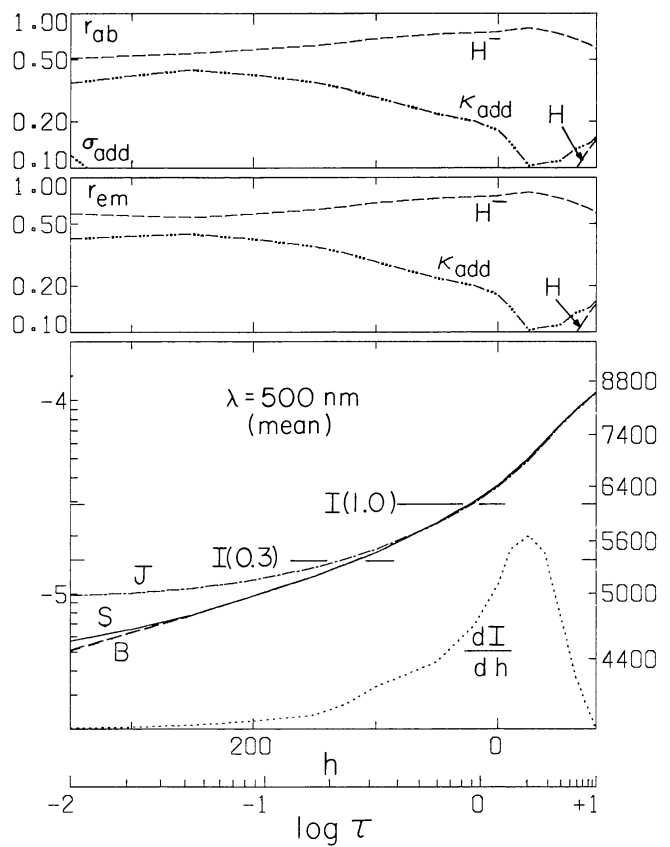


FIG. 36—Continued

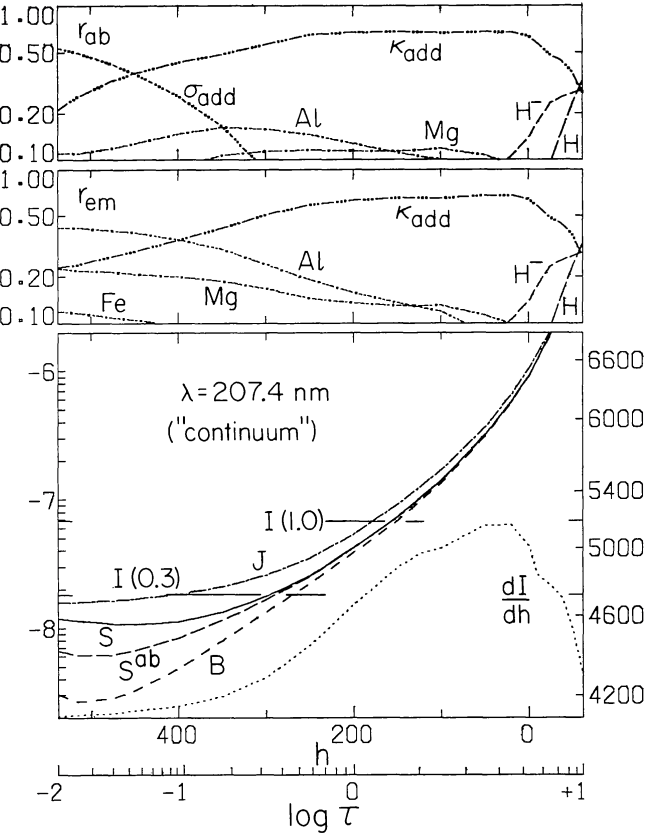
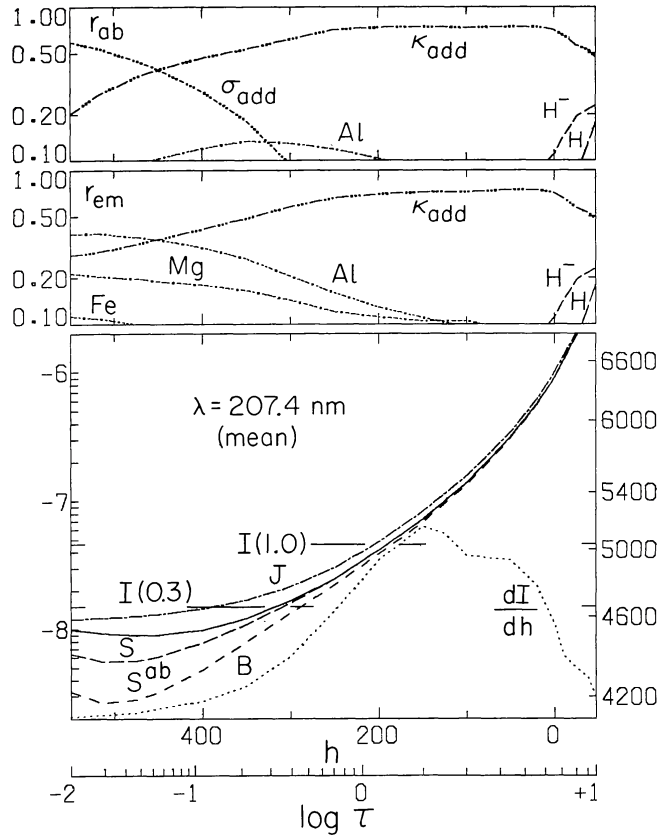
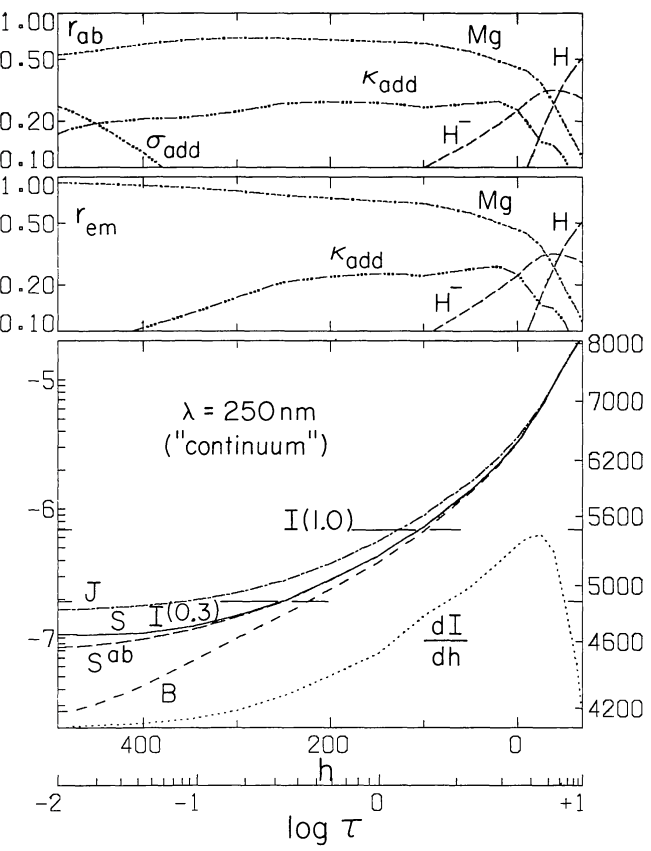
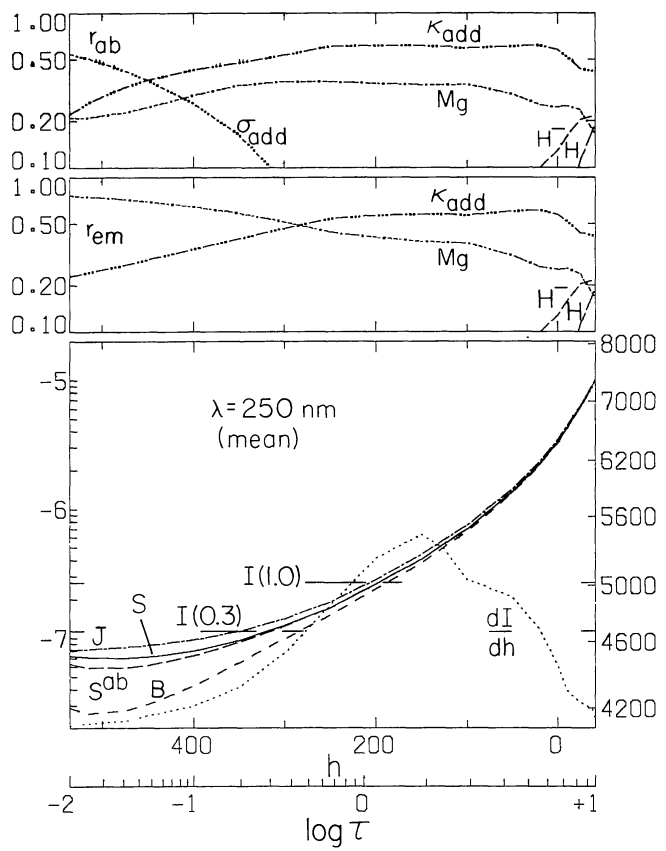


FIG. 36—Continued

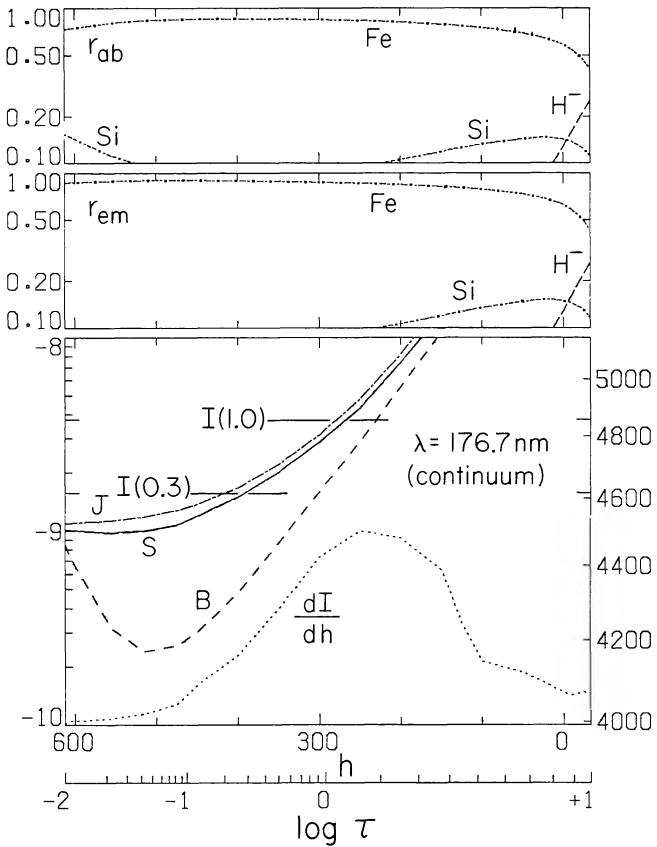
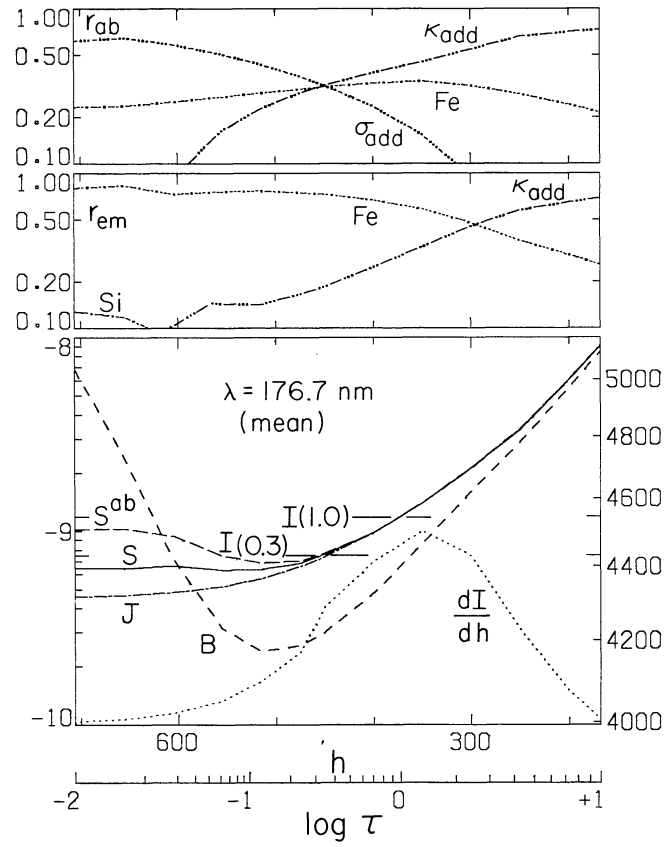
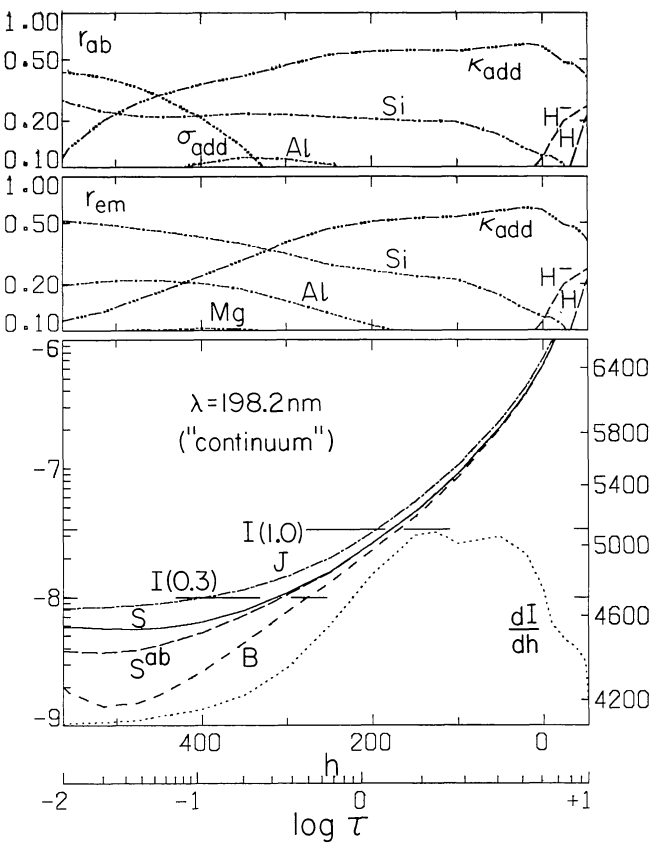
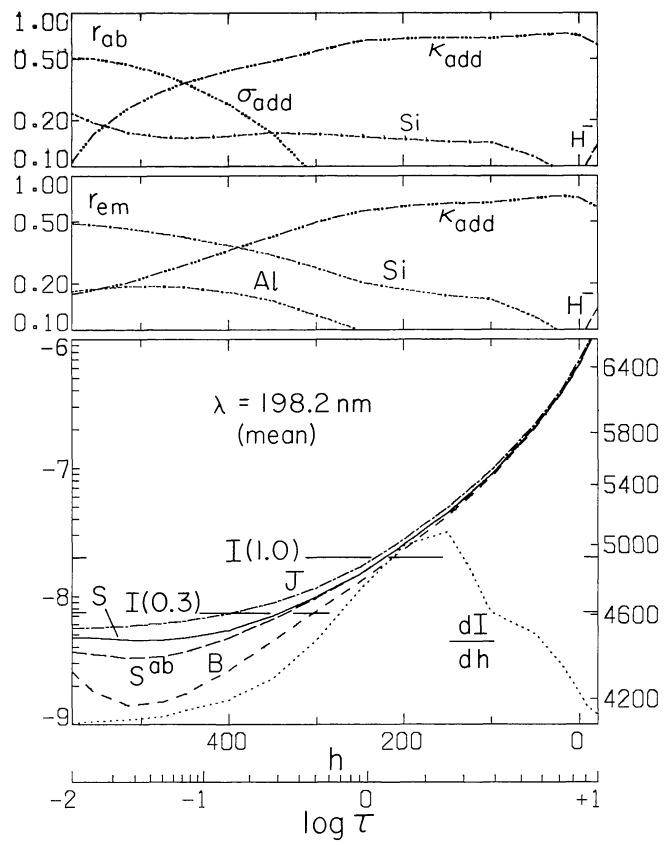


FIG. 36—Continued

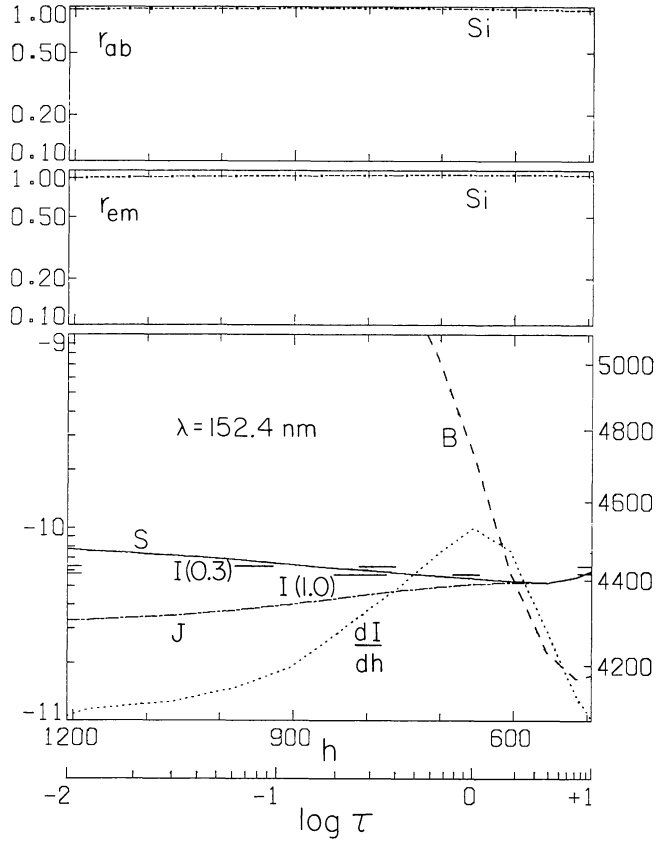
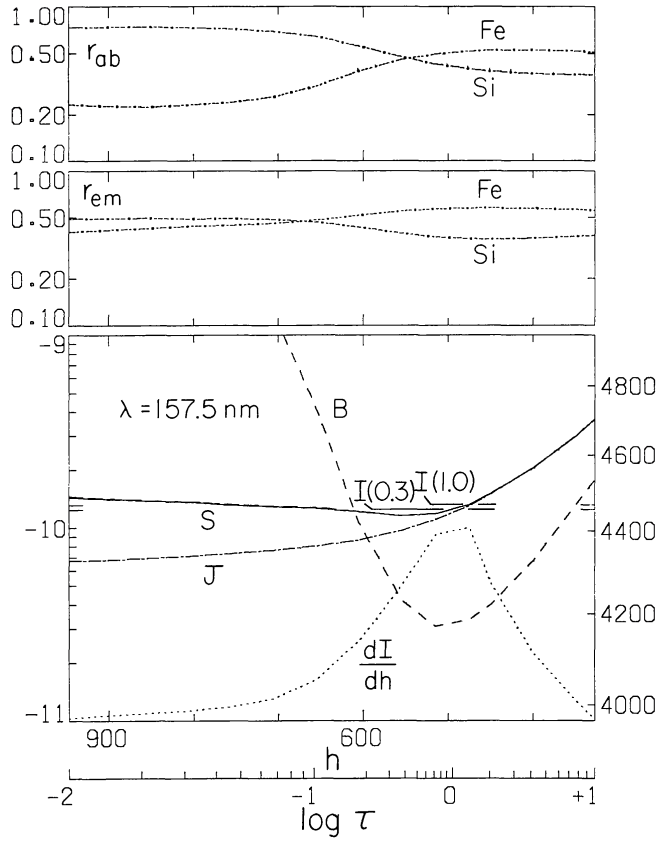
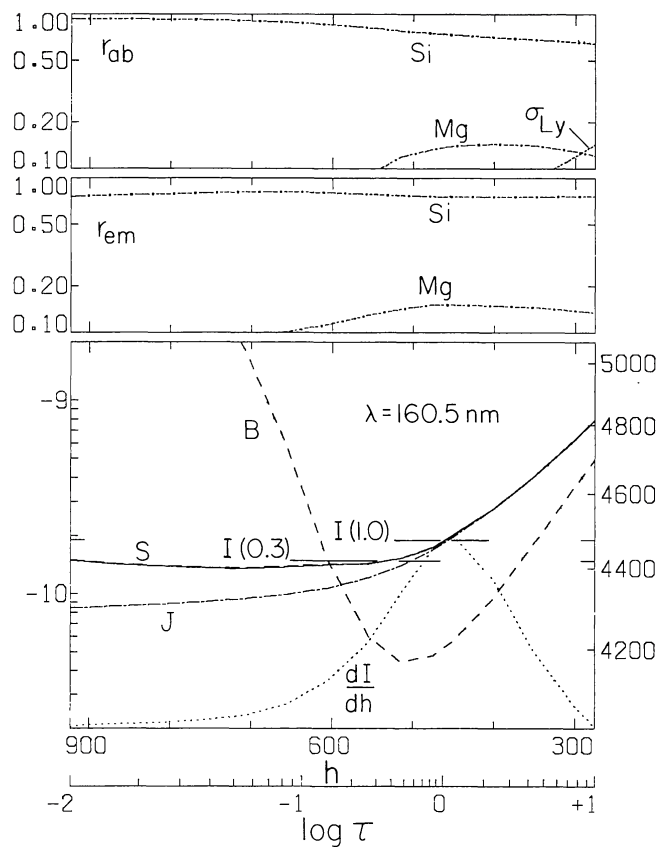
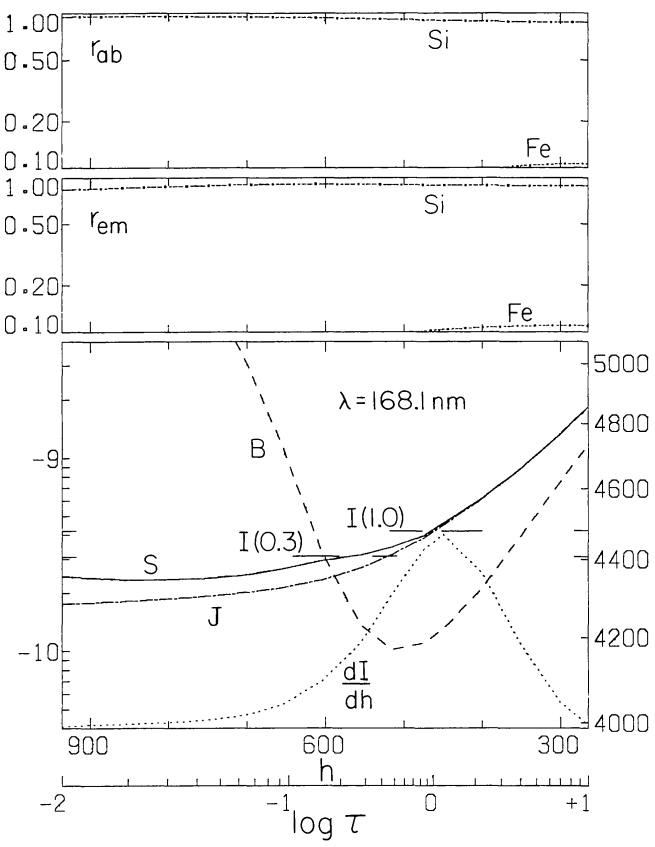


FIG. 36—Continued

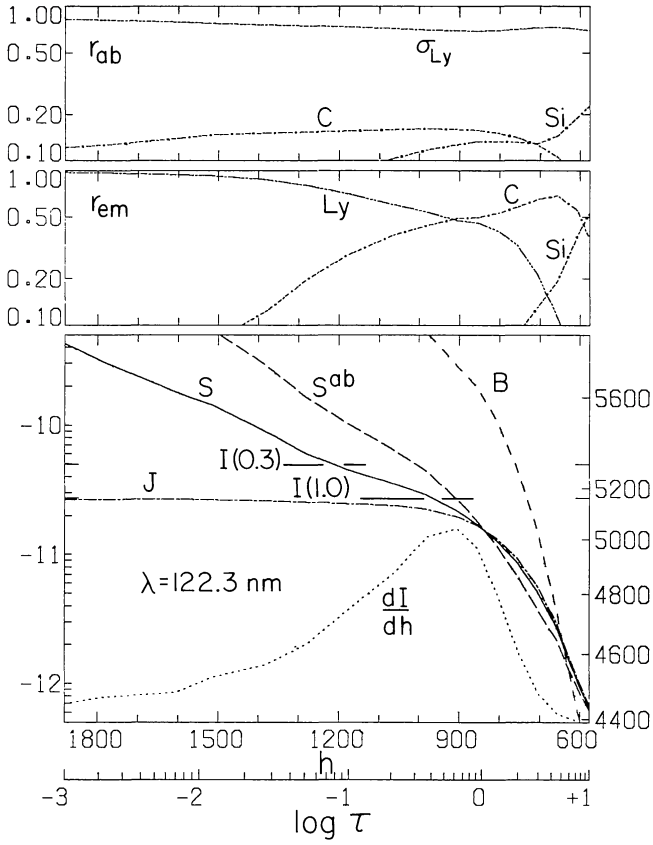
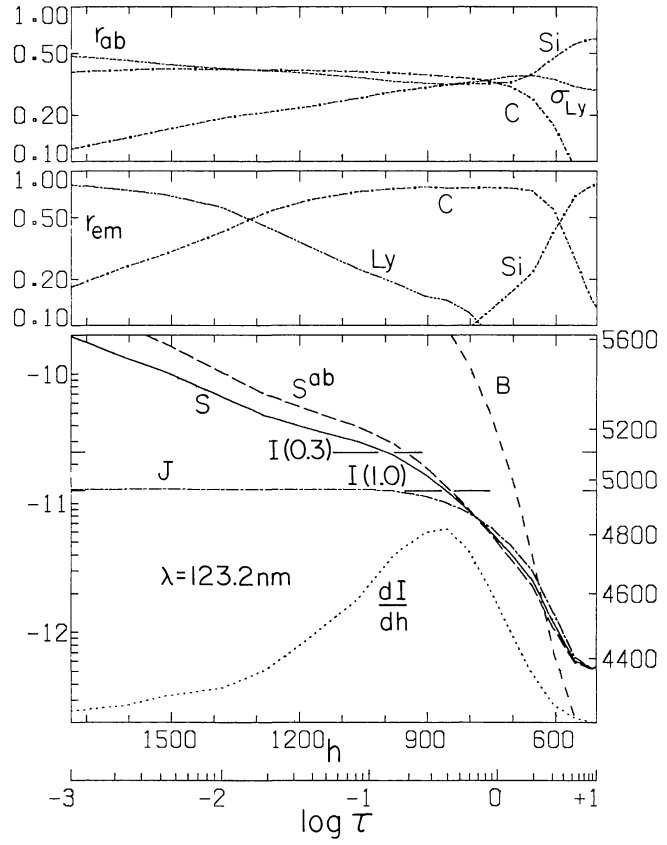
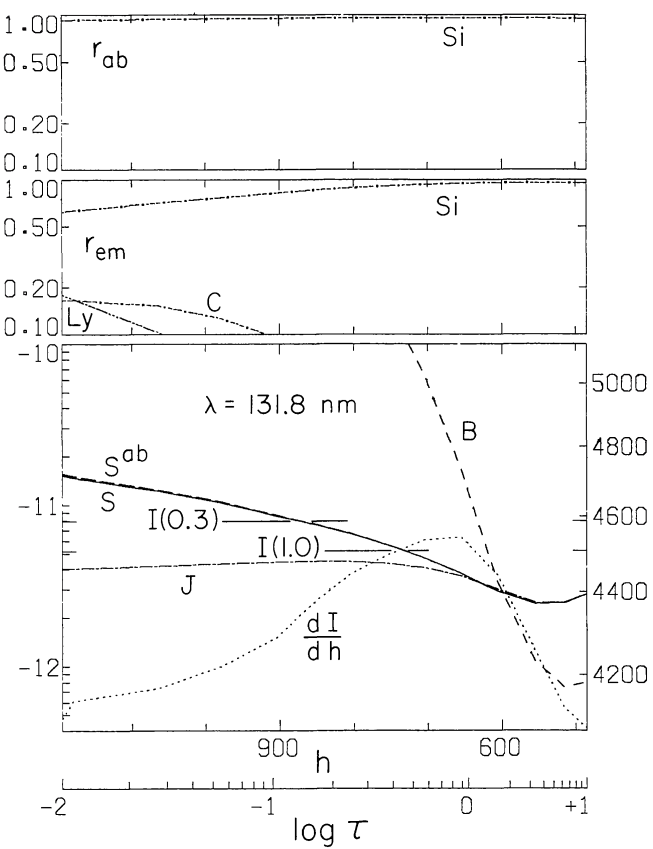
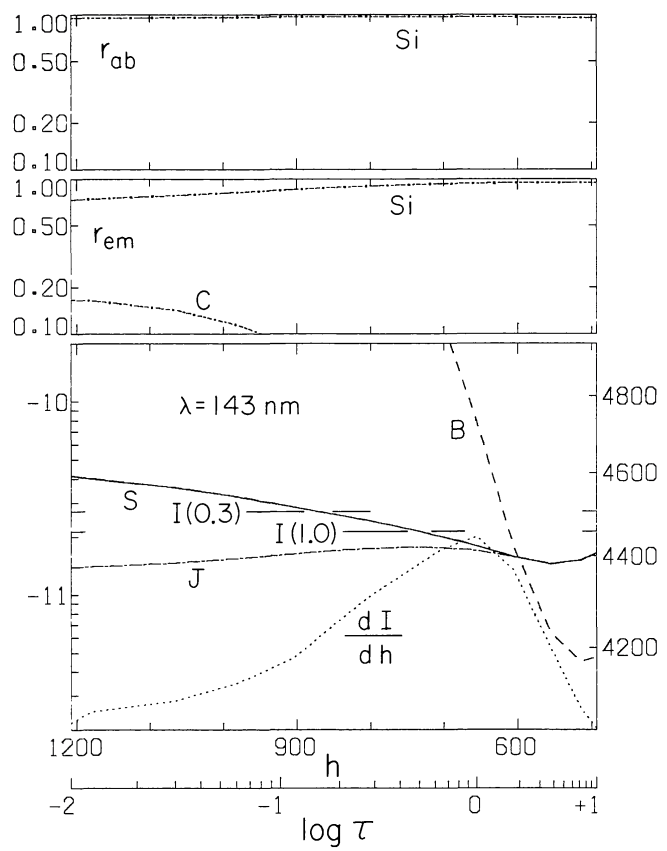


FIG. 36—Continued

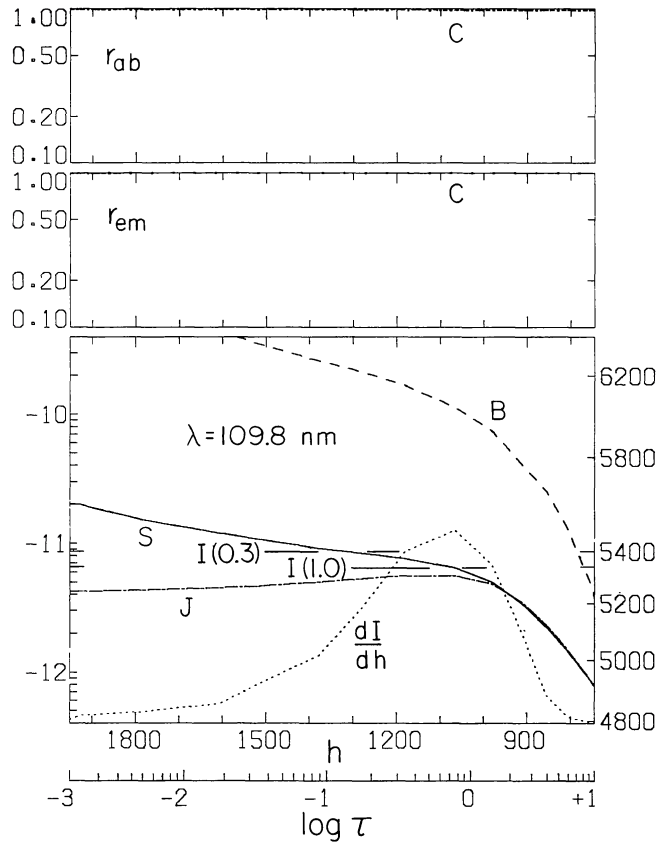
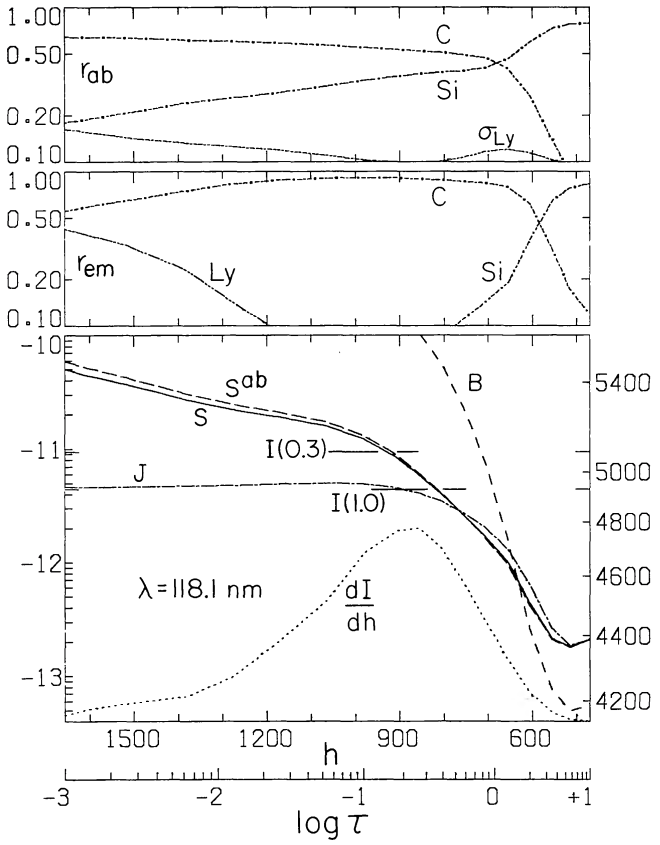
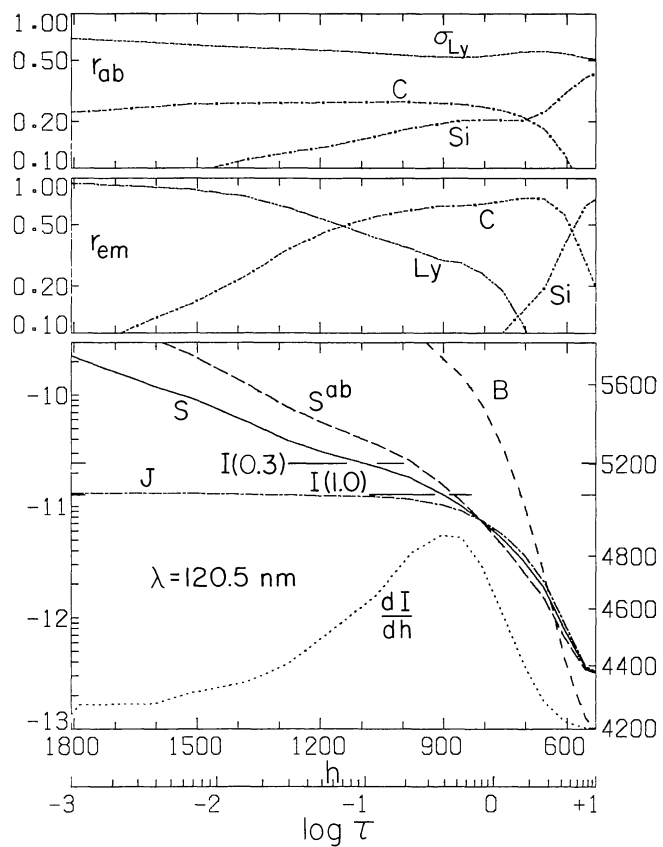
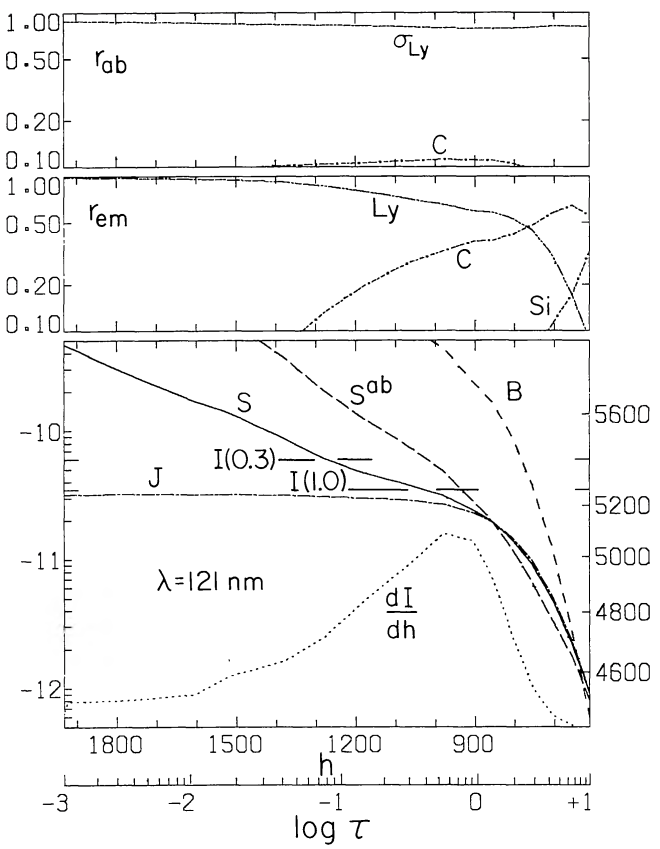


FIG. 36—Continued

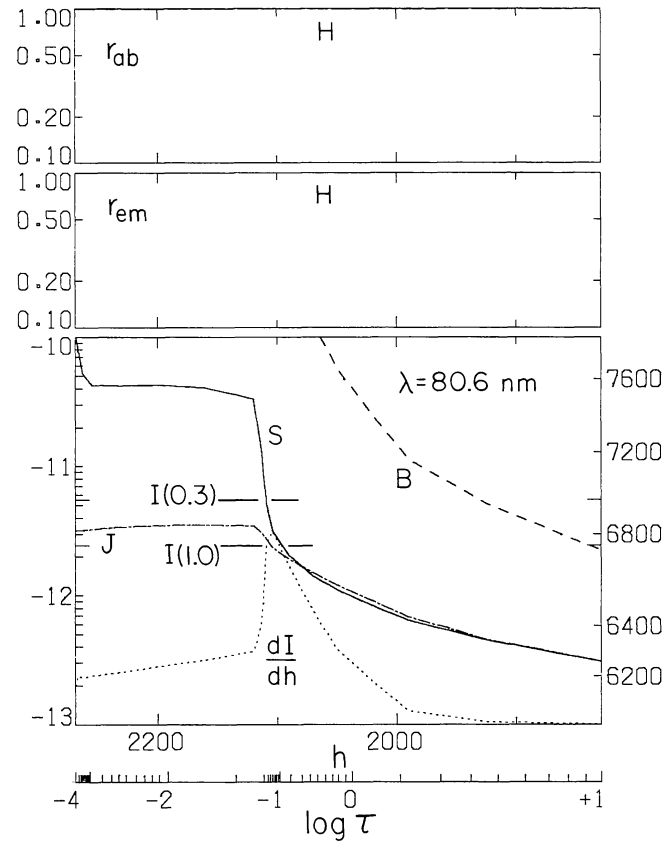
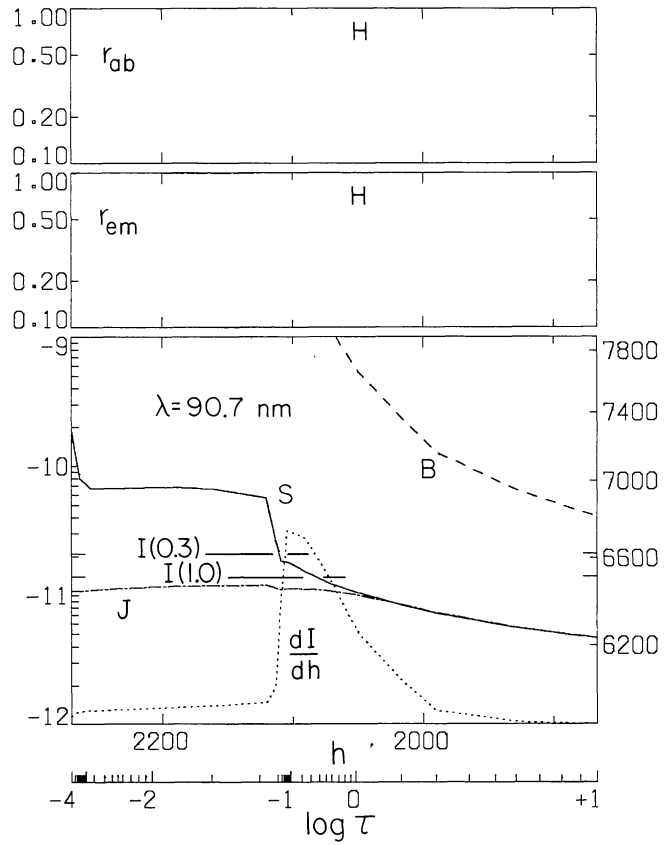
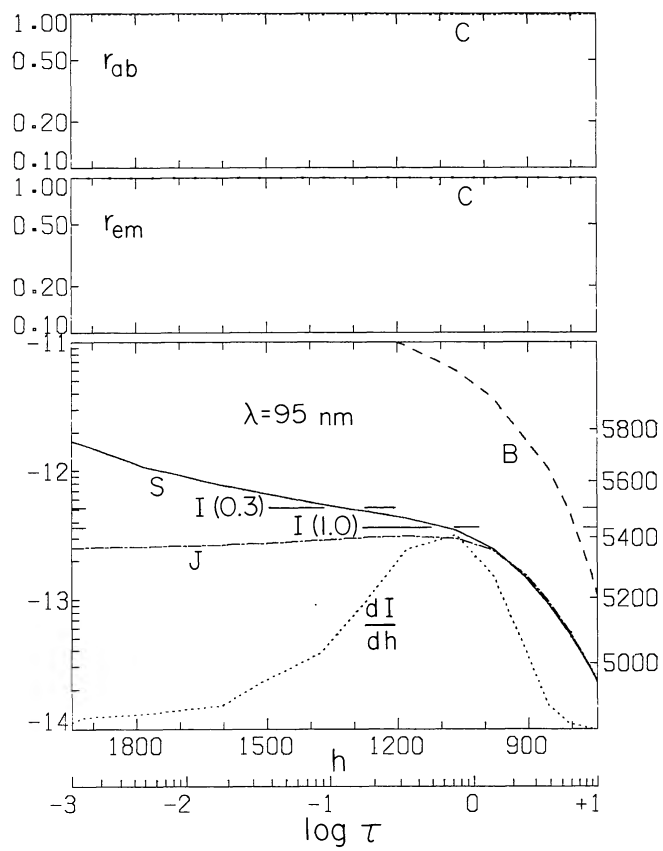
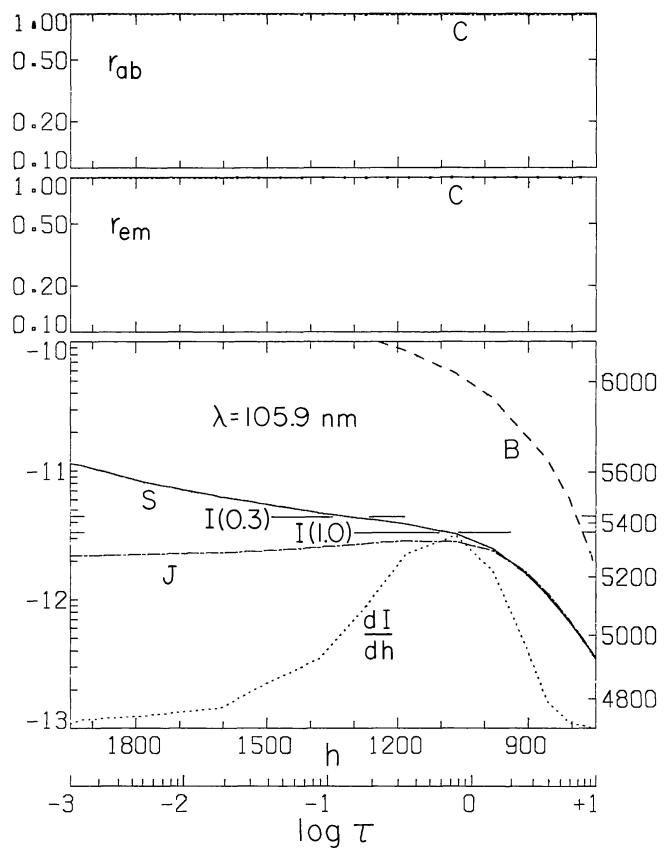


FIG. 36—Continued

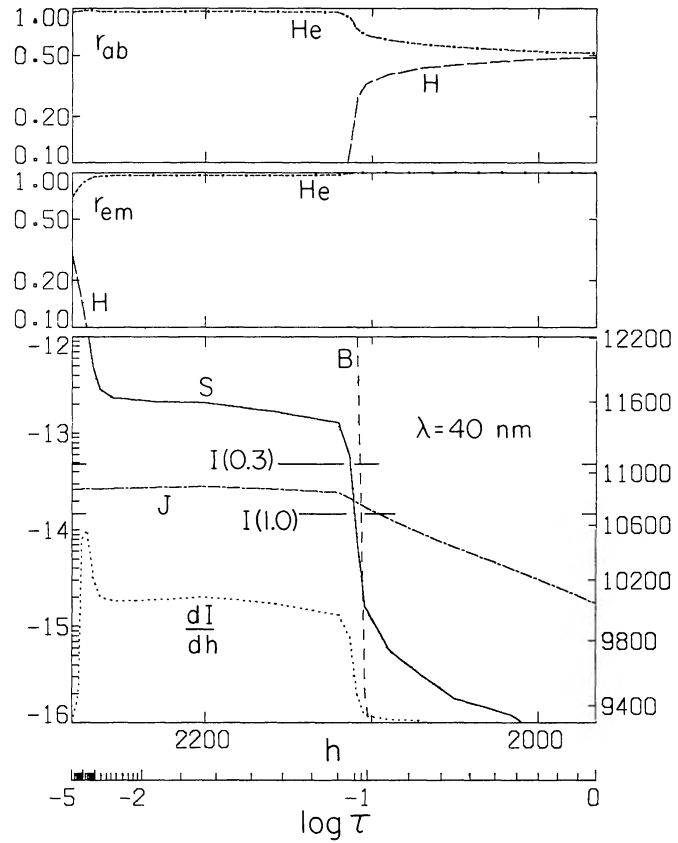
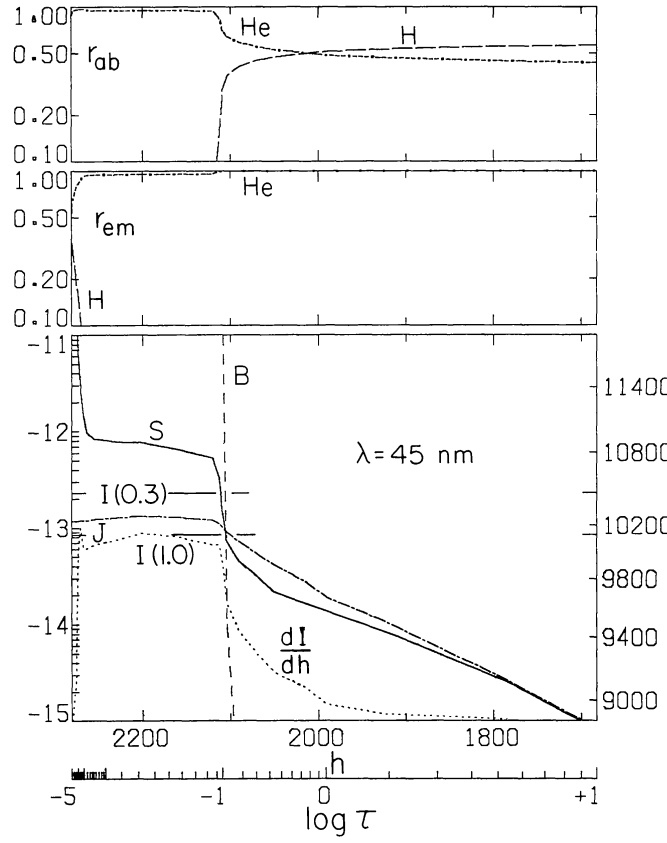
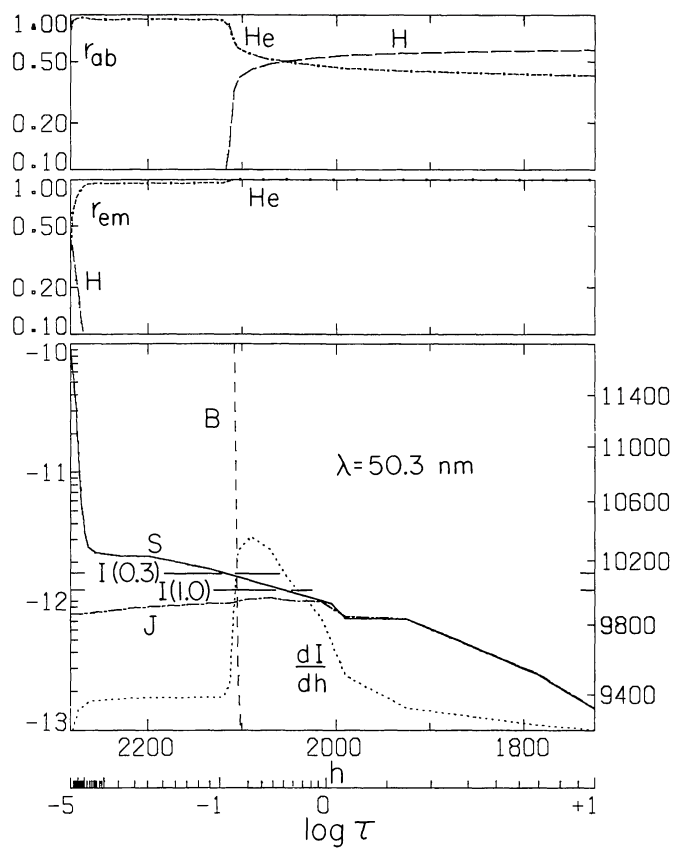
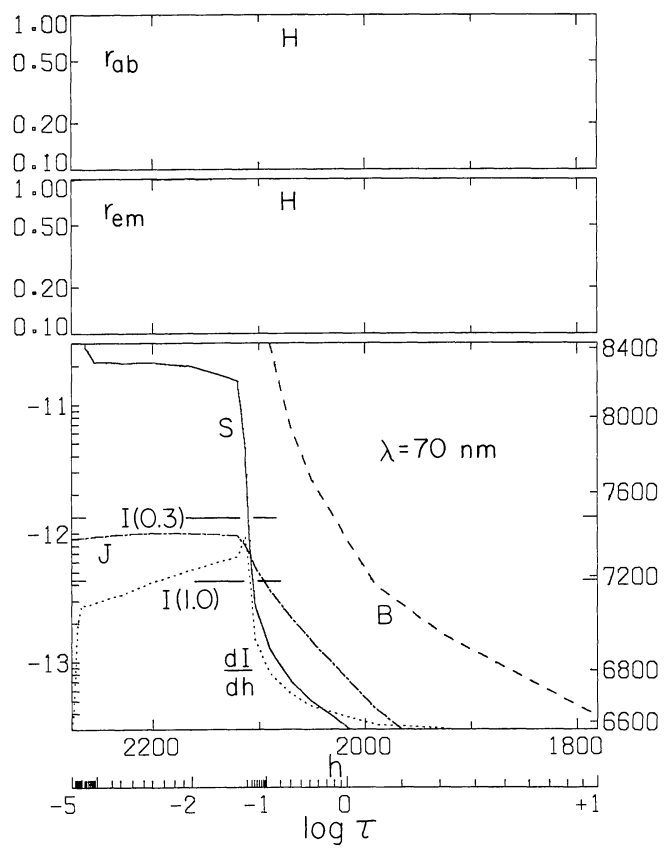


FIG. 36—Continued

figures in Paper II, are plotted as functions of  $\log \tau$  for the particular wavelength and height  $h$  in km above  $\tau_{500\text{nm}}=1$  in the photosphere. The units for  $B$ ,  $S$ ,  $J$ , and  $I$  shown on the left of each large panel are  $\text{ergs cm}^{-2} \text{ s}^{-1} \text{ sr}^{-1} \text{ Hz}^{-1}$ . The corresponding brightness temperatures in K appear on the right.

The depths indicated in Figure 1 at which the intensities at various wavelengths are formed were obtained from the contribution functions plotted in the various panels of Figure 36.

For each of the wavelengths 500, 300, 250, 207.4, 198.2, and 176.7 nm we show a pair of results. The first of each pair includes a mean line opacity, while the second uses real or supposed continuum opacities only. Each panel on the left for these six wavelengths includes an additional opacity determined as follows. We take the  $k=4$  component line opacity distribution function computed for us by R. Kurucz, which was shown in Paper II, and we multiply it by the correction factor necessary to bring the computed central intensity into agreement with the observed broad-band central intensity at the given wavelength. In this way we calculate mean intensities  $J$ , as functions of depth which are appropriate for our determinations of the various photoionization rates.

On the photospheric side of the temperature-minimum region we treat the additional opacity as the absorption coefficient  $\kappa_{\text{add}}$  with the component source function equal to the Planck function, and on the chromospheric side as the scattering coefficient  $\sigma_{\text{add}}$  with the component source function equal to the mean intensity.

For the two wavelengths 500 and 176.7 nm the panel on the right shows the solution with continuum opacity sources alone. At these wavelengths our continuum opacities seem large enough to provide a computed continuum in general agreement with the maximum intensity values observed between the numerous absorption lines.

However, for the wavelengths 300, 250, 207.4, and 198.2 nm the highest intensities observed between absorption lines are much smaller than those computed with the continuum opacities we include. For this reason we show in the right-hand panels results similar to those on the left, but with the additional opacity adjusted to bring the computed intensity into agreement with the highest intensities observed between absorption lines near the given wavelength. We do not use these results in any way but include them to indicate the additional opacity needed to account for the intensity maxima in this region dominated by absorption lines.

Figure 36 represents an extension to a greater wavelength and height range of results presented in a similar figure in Paper II.

## VI. TABLES

In Tables 10 through 15 we list the following atmospheric parameters for models A through F: height

$h$ (km) above the photospheric level at which  $\tau_{500}=1$ , where  $\tau_{500}$  is the continuum optical depth at 500 nm, column mass  $m(\text{g cm}^{-2})$ ,  $\tau_{500}$ , temperature  $T(\text{K})$ , microvelocity  $V(\text{km s}^{-1})$ , total hydrogen number density  $n_{\text{H}}(\text{cm}^{-3})$ , electron number density  $n_e(\text{cm}^{-3})$ , total pressure  $P_{\text{total}}(\text{dynes cm}^{-2})=P_{\text{gas}}+P_{\text{turb}}$ , the fraction  $P_{\text{gas}}/P_{\text{total}}$ , and the gas density  $\rho(\text{g cm}^{-3})$ . The column mass and total pressure are related by  $m=P_{\text{total}}/g$ , where  $g$  is the acceleration of gravity  $=2.74\times 10^4 \text{ cm s}^{-2}$ . The values of these parameters are given at 52 depths in the atmosphere from the low corona to the photosphere. Our temperature distributions are somewhat arbitrary in the region  $T>4\times 10^4 \text{ K}$  where the  $\text{L}\alpha$  line becomes optically thin. As noted earlier, the microvelocity table that we adopt for model C is used without modification for the other five models as well.

The models listed in these tables represent hydrostatic equilibrium solutions obtained when  $T$  and  $V$  are specified functions of  $h$  (or  $m$ ), with  $n_e$  determined from non-LTE ionization calculations for H, Fe, Mg, Si (see Fig. 47 of § VIII), He, He II, C, and Al, and LTE calculations for other atoms that affect  $n_e$ .

We now give further details of our calculations for model C, namely, the number densities and non-LTE departure coefficients for H, C, Si, Fe, Mg, Al, He, and He II. In Table 16 we list the following atomic data for levels 1–8 that we have adopted for these atoms and ions: the term designation, the statistical weight  $g_i$ , the threshold ionization wavelength  $\lambda_i$ , the threshold photoionization cross section  $a_i$  in units of  $10^{-18} \text{ cm}^2$ , and the index  $s_i$  for the wavelength dependence of the photoionization cross section  $a_i(\lambda)=a_i \times 10^{-18}(\lambda/\lambda_i)^{s_i}$ . In the case of Fe, each of the eight indicated levels represents a group of sublevels as specified in Table 4.

In Tables 17–24 for H–He II we give  $n_{\text{ion}}$ , the total number density of the next higher stage of ionization, and the number densities  $n_i$  and departure coefficients  $b_i$  for the eight bound levels listed in Table 16. In the case of H, He, and He II we give the values at all 52 depths as in Table 12. For C, Si, Fe, Mg, and Al we list only the values starting near  $T=10^4 \text{ K}$  in the upper chromosphere because our solution is unaffected by these neutral atoms at higher temperatures.

Finally we give the details of our  $\text{H}^-$  calculation for model C. The equations we solve to obtain the departure coefficient  $b_{\text{H}^-}$  are given in § IX. The quantities  $\delta$ ,  $r$ ,  $\int L/v$ ,  $\int J/v$ ,  $b_{\text{H}^-} \int L$ ,  $\int J$ ,  $n_{\text{H}^-}^*$ , and  $\Phi_{\text{H}^-}$  defined by equations (39)–(54) are listed in Table 25. Again we give only the values starting near  $T=10^4 \text{ K}$ .

The two integrals  $\int J/v$  and  $\int J$  depend on the values of  $J$  throughout an extended wavelength range, and in Table 26 we list the values used in our calculation for the same depths as in Table 25 and for 15 wavelengths between 1642 nm and 100 nm. These wavelengths appear in the first column, and in the second column we give our adopted  $\text{H}^-$  bound-free cross sections from Doughty, Fraser, and McEachran (1966) in units of

TABLE 10  
ATMOSPHERIC PARAMETERS FOR MODEL A

	<i>h</i>	<i>m</i>	$\tau_{500}$	T	V	$n_H$	$n_e$	$P_{\text{total}}$	$\frac{P_{\text{gas}}}{P_{\text{total}}}$	$\sigma$
	(km)	(g cm $^{-2}$ )		(K)	(km s $^{-1}$ )	(cm $^{-3}$ )	(cm $^{-3}$ )	(dyn cm $^{-2}$ )		(g cm $^{-3}$ )
1	2735	2.376-06	0.	447000	11.28	4.544+08	5.443+08	6.510-02	.9896	1.063-15
2	2439	2.436-06	2.031-08	141000	9.87	1.456+09	1.742+09	6.674-02	.9752	3.404-15
3	2430	2.440-06	2.162-08	89100	9.82	2.290+09	2.705+09	6.684-02	.9614	5.356-15
4	2416	2.450-06	2.492-08	50000	9.76	4.112+09	4.539+09	6.713-02	.9318	9.615-15
5	2409	2.458-06	2.737-08	36500	9.73	5.532+09	6.065+09	6.734-02	.9091	1.294-14
6	2405	2.463-06	2.914-08	30000	9.71	6.652+09	7.210+09	6.749-02	.8914	1.555-14
7	2400	2.473-06	3.166-08	26700	9.70	7.443+09	7.971+09	6.775-02	.8791	1.741-14
8	2395	2.483-06	3.444-08	24000	9.68	8.263+09	8.710+09	6.803-02	.8669	1.932-14
9	2375	2.523-06	4.633-08	23100	9.64	8.718+09	9.118+09	6.913-02	.8630	2.039-14
10	2345	2.586-06	6.490-08	22800	9.49	9.087+09	9.472+09	7.084-02	.8649	2.124-14
11	2300	2.684-06	9.399-08	22600	9.33	9.560+09	9.934+09	7.353-02	.8677	2.236-14
12	2240	2.823-06	1.350-07	22400	9.08	1.022+10	1.058+10	7.734-02	.8726	2.391-14
13	2190	2.947-06	1.713-07	22100	8.87	1.089+10	1.120+10	8.073-02	.8759	2.546-14
14	2164	3.014-06	1.910-07	21700	8.81	1.137+10	1.162+10	8.258-02	.8751	2.658-14
15	2154	3.042-06	1.990-07	20700	8.78	1.205+10	1.211+10	8.335-02	.8697	2.818-14
16	2150	3.055-06	2.023-07	18200	8.77	1.380+10	1.319+10	8.369-02	.8517	3.227-14
17	2146	3.070-06	2.063-07	12300	8.74	2.044+10	1.630+10	8.412-02	.7830	4.780-14
18	2143	3.085-06	2.097-07	10700	8.73	2.342+10	1.738+10	8.453-02	.7537	5.476-14
19	2141	3.097-06	2.121-07	9500	8.71	2.613+10	1.829+10	8.485-02	.7269	6.110-14
20	2126	3.199-06	2.313-07	8150	8.60	3.146+10	1.912+10	8.764-02	.6896	7.356-14
21	2114	3.292-06	2.471-07	7600	8.55	3.476+10	1.942+10	9.020-02	.6706	8.128-14
22	2096	3.448-06	2.711-07	7150	8.50	3.888+10	1.965+10	9.446-02	.6523	9.092-14
23	2074	3.661-06	3.009-07	6800	8.42	4.377+10	2.006+10	1.003-01	.6383	1.024-13
24	2040	4.038-06	3.485-07	6620	8.22	5.102+10	2.082+10	1.106-01	.6356	1.193-13
25	1990	4.703-06	4.220-07	6460	8.01	6.313+10	2.195+10	1.289-01	.6325	1.476-13
26	1915	6.011-06	5.403-07	6340	7.63	8.761+10	2.367+10	1.647-01	.6379	2.049-13
27	1785	9.669-06	7.766-07	6180	6.92	1.606+11	2.837+10	2.649-01	.6605	3.756-13
28	1605	2.076-05	1.190-06	6080	5.85	4.073+11	3.527+10	5.687-01	.7134	9.525-13
29	1505	3.353-05	1.485-06	6030	5.26	7.128+11	4.247+10	9.186-01	.7490	1.667-12
30	1380	6.445-05	1.944-06	5990	4.51	1.505+12	4.707+10	1.766+00	.7973	3.519-12
31	1280	1.135-04	2.372-06	5945	3.92	2.838+12	4.585+10	3.109+00	.8360	6.636-12
32	1205	1.781-04	2.757-06	5880	3.48	4.676+12	5.115+10	4.879+00	.8643	1.094-11
33	1080	3.954-04	3.701-06	5790	2.73	1.117+13	5.572+10	1.083+01	.9102	2.611-11
34	980	7.821-04	4.926-06	5650	2.14	2.346+13	5.704+10	2.143+01	.9414	5.486-11
35	905	1.340-03	6.397-06	5530	1.70	4.199+13	5.759+10	3.672+01	.9614	9.819-11
36	855	1.947-03	7.828-06	5370	1.53	6.326+13	5.515+10	5.336+01	.9675	1.479-10
37	755	4.301-03	1.256-05	5000	1.23	1.516+14	4.869+10	1.178+02	.9772	3.546-10
38	705	6.577-03	1.677-05	4740	1.09	2.456+14	4.772+10	1.802+02	.9811	5.742-10
39	655	1.034-02	2.484-05	4430	.96	4.146+14	6.036+10	2.834+02	.9842	9.694-10
40	605	1.686-02	4.763-05	4110	.83	7.305+14	9.288+10	4.618+02	.9873	1.708-09
41	560	2.696-02	1.126-04	3930	.70	1.226+15	1.413+11	7.386+02	.9905	2.866-09
42	510	4.610-02	3.214-04	3900	.60	2.118+15	2.260+11	1.263+03	.9929	4.952-09
43	450	8.745-02	1.063-03	4000	.53	3.923+15	4.005+11	2.396+03	.9946	9.174-09
44	350	2.413-01	5.970-03	4330	.52	1.000+16	1.035+12	6.611+03	.9952	2.340-08
45	250	6.120-01	2.767-02	4720	.63	2.324+16	2.593+12	1.677+04	.9936	5.435-08
46	150	1.429+00	1.130-01	5165	1.00	4.919+16	6.406+12	3.916+04	.9853	1.150-07
47	100	2.115+00	2.209-01	5450	1.20	6.860+16	1.059+13	5.794+04	.9801	1.604-07
48	50	3.052+00	4.387-01	5840	1.40	9.188+16	2.115+13	8.361+04	.9748	2.149-07
49	0	4.272+00	9.905-01	6420	1.60	1.164+17	6.414+13	1.170+05	.9702	2.723-07
50	-25	4.983+00	1.673+00	6910	1.70	1.259+17	1.542+14	1.365+05	.9688	2.945-07
51	-50	5.738+00	3.317+00	7610	1.76	1.315+17	4.631+14	1.572+05	.9697	3.075-07
52	-75	6.523+00	7.396+00	8320	1.80	1.363+17	1.201+15	1.787+05	.9711	3.187-07

TABLE 11  
ATMOSPHERIC PARAMETERS FOR MODEL B

	<i>h</i>	<i>m</i>	$\tau_{500}$	T	V	$n_H$	$n_e$	$P_{\text{total}}$	$\frac{P_{\text{gas}}}{P_{\text{total}}}$	$\sigma$
	(km)	(g cm $^{-2}$ )		(K)	(km s $^{-1}$ )	(cm $^{-3}$ )	(cm $^{-3}$ )	(dyn cm $^{-2}$ )		(g cm $^{-3}$ )
1	2591	3.611-06	0.	447000	11.28	6.890+08	8.287+08	9.893-02	.9896	1.611-15
2	2346	3.685-06	2.554-08	141000	9.87	2.198+09	2.641+09	1.010-01	.9752	5.140-15
3	2338	3.691-06	2.730-08	89100	9.82	3.457+09	4.101+09	1.011-01	.9614	8.085-15
4	2328	3.701-06	3.090-08	50000	9.76	6.199+09	6.873+09	1.014-01	.9319	1.450-14
5	2322	3.711-06	3.406-08	37000	9.73	8.233+09	9.068+09	1.017-01	.9104	1.925-14
6	2319	3.718-06	3.601-08	31700	9.71	9.522+09	1.040+10	1.019-01	.8969	2.227-14
7	2315	3.727-06	3.902-08	26600	9.70	1.125+10	1.207+10	1.021-01	.8788	2.630-14
8	2310	3.741-06	4.319-08	24500	9.68	1.223+10	1.290+10	1.025-01	.8693	2.859-14
9	2294	3.788-06	5.722-08	23700	9.64	1.280+10	1.339+10	1.038-01	.8660	2.993-14
10	2277	3.840-06	7.265-08	23300	9.49	1.325+10	1.380+10	1.052-01	.8674	3.098-14
11	2245	3.942-06	1.027-07	23000	9.33	1.383+10	1.436+10	1.080-01	.8696	3.235-14
12	2200	4.092-06	1.471-07	22700	9.08	1.466+10	1.514+10	1.121-01	.8739	3.428-14
13	2165	4.215-06	1.832-07	22500	8.87	1.535+10	1.575+10	1.155-01	.8777	3.589-14
14	2148	4.277-06	2.014-07	22000	8.81	1.595+10	1.627+10	1.172-01	.8765	3.730-14
15	2138	4.316-06	2.125-07	20700	8.78	1.714+10	1.712+10	1.182-01	.8694	4.007-14
16	2135	4.328-06	2.161-07	18000	8.77	1.981+10	1.876+10	1.186-01	.8498	4.633-14
17	2131	4.351-06	2.218-07	12300	8.74	2.894+10	2.314+10	1.192-01	.7831	6.768-14
18	2129	4.365-06	2.251-07	10700	8.72	3.302+10	2.477+10	1.196-01	.7545	7.722-14
19	2125	4.398-06	2.320-07	9500	8.71	3.711+10	2.596+10	1.205-01	.7268	8.678-14
20	2104	4.601-06	2.701-07	8330	8.60	4.476+10	2.672+10	1.260-01	.6929	1.047-13
21	2093	4.722-06	2.904-07	7830	8.55	4.906+10	2.694+10	1.294-01	.6759	1.147-13
22	2077	4.914-06	3.201-07	7550	8.50	5.349+10	2.700+10	1.346-01	.6644	1.251-13
23	2058	5.165-06	3.556-07	7300	8.42	5.887+10	2.724+10	1.415-01	.6551	1.377-13
24	2026	5.641-06	4.163-07	7110	8.22	6.812+10	2.770+10	1.546-01	.6518	1.593-13
25	1980	6.456-06	5.057-07	6890	8.01	8.341+10	2.843+10	1.769-01	.6463	1.950-13
26	1915	7.932-06	6.374-07	6715	7.63	1.115+11	2.992+10	2.173-01	.6508	2.607-13
27	1785	1.255-05	9.299-07	6470	6.92	2.033+11	3.378+10	3.438-01	.6688	4.755-13
28	1605	2.642-05	1.443-06	6300	5.85	5.052+11	4.414+10	7.239-01	.7202	1.181-12
29	1505	4.219-05	1.827-06	6220	5.26	8.754+11	5.340+10	1.156+00	.7550	2.047-12
30	1380	7.995-05	2.413-06	6140	4.51	1.831+12	5.615+10	2.191+00	.8012	4.282-12
31	1280	1.392-04	2.979-06	6090	3.92	3.408+12	6.022+10	3.815+00	.8395	7.970-12
32	1205	2.164-04	3.519-06	6030	3.48	5.556+12	6.561+10	5.928+00	.8673	1.299-11
33	1080	4.724-04	4.825-06	5920	2.73	1.307+13	7.059+10	1.294+01	.9120	3.056-11
34	980	9.208-04	6.566-06	5785	2.14	2.700+13	7.624+10	2.523+01	.9427	6.315-11
35	905	1.562-03	8.703-06	5625	1.70	4.812+13	7.552+10	4.279+01	.9620	1.125-10
36	855	2.253-03	1.076-05	5500	1.53	7.149+13	7.413+10	6.172+01	.9683	1.672-10
37	755	4.874-03	1.739-05	5140	1.23	1.672+14	6.383+10	1.335+02	.9778	3.911-10
38	705	7.364-03	2.286-05	4890	1.09	2.667+14	5.945+10	2.018+02	.9816	6.236-10
39	655	1.142-02	3.236-05	4580	.96	4.429+14	6.878+10	3.128+02	.9847	1.036-09
40	605	1.831-02	5.624-05	4255	.83	7.668+14	1.014+11	5.017+02	.9877	1.793-09
41	555	3.031-02	1.329-04	4070	.70	1.331+15	1.608+11	8.303+02	.9908	3.112-09
42	505	5.096-02	3.653-04	4020	.60	2.271+15	2.577+11	1.396+03	.9932	5.311-09
43	450	9.018-02	1.064-03	4100	.53	3.948+15	4.313+11	2.471+03	.9948	9.231-09
44	350	2.444-01	5.993-03	4370	.52	1.004+16	1.078+12	6.696+03	.9953	2.348-08
45	250	6.159-01	2.770-02	4755	.63	2.322+16	2.645+12	1.687+04	.9936	5.429-08
46	150	1.433+00	1.136-01	5170	1.00	4.926+16	6.464+12	3.925+04	.9853	1.152-07
47	100	2.119+00	2.229-01	5450	1.20	6.876+16	1.065+13	5.807+04	.9801	1.608-07
48	50	3.058+00	4.437-01	5840	1.40	9.209+16	2.128+13	8.380+04	.9748	2.154-07
49	0	4.282+00	1.003+00	6420	1.60	1.167+17	6.452+13	1.173+05	.9702	2.729-07
50	-25	4.995+00	1.695+00	6910	1.70	1.262+17	1.551+14	1.368+05	.9688	2.951-07
51	-50	5.751+00	3.361+00	7610	1.76	1.318+17	4.658+14	1.576+05	.9697	3.082-07
52	-75	6.538+00	7.494+00	8320	1.80	1.366+17	1.208+15	1.791+05	.9711	3.194-07

TABLE 12  
ATMOSPHERIC PARAMETERS FOR MODEL C

	<i>h</i>	<i>m</i>	$\tau_{500}$	T	V	$n_H$	$n_e$	$P_{\text{total}}$	$\frac{P_{\text{gas}}}{P_{\text{total}}}$	$\sigma$
	(km)	(g cm $^{-2}$ )		(K)	(km s $^{-1}$ )	(cm $^{-3}$ )	(cm $^{-3}$ )	(dyn cm $^{-2}$ )		(g cm $^{-3}$ )
1	2543	5.257-06	0.	447000	11.28	1.005+09	1.205+09	1.440-01	.9896	2.349-15
2	2298	5.365-06	3.712-08	141000	9.87	3.205+09	3.839+09	1.470-01	.9752	7.494-15
3	2290	5.373-06	3.969-08	89100	9.82	5.041+09	5.961+09	1.472-01	.9614	1.179-14
4	2280	5.389-06	4.491-08	50000	9.76	9.038+09	9.993+09	1.477-01	.9318	2.113-14
5	2274	5.404-06	4.952-08	37000	9.73	1.201+10	1.318+10	1.481-01	.9102	2.808-14
6	2271	5.413-06	5.234-08	32000	9.71	1.378+10	1.498+10	1.483-01	.8976	3.222-14
7	2267	5.427-06	5.657-08	28000	9.70	1.567+10	1.677+10	1.487-01	.8840	3.665-14
8	2263	5.443-06	6.124-08	25500	9.68	1.718+10	1.812+10	1.491-01	.8738	4.017-14
9	2255	5.476-06	7.110-08	24500	9.64	1.797+10	1.881+10	1.500-01	.8698	4.203-14
10	2230	5.583-06	1.030-07	24200	9.49	1.862+10	1.943+10	1.530-01	.8718	4.355-14
11	2200	5.716-06	1.426-07	24000	9.33	1.932+10	2.009+10	1.566-01	.8645	4.517-14
12	2160	5.902-06	1.977-07	23500	9.08	2.051+10	2.120+10	1.617-01	.8778	4.795-14
13	2129	6.055-06	2.427-07	23000	8.87	2.163+10	2.219+10	1.659-01	.8801	5.058-14
14	2120	6.101-06	2.562-07	22500	8.81	2.231+10	2.276+10	1.672-01	.8789	5.216-14
15	2115	6.128-06	2.640-07	21000	8.78	2.403+10	2.402+10	1.679-01	.8710	5.619-14
16	2113	6.140-06	2.674-07	18500	8.77	2.732+10	2.620+10	1.682-01	.8539	6.390-14
17	2109	6.172-06	2.754-07	12300	8.74	4.092+10	3.306+10	1.691-01	.7839	9.569-14
18	2107	6.193-06	2.801-07	10700	8.72	4.673+10	3.535+10	1.697-01	.7552	1.093-13
19	2104	6.228-06	2.877-07	9500	8.71	5.239+10	3.705+10	1.706-01	.7277	1.225-13
20	2090	6.416-06	3.243-07	8440	8.60	6.127+10	3.799+10	1.758-01	.6986	1.433-13
21	2080	6.564-06	3.507-07	8180	8.55	6.541+10	3.780+10	1.798-01	.6891	1.530-13
22	2070	6.722-06	3.770-07	7940	8.50	6.960+10	3.783+10	1.842-01	.6808	1.628-13
23	2050	7.066-06	4.299-07	7660	8.42	7.705+10	3.792+10	1.936-01	.6701	1.802-13
24	2016	7.732-06	5.203-07	7360	8.22	9.075+10	3.811+10	2.118-01	.6616	2.122-13
25	1990	8.322-06	5.903-07	7160	8.01	1.033+11	3.858+10	2.280-01	.6600	2.417-13
26	1925	1.015-05	7.717-07	6940	7.63	1.380+11	4.028+10	2.780-01	.6620	3.227-13
27	1785	1.647-05	1.212-06	6630	6.92	2.601+11	4.771+10	4.511-01	.6772	6.082-13
28	1605	3.407-05	1.958-06	6440	5.85	6.386+11	6.005+10	9.334-01	.7262	1.493-12
29	1515	5.144-05	2.420-06	6370	5.26	1.048+12	6.456+10	1.409+00	.7595	2.450-12
30	1380	1.012-04	3.286-06	6280	4.51	2.273+12	7.600+10	2.774+00	.8051	5.315-12
31	1280	1.747-04	4.084-06	6220	3.92	4.200+12	7.486+10	4.786+00	.8423	9.822-12
32	1180	3.112-04	5.075-06	6150	3.48	7.865+12	8.108+10	8.527+00	.8694	1.839-11
33	1065	6.299-04	6.861-06	6040	2.73	1.711+13	9.349+10	1.726+01	.9136	4.000-11
34	980	1.098-03	9.148-06	5925	2.14	3.147+13	1.041+11	3.008+01	.9440	7.359-11
35	905	1.840-03	1.239-05	5755	1.70	5.546+13	1.049+11	5.043+01	.9628	1.297-10
36	855	2.632-03	1.553-05	5650	1.53	8.135+13	1.064+11	7.210+01	.9691	1.902-10
37	755	5.577-03	2.537-05	5280	1.23	1.864+14	8.838+10	1.528+02	.9784	4.358-10
38	705	8.333-03	3.288-05	5030	1.09	2.935+14	7.664+10	2.283+02	.9821	6.864-10
39	655	1.276-02	4.452-05	4730	.96	4.794+14	8.085+10	3.495+02	.9852	1.121-09
40	605	2.013-02	7.022-05	4420	.83	8.119+14	1.112+11	5.516+02	.9881	1.899-09
41	555	3.270-02	1.456-04	4230	.70	1.382+15	1.733+11	8.958+02	.9912	3.232-09
42	515	4.878-02	3.014-04	4170	.60	2.096+15	2.495+11	1.336+03	.9934	4.902-09
43	450	9.378-02	1.017-03	4220	.53	3.989+15	4.516+11	2.569+03	.9949	9.327-09
44	350	2.481-01	5.626-03	4465	.52	9.979+15	1.110+12	6.798+03	.9954	2.334-08
45	250	6.172-01	2.670-02	4780	.63	2.315+16	2.674+12	1.691+04	.9936	5.413-08
46	150	1.433+00	1.117-01	5180	1.00	4.917+16	6.476+12	3.926+04	.9854	1.150-07
47	100	2.118+00	2.201-01	5455	1.20	6.866+16	1.066+13	5.804+04	.9801	1.606-07
48	50	3.056+00	4.395-01	5840	1.40	9.203+16	2.122+13	8.274+04	.9748	2.152-07
49	0	4.279+00	9.953-01	6420	1.60	1.166+17	6.433+13	1.172+05	.9702	2.727-07
50	-25	4.991+00	1.683+00	6910	1.70	1.261+17	1.547+14	1.368+05	.9688	2.949-07
51	-50	5.747+00	3.338+00	7610	1.76	1.317+17	4.645+14	1.575+05	.9697	3.080-07
52	-75	6.534+00	7.445+00	8320	1.80	1.365+17	1.204+15	1.790+05	.9711	3.192-07

TABLE 13  
ATMOSPHERIC PARAMETERS FOR MODEL D

	<i>h</i>	<i>m</i>	$\tau_{500}$	<i>T</i>	<i>V</i>	$n_H$	$n_e$	$P_{\text{total}}$	$\frac{P_{\text{gas}}}{P_{\text{total}}}$	$\sigma$
	(km)	(g cm $^{-2}$ )		(K)	(km s $^{-1}$ )	(cm $^{-3}$ )	(cm $^{-3}$ )	(dyn cm $^{-2}$ )		(g cm $^{-3}$ )
1	2508	6.699-06	0.	447000	11.28	1.280+09	1.535+09	1.835-01	.9896	2.994-15
2	2263	6.838-06	4.735-08	141000	9.87	4.084+09	4.893+09	1.873-01	.9752	9.551-15
3	2255	6.847-06	5.062-08	89100	9.82	6.425+09	7.596+09	1.876-01	.9614	1.502-14
4	2245	6.868-06	5.729-08	50000	9.76	1.152+10	1.273+10	1.882-01	.9318	2.694-14
5	2239	6.886-06	6.319-08	37100	9.73	1.527+10	1.674+10	1.887-01	.9104	3.570-14
6	2235	6.901-06	6.796-08	32300	9.71	1.742+10	1.893+10	1.891-01	.8984	4.074-14
7	2231	6.920-06	7.326-08	29000	9.70	1.934+10	2.076+10	1.896-01	.8878	4.523-14
8	2226	6.945-06	8.042-08	27000	9.68	2.079+10	2.207+10	1.903-01	.8803	4.861-14
9	2219	6.980-06	9.093-08	26000	9.64	2.168+10	2.287+10	1.912-01	.8768	5.069-14
10	2198	7.088-06	1.239-07	25000	9.49	2.295+10	2.402+10	1.942-01	.8755	5.367-14
11	2166	7.263-06	1.764-07	24500	9.33	2.410+10	2.508+10	1.990-01	.8767	5.635-14
12	2135	7.442-06	2.296-07	24000	9.08	2.537+10	2.625+10	2.039-01	.8800	5.933-14
13	2111	7.588-06	2.726-07	23500	8.87	2.659+10	2.730+10	2.079-01	.8824	6.217-14
14	2104	7.632-06	2.856-07	23000	8.81	2.735+10	2.796+10	2.091-01	.8813	6.395-14
15	2100	7.658-06	2.932-07	22000	8.78	2.873+10	2.896+10	2.098-01	.8766	6.718-14
16	2098	7.673-06	2.973-07	19500	8.77	3.240+10	3.163+10	2.102-01	.8614	7.578-14
17	2094	7.711-06	3.070-07	13000	8.74	4.847+10	4.029+10	2.113-01	.7951	1.133-13
18	2093	7.725-06	3.099-07	10800	8.72	5.743+10	4.453+10	2.116-01	.7587	1.343-13
19	2090	7.767-06	3.195-07	9610	8.71	6.435+10	4.661+10	2.128-01	.7318	1.505-13
20	2076	7.998-06	3.663-07	8520	8.60	7.537+10	4.800+10	2.191-01	.7026	1.762-13
21	2062	8.256-06	4.135-07	8250	8.55	8.160+10	4.762+10	2.262-01	.6917	1.908-13
22	2048	8.534-06	4.604-07	8000	8.50	8.809+10	4.745+10	2.338-01	.6818	2.060-13
23	2024	9.060-06	5.406-07	7740	8.42	9.873+10	4.712+10	2.482-01	.6703	2.309-13
24	1996	9.755-06	6.343-07	7530	8.22	1.128+11	4.730+10	2.673-01	.6666	2.638-13
25	1960	1.079-05	7.566-07	7340	8.01	1.325+11	4.784+10	2.955-01	.6637	3.098-13
26	1910	1.253-05	9.312-07	7140	7.63	1.671+11	4.912+10	3.434-01	.6687	3.908-13
27	1785	1.911-05	1.415-06	6830	6.92	2.941+11	5.706+10	5.235-01	.6854	6.877-13
28	1605	3.895-05	2.331-06	6580	5.85	7.153+11	7.282+10	1.067+00	.7318	1.673-12
29	1505	6.103-05	2.962-06	6500	5.26	1.225+12	7.489+10	1.672+00	.7631	2.864-12
30	1380	1.132-04	3.934-06	6390	4.51	2.503+12	8.844+10	3.102+00	.8081	5.853-12
31	1280	1.936-04	4.916-06	6320	3.92	4.588+12	8.883+10	5.305+00	.8446	1.073-11
32	1205	2.967-04	5.804-06	6250	3.48	7.380+12	9.280+10	8.129+00	.8715	1.726-11
33	1080	6.316-04	8.066-06	6140	2.73	1.688+13	1.131+11	1.731+01	.9150	3.947-11
34	980	1.202-03	1.152-05	6020	2.14	3.392+13	1.318+11	3.294+01	.9449	7.932-11
35	905	1.998-03	1.589-05	5860	1.70	5.914+13	1.350+11	5.473+01	.9635	1.383-10
36	855	2.841-03	2.005-05	5730	1.53	8.660+13	1.320+11	7.783+01	.9695	2.025-10
37	755	5.960-03	3.250-05	5360	1.23	1.963+14	1.073+11	1.633+02	.9787	4.589-10
38	705	8.856-03	4.161-05	5100	1.09	3.077+14	9.045+10	2.426+02	.9824	7.195-10
39	655	1.348-02	5.498-05	4800	.96	4.991+14	8.959+10	3.693+02	.9854	1.167-09
40	605	2.111-02	8.229-05	4500	.83	8.366+14	1.177+11	5.785+02	.9884	1.956-09
41	555	3.400-02	1.584-04	4310	.70	1.411+15	1.809+11	9.315+02	.9913	3.299-09
42	505	5.713-02	3.889-04	4270	.60	2.398+15	2.900+11	1.565+03	.9936	5.608-09
43	450	9.522-02	9.885-04	4300	.53	3.975+15	4.623+11	2.609+03	.9950	9.295-09
44	350	2.487-01	5.441-03	4500	.52	9.923+15	1.121+12	6.813+03	.9954	2.321-08
45	250	6.167-01	2.638-02	4775	.63	2.315+16	2.668+12	1.690+04	.9936	5.414-08
46	150	1.434+00	1.117-01	5175	1.00	4.925+16	6.472+12	3.928+04	.9853	1.152-07
47	100	2.121+00	2.205-01	5450	1.20	6.879+16	1.064+13	5.810+04	.9801	1.609-07
48	50	3.060+00	4.405-01	5840	1.40	9.214+16	2.124+13	8.384+04	.9748	2.155-07
49	0	4.284+00	9.975-01	6420	1.60	1.168+17	6.438+13	1.174+05	.9702	2.730-07
50	-25	4.997+00	1.687+00	6910	1.70	1.263+17	1.548+14	1.369+05	.9688	2.953-07
51	-50	5.754+00	3.346+00	7610	1.76	1.319+17	4.649+14	1.577+05	.9697	3.048-07
52	-75	6.541+00	7.461+00	8320	1.80	1.367+17	1.205+15	1.792+05	.9711	3.196-07

TABLE 14  
ATMOSPHERIC PARAMETERS FOR MODEL E

	<i>h</i>	<i>m</i>	$\tau_{500}$	T	V	$n_H$	$n_e$	$P_{\text{total}}$	$P_{\text{gas}}/P_{\text{total}}$	$\sigma$
	(km)	(g cm $^{-2}$ )		(K)	(km s $^{-1}$ )	(cm $^{-3}$ )	(cm $^{-3}$ )	(dyn cm $^{-2}$ )		(g cm $^{-3}$ )
1	2468	8.658-06	0.	447000	11.28	1.654+09	1.985+09	2.372-01	.9896	3.868-15
2	2223	8.837-06	6.116-08	141000	9.87	5.277+09	6.326+09	2.421-01	.9752	1.234-14
3	2215	8.850-06	6.539-08	89100	9.82	8.301+09	9.821+09	2.425-01	.9614	1.941-14
4	2205	8.876-06	7.400-08	50000	9.76	1.488+10	1.646+10	2.432-01	.9318	3.480-14
5	2199	8.901-06	8.167-08	37000	9.73	1.977+10	2.172+10	2.439-01	.9103	4.622-14
6	2195	8.920-06	8.778-08	33000	9.71	2.206+10	2.405+10	2.444-01	.9005	5.158-14
7	2188	8.959-06	9.972-08	29000	9.70	2.503+10	2.690+10	2.455-01	.8878	5.854-14
8	2182	8.996-06	1.108-07	27300	9.68	2.668+10	2.830+10	2.465-01	.8814	6.238-14
9	2175	9.041-06	1.244-07	25800	9.64	2.830+10	2.979+10	2.477-01	.8759	6.617-14
10	2163	9.122-06	1.486-07	25300	9.49	2.920+10	3.063+10	2.499-01	.8770	6.828-14
11	2149	9.240-06	1.841-07	24700	9.33	3.039+10	3.175+10	2.532-01	.8778	7.106-14
12	2129	9.363-06	2.208-07	24300	9.08	3.151+10	3.276+10	2.565-01	.8816	7.369-14
13	2115	9.469-06	2.519-07	23900	8.87	3.260+10	3.367+10	2.594-01	.8844	7.624-14
14	2095	9.626-06	2.982-07	23000	8.81	3.443+10	3.534+10	2.637-01	.8815	8.052-14
15	2091	9.658-06	3.078-07	22500	8.78	3.540+10	3.598+10	2.646-01	.8794	8.278-14
16	2088	9.685-06	3.154-07	19900	8.77	4.002+10	3.946+10	2.653-01	.8644	9.359-14
17	2084	9.732-06	3.277-07	13000	8.74	6.091+10	5.127+10	2.666-01	.7960	1.424-13
18	2082	9.763-06	3.353-07	10800	8.72	7.251+10	5.642+10	2.675-01	.7590	1.696-13
19	2078	9.836-06	3.517-07	9555	8.71	8.187+10	5.919+10	2.695-01	.7305	1.914-13
20	2062	1.017-05	4.197-07	8660	8.60	9.479+10	6.016+10	2.785-01	.7057	2.217-13
21	2050	1.044-05	4.711-07	8420	8.55	1.015+11	5.987+10	2.861-01	.6968	2.374-13
22	2030	1.094-05	5.562-07	8170	8.50	1.117+11	5.931+10	2.998-01	.6853	2.612-13
23	2010	1.149-05	6.409-07	7980	8.42	1.224+11	5.900+10	3.248-01	.6777	2.863-13
24	1984	1.228-05	7.515-07	7790	8.22	1.382+11	5.944+10	3.366-01	.6756	3.232-13
25	1950	1.347-05	8.994-07	7600	8.01	1.604+11	6.058+10	3.691-01	.6739	3.751-13
26	1904	1.539-05	1.110-06	7370	7.63	1.981+11	6.402+10	4.217-01	.6802	4.632-13
27	1785	2.267-05	1.735-06	7020	6.92	3.380+11	7.397+10	6.212-01	.6954	7.903-13
28	1605	4.540-05	2.950-06	6710	5.85	8.190+11	8.805+10	1.244+00	.7365	1.915-12
29	1515	6.762-05	3.663-06	6620	5.26	1.332+12	9.024+10	1.853+00	.7674	3.115-12
30	1380	1.302-04	4.980-06	6500	4.51	2.835+12	1.051+11	3.567+00	.8110	6.630-12
31	1280	2.212-04	6.270-06	6410	3.92	5.170+12	1.113+11	6.060+00	.8467	1.209-11
32	1180	3.878-04	7.964-06	6340	3.48	9.525+12	1.211+11	1.062+01	.8731	2.227-11
33	1065	7.694-04	1.107-05	6225	2.73	2.030+13	1.453+11	2.108+01	.9161	4.746-11
34	980	1.320-03	1.513-05	6100	2.14	3.678+13	1.633+11	3.617+01	.9456	8.600-11
35	905	2.178-03	2.099-05	5960	1.70	6.341+13	1.734+11	5.968+01	.9641	1.483-10
36	855	3.078-03	2.668-05	5840	1.53	9.209+13	1.728+11	8.433+01	.9701	2.153-10
37	755	6.365-03	4.333-05	5470	1.23	2.055+14	1.390+11	1.744+02	.9792	4.804-10
38	705	9.379-03	5.504-05	5220	1.09	3.185+14	1.153+11	2.570+02	.9828	7.448-10
39	655	1.415-02	7.099-05	4900	.96	5.135+14	1.037+11	3.877+02	.9857	1.201-09
40	605	2.197-02	1.001-04	4600	.83	8.520+14	1.260+11	6.021+02	.9886	1.992-09
41	555	3.506-02	1.764-04	4390	.70	1.429+15	1.884+11	9.606+02	.9915	3.341-09
42	515	5.149-02	3.240-04	4350	.60	2.122+15	2.664+11	1.411+03	.9937	4.962-09
43	450	9.655-02	9.844-04	4360	.53	3.975+15	4.736+11	2.645+03	.9951	9.296-09
44	350	2.499-01	5.393-03	4520	.52	9.928+15	1.135+12	6.847+03	.9954	2.322-08
45	250	6.177-01	2.617-02	4795	.63	2.309+16	2.690+12	1.692+04	.9937	5.401-08
46	150	1.433+00	1.113-01	5175	1.00	4.923+16	6.475+12	3.927+04	.9853	1.151-07
47	100	2.120+00	2.202-01	5450	1.20	6.877+16	1.064+13	5.808+04	.9801	1.608-07
48	50	3.059+00	4.403-01	5840	1.40	9.211+16	2.125+13	8.382+04	.9748	2.154-07
49	0	4.283+00	9.975-01	6420	1.60	1.167+17	6.441+13	1.173+05	.9702	2.729-07
50	-25	4.996+00	1.687+00	6910	1.70	1.262+17	1.549+14	1.369+05	.9688	2.952-07
51	-50	5.752+00	3.347+00	7610	1.76	1.318+17	4.650+14	1.576+05	.9697	3.083-07
52	-75	6.539+00	7.466+00	8320	1.80	1.366+17	1.206+15	1.792+05	.9711	3.195-07

TABLE 15  
ATMOSPHERIC PARAMETERS FOR MODEL F

	<i>h</i>	<i>m</i>	$\tau_{500}$	T	V	$n_H$	$n_e$	$P_{\text{total}}$	$\frac{P_{\text{gas}}}{P_{\text{total}}}$	$\sigma$
	(km)	(g cm $^{-2}$ )		(K)	(km s $^{-1}$ )	(cm $^{-3}$ )	(cm $^{-3}$ )	(dyn cm $^{-2}$ )		(g cm $^{-3}$ )
1	2429	1.119-05	0.	447000	11.28	2.137+09	2.567+09	3.067-01	.9896	4.998-15
2	2184	1.142-05	7.909-08	141000	9.87	6.819+09	8.181+09	3.130-01	.9752	1.595-14
3	2176	1.144-05	8.456-08	89100	9.82	1.073+10	1.270+10	3.134-01	.9614	2.508-14
4	2166	1.147-05	9.570-08	50000	9.76	1.923+10	2.129+10	3.144-01	.9319	4.497-14
5	2160	1.151-05	1.056-07	37000	9.73	2.555+10	2.808+10	3.152-01	.9103	5.974-14
6	2156	1.153-05	1.135-07	33000	9.71	2.850+10	3.111+10	3.159-01	.9006	6.664-14
7	2150	1.157-05	1.266-07	30000	9.70	3.130+10	3.382+10	3.171-01	.8914	7.319-14
8	2144	1.162-05	1.406-07	28000	9.68	3.356+10	3.592+10	3.183-01	.8845	7.849-14
9	2136	1.168-05	1.601-07	27000	9.64	3.497+10	3.722+10	3.201-01	.8813	8.177-14
10	2130	1.173-05	1.754-07	26000	9.49	3.654+10	3.865+10	3.215-01	.8803	8.546-14
11	2122	1.180-05	1.963-07	25500	9.33	3.760+10	3.963+10	3.234-01	.8817	8.792-14
12	2110	1.191-05	2.287-07	25000	9.08	3.893+10	4.086+10	3.263-01	.8850	9.104-14
13	2094	1.206-05	2.733-07	24500	8.87	4.045+10	4.219+10	3.304-01	.8874	9.459-14
14	2082	1.218-05	3.081-07	23500	8.81	4.259+10	4.408+10	3.336-01	.8841	9.959-14
15	2074	1.226-05	3.320-07	23000	8.78	4.393+10	4.498+10	3.358-01	.8821	1.027-13
16	2070	1.230-05	3.448-07	20000	8.77	5.046+10	5.013+10	3.370-01	.8654	1.180-13
17	2067	1.234-05	3.566-07	13500	8.74	7.415+10	6.438+10	3.382-01	.8042	1.734-13
18	2065	1.238-05	3.663-07	10800	8.72	9.136+10	7.259+10	3.393-01	.7606	2.136-13
19	2063	1.243-05	3.770-07	9555	8.71	1.024+11	7.661+10	3.405-01	.7332	2.395-13
20	2044	1.292-05	4.835-07	8660	8.60	1.195+11	7.823+10	3.541-01	.7081	2.795-13
21	2023	1.354-05	6.021-07	8400	8.55	1.320+11	7.740+10	3.710-01	.6958	3.088-13
22	2010	1.396-05	6.751-07	8250	8.50	1.405+11	7.693+10	3.824-01	.6895	3.286-13
23	1992	1.457-05	7.762-07	8110	8.42	1.521+11	7.678+10	3.993-01	.6843	3.556-13
24	1968	1.548-05	9.126-07	7950	8.22	1.696+11	7.771+10	4.240-01	.6840	3.966-13
25	1937	1.679-05	1.094-06	7780	8.01	1.938+11	7.976+10	4.600-01	.6840	4.532-13
26	1890	1.915-05	1.389-06	7550	7.63	2.386+11	8.533+10	5.248-01	.6906	5.578-13
27	1785	2.671-05	2.154-06	7150	6.92	3.863+11	9.733+10	7.317-01	.7044	9.033-13
28	1605	5.247-05	3.831-06	6840	5.85	9.244+11	1.140+11	1.438+00	.7427	2.161-12
29	1515	7.746-05	4.837-06	6740	5.26	1.494+12	1.181+11	2.122+00	.7723	3.494-12
30	1380	1.475-04	6.613-06	6600	4.51	3.166+12	1.269+11	4.042+00	.8137	7.404-12
31	1280	2.484-04	8.277-06	6510	3.92	5.723+12	1.346+11	6.807+00	.8489	1.338-11
32	1210	3.658-04	9.744-06	6450	3.48	8.828+12	1.421+11	1.002+01	.8753	2.064-11
33	1065	8.571-04	1.475-05	6315	2.73	2.229+13	1.889+11	2.348+01	.9173	5.213-11
34	980	1.459-03	2.047-05	6190	2.14	4.005+13	2.104+11	3.997+01	.9463	9.366-11
35	905	2.392-03	2.841-05	6020	1.70	6.895+13	2.138+11	6.553+01	.9645	1.612-10
36	855	3.369-03	3.584-05	5890	1.53	9.996+13	2.091+11	9.231+01	.9704	2.338-10
37	750	7.174-03	5.922-05	5540	1.23	2.287+14	1.743+11	1.966+02	.9794	5.348-10
38	700	1.052-02	7.477-05	5280	1.09	3.533+14	1.411+11	2.883+02	.9830	8.262-10
39	650	1.579-02	9.516-05	4975	.96	5.645+14	1.236+11	4.326+02	.9859	1.320-09
40	600	2.434-02	1.302-04	4690	.83	9.258+14	1.429+11	6.669+02	.9888	2.165-09
41	550	3.843-02	2.152-04	4500	.70	1.528+15	2.076+11	1.053+03	.9917	3.573-09
42	500	6.148-02	4.358-04	4440	.60	2.483+15	3.179+11	1.685+03	.9938	5.806-09
43	450	9.875-02	9.882-04	4440	.53	3.993+15	4.910+11	2.706+03	.9952	9.337-09
44	350	2.521-01	5.286-03	4570	.52	9.907+15	1.160+12	6.907+03	.9955	2.317-08
45	250	6.192-01	2.590-02	4810	.63	2.308+16	2.716+12	1.697+04	.9937	5.397-08
46	150	1.434+00	1.109-01	5185	1.00	4.917+16	6.518+12	3.930+04	.9854	1.150-07
47	100	2.121+00	2.199-01	5450	1.20	6.880+16	1.065+13	5.810+04	.9801	1.609-07
48	50	3.060+00	4.406-01	5840	1.40	9.215+16	2.126+13	8.385+04	.9748	2.155-07
49	0	4.285+00	9.991-01	6420	1.60	1.168+17	6.445+13	1.174+05	.9702	2.731-07
50	-25	4.998+00	1.690+00	6910	1.70	1.263+17	1.550+14	1.369+05	.9688	2.953-07
51	-50	5.755+00	3.353+00	7610	1.76	1.319+17	4.653+14	1.577+05	.9697	3.084-07
52	-75	6.542+00	7.479+00	8320	1.80	1.367+17	1.207+15	1.792+05	.9711	3.196-07

TABLE 16  
PHOTOIONIZATION DATA FOR H-He II

	<i>g</i>	$\lambda$	<i>a</i>	<i>s</i>		<i>g</i>	$\lambda$	<i>a</i>	<i>s</i>
<b>H</b>					<b>Mg</b>				
<i>n</i> =1	2	91.18	7.91	3 <sup>a</sup>	3s <sup>2</sup> 1S	1	162.2	2.85	10
<i>n</i> =2	8	364.7	13.85	3	3p <sup>3</sup> P°	9	251.4	40	7
<i>n</i> =3	18	820.6	21.58	3	3p <sup>1</sup> P°	3	375.7	131	2.1
<i>n</i> =4	32	1459	29.09	3	4s <sup>3</sup> S	3	488.5	2.2	2.3
<i>n</i> =5	50	2279	36.33	3	4s <sup>1</sup> S	1	505.5	0.5	9.1
<i>n</i> =6	72	3282	44.43	3	3d <sup>1</sup> D	5	655.0	40.1	1.7
<i>n</i> =7	98	4468	54.7	3	4p <sup>3</sup> P°	9	723.5	26.3	3
<i>n</i> =8	128	5835	63.2	3	3d <sup>3</sup> D	15	729.2	34.2	2
<b>C</b>					<b>Al</b>				
2p <sup>2</sup> 3P	9	110.0	12.19 <sup>b</sup>	2	3p <sup>2</sup> P°	6	207.6	65	4.4
2p <sup>2</sup> 1D	5	123.9	10.3 <sup>b</sup>	1.5	4s <sup>2</sup> S	2	436.0	10	2
2p <sup>2</sup> 1S	1	144.4	9.59 <sup>b</sup>	1.5	3p <sup>2</sup> 4P	12	520.5 <sup>d</sup>	10	2
2p <sup>3</sup> 5S°	5	174.5 <sup>d</sup>	1	3	3d <sup>2</sup> D	10	631.1	47	1.8
3s <sup>3</sup> P°	9	325.7	0.2	1.2	4p <sup>2</sup> P°	6	652.5	14.5	1
3s <sup>1</sup> P°	3	343.7	1.54	1.2	5s <sup>2</sup> S	2	944.2	56.7	1.9
3p <sup>3</sup> 3P°	15	370.5 <sup>d</sup>	16	3	4d <sup>2</sup> D	10	1070	50	3
3p <sup>3</sup> S, 3P, 3D	27	631.6	2.1	1.5	5p <sup>2</sup> P°	6	1250	50	3
<b>Si</b>					<b>He</b>				
3p <sup>2</sup> 3P	9	152.5	37	5	1s <sup>2</sup> 1S	1	50.40	7.39	1.7
3p <sup>2</sup> 1D	5	168.2	35	3	2s <sup>3</sup> S	3	260.1	1	1
3p <sup>2</sup> 1S	1	198.6	46	0.5	2s <sup>1</sup> S	1	312.2	11.6	1.9
3p <sup>3</sup> 5S°	5	308.5 <sup>d</sup>	15	3	2p <sup>3</sup> P°	9	342.2	14.6	2.9
4s <sup>3</sup> P°	9	386.4	1.25	2	2p <sup>1</sup> P°	3	368.0	10.5	3.5
4s <sup>1</sup> P°	3	404.0	4.09	2	3p <sup>1</sup> P°	3	826.7	27.1	3
3d <sup>3</sup> D°	15	489.2	18	3	4p <sup>1</sup> P°	3	1468	30	3
4p <sup>3</sup> S, 3P, 3D	27	584.0	14.1	3	5p <sup>1</sup> P°	3	2293	40	3
<b>Fe</b>					<b>He II</b>				
<i>a</i> 5D	25 <sup>c</sup>	157.5 <sup>c</sup>	6.3 <sup>c</sup>	3	<i>n</i> =1	2	22.78	1.98	3
<i>a</i> 5F	35	176.8	5	3	<i>n</i> =2	8	91.13	3.94	3
<i>a</i> 3F	21	194.2	3	3	<i>n</i> =3	18	205.0	5.93	3
<i>a</i> 5P	15	217.7	3	3	<i>n</i> =4	32	364.5	7.91	3
<i>a</i> 3P	9	221.7	0.44	3	<i>n</i> =5	50	569.5	9.88	3
<i>z</i> 7D°	35	226.6	1.7	3	<i>n</i> =6	72	820.2	11.85	3
<i>a</i> 3H	33	226.8	1.61	3	<i>n</i> =7	98	1116	13.83	3
<i>b</i> 3F	21	233.4	1.02	3	<i>n</i> =8	128	1458	15.81	3

<sup>a</sup> For hydrogen we use the Gaunt factors of Karsas and Latter (1961).

<sup>b</sup> See Table 5 and equation (8) of Paper II.

<sup>c</sup> See Table 4 in § II.

<sup>d</sup> These wavelengths and photoionization cross sections are simplified approximations. The onset of photoionization occurs at 99.9, 143.3, 132.6, and 178.9 nm for C levels 4 and 7, Si level 4, and Al level 3, respectively, because the upper state is an excited level of the next stage of ionization.

$10^{-17}$  cm<sup>2</sup>. The remaining columns list *J* for the depth indices 18 to 52, as in Table 25.

These values of *J* were determined with line opacity contributions adjusted to give calculated central intensities in agreement with observed broad-band central intensities, as described in the previous section.

#### VII. COMPARISON WITH OTHER MODELS

Figure 37 shows the temperature as a function of height in the temperature-minimum region for models A-F, the HSRA (Harvard-Smithsonian Reference Atmosphere) model of Gingerich *et al.* (1971), and the

models of Ayres and Linsky (1976) and Basri *et al.* (1979). The difference between model C and the HSRA model in this region is due mainly to improvements since 1971 in the quality of available observations and improvements of computational procedure. Both models attempt to account for similar observations and are determined in the same basic way.

As explained in § IV we used the observed intensity and flux in the UV continuum between 135 and 168 nm to determine models A-F in the temperature-minimum region, but the intensity-minimum features in the Ca II and Mg II resonance line cores computed from these

TABLE 17  
HYDROGEN NUMBER DENSITIES AND DEPARTURE COEFFICIENTS

$n_{\text{ion}}$	$n_1$	$n_2$	$n_3$	$n_4$	$n_5$	$n_6$	$n_7$	$n_8$	$b_1$	$b_2$	$b_3$	$b_4$	$b_5$	$b_6$	$b_7$	$b_8$	
1	1.003+09	2.384+03	7.984-04	2.092-04	2.311-04	2.947-04	3.682-04	4.471-04	5.292-04	1.00+09	1.09+02	1.33+01	8.44+00	6.94+00	6.05+00	5.42+00	4.91+00
2	3.199+09	5.340+04	1.879-02	7.056-03	8.175-03	1.043-02	1.308-02	1.604-02	1.928-02	1.81+08	3.69+01	7.12+00	4.96+00	4.15+00	3.66+00	3.33+00	3.08+00
3	0.031+09	2.031+05	7.574-02	2.440-02	3.155-02	4.010-02	6.199-02	6.507-02	8.76+07	2.60-01	5.74+00	3.78+00	3.03+00	2.04+00	2.61+00	2.04+00	2.44+00
4	9.017+09	2.739+06	6.771-01	1.723-01	2.143-01	2.674-01	3.309-01	4.041-01	3.49+07	2.30-01	4.03+00	2.63+00	2.03+00	1.89+00	1.89+00	1.80+00	1.80+00
5	1.197+10	1.385+07	3.258+00	4.758+01	5.244+01	6.468+01	7.074+01	9.760+01	3.05+01	2.25+00	1.91+00	1.73+00	1.73+00	1.62+00	1.62+00	1.55+00	1.55+00
6	1.371+10	3.627+07	9.224+00	8.639+01	7.218+01	8.533+01	1.038+00	1.269+00	1.552+00	1.75+07	4.51+01	3.72+00	2.22+00	1.87+00	1.68+00	1.57+00	1.51+00
7	1.554+10	9.794+07	3.281+01	1.691+00	1.253+00	1.220+00	1.686+00	2.033+00	2.477+00	1.51+07	8.68+01	4.55+00	2.38+00	1.95+00	1.72+00	1.60+00	1.54+00
8	1.694+10	2.034+08	9.712+01	3.997+00	1.982+00	2.146+00	2.478+00	3.941+00	3.565+00	1.33+07	1.65+02	5.34+00	2.68+00	2.13+00	1.84+00	1.69+00	1.62+00
9	1.766+10	2.779+08	2.203+02	4.359+02	2.647+00	2.647+00	3.166+00	3.648+00	4.404+00	1.23+07	3.05+02	6.38+00	3.07+00	2.36+00	1.82+00	1.73+00	1.73+00
10	1.828+10	3.015+08	4.711+02	6.171+00	3.438+00	3.438+00	3.558+00	3.812+00	4.397+00	1.13+07	5.88+02	8.47+00	3.64+00	2.24+00	2.01+00	1.91+00	1.91+00
11	1.896+10	3.210+08	7.068+02	7.800+00	4.130+00	4.084+00	4.451+00	5.098+00	6.114+00	1.05+07	8.02+02	9.01+00	4.02+00	2.94+00	2.41+00	2.14+00	2.03+00
12	2.008+10	3.839+08	1.051+03	1.027+01	5.192+00	5.058+00	5.470+00	6.235+00	7.472+00	9.48+07	9.99+02	1.10+01	4.34+00	3.13+00	2.55+00	2.27+00	2.15+00
13	2.112+10	4.557+08	1.365+03	1.242+01	6.072+00	5.869+00	6.341+00	7.232+00	8.673+00	8.74+06	1.09+03	1.15+01	4.42+00	3.18+00	2.59+00	2.31+00	2.19+00
14	2.170+10	5.567+08	2.282+03	2.663+03	2.070+01	6.753+00	6.513+00	8.24+00	9.625+00	8.24+06	1.15+02	1.27+01	4.47+00	3.22+00	2.34+00	2.22+00	2.22+00
15	2.305+10	9.282+08	2.663+03	2.070+01	9.526+00	9.055+00	9.691+00	1.098+01	1.315+01	6.69+06	1.34+03	1.32+01	4.92+00	3.53+00	2.87+00	2.55+00	2.42+00
16	2.519+10	2.078+09	5.841+03	3.969+01	1.722+01	1.598+01	1.683+01	1.885+01	2.451+00	6.114+00	7.66+06	5.02+02	4.79+00	4.14+00	2.41+00	2.14+00	2.03+00
17	3.201+10	8.827+09	2.216+04	1.216+04	5.192+00	5.058+00	5.470+00	6.235+00	7.472+00	7.31+04	6.92+02	1.10+01	4.34+00	3.13+00	2.66+00	2.47+00	2.39+00
18	3.422+10	1.235+10	2.881+04	1.409+02	5.424+01	5.005+01	5.391+01	6.096+01	7.244+01	1.06+04	3.94+02	6.50+01	2.40+00	2.15+00	2.03+00	1.98+00	1.98+00
19	3.598+10	1.630+10	3.475+04	1.649+02	6.272+01	5.783+01	6.230+01	7.021+01	8.312+01	1.65+03	2.26+02	4.80+00	2.30+00	1.95+00	1.79+00	1.71+00	1.68+00
20	3.688+10	2.426+10	3.812+04	1.786+02	6.624+01	6.128+01	6.630+01	7.049+01	8.776+01	2.43+02	1.17+02	3.98+00	1.70+00	1.51+00	1.43+00	1.38+00	1.37+00
21	3.665+10	2.863+10	3.722+04	1.718+02	6.295+01	5.853+01	6.361+01	7.156+01	8.424+01	1.52+02	9.54+01	8.85+00	1.50+00	1.36+00	1.30+00	1.27+00	1.25+00
22	3.279+10	3.013+10	3.655+04	1.748+02	6.333+01	5.886+01	6.453+01	7.196+01	8.458+01	9.33+01	7.80+01	8.01+00	1.39+00	1.27+00	1.23+00	1.20+00	1.19+00
23	3.674+10	4.013+10	1.825+04	1.825+01	6.455+01	5.986+01	6.513+01	7.307+01	8.573+01	5.21+01	6.08+01	2.35+00	1.27+00	1.15+00	1.13+00	1.13+00	1.13+00
24	3.691+10	5.664+10	3.712+04	1.939+02	6.643+01	6.144+01	6.684+01	7.483+01	8.759+01	2.80+01	4.66+01	2.12+00	1.16+00	1.10+00	1.07+00	1.06+00	1.06+00
25	3.735+10	6.577+10	3.891+04	2.096+02	6.989+01	6.450+01	7.011+01	7.834+01	9.153+01	1.76+01	3.94+01	2.01+00	1.10+00	1.05+00	1.04+00	1.03+00	1.03+00
26	3.922+10	9.843+10	4.390+04	2.635+02	8.277+01	7.520+01	8.126+01	9.036+01	1.053+02	1.14+01	3.24+01	2.03+00	1.08+00	1.03+00	1.02+00	1.02+00	1.02+00
27	4.524+10	2.151+11	5.914+04	1.748+02	6.333+01	5.986+01	6.513+01	7.307+01	8.573+01	5.96+00	2.31+01	1.89+00	9.62+01	9.20+01	9.18+01	9.19+01	9.19+01
28	5.783+10	5.820+11	9.283+04	7.945+02	2.032+02	1.740+02	1.844+02	2.027+02	2.350+02	5.21+00	6.08+01	2.35+00	1.27+00	1.18+00	1.13+00	1.13+00	1.13+00
29	6.589+10	9.812+11	1.200+05	1.209+03	2.977+02	2.297+02	2.591+02	2.608+02	2.959+02	4.74+00	1.78+01	2.04+00	9.68+01	9.07+01	9.01+01	9.02+01	9.01+01
30	7.564+10	2.197+12	1.516+05	1.782+03	4.235+02	3.430+02	3.548+02	3.856+02	4.453+02	5.41+00	1.44+01	2.48+00	1.12+00	1.12+00	1.01+00	9.85+01	9.77+01
31	7.215+10	4.129+12	1.441+05	1.725+03	4.018+02	3.191+02	3.279+02	3.553+02	4.098+02	8.62+00	1.38+01	2.48+00	1.11+00	9.88+01	9.81+01	9.55+01	9.52+01
32	7.848+10	7.787+12	1.628+05	2.227+03	5.196+02	4.050+02	4.121+02	4.444+02	5.117+02	1.00+01	1.19+01	2.56+00	1.17+00	1.02+00	9.90+01	9.81+01	9.78+01
33	8.877+10	1.021+13	3.14+03	3.14+03	7.31+02	7.31+02	7.31+02	7.31+02	7.31+02	1.02+01	1.02+01	1.02+01	1.02+01	1.03+00	9.94+01	9.85+01	9.82+01
34	9.680+10	3.137+13	2.481+05	3.989+03	9.512+02	7.148+02	7.146+02	7.632+02	8.750+02	9.10+00	8.52+00	2.46+00	1.20+00	1.03+00	9.95+01	9.83+01	9.83+01
35	9.376+10	5.337+13	2.422+05	4.101+03	9.947+02	7.382+02	7.319+02	7.770+02	8.876+02	7.17+00	6.69+00	2.27+00	1.17+00	1.01+00	9.77+01	9.68+01	9.66+01
36	9.148+10	8.126+13	2.399+05	4.179+03	1.027+03	7.570+02	7.466+02	7.895+02	9.000+02	6.21+00	5.73+00	2.14+00	1.15+00	1.00+00	9.65+01	9.56+01	9.55+01
37	5.870+10	1.063+14	1.332+05	2.14+03	6.065+02	4.224+02	4.303+02	4.495+02	5.083+02	3.40+00	3.30+00	1.58+00	1.02+00	9.14+01	8.89+01	8.86+01	8.85+01
38	3.261+10	2.935+14	6.664+04	1.224+03	3.091+02	2.091+02	2.239+02	2.165+02	2.523+02	2.34+00	2.19+00	1.39+00	9.13+01	8.40+00	8.27+01	8.28+01	8.29+01
39	1.359+10	4.794+14	3.102+05	5.696+02	1.444+02	1.047+02	1.008+02	1.235+02	1.515+02	1.08+00	1.29+00	1.08+00	1.08+00	1.03+00	9.85+01	9.83+01	9.83+01
40	3.343+09	8.120+14	1.122+04	2.072+02	5.277+01	3.829+01	3.665+01	3.15+01	4.110+01	4.71+01	6.93+01	8.10+01	6.58+01	6.66+01	6.84+01	6.96+01	7.00+01
41	1.018+10	1.302+15	5.762+03	1.061+02	2.711+01	1.968+01	1.870+01	1.873+01	2.057+01	3.18+01	4.69+01	6.83+01	6.02+01	6.32+01	6.57+01	6.70+01	6.74+01
42	6.737+09	2.097+15	5.791+03	1.064+02	2.731+01	1.882+01	1.873+01	1.864+01	2.041+01	2.89+01	4.23+01	6.63+01	6.02+01	6.39+01	6.65+01	6.77+01	6.81+01
43	8.584+08	3.989+15	1.406+04	2.582+02	6.685+01	4.842+01	4.557+01	4.530+01	4.963+01	3.80+01	5.08+01	7.4+01	6.7+01	7.03+01	7.25+01	7.34+01	7.37+01
44	3.456+09	9.980+15	1.344+05	2.102+02	6.616+02	4.856+02	4.558+02	4.576+02	4.766+02	8.16+01	8.92+01	9.94+01	8.30+01	8.38+01	8.89+01	8.54+01	8.55+01
45	2.398+10	2.315+16	1.664+06	3.371+04	9.900+03	7.425+03	7.167+03	7.323+03	8.166+03	1.29+00	1.31+00	1.16+00	9.53+01	9.45+01	9.45+01	9.45+01	9.45+01
46	3.407+11	4.917+16	2.355+05	2.727+05	7.061+02	2.14+02	1.82+02	1.82+02	2.513+05	2.523+05	2.516+05	2.516+05	2.516+05	2.516+05	2.516+05	2.516+05	2.516+05
47	1.611+12	6.866+16	1.038+08	4.166+07	1.774+06	1.466+06	1.483+06	1.568+06	1.782+06	1.03+00	1.03+00	1.03+00	1.03+00	1.03+00	1.03+00	1.03+00	1.03+00
48	8.366+12	9.203+16	5.816+08	3.068+07	1.264+07	1.309+07	1.309+07	1.309+07	1.614+07	1.40+00	1.00+00	1.00+00	1.0				

TABLE 18  
CARBON NUMBER DENSITIES AND DEPARTURE COEFFICIENTS

$n_{\text{ion}}$	$n_1$	$n_2$	$n_3$	$n_4$	$n_5$	$n_6$	$n_7$	$n_8$	$b_1$	$b_2$	$b_3$	$b_4$	$b_5$	$b_6$	$b_7$	$b_8$	
18	1.528+07	7.593+05	1.094+05	4.349+03	1.343+03	1.010-03	3.613-03	1.405-03	7.540-04	3.06+04	3.07+04	2.78+04	8.50+03	1.24+01	1.61+00	1.66+01	1.14+01
19	1.715+07	1.243+06	1.075+05	4.733+03	1.277+03	1.190-03	4.121-03	1.949-03	4.469-04	6.06+03	6.07+03	5.33+03	1.85+03	5.11+02	9.41+02	3.12+02	1.12+02
20	1.941+07	2.089+06	2.042+05	5.196+03	1.237+03	1.016+03	4.954-03	3.265-03	3.773-04	1.30+03	1.30+03	1.17+03	4.37+02	3.73+02	3.60+01	6.83+01	2.18+02
21	2.040+07	2.530+06	2.333+05	5.556+03	1.249+03	1.161-03	4.161-03	3.959-04	8.50+02	8.51+02	7.64+02	2.92+02	3.53+02	3.06+01	6.77+02	1.08+02	1.08+02
22	2.138+07	3.005+06	2.633+05	5.922+03	1.294+03	5.214-03	4.191-04	4.015-03	5.214-04	5.86+02	5.87+02	5.27+02	3.40+02	2.05+02	6.79+02	9.52+02	1.08+02
23	2.309+07	3.808+06	3.141+05	6.613+03	1.373+03	4.286+03	7.002+03	7.483+03	4.833+04	3.13+02	3.83+02	3.45+02	1.38+02	3.49+02	2.30+01	7.08+02	8.81+03
24	2.622+07	5.489+06	4.156+05	7.986+03	1.275+03	3.275+03	9.009+03	1.322+02	6.701+04	2.11+02	1.11+02	1.90+02	7.94+01	3.76+02	1.90+01	8.58+02	8.19+03
25	2.880+07	6.886+06	5.014+05	9.262+03	1.750+03	1.038+02	1.919+02	8.647+04	1.63+02	1.63+02	1.48+02	6.29+01	4.07+02	1.79+01	9.67+02	8.16+03	
26	3.637+07	9.170+07	7.846+05	1.343+04	2.425+03	2.150+02	4.611+02	1.713+02	4.611+03	9.57+01	9.57+01	8.82+01	3.90+01	5.41+02	1.60+01	1.34+01	9.79+03
27	6.006+07	3.047+07	1.851+06	2.923+04	4.990+03	1.159+01	4.582+02	2.312+01	6.361+03	5.15+01	5.15+01	4.89+01	2.30+01	9.66+01	1.62+01	2.59+01	1.55+01
28	1.211+08	1.003+08	5.03+06	8.672+04	1.433+04	1.433+04	7.697+01	1.745+01	1.579+00	3.533+02	3.64+01	3.64+01	1.77+01	2.03+01	1.97+01	5.4+01	2.91+01
29	1.747+08	1.864+08	1.034+07	1.546+05	2.570+04	2.896+00	3.417+01	3.885+00	8.002+02	3.23+01	3.23+01	3.23+01	1.64+01	2.77+01	2.15+01	7.90+01	3.75+02
30	3.281+08	4.540+08	2.436+07	3.529+05	5.720+04	6.306+00	8.818+01	1.287+01	2.384+01	2.82+01	2.82+01	2.82+01	1.46+01	4.02+01	2.43+01	1.15+00	5.03+02
31	5.453+08	8.981+08	7.712+07	6.659+05	1.068+05	1.437+01	1.857+00	9.918+01	4.986+01	2.52+01	2.52+01	2.53+01	1.33+01	4.74+01	2.66+01	5.36+00	5.56+02
32	9.083+08	1.791+09	9.148+07	1.254+06	1.999+05	3.062+01	1.998+05	7.182+01	9.162+01	2.17+01	2.17+01	2.17+01	1.17+01	5.11+01	1.47+00	5.77+02	
33	1.562+09	4.298+09	2.102+08	2.744+06	4.358+05	1.13+01	1.398+02	2.106+00	1.73+01	1.73+01	1.73+01	1.73+01	9.82+00	5.14+01	3.55+00	5.47+00	
34	2.123+09	8.641+09	4.031+08	4.991+06	7.752+05	1.328+02	2.477+01	2.409+02	3.621+00	1.46+01	1.46+01	1.46+01	8.60+00	5.30+01	4.37+01	1.42+00	5.49+02
35	2.530+09	1.644+10	7.128+08	8.130+06	1.162+06	2.171+02	4.777+01	3.500+02	5.639+00	1.16+01	1.16+01	1.16+01	6.84+00	5.56+01	5.48+01	1.36+00	5.90+02
36	2.543+09	5.258+10	1.045+09	1.129+07	6.537+06	2.976+02	7.326+01	4.211+02	7.628+00	1.12+01	1.12+01	1.12+01	6.64+00	6.34+01	7.04+01	1.38+00	6.94+02
37	2.619+09	6.139+10	2.116+09	1.863+07	2.037+06	5.112+02	2.176+06	6.740+02	1.965+01	5.65+00	5.65+00	5.65+00	3.34+00	6.45+00	6.45+00	8.56+00	
38	2.528+09	9.856+10	2.959+09	2.219+07	4.057+06	2.364+02	8.739+02	1.695+01	2.89+00	2.87+00	1.79+00	1.79+00	6.33+00	5.14+01	3.55+00	5.47+02	
39	1.843+09	1.591+11	4.131+09	2.410+07	2.320+06	9.385+02	2.294+02	6.187+02	2.253+01	9.37+01	9.37+01	9.37+01	7.48+01	5.49+01	6.77+01	7.07+01	9.99+02
40	1.003+09	2.568+11	5.155+09	2.472+07	2.471+06	1.160+03	2.582+02	6.349+02	2.995+01	3.03+01	3.03+01	3.03+01	3.11+01	4.76+01	5.37+01	5.25+01	1.07+01
41	4.005+08	3.058+11	5.496+09	2.339+07	1.537+06	2.295+06	1.721+02	5.332+02	3.235+01	1.77+01	1.77+01	1.78+01	2.15+01	5.42+01	6.14+01	4.89+01	1.40+01
42	1.921+08	3.517+11	5.785+09	2.237+07	2.164+06	2.735+02	3.436+02	3.441+01	1.49+01	1.49+01	1.49+01	1.49+01	1.88+01	6.44+01	6.84+01	4.44+00	8.56+02
43	2.147+08	5.872+11	8.138+10	4.065+08	3.718+07	2.117+06	4.057+02	1.872+01	1.872+01	1.82+01	1.82+01	1.82+01	2.06+01	7.41+01	4.99+01	1.92+01	
44	8.673+08	1.992+12	4.149+12	2.065+08	2.144+07	1.489+04	3.021+03	5.978+03	5.765+02	3.58+01	3.58+01	3.58+01	3.67+01	7.61+01	7.99+01	6.24+01	2.54+01
45	5.077+09	6.220+12	1.603+11	1.017+09	1.338+08	1.065+05	2.215+04	5.116+04	8.265+03	6.29+01	6.29+01	6.29+01	6.31+01	8.51+01	8.62+01	7.52+01	4.49+01
46	3.821+10	1.556+13	5.083+11	4.211+09	7.326+08	8.721+05	1.919+05	4.988+05	1.465+05	8.06+01	8.06+01	8.07+01	8.77+01	9.05+01	8.45+01	7.94+01	
47	1.284+11	2.265+13	8.002+11	8.440+09	1.753+09	2.371+06	2.961+06	6.607+05	1.822+06	6.304+05	6.304+05	6.304+05	6.304+05	8.95+01	8.95+01	8.95+01	9.05+01
48	4.197+11	3.085+13	1.383+12	1.656+10	4.257+09	1.117+07	2.529+06	8.593+02	6.971+01	9.42+01	9.42+01	9.42+01	9.43+01	9.61+01	9.69+01	9.54+01	
49	1.433+12	3.784+13	2.149+12	3.304+10	1.107+10	5.180+07	1.209+07	3.756+07	1.655+07	9.85+01	9.85+01	9.85+01	9.85+01	9.91+01	9.94+01	9.94+01	9.90+01
50	2.904+12	3.898+13	2.627+12	4.803+10	1.965+10	1.426+08	3.412+07	1.100+08	5.377+07	1.00+00	1.00+00	1.00+00	1.00+00	9.99+01	1.00+00	1.00+00	1.00+00
51	5.896+12	3.771+13	3.045+12	6.974+10	3.542+10	4.129+08	1.016+08	3.407+08	1.863+08	1.00+00	1.00+00	1.00+00	1.00+00	1.00+00	1.00+00	1.00+00	1.00+00
52	1.037+13	3.464+13	3.298+12	9.087+10	5.610+10	1.005+09	2.537+08	8.806+08	5.332+08	1.00+00	1.00+00	1.00+00	1.00+00	1.00+00	1.00+00	1.00+00	1.00+00

TABLE 19  
SILICON NUMBER DENSITIES AND DEPARTURE COEFFICIENTS

$n_{ion}$	$n_1$	$n_2$	$n_3$	$n_4$	$n_5$	$n_6$	$n_7$	$n_8$	$b_1$	$b_2$	$b_3$	$b_4$	$b_5$	$b_6$	$b_7$	$b_8$	
18	1.645+06	7.230+03	1.736+03	1.523+01	6.910-01	2.050-03	2.723-03	5.714-04	1.824-04	6.37+04	6.43+04	9.58+03	9.76+02	3.85+00	1.78+01	1.34+00	3.98-01
19	1.771+06	9.219+03	2.044+03	1.679+01	7.373-01	3.128-03	6.669-04	2.177-04	2.91+04	2.92+04	4.56+03	5.60+02	2.76+00	1.21+01	9.75+01	3.09+01	2.06+01
20	2.124+06	1.595+04	3.045+03	2.207+01	9.223+01	4.095-03	4.435-03	9.957-04	3.294-04	7.19+03	7.19+03	1.21+03	2.14+02	1.59+00	6.27+00	5.86+01	2.06+01
21	2.392+06	1.957+04	3.585+03	2.510+01	1.043+00	4.250-03	5.140-03	1.187-03	3.881-04	5.06+03	5.06+03	8.77+02	1.72+02	1.42+00	5.35+01	1.90+01	
22	2.423+06	2.249+04	3.999+03	2.735+01	1.141+00	5.644-03	5.681-03	1.345-03	4.357-04	3.93+03	3.92+03	6.92+02	1.47+02	1.31+00	4.87+00	5.03+01	1.80+01
23	2.693+06	2.887+04	4.895+03	3.232+01	1.352+00	7.151-03	6.830-03	1.683-03	5.368-04	2.61+03	2.60+03	4.75+02	1.16+02	1.16+00	4.11+01	4.57+01	1.66+01
24	3.164+06	6.058+04	6.551+03	4.231+00	1.745+00	9.231+00	8.901-02	1.466-04	2.77+03	1.77+03	3.37+02	3.37+02	9.33+01	1.04+01	3.53+00	4.23+01	1.55+01
25	3.562+06	5.048+04	7.958+03	5.128+01	2.073+00	1.217+02	1.060+02	2.784+03	8.598+04	1.45+03	1.45+03	2.86+02	2.86+02	8.34+01	9.94+01	3.25+00	4.04+01
26	4.785+06	8.492+04	1.274+04	8.256+01	3.187+00	2.032+02	1.631+02	4.489+03	1.361+03	9.70+02	9.68+02	2.06+02	6.62+01	9.05+01	2.75+00	3.71+01	1.38+01
27	8.977+06	2.302+05	3.257+04	2.255+02	7.567+00	5.939+02	4.004+02	1.189+02	3.602+03	6.10+02	6.10+02	1.52+02	5.04+01	9.03+01	2.33+00	3.54+01	1.36+01
28	2.175+07	8.677+05	1.184+05	1.012+03	2.395+01	2.396+01	1.481+01	4.940+02	1.514+02	4.73+02	4.75+02	1.56+02	4.08+01	1.18+00	2.31+00	4.05+01	1.62+01
29	3.507+07	1.744+06	2.347+05	2.347+03	4.323+01	2.368+03	1.336+01	1.140+01	3.86+02	4.38+02	4.41+02	1.74+02	1.74+02	1.67+01	4.48+00	2.50+00	4.82+01
30	7.512+07	4.975+06	6.551+05	8.484+03	1.048+02	3.176+00	1.089+00	4.668+01	1.263+01	3.93+02	3.95+02	2.06+02	3.13+01	2.34+00	7.12+00	7.20+01	2.60+01
31	1.364+08	1.042+07	1.350+06	1.940+02	9.093+04	2.264+00	1.378+00	3.269+01	8.465+01	3.64+02	3.66+02	2.06+02	6.62+01	9.05+01	2.75+00	3.71+01	1.38+01
32	2.547+08	2.184+07	2.781+06	5.162+00	3.254+02	7.722+01	7.408+00	4.283+00	8.283+00	3.38+02	3.38+02	2.63+02	5.04+01	9.03+01	2.33+00	3.54+01	1.36+01
33	5.212+08	5.821+07	7.210+06	1.999+05	7.071+02	9.333+01	2.455+01	1.710+01	2.392+00	2.70+02	2.70+02	2.45+02	1.67+01	5.9+00	2.33+00	4.51+01	1.31+01
34	9.756+08	1.266+08	1.523+07	3.200+05	1.261+03	2.210+02	6.397+01	4.863+01	4.866+00	2.10+02	2.10+02	2.00+02	1.24+01	5.89+00	6.72+00	2.92+00	4.11+01
35	1.695+09	2.457+08	2.824+07	5.709+05	1.964+03	4.493+02	1.425+02	1.078+02	8.950+00	1.39+02	1.39+02	1.36+02	8.37+00	1.36+02	8.37+00	3.06+00	3.67+01
36	4.460+09	3.854+08	4.303+07	8.232+05	7.332+02	2.128+00	1.378+00	3.269+01	8.465+01	3.64+02	3.66+02	2.71+02	6.71+01	1.03+02	5.20+00	6.77+00	3.34+01
37	5.661+09	8.701+09	8.682+08	1.438+03	1.629+03	5.633+02	3.260+03	3.183+01	3.50+01	3.45+01	3.45+01	2.84+00	3.45+00	1.48+01	1.82+00	2.80+00	
38	8.967+09	1.333+09	1.223+08	1.725+06	5.709+03	2.346+03	7.763+02	4.431+02	4.713+01	1.48+01	1.48+01	1.48+01	1.58+00	2.32+00	4.75+00	5.05+00	1.60+00
39	1.429+10	2.527+09	2.066+08	2.419+06	9.529+03	4.029+03	1.239+03	7.519+02	8.601+01	4.63+00	4.64+00	4.32+00	7.98+01	1.37+00	1.78+00	8.05+01	1.64+01
40	2.227+10	6.130+09	4.376+08	4.527+06	2.140+04	8.877+03	2.650+03	1.662+03	2.144+02	1.17+00	1.17+00	1.17+00	3.80+01	7.37+01	9.54+01	4.87+01	1.21+01
41	3.289+10	1.520+10	9.895+08	9.060+06	5.328+04	2.771+03	7.332+02	2.305+02	1.704+02	1.431+01	1.06+02	1.06+02	6.71+01	2.39+01	4.55+01	4.92+01	6.27+01
42	4.462+10	1.806+10	1.770+09	1.578+07	1.076+05	4.185+04	1.205+04	7.794+03	1.643+03	3.01+01	3.01+01	3.01+01	3.10+01	2.06+01	4.46+01	5.44+01	1.37+01
43	7.141+10	6.151+10	3.974+09	3.226+07	1.076+05	1.183+03	2.316+04	7.565+03	2.86+00	2.85+01	2.85+01	2.89+01	2.34+01	4.41+01	5.31+01	3.22+01	2.22+01
44	1.865+11	1.564+11	1.140+10	1.215+08	1.690+06	5.234+05	1.319+05	1.260+05	6.594+04	4.49+01	4.49+01	4.49+01	5.74+01	6.25+01	4.79+01	4.78+01	
45	4.728+11	3.221+11	2.684+10	3.469+08	7.481+06	2.172+06	5.272+05	6.474+05	3.825+05	6.79+01	6.79+01	6.79+01	6.48+01	7.50+01	7.68+01	6.90+01	7.17+01
46	1.226+12	4.742+11	4.574+10	7.304+08	2.443+07	7.735+06	1.884+06	2.788+06	1.747+06	8.29+01	8.29+01	8.29+01	8.09+01	8.76+01	8.76+01	8.60+01	8.67+01
47	1.910+12	4.779+11	5.035+10	9.132+08	3.964+07	1.345+07	3.45+06	5.322+06	3.484+06	8.84+01	8.84+01	8.84+01	8.71+01	9.23+01	9.19+01	9.19+01	
48	2.790+12	4.275+11	5.026+10	1.068+09	6.367+07	2.361+07	5.928+06	1.034+07	7.206+06	9.46+01	9.46+01	9.46+01	9.38+01	9.68+01	9.74+01	9.67+01	
49	3.737+12	3.556+11	4.810+10	1.251+09	4.716+07	1.214+07	2.333+07	1.771+07	9.66+01	9.66+01	9.66+01	9.66+01	9.77+01	9.73+01	9.83+01	9.77+01	
50	4.129+12	3.040+11	4.545+10	1.366+09	1.628+08	7.548+07	1.983+07	4.059+07	3.284+07	9.88+01	9.88+01	9.88+01	9.88+01	9.88+01	9.90+01	9.95+01	
51	4.394+12	2.411+11	4.068+10	1.456+09	2.448+08	1.280+08	3.443+07	7.622+07	6.550+07	9.99+01	9.99+01	9.99+01	9.99+01	1.00+00	1.00+00	1.00+00	9.99+01
52	4.610+12	1.986+11	3.709+10	1.537+09	3.452+08	2.006+08	5.497+07	1.303+08	1.210+08	1.00+00	1.00+00	1.00+00	1.00+00	1.00+00	1.00+00	1.00+00	

TABLE 20  
IRON NUMBER DENSITIES AND DEPARTURE COEFFICIENTS

$n_{\text{ion}}$	$n_1$	$n_2$	$n_3$	$n_4$	$n_5$	$n_6$	$n_7$	$n_8$	$b_1$	$b_2$	$b_3$	$b_4$	$b_5$	$b_6$	$b_7$	$b_8$		
18	1.904+06	3.821+02	8.924+01	1.774+01	4.989+00	6.403+00	9.921+00	1.389+01	8.464+00	9.21+04	3.23+04	1.84+04	1.31+04	3.07+04	1.36+04	2.02+04	2.21+04	
19	2.045+06	5.764+02	1.327+02	2.557+01	6.834+00	8.559+00	1.107+01	1.348+01	1.868+01	6.60+04	4.42+04	1.39+04	1.03+04	1.53+04	1.03+04	1.66+04	1.66+04	
20	2.793+06	3.385+03	7.310+02	1.234+02	2.650+01	2.987+01	5.048+01	6.698+01	3.735+01	1.56+04	6.95+03	4.24+03	2.98+03	6.37+03	3.21+03	4.55+03	4.82+03	
21	3.415+06	1.032+04	2.142+03	4.159+02	1.159+01	2.159+01	6.562+01	1.497+02	7.976+01	6.28+03	3.15+03	1.99+03	1.39+03	2.83+03	1.52+03	2.10+03	2.20+03	
22	3.589+06	1.136+04	2.344+03	3.616+02	6.650+01	1.235+02	5.956+01	1.589+02	8.428+01	5.42+03	2.75+03	1.75+03	1.22+03	2.47+03	1.34+03	1.84+03	1.9+03	
23	3.961+06	1.369+04	2.98+03	4.257+02	7.592+01	7.816+01	1.400+02	1.789+02	9.410+01	4.10+03	2.14+03	1.37+03	9.57+02	1.91+03	1.03+03	1.44+03	1.50+03	
24	4.672+06	1.852+04	3.731+03	5.565+02	9.474+01	1.181+02	2.177+02	1.181+02	1.133+02	2.67+03	1.45+03	9.49+02	6.58+02	1.29+03	9.82+02	1.01+03	1.01+03	
25	5.291+06	2.305+04	4.600+03	6.168+02	6.780+02	1.100+02	2.023+02	1.100+02	1.100+02	1.99+03	1.11+03	1.11+03	7.39+02	5.11+02	9.89+02	5.66+02	7.84+02	
26	7.187+06	3.816+04	7.473+03	1.032+03	1.687+02	2.976+02	3.658+02	1.850+02	1.850+02	1.10+03	6.52+02	4.49+02	3.10+02	5.77+02	3.42+02	4.49+02	4.63+02	
27	9.109+07	9.109+04	1.761+04	2.607+03	3.926+02	7.349+02	7.804+02	3.884+02	3.884+02	6.19+02	3.84+02	2.84+02	2.00+02	3.43+02	2.12+02	2.71+02	2.78+02	
28	3.322+07	2.852+05	5.481+04	8.742+03	1.321+03	9.365+02	2.030+03	2.337+03	1.152+03	4.06+02	2.61+02	2.14+02	1.56+02	2.38+02	1.54+02	1.91+02	1.96+02	
29	5.403+07	5.146+05	9.774+04	1.633+04	2.460+03	1.752+03	3.633+03	4.121+03	2.023+03	3.45+02	2.24+02	1.93+02	1.44+02	2.08+02	1.37+02	1.67+02	1.7+02	
30	1.177+08	1.247+06	2.362+05	4.168+04	6.384+03	4.186+03	8.818+03	8.893+03	4.831+03	2.70+02	1.78+02	1.66+02	1.27+02	1.69+02	1.37+02	1.40+02	1.40+02	
31	2.158+08	2.401+06	4.559+05	8.234+04	1.295+04	1.687+04	1.606+04	1.890+04	1.890+04	2.22+02	1.49+02	1.45+02	1.15+02	1.43+02	1.21+02	1.17+02	1.20+02	
32	4.050+08	4.613+06	8.807+05	1.622+05	2.629+04	1.512+04	3.626+04	3.607+04	1.746+04	1.81+02	1.25+02	1.25+02	1.04+02	1.43+01	8.43+01	1.00+02	1.02+02	
33	8.817+08	1.081+07	2.127+06	3.866+05	6.642+04	3.385+04	7.720+04	8.405+04	1.039+04	1.25+02	1.25+02	1.25+02	1.28+01	8.44+01	8.97+01	6.44+01	7.64+01	
34	1.625+09	2.104+07	4.246+06	7.527+05	1.328+05	6.579+04	1.498+05	1.606+05	7.654+04	8.63+01	6.70+01	6.75+01	6.45+01	6.51+01	4.83+01	5.55+01	5.63+01	
35	2.865+09	3.715+07	7.581+06	1.294+06	2.264+05	1.080+05	2.507+05	2.667+05	1.256+05	5.21+01	4.30+01	4.33+01	4.27+01	4.17+01	3.18+01	3.62+01	3.66+01	
36	4.201+09	5.528+07	1.128+07	1.873+06	3.209+05	1.295+04	7.962+03	1.606+04	1.898+03	3.80+01	3.24+01	3.25+01	1.14+01	2.14+01	2.76+01	2.44+01	2.78+01	
37	9.630+09	1.239+08	2.405+07	3.651+06	5.712+05	3.665+05	6.665+05	3.033+05	3.926+05	5.93+00	5.68+00	5.68+00	5.72+00	5.52+00	4.65+00	5.14+00	5.16+00	
38	1.516+10	1.992+08	3.661+07	5.175+06	7.557+05	8.533+05	8.799+05	3.926+05	3.926+05	2.12+00	2.10+00	2.14+00	2.07+00	1.88+00	1.99+00	1.99+00	1.99+00	
39	2.466+10	4.241+08	7.113+07	9.163+06	1.222+06	1.492+06	1.426+06	1.447+06	1.426+06	6.208+05	6.12+01	6.70+01	6.75+01	6.45+01	6.51+01	4.83+01	5.55+01	5.63+01
40	4.110+10	1.303+09	1.914+08	2.213+07	2.632+06	1.175+06	3.287+06	3.077+06	1.303+06	6.65+01	6.69+01	6.68+01	4.33+01	4.27+01	4.17+01	3.18+01	3.62+01	
41	6.775+10	4.165+09	5.537+08	5.965+07	1.128+07	1.873+06	3.132+06	5.151+05	3.570+05	3.772+05	1.763+05	1.763+05	1.763+05	1.763+05	1.763+05	1.763+05	1.763+05	
42	9.961+10	9.081+09	1.171+09	1.231+08	1.301+07	1.405+07	1.631+07	5.847+06	5.847+06	3.29+01	1.19+01	1.19+01	1.19+01	1.19+01	1.19+01	1.05+01	1.05+01	
43	1.816+11	2.407+10	3.197+09	3.448+08	3.703+07	1.673+07	4.354+07	4.682+07	4.682+07	2.47+01	2.21+01	2.48+01	2.48+01	2.48+01	2.48+01	2.33+01	2.33+01	
44	4.405+11	7.055+10	1.063+10	1.256+09	1.492+08	1.853+07	1.949+08	1.815+08	7.719+07	4.28+01	2.29+01	4.29+01	4.29+01	4.29+01	4.29+01	4.29+01	4.29+01	
45	1.035+12	1.485+11	2.580+10	3.384+09	4.510+08	2.109+08	6.117+08	5.700+08	2.489+08	6.69+01	6.68+01	6.68+01	6.68+01	6.68+01	6.68+01	6.68+01	6.68+01	
46	2.331+12	1.978+11	4.036+10	5.953+09	9.032+08	4.305+08	8.127+09	1.191+09	5.355+08	8.06+01	8.05+01	8.05+01	8.05+01	8.05+01	8.05+01	8.05+01	8.05+01	
47	3.359+12	1.892+11	4.258+10	6.716+09	1.107+09	1.319+08	5.340+08	1.406+09	1.499+09	6.858+08	8.57+01	8.57+01	8.57+01	8.57+01	8.57+01	8.57+01	8.57+01	
48	4.607+12	1.659+11	4.213+10	7.289+09	1.319+09	1.452+08	1.452+08	1.974+09	1.844+09	8.621+08	9.22+01	9.22+01	9.22+01	9.22+01	9.22+01	9.22+01	9.22+01	
49	5.923+12	1.398+11	4.143+10	8.019+09	1.642+09	8.185+08	2.561+09	2.392+09	1.150+09	9.44+01	9.44+01	9.44+01	9.44+01	9.44+01	9.44+01	9.44+01	9.44+01	
50	6.433+12	1.237+11	4.093+10	8.584+09	1.921+09	9.700+08	3.081+09	2.881+09	1.413+09	9.80+01	9.80+01	9.80+01	9.80+01	9.80+01	9.80+01	9.80+01	9.80+01	
51	6.747+12	1.019+11	3.849+10	8.893+09	2.214+09	1.136+09	3.676+09	3.440+09	1.728+09	9.99+01	9.99+01	9.99+01	9.99+01	9.99+01	9.99+01	9.99+01	9.99+01	
52	7.011+12	8.630+10	3.646+10	9.138+09	2.490+09	1.294+09	4.255+09	3.984+09	2.042+09	1.00+00	1.00+00	1.00+00	1.00+00	1.00+00	1.00+00	1.00+00	1.00+00	

TABLE 21  
MAGNESIUM NUMBER DENSITIES AND DEPARTURE COEFFICIENTS

$\eta_{10n}$	$\eta_1$	$\eta_2$	$\eta_3$	$\eta_4$	$\eta_5$	$\eta_6$	$\eta_7$	$\eta_8$	$b_1$	$b_2$	$b_3$	$b_4$	$b_5$	$b_6$	$b_7$	$b_8$	
18	$1.636+06$	$1.577+02$	$5.040+01$	$7.593-04$	$1.038-02$	$5.321-05$	$1.290-04$	$2.321-03$	$7.321-03$	$7.47+03$	$5.03+03$	$1.33+00$	$4.17+01$	$8.75-01$	$6.26-01$	$7.50+00$	$1.46+01$
19	$1.721+06$	$1.928+02$	$5.511-01$	$9.185-04$	$1.126-02$	$5.550-05$	$1.414-04$	$2.514-03$	$7.922-03$	$5.77+03$	$3.93+03$	$1.24+00$	$3.60+01$	$7.35-01$	$5.62-01$	$6.80+00$	$1.30+01$
20	$2.127+06$	$4.398+02$	$7.971+01$	$2.011-03$	$1.577-02$	$6.668-05$	$2.070-04$	$3.502-03$	$1.098-02$	$2.01+03$	$1.43+03$	$9.24-01$	$1.97+01$	$3.64-01$	$3.62-01$	$4.31+00$	$8.25+00$
21	$2.418+06$	$7.092+02$	$9.895+01$	$3.169-01$	$1.921-02$	$7.502-05$	$2.595-04$	$4.250-03$	$1.329-02$	$1.10+03$	$8.03+02$	$7.81-01$	$1.39+01$	$2.45-01$	$2.82-01$	$3.31+00$	$6.34+00$
22	$2.559+06$	$8.225+02$	$1.063+02$	$3.664-03$	$2.054-02$	$8.114-05$	$2.830-04$	$4.525-03$	$1.418-02$	$9.34+02$	$6.84+02$	$7.51-01$	$1.22+01$	$2.27-01$	$2.67-01$	$3.07+00$	$5.90+00$
23	$2.861+06$	$1.087+03$	$1.223+02$	$4.817+03$	$2.338+02$	$9.463+05$	$3.347+04$	$5.110+03$	$1.607+02$	$6.92+02$	$5.10+02$	$7.00-01$	$1.06+01$	$2.41-01$	$2.68+00$	$5.16+00$	
24	$3.124+06$	$1.649+03$	$1.533+02$	$7.265+03$	$2.875+02$	$1.215+04$	$4.359+04$	$6.200+03$	$1.960+02$	$4.57+02$	$3.40+02$	$6.35+01$	$8.35+00$	$1.66+01$	$2.10+01$	$2.20+00$	$4.27+00$
25	$3.872+06$	$2.075+03$	$1.786+02$	$9.121+03$	$3.291+02$	$1.447+04$	$5.161+04$	$7.032+03$	$2.28+02$	$3.85+02$	$2.89+02$	$6.10+01$	$7.49+00$	$1.56+01$	$1.99+01$	$2.00+00$	$3.90+00$
26	$5.257+06$	$3.562+03$	$2.614+02$	$1.573+02$	$4.615+02$	$2.232+04$	$7.836+04$	$9.644+03$	$3.072+02$	$2.68+02$	$2.04+02$	$5.65+01$	$5.93+00$	$1.38+01$	$1.77+01$	$1.64+00$	$3.20+00$
27	$1.004+07$	$9.619+03$	$5.887+02$	$4.535+02$	$9.610+02$	$5.586+04$	$1.875+03$	$1.930+02$	$6.234+02$	$1.71+02$	$1.35+02$	$5.42+01$	$4.36+00$	$1.25+01$	$1.58+01$	$1.23+00$	$2.45+00$
28	$2.467+07$	$3.315+04$	$1.833+03$	$1.949+01$	$2.622+01$	$2.022+03$	$6.341+03$	$4.941+02$	$1.658+01$	$1.26+02$	$1.02+02$	$6.21+01$	$3.30+00$	$1.27+01$	$1.53+01$	$9.15+01$	
29	$4.026+07$	$6.246+04$	$3.330+03$	$4.553+01$	$4.399+01$	$1.243+02$	$7.981+01$	$2.784+01$	$1.11+02$	$9.26+01$	$7.27+01$	$7.01+01$	$1.28+00$	$1.37+01$	$1.58+01$	$7.81+01$	
30	$8.847+07$	$1.616+05$	$8.162+03$	$1.740+00$	$9.754+01$	$1.355+02$	$3.696+02$	$1.660+01$	$6.22+01$	$9.36+01$	$7.92+01$	$1.03+00$	$2.36+00$	$1.67+01$	$1.77+01$	$1.43+00$	
31	$1.628+08$	$3.268+05$	$2.614+02$	$1.573+02$	$4.615+02$	$2.232+04$	$7.836+04$	$9.644+03$	$3.072+02$	$2.68+02$	$2.04+02$	$5.65+01$	$5.93+00$	$1.38+01$	$1.77+01$	$1.64+00$	$3.20+00$
32	$3.060+08$	$6.601+05$	$3.079+04$	$1.561+01$	$3.361+00$	$9.411+02$	$2.246+01$	$2.450+00$	$6.88+01$	$5.97+01$	$1.97+01$	$1.79+00$	$2.58+01$	$2.42+01$	$2.42+01$	$1.27+00$	
33	$6.554+08$	$1.690+06$	$7.336+05$	$5.742+01$	$8.001+00$	$3.036+01$	$6.759+01$	$1.143+00$	$6.638+00$	$5.23+01$	$6.64+01$	$2.50+00$	$1.51+00$	$2.97+01$	$2.64+01$	$3.50+01$	
34	$1.224+09$	$3.583+06$	$1.429+05$	$1.721+01$	$1.685+01$	$2.442+00$	$1.551+01$	$2.442+00$	$3.172+00$	$3.95+01$	$3.56+01$	$2.74+00$	$1.37+01$	$2.65+01$	$3.05+01$	$1.30+00$	
35	$2.156+09$	$6.912+06$	$2.384+05$	$3.348+02$	$3.238+01$	$1.482+00$	$3.086+00$	$4.056+00$	$3.172+01$	$2.64+01$	$2.41+01$	$2.72+00$	$1.22+00$	$2.99+01$	$2.57+01$	$2.70+01$	
36	$3.162+09$	$7.071+07$	$3.475+02$	$8.874+02$	$2.943+01$	$1.219+00$	$8.07+01$	$9.92+01$	$1.42+00$	$2.06+00$	$2.07+01$	$5.65+01$	$5.93+00$	$1.39+01$	$1.77+01$	$1.35+00$	
37	$7.259+09$	$2.759+07$	$5.932+05$	$1.415+03$	$2.09+02$	$7.778+03$	$1.175+01$	$1.403+01$	$1.69+01$	$8.06+00$	$7.55+00$	$1.94+00$	$8.89+01$	$2.36+01$	$2.42+01$	$1.27+00$	
38	$1.140+10$	$4.768+07$	$7.790+05$	$2.334+03$	$1.828+02$	$8.896+00$	$1.817+01$	$2.080+01$	$1.718+02$	$4.11+00$	$3.91+00$	$1.45+00$	$6.89+01$	$1.94+01$	$1.82+01$	$1.75+01$	
39	$1.858+10$	$1.121+08$	$1.269+06$	$4.400+03$	$3.447+02$	$1.756+01$	$3.963+01$	$3.910+01$	$3.08+02$	$1.68+00$	$1.65+01$	$9.41+01$	$4.78+01$	$1.77+01$	$1.44+01$	$1.33+01$	
40	$3.129+10$	$3.724+08$	$2.736+06$	$1.164+04$	$8.918+02$	$4.843+01$	$9.738+01$	$1.035+02$	$7.536+02$	$5.91+01$	$6.00+01$	$5.56+01$	$3.15+01$	$1.08+01$	$1.12+01$	$1.06+01$	
41	$5.258+10$	$1.318+09$	$7.061+06$	$3.168+04$	$2.499+02$	$5.189+03$	$1.354+02$	$1.169+01$	$2.188+03$	$3.04+01$	$1.86+01$	$2.67+00$	$1.17+00$	$2.55+01$	$2.54+01$	$1.30+00$	
42	$7.259+09$	$2.759+07$	$5.932+05$	$1.415+03$	$2.09+02$	$7.778+03$	$1.175+01$	$1.403+01$	$1.69+01$	$8.06+00$	$7.55+00$	$1.94+00$	$8.89+01$	$2.36+01$	$2.42+01$	$1.27+00$	
43	$1.464+11$	$9.124+09$	$4.750+07$	$2.095+05$	$2.861+04$	$1.835+03$	$3.538+03$	$1.368+03$	$1.700+04$	$2.76+01$	$2.57+01$	$3.00+01$	$3.63+01$	$1.53+01$	$1.59+01$	$4.33+01$	
44	$3.608+11$	$2.815+10$	$2.195+08$	$1.062+06$	$1.513+05$	$1.874+04$	$3.534+04$	$5.508+04$	$9.873+04$	$4.84+01$	$4.85+01$	$4.89+01$	$5.05+01$	$3.95+01$	$3.05+01$	$5.82+01$	
45	$8.443+11$	$5.771+10$	$7.151+08$	$4.439+06$	$7.069+05$	$1.080+05$	$2.277+05$	$2.923+05$	$4.929+05$	$7.23+01$	$7.23+01$	$7.08+01$	$7.17+01$	$6.57+01$	$7.31+01$	$7.64+01$	
46	$1.841+12$	$7.509+10$	$1.547+09$	$1.318+07$	$2.467+06$	$4.122+05$	$9.312+05$	$1.177+06$	$1.918+06$	$8.42+01$	$8.43+01$	$8.33+01$	$8.60+01$	$8.18+01$	$8.27+01$	$8.74+01$	
47	$2.041+12$	$7.176+10$	$2.008+09$	$2.071+07$	$4.21+06$	$7.421+05$	$1.241+05$	$2.04+06$	$3.562+06$	$8.86+01$	$8.86+01$	$8.82+01$	$9.09+01$	$8.81+01$	$9.13+01$		
48	$3.523+12$	$6.380+11$	$2.611+09$	$3.395+07$	$7.590+06$	$1.415+06$	$3.487+06$	$4.439+06$	$7.180+06$	$9.47+01$	$9.47+01$	$9.46+01$	$9.61+01$	$9.55+01$	$9.61+01$	$4.33+01$	
49	$4.189+12$	$5.528+10$	$3.683+09$	$6.438+07$	$1.635+07$	$3.239+06$	$8.487+06$	$1.107+07$	$1.795+07$	$9.66+01$	$9.66+01$	$9.68+01$	$9.75+01$	$9.71+01$	$9.76+01$	$9.73+01$	
50	$4.864+12$	$4.977+10$	$4.695+09$	$1.012+08$	$2.816+07$	$5.806+06$	$1.588+07$	$2.116+07$	$3.444+07$	$9.94+01$	$9.94+01$	$9.95+01$	$9.96+01$	$9.96+01$	$9.95+01$	$9.95+01$	
51	$5.089+12$	$4.179+10$	$5.996+09$	$1.660+08$	$5.193+07$	$1.120+07$	$3.235+07$	$4.431+07$	$7.234+07$	$1.00+00$	$1.00+00$	$1.00+00$	$1.00+00$	$1.00+00$	$1.00+00$	$1.00+00$	
52	$5.279+12$	$3.633+10$	$7.421+09$	$2.541+08$	$8.777+07$	$1.964+07$	$5.946+07$	$8.337+07$	$1.364+08$	$1.00+00$	$1.00+00$	$1.00+00$	$1.00+00$	$1.00+00$	$1.00+00$	$1.00+00$	

TABLE 22  
ALUMINUM NUMBER DENSITIES AND DEPARTURE COEFFICIENTS

$n_{ion}$	$n_1$	$n_2$	$n_3$	$n_4$	$n_5$	$n_6$	$n_7$	$n_8$	$b_1$	$b_2$	$b_3$	$b_4$	$b_5$	$b_6$	$b_7$	$b_8$		
18	1.252+05	6.136+00	6.224-04	9.677-04	1.061-04	6.719-08	2.042-07	1.423-07	1.12+04	1.03+02	4.41+01	4.70+01	1.63+01	3.88-01	6.94-01	1.00+00		
19	1.283+05	6.389+00	6.450-04	9.985-04	5.639-04	1.098-04	6.970-08	2.939-07	1.467-07	9.87+03	9.63+01	4.13+01	4.45+01	1.54+01	3.88-01	6.94-01	1.00+00	
20	1.432+05	7.679+00	7.586-04	1.152-03	6.599-04	1.282-04	8.268-08	3.438-07	1.692-07	5.52+03	6.99+01	3.07+01	3.48+01	1.21+01	3.88-01	6.94-01	1.00+00	
21	1.547+05	8.718+00	8.482-04	1.273-03	7.353-04	1.426-04	9.331-08	3.844-07	1.874-07	3.72+03	5.63+01	2.51+01	2.94+01	1.03+01	3.88-01	6.94-01	1.00+00	
22	1.668+05	9.862+00	9.150-04	1.402-03	8.165-04	1.581-04	1.052-07	4.397-07	2.075-07	2.56+03	4.58+01	2.07+01	2.51+01	8.81+00	3.87-01	6.93-01	1.00+00	
23	1.928+05	1.248+01	1.160-03	1.691-03	9.965-04	1.923-04	1.335-07	5.363-07	2.544-07	1.28+03	3.11+01	1.45+01	1.86+01	6.57+00	3.87-01	6.93-01	1.00+00	
24	2.431+05	1.802+01	1.802-03	1.592-03	2.272-03	2.598-04	1.988-07	7.196-07	3.596-07	4.71+02	1.77+01	8.72+00	1.20+01	4.27+00	3.86-01	6.93-01	1.00+00	
25	2.738+05	2.104+01	1.794-03	2.623-03	1.522-03	2.901-04	2.689-07	1.051-06	4.720-07	4.10+02	1.61+01	8.14+00	1.11+01	3.92+00	4.41-01	7.32-01	1.00+00	
26	3.687+05	3.100+01	2.417-03	3.755-03	2.035-03	3.822-04	5.572-07	2.159-06	9.316-07	2.96+02	1.26+01	6.92+00	9.16+00	3.18+00	6.12-01	8.38-01	1.00+00	
27	6.999+05	7.142+01	4.591-03	8.132-03	3.804-03	6.922-04	2.355-06	8.990-06	4.029-06	1.65+02	7.83+00	5.17+00	6.04+00	2.05+00	1.24+00	1.12+00	1.00+00	
28	1.752+06	2.284+02	1.072-02	2.433-02	8.509-03	1.506-03	8.258-06	3.133-05	1.395-05	1.24+02	4.91+00	3.68+00	3.68+00	1.23+00	1.32+00	1.16+00	1.00+00	
29	2.859+06	4.207+02	1.651-02	4.351-02	2.231-03	1.546-05	5.848-05	2.594-05	1.20+02	3.89+00	4.33+00	2.87+00	9.56-01	1.36+00	1.18+00	1.00+00	1.00+00	
30	6.190+06	1.091+03	3.184-02	1.086-01	2.329-02	4.047-03	3.962-05	1.991-04	6.583-05	1.03+02	2.74+00	3.97+00	1.98+00	6.53-01	1.11+00	1.20+00	1.00+00	
31	1.130+07	2.274+03	5.218-02	2.207-01	3.645-02	6.317-03	7.955-05	2.984-04	1.312-04	9.17+01	2.12+00	3.72+00	1.50+00	4.92-01	1.44+00	1.22+00	1.00+00	
32	2.117+07	4.855+03	8.005-02	4.613-01	5.06-02	9.898-03	1.597-04	5.970-04	2.616-04	8.16+01	1.63+00	3.48+00	1.14+00	3.71-01	1.46+00	1.23+00	1.00+00	
33	4.604+07	1.252+04	1.637-01	1.170+00	1.035-01	1.776-02	4.111-04	1.528-03	6.658-04	6.64+01	1.09+00	3.15+00	7.50-01	2.42+01	1.48+00	1.24+00	1.00+00	
34	8.482+07	2.540+04	2.025-01	2.352-01	1.761-01	2.335-02	8.335-04	1.375-03	1.328-03	5.04+01	8.13-01	2.77+00	5.64-01	1.78+00	1.24+00	1.00+00	1.00+00	
35	1.493+08	4.741+04	4.803-01	4.355+00	2.995-01	4.802-02	1.555-03	5.698-03	2.443-03	3.62+01	6.26-01	2.38+00	4.60-01	1.39-01	1.49+00	1.24+00	1.00+00	
36	2.201+08	6.988+04	7.027+01	6.395+00	2.207+01	3.748+01	3.684+00	7.322+02	2.398+01	9.109-02	3.563+02	6.911-03	2.71+01	5.40+01	2.09+00	4.16+00	1.24+00	1.00+00
37	5.031+08	1.416+05	1.552+00	1.287+01	9.826+01	1.458+01	4.682+03	1.665+02	6.911-03	1.12+01	3.68+01	1.41+00	3.22+00	9.17-02	1.49+00	1.23+00	1.00+00	
38	7.899+08	1.985+05	2.395+00	1.799+01	1.462+00	2.103+02	6.595+03	2.311+02	9.438+03	5.78+00	2.74+00	1.03+00	2.66+01	7.37-02	1.50+00	1.25+00	1.00+00	
39	1.290+09	3.517+05	4.466+00	3.192+01	2.859+00	3.192+01	3.984+01	1.172+02	4.013+02	1.60+02	2.18+00	1.86+01	2.07+01	5.61-02	1.50+00	1.25+00	1.00+00	
40	2.185+09	8.344+05	1.247+01	7.648+01	7.989+00	1.082+00	2.779+02	9.269+02	3.591-02	7.21+01	1.24+01	4.25+01	1.60+01	4.28+02	1.50+00	1.25+00	1.00+00	
41	3.718+09	2.193+06	4.343+01	2.071+02	2.748+01	3.684+00	7.322+02	2.398+01	9.109-02	3.30+01	1.09+01	3.07+01	1.55+01	4.12+02	1.47+00	1.23+00	1.00+00	
42	5.639+09	4.600+06	1.224+02	4.542+02	7.540+01	1.032+01	1.554+01	1.906+01	1.909+01	2.45+01	3.68+01	1.41+00	3.22+00	9.17-02	1.21+00	1.21+00	1.00+00	
43	1.072+10	1.367+07	6.445+02	1.543+03	3.671+02	5.661+01	4.928+01	1.613+00	6.119+01	2.63+01	2.12+01	2.99+01	2.71+01	8.32+00	1.32+00	1.16+00	1.00+00	
44	2.681+10	5.469+07	6.227+03	9.016+03	3.048+03	7.498+02	6.646+00	8.862+00	3.448+00	4.53+01	5.58+01	4.43+01	5.34+01	2.60+01	1.17+00	1.08+00	1.00+00	
45	6.216+10	1.478+08	2.960+04	4.464+04	1.546+04	6.528+03	1.333+01	4.586+01	1.836+01	6.86+01	8.53+01	6.55+01	7.54+01	6.21+01	1.09+00	1.04+00	1.00+00	
46	1.321+11	2.507+08	8.135+04	1.678+05	5.769+04	2.805+04	6.295+01	2.228+02	9.204+01	7.85+01	8.76+01	8.44+01	8.92+01	8.34+01	1.04+00	1.02+00	1.00+00	
47	1.846+11	2.833+08	1.267+05	2.951+05	1.019+05	5.064+04	1.389+02	5.001+02	2.105+02	8.20+01	8.84+01	9.13+01	9.25+01	8.77+01	1.03+00	1.01+00	1.00+00	
48	2.474+11	3.131+08	2.113+05	5.403+05	1.911+05	9.747+04	3.500+02	1.388+03	5.551+02	8.72+01	9.13+01	9.70+01	9.48+01	9.16+01	1.00+00	1.01+00	1.00+00	
49	3.136+11	3.654+08	4.258+05	1.182+06	4.440+05	2.329+05	1.246+03	4.714+03	2.092+03	8.95+01	9.20+01	9.77+01	9.41+01	9.23+01	1.00+00	1.00+00	1.00+00	
50	3.391+11	4.148+08	7.123+05	2.045+06	8.210+05	4.387+05	3.055+03	1.179+04	5.347+03	9.40+01	9.52+01	9.86+01	9.61+01	9.53+01	1.00+00	1.00+00	1.00+00	
51	3.541+11	4.659+08	1.287+06	3.871+06	1.687+06	9.160+05	8.847+03	3.497+04	1.627+04	9.81+01	9.84+01	9.94+01	9.86+01	9.84+01	1.00+00	1.00+00	1.00+00	
52	3.669+11	5.058+08	2.104+06	6.677+06	3.089+06	1.693+06	2.199+04	8.70+04	4.218+04	9.38+01	9.91+01	9.95+01	9.92+01	9.91+01	1.00+00	1.00+00	1.00+00	

TABLE 23  
HELIUM NUMBER DENSITIES AND DEPARTURE COEFFICIENTS

$\Pi_{\text{ion}}$	$\Pi_1$	$\Pi_2$	$\Pi_3$	$\Pi_4$	$\Pi_5$	$\Pi_6$	$\Pi_7$	$\Pi_8$	$b_1$	$b_2$	$b_3$	$b_4$	$b_5$	$b_6$	$b_7$	$b_8$	
1	1.987+04	9.011+00	4.419-03	3.453-06	6.490-04	9.114-09	2.856-06	4.216-08	1.414-05	5.73+11	1.56+08	3.75+05	7.91+06	3.35+02	1.09+05	4.86+03	1.81+05
2	4.180+06	4.400+03	1.714-03	1.896-01	4.998-04	9.114-09	2.856-06	4.216-08	1.414-05	1.85+10	9.32+06	4.07+04	4.97+05	4.01+01	7.13+03	6.59+02	1.30+01
3	8.833+09	1.125+05	1.435+01	2.536+02	2.087+00	9.453-04	3.280-04	6.628-02	2.14+06	7.34+03	7.03+04	8.15+00	1.20+03	1.28+02	2.04+02	2.04+03	2.04+03
4	8.306+08	5.583+06	1.099+02	2.715-01	1.599+01	1.313-03	3.086-03	3.539-01	2.40+08	1.57+05	1.40+03	9.94+03	2.59+00	2.04+02	2.71+01	3.53+02	3.53+02
5	1.098+09	5.516+07	2.406+02	7.365+01	3.497+01	8.760-03	1.596-01	7.453-03	7.697-01	1.16+08	8.50+04	1.00+03	5.89+03	4.80+00	1.40+02	2.09+01	2.46+02
6	1.167+09	1.700+08	3.251+02	1.151+00	4.722+01	2.836-02	2.142-01	1.128-02	1.034+00	7.17+07	6.05+04	8.58+02	4.43+03	8.76+00	1.14+02	1.93+01	2.03+02
7	1.139+09	3.950+08	3.372+02	1.523+00	4.894+01	8.632-02	1.558-02	1.068+00	3.49+07	3.67+04	6.92+02	2.85+03	1.67+01	7.99+01	1.84+01	1.45+02	1.45+02
8	1.086+09	5.991+08	2.993+02	1.228+00	2.789+02	3.197+00	4.077+01	1.740+00	1.695+01	1.64+07	1.462+01	1.85+02	1.84+03	2.42+01	5.52+01	1.72+01	1.01+02
9	1.067+09	6.990+08	2.843+02	1.970+00	4.124+01	2.766+01	1.855+01	2.045+02	8.985+01	1.12+07	1.81+04	5.51+02	1.43+01	4.68+01	1.70+01	8.66+01	8.66+01
10	1.063+09	7.113+08	2.956+02	2.451+00	4.293+01	4.889+01	1.931+01	2.315+02	9.333+01	1.02+07	1.75+04	6.38+02	1.46+03	5.67+01	1.82+01	8.50+01	8.50+01
11	1.055+09	8.589+08	3.056+02	2.912+00	4.447+01	6.703-01	2.001+01	2.601+02	9.641+01	9.34+06	1.66+04	7.21+02	1.41+03	7.40+01	4.47+01	8.26+01	8.26+01
12	1.039+09	9.911+08	3.125+02	3.261+00	4.558+01	8.815+01	2.052+01	2.705+02	9.850+01	8.29+06	1.55+04	7.20+02	1.33+03	8.73+01	4.26+01	7.87+01	7.87+01
13	1.000+09	1.165+09	2.888+02	3.211+00	4.219+01	9.579+01	9.03+01	2.107+01	6.15+06	2.44+04	6.33+02	1.08+01	8.55+01	1.00+03	6.60+01	6.65+01	6.65+01
14	9.863+08	3.597+08	2.228+00	2.789+02	3.197+00	4.077+01	9.813+01	2.463+02	8.797+01	5.50+06	1.14+04	5.94+02	1.00+03	8.29+01	3.37+01	6.24+01	6.24+01
15	9.408+08	1.593+09	2.273+02	3.467+00	3.320+01	1.216+00	1.502+01	2.555+02	7.202+01	8.47+05	5.08+03	3.569+02	4.87+02	6.17+01	1.86+01	3.54+01	3.54+01
16	9.232+08	1.794+09	2.094+02	3.600+00	3.058+01	1.342+00	1.385+01	2.601+02	6.648+01	3.58+05	3.49+03	2.97+02	3.49+02	5.38+01	1.42+01	9.11+00	2.73+01
17	9.477+08	3.138+09	3.054+02	5.072+00	4.446+01	5.235+00	2.013+01	3.819+02	9.668+01	1.09+02	4.70+02	5.58+01	6.72+01	1.28+01	4.78+01	3.29+00	1.00+01
18	9.506+08	3.597+09	3.452+02	6.344+00	5.021+01	2.499+00	2.273+01	4.183+02	1.091+00	4.58+00	2.32+02	2.99+01	3.82+01	7.49+00	3.38+00	7.37+00	7.37+00
19	9.550+08	4.267+09	4.001+02	7.185+00	5.814+01	2.618+00	2.630+01	1.262+01	6.559+02	9.59+02	9.80+01	1.39+01	1.92+01	3.84+00	2.22+00	1.51+00	5.06+00
20	9.837+08	5.126+09	4.479+02	7.302+00	6.511+01	2.827+00	2.946+01	4.862+02	1.414+00	2.09+03	4.18+01	9.77+00	1.80+00	1.48+00	9.67+01	3.52+00	3.52+00
21	1.005+09	5.520+09	4.645+01	6.721+00	3.056+01	4.893+02	1.467+00	6.76+04	3.24+01	4.66+00	8.00+00	1.31+00	8.41+00	8.41+00	8.41+01	3.16+00	3.16+00
22	1.024+09	5.917+09	4.795+02	7.061+00	6.978+01	2.618+00	3.156+01	4.922+02	1.515+00	2.53+04	6.60+01	3.68+00	6.73+00	1.09+00	1.18+00	7.45+01	2.89+00
23	1.049+09	6.622+09	5.001+02	6.942+00	7.290+01	2.489+00	3.297+01	5.989+02	1.581+00	8.15+05	2.01+01	7.78+00	5.49+00	8.26+01	1.05+00	6.48+01	2.60+00
24	1.070+09	7.980+09	5.695+01	2.324+00	6.775+00	7.695+01	5.067+02	1.664+00	1.70+05	1.39+01	1.89+00	4.13+00	5.59+01	8.91+01	5.35+01	2.24+00	2.24+00
25	1.069+09	9.143+09	5.376+02	6.705+00	7.881+01	2.275+00	3.562+01	5.095+02	1.700+00	8.77+06	1.18+01	1.61+00	3.63+00	4.78+01	8.26+01	4.94+01	2.08+00
26	9.977+08	1.276+10	5.309+02	6.535+00	7.835+01	2.153+01	5.042+02	1.677+00	2.729+03	7.442+02	2.41+06	8.26+00	1.15+00	5.12+01	1.08+00	3.48+01	4.20+01
27	6.419+08	6.539+10	3.857+02	1.455+00	4.880+00	5.768+01	1.592+01	3.764+02	1.214+00	8.91+07	5.25+00	8.00+00	1.94+00	2.50+01	3.49+01	1.46+00	1.46+00
28	2.018+08	6.378+08	6.378+01	1.455+02	2.001+00	1.651+01	1.002+01	1.521+02	4.539+01	1.51+06	3.72+00	6.44+01	1.47+01	2.11+01	4.76+01	1.20+00	1.20+00
29	1.099+08	1.043+01	8.919+01	1.352+00	1.282+00	1.352+01	4.307+01	6.182+02	9.645+03	2.767+01	2.31+06	3.20+00	6.01+01	1.30+00	4.36+01	1.09+00	1.09+00
30	4.784+07	2.212+11	4.267+01	6.574+01	6.487+00	2.979+02	4.832+06	7.444+07	2.196+08	7.69+00	2.71+00	5.46+01	1.44+00	1.89+01	4.01+01	2.85+01	1.00+00
31	2.746+07	4.200+11	2.416+01	3.713+01	3.676+00	1.278+01	1.686+02	2.729+03	7.442+02	1.14+05	2.51+00	5.12+01	1.08+00	2.75+00	3.48+01	4.20+01	4.20+00
32	5.283+06	7.865+11	5.036+02	2.001+00	2.804+01	7.672+01	5.861+04	1.537+01	1.750+01	5.91+05	2.20+00	8.00+00	1.67+00	2.50+01	3.66+01	2.67+01	2.67+01
33	6.246+04	1.711+12	6.711+12	6.575+02	1.151+03	1.028+02	4.07+04	4.745+05	8.203+04	2.04+03	3.94+04	1.78+00	4.22+00	8.18+01	1.58+01	2.52+01	8.23+00
34	6.995+04	3.147+12	3.147+12	1.028+04	1.568+05	1.065+06	3.240+04	4.963+11	2.160+10	2.25+00	1.77+00	7.54+01	1.99+01	4.78+01	8.38+01	3.63+01	3.59+01
35	1.066+01	5.522+12	3.167+05	1.438+06	4.832+06	7.466+10	7.420+12	2.758+12	3.079+11	3.15+01	3.23+01	5.69+01	1.19+00	9.23+01	5.60+01	7.21+01	1.41+00
36	3.565+00	8.135+12	1.445+05	8.680+07	2.205+06	4.800+07	9.942+09	3.356+09	4.189+08	9.98+00	2.82+00	5.61+00	1.50+00	1.65+00	7.48+01	1.14+00	1.90+00
37	5.836+01	1.864+13	2.567+06	1.657+07	3.914+07	9.260+08	1.751+09	7.546+09	4.39+00	1.67+00	5.86+00	1.05+00	1.57+00	1.30+00	6.67+01	1.10+00	1.80+00
38	1.111+02	2.946+13	5.443+07	3.780+08	8.299+08	1.244+09	3.705+09	1.372+09	1.607+09	2.18+00	1.58+00	1.99+01	1.06+00	1.04+00	1.04+00	1.65+00	1.65+00
39	1.278+02	4.794+13	7.301+08	5.591+09	1.835+08	4.049+09	9.399+11	2.425+11	2.338+10	3.90+01	3.61+01	4.78+01	3.67+01	5.38+01	9.47+01	1.45+00	1.45+00
40	1.086+03	8.140+13	1.078+08	7.984+10	1.646+09	4.665+10	7.420+12	2.758+12	3.079+11	8.77+01	6.61+01	7.30+01	5.87+01	6.76+01	7.07+01	8.03+01	9.34+01
41	9.222+05	1.382+14	1.592+09	1.140+10	2.433+10	6.716+11	1.109+12	3.932+13	4.388+12	1.12+01	1.77+01	3.38+01	7.94+01	2.08+01	3.46+01	3.50+01	6.49+01
42	6.180+05	2.094+11	1.610+09	1.077+10	2.458+10	6.353+11	1.140+12	3.787+13	4.204+12	1.00+01	1.64+01	2.98+01	1.98+01	3.10+01	3.53+01	6.15+01	9.64+01
43	8.088+03	3.988+14	3.862+09	2.362+10	5.919+10	1.406+10	2.838+12	8.507+13	1.64+02	1.337+02	6.389+04	1.435+04	1.090+03	1.02+00	2.15+01	3.86+01	6.05+01
44	1.130+03	9.980+14	1.179+07	6.575+09	1.835+08	4.049+09	9.399+11	2.425+11	2.338+10	3.90+01	3.61+01	4.78+01	3.67+01	5.38+01	9.47+01	1.45+00	1.45+00
45	3.626+02	2.315+15	6.639+06	3.538+07	1.098+08	7.984+10	1.646+09	4.665+10	7.420+12	2.126+08	2.274+00	9.92+01	9.93+01	9.30+01	9.85+01	7.07+01	9.76+01
46	3.153+00	4.917+15	7.085+04	4.018+05	1.404+04	2.900+05	9.662+07	2.142+07	1.661+06	1.00+00	9.26+01	7.93+01	2.08+01	3.46+01	3.50+01	6.49+01	1.02+00
47	4.948+01	6.901+15	1.101+02	6.730+04	2.539+03	5.302+04	2.072+05	4.571+04	4.97+05	1.00+00	1.00+00	8.91+01	9.47+01	8.39+01	9.08+01	9.22+01	9.22+01
48	1.098+03	9.203+15	2.246+01	1.524+02	6.416+01	1.337+02	6.67+02	1.84+03	1.02+00	1.03+00	1.02+0						

TABLE 24  
HELIUM II NUMBER DENSITIES AND DEPARTURE COEFFICIENTS

$\eta_{\text{ion}}$	$\eta_1$	$\eta_2$	$\eta_3$	$\eta_4$	$\eta_5$	$\eta_6$	$\eta_7$	$\eta_8$	$b_1$	$b_2$	$b_3$	$b_4$	$b_5$	$b_6$	$b_7$	$b_8$
1	1.002+08	1.988+04	1.683-05	2.241-05	1.161-05	1.445-05	4.588-05	6.180-05	8.017-05	2.899+10	1.77+01	1.27+01	3.97+00	3.26+00	7.32+00	4.16+00
2	3.332+08	4.184+06	1.518-03	9.203-04	4.255-04	5.203-04	4.216-03	5.537-03	6.552-03	3.899+09	1.00+01	1.53+00	3.1+00	3.1+00	2.20+00	1.00+00
3	1.187+08	8.429+07	1.633-02	3.249-03	1.428-03	1.537-03	1.421-03	1.447-03	6.877-03	1.81+09	1.00+01	4.23+00	1.47+00	1.19+00	2.47+00	1.73+00
4	6.574+07	8.306+08	1.226-01	1.181-03	8.474-04	6.781-04	1.401-03	1.738-03	2.137-03	1.12+08	5.37+01	1.33+00	9.93-01	6.75-01	1.13+00	1.06+00
5	4.482+07	1.098+09	1.458-01	6.631-04	6.370-04	5.721-04	1.400-03	1.166-03	1.685-03	1.24+06	1.49+01	3.23+01	4.01-01	3.38+01	5.90-01	7.95-01
6	3.746+07	1.116+09	1.428-01	5.645-04	5.619-04	5.378-04	1.094-03	1.290-03	1.534-03	1.07+05	7.27+00	1.86+01	2.69+01	2.56+01	4.59+01	7.35+01
7	3.006+07	1.138+09	1.388-01	4.618-04	4.804-04	4.974-04	1.009-03	1.163-03	1.364-03	4.11+03	2.78+00	9.44+02	1.65+01	1.82+01	3.37+01	6.68+01
8	2.937+07	1.131+09	1.346-01	4.262-04	4.518-04	4.779-04	9.622-04	1.107-03	1.297-03	3.19+03	2.51+00	8.43+02	1.52+01	1.72+01	3.18+01	6.61+01
9	2.804+07	1.131+09	1.261-01	3.655-04	4.014-04	4.422-04	8.773-04	1.006-03	1.175-03	1.94+03	2.05+00	7.99+02	1.30+01	1.54+01	2.83+01	6.46+01
10	2.424+07	1.104+09	9.858-02	2.392-04	2.888-04	3.546-04	6.739-04	7.646-04	8.873-04	4.44+02	1.09+00	3.72+02	8.40+02	1.15+01	2.05+01	6.08+01
11	2.035+07	1.049+09	6.753-02	1.608-04	2.108-04	2.840-04	5.159-04	5.785-04	6.662-04	8.62+01	5.17+01	2.11+02	5.59+02	8.72+02	1.51+01	5.75+01
12	1.573+07	9.232+08	3.556-02	1.145-04	1.589-04	2.274-04	3.929-04	4.343-04	4.762-04	1.41+01	1.91+01	1.52+02	4.50+02	7.45+02	1.26+01	5.64+01
13	1.273+07	8.363+08	2.163-02	1.022-04	1.422-04	2.028-04	3.397-04	3.720-04	4.126-04	3.48+00	8.84+02	1.18+02	6.59+02	1.10+02	2.55+01	1.00+00
14	1.194+07	8.126+08	1.876-02	1.014-04	1.401-04	1.980+04	3.292-04	3.595-04	4.034-04	2.32+00	7.06+02	1.06+02	3.63+02	1.06+01	5.53+01	1.00+00
15	1.152+07	7.998+08	1.728-02	1.014-04	1.394-04	2.342+04	3.242-04	3.535-04	3.999-04	1.85+00	6.24+02	1.06+02	3.53+02	6.24+02	1.03+01	5.51+01
16	1.006+07	8.601+08	1.793-02	1.092-04	1.519-04	2.157-04	3.532-04	3.652-04	3.991-04	1.15+03	8.55+03	4.12+03	1.97+02	4.15+02	5.42+01	1.00+00
17	7.670+06	9.947+08	1.929-02	1.266-04	1.804-04	2.618-04	4.193-04	3.897-04	3.974-04	4.52+10	1.60+04	6.22+04	6.18+03	1.84+02	3.85+02	5.3+01
18	6.697+06	1.070+09	2.001-02	1.363-04	1.966-04	2.885-04	4.569-04	4.026-04	3.965-04	2.82+13	2.20+05	2.42+04	3.45+03	1.22+02	2.77+02	1.13+01
19	6.202+06	1.056+09	1.881-02	1.343-04	1.939-04	2.865-04	4.509-04	4.509-04	3.892-04	2.57+15	1.81+06	1.55+04	2.64+03	1.06+03	5.55+03	1.12+01
20	4.854+06	9.949+08	1.410-02	1.253-04	1.816-04	2.774-04	4.240-04	3.325-04	3.036-04	3.23+20	2.68+07	3.45+05	1.06+03	1.48+02	5.07+01	1.00+00
21	4.790+06	1.015+09	1.262-02	1.262-04	1.827-04	2.774-04	4.242-04	3.270-04	2.953-04	2.57+21	1.23+07	2.53+07	5.87+04	4.91+03	1.34+02	5.06+01
22	4.728+06	1.035+09	1.134-02	1.264-04	1.839-04	2.805-04	4.245-04	3.216-04	2.871-04	2.84+22	1.24+08	1.93+05	7.56+04	4.41+03	1.22+02	5.06+01
23	4.737+06	1.061+09	9.391-03	1.253-04	1.830-04	2.810-04	4.177-04	3.085-04	2.710-04	2.12+22	1.26+08	1.40+05	6.24+04	3.89+03	1.09+02	5.05+01
24	4.254+06	1.084+09	6.813-03	1.190-04	1.745-04	2.694-04	3.901-04	2.822-04	2.445-04	5.55+25	7.69+09	8.92+06	4.76+04	3.24+03	9.30+03	5.04+01
25	3.912+06	1.084+09	5.242-03	1.118-04	1.642-04	2.547-04	3.633-04	2.586-04	2.218-04	1.07+25	4.10+09	7.24+06	4.20+04	2.98+03	8.63+03	5.04+01
26	2.889+06	1.014+09	2.597-03	8.693-05	1.277-04	2.790-04	1.942-04	1.641-04	3.67+27	1.01+09	4.65+06	3.20+04	2.47+03	7.31+03	5.03+01	1.00+00
27	8.552+05	6.577+08	3.211-04	2.922-05	4.261-05	6.767-05	9.150-05	5.173-05	5.815-05	9.13+29	1.15+10	2.60+16	1.15+10	1.89+03	5.69+03	5.02+01
28	4.576+05	6.123+08	3.630-08	1.659-06	2.317-06	3.919-06	5.213-06	3.445-06	3.965-06	2.57+29	9.52+12	1.58+06	1.46+04	4.39+03	5.02+01	1.00+00
29	6.087+03	1.224+08	2.814-07	2.378-07	3.284-07	5.657-07	7.473-07	4.905-07	3.987-07	3.64+29	3.38+12	1.35+06	1.29+04	4.08+03	5.02+01	1.00+00
30	2.953+02	5.362+07	6.074+09	1.291+08	1.752+08	3.102+08	4.056+08	2.632+08	2.125+08	6.12+29	9.77+13	1.07+06	1.08+04	1.17+03	3.65+03	5.01+01
31	4.101+01	2.732+07	5.372+10	1.573+09	1.998+09	3.837+09	5.062+09	3.261+09	2.621+09	8.50+29	4.93+13	8.51+07	8.45+05	1.02+03	3.23+03	5.01+01
32	1.029+01	5.355+06	1.251+11	4.341+11	1.493+11	2.065+10	4.261+10	8.94+10	1.15+11	1.15+11	1.15+10	2.60+16	1.15+10	1.89+03	5.69+03	5.02+01
33	1.830+01	6.313+04	2.543+15	9.026+15	1.143+14	2.226+14	4.914+14	1.836+14	1.454+14	1.63+27	1.85+13	5.91+07	6.77+05	8.88+03	5.01+01	1.00+00
34	6.533+10	8.533+10	1.110+01	1.090+01	1.224+01	2.946+20	4.834+20	3.81+20	1.231+19	7.639+20	5.993+20	6.75+26	1.10+13	4.65+07	5.89+05	8.12+04
35	2.034+15	1.116+01	3.382+26	1.197+25	1.519+25	2.994+25	3.859+25	2.346+25	1.816+25	7.47+23	4.97+14	3.34+07	4.86+05	7.18+04	2.44+03	5.01+01
36	1.740+19	3.529+00	2.914+30	1.029+29	1.315+29	2.592+29	3.315+29	1.980+29	1.515+29	5.56+20	2.92+14	2.52+07	4.12+05	6.46+04	2.24+03	5.01+01
37	5.156+36	5.775+01	6.649+40	2.916+46	3.416+46	6.883+46	8.578+46	4.837+46	3.565+46	1.31+07	3.40+08	1.09+07	2.41+05	4.58+04	1.71+03	5.01+01
38	1.789+44	1.110+01	1.090+01	5.546+50	7.949+51	1.943+52	4.270+52	2.291+52	1.636+52	4.12+03	1.94+04	2.19+04	5.03+03	2.32+02	4.83+02	7.69+01
39	1.257+39	1.297+02	1.785+45	1.388+53	9.046+56	7.813+57	2.557+57	1.302+57	1.976+58	1.06+06	1.11+00	4.39+01	1.05+00	1.17+00	1.38+00	1.18+00
40	1.203+55	1.054+03	9.241+49	6.113+58	1.897+60	2.022+61	6.784+62	3.205+62	2.106+62	2.02+01	5.03+01	4.33+01	8.31+01	1.33+00	1.80+00	1.00+00
41	1.270+58	8.555+05	4.783+52	1.980+60	3.823+63	4.678+64	1.597+64	7.236+65	4.622+65	3.85+02	2.27+01	4.27+01	6.54+01	1.47+00	2.16+00	1.58+00
42	1.673+58	5.625+05	6.692+52	3.968+60	6.946+63	9.007+64	3.084+64	1.410+64	9.07+65	3.46+02	2.18+01	4.87+01	6.72+01	1.56+00	2.27+00	1.63+00
43	3.181+58	7.309+05	1.24+51	1.393+59	2.377+62	3.068+63	1.887+64	1.060+63	3.162+64	4.29+02	2.23+01	6.04+01	7.27+01	1.64+00	2.36+00	1.68+00
44	1.371+57	1.069+03	1.949+50	1.304+58	2.959+61	2.988+62	1.053+62	4.855+63	3.141+63	1.52+01	2.84+01	5.57+01	8.90+01	1.55+00	2.30+00	1.65+00
45	4.211+56	3.510+02	7.808+49	4.572+57	2.143+59	1.397+60	5.372+61	2.478+61	1.603+61	1.87+01	1.78+01	2.61+01	9.61+01	9.61+01	1.27+00	1.00+00
46	5.156+45	3.087+00	2.344+39	2.600+46	1.224+48	1.403+49	4.733+50	2.624+50	1.913+50	9.45+01	8.74+01	1.01+00	1.01+00	1.15+00	1.19+00	1.00+00
47	5.657+41	4.877+01	7.665+36	2.194+42	1.429+44	1.808+45	6.112+46	3.798+46	2.862+46	9.64+01	9.33+01	1.01+00	1.07+00	1.73+00	1.03+00	1.00+00
48	6.208+37	1.091+03	2.618+32	1.852+38	1.668+40	2.330+41	8.960+42	5.498+42	4.281+42	9.78+01	9.72+01	1.01+00	1.00+00	1.64+00	1.00+00	1.00+00
49	1.643+31	4.383+04	1.110+27	1.204+33	1.304+36	3.082+36	1.081+35	4.67+36	3.241+36	9.88+01	9.88+01	1.02+00	9.93+01	9.92+01	1.91+00	1.00+00
50	1.751+27	6.008+05	6.076+27	4.568+27	4.568+29	7.981+31	9.283+31	6.468+32	5.470+32	9.92+01	9.96+01	1.01+00	1.01+00	9.95+01	9.97+01	1.00+00
51	1.788+23	8.032+06	2.333+20	4.711+27	1.446+26											

## QUIET SUN EUV BRIGHTNESS COMPONENTS

693

TABLE 25  
DETAILS OF OUR H<sup>-</sup> CALCULATION FOR MODEL C

	$\delta$	r	$\int L/\nu$	$\int J/\nu$	$b_{H^-}$	$\int L$	$\int J$	$n_{H^-}^*$	$\Phi_{H^-}$
18	1.67+02	2.18+02	1.56+07	1.12+06	1.40+01	6.06-05	2.98-06	9.23-02	1.76-06
19	1.56+02	1.92+02	1.13+07	1.12+06	1.01+01	4.08-05	2.98-06	1.69-01	1.80-06
20	1.30+02	1.65+02	8.12+06	1.12+06	7.27+00	2.73-05	2.98-06	3.46-01	1.96-06
21	1.13+02	1.56+02	7.42+06	1.12+06	6.63+00	2.45-05	2.98-06	4.40-01	2.08-06
22	1.04+02	1.50+02	6.79+06	1.12+06	6.08+00	2.21-05	2.98-06	5.45-01	2.16-06
23	9.01+01	1.43+02	6.10+06	1.12+06	5.46+00	1.94-05	2.98-06	7.35-01	2.33-06
24	7.24+01	1.36+02	5.40+06	1.12+06	4.84+00	1.68-05	2.98-06	1.10+00	2.68-06
25	6.27+01	1.33+02	4.96+06	1.12+06	4.44+00	1.52-05	2.98-06	1.47+00	2.96-06
26	4.63+01	1.35+02	4.50+06	1.12+06	4.03+00	1.36-05	2.98-06	2.50+00	4.02-06
27	2.63+01	1.55+02	3.89+06	1.12+06	3.48+00	1.15-05	2.98-06	7.12+00	7.91-06
28	1.30+01	2.52+02	3.54+06	1.12+06	3.17+00	1.03-05	2.98-06	2.65+01	2.27-05
29	8.93+00	3.86+02	3.42+06	1.12+06	3.06+00	9.88-06	2.98-06	5.23+01	4.05-05
30	4.72+00	9.81+02	3.26+06	1.12+06	2.92+00	9.36-06	2.98-06	1.41+02	9.50-05
31	2.46+00	2.59+03	3.16+06	1.12+06	2.82+00	9.02-06	2.98-06	2.62+02	1.62-04
32	1.47+00	6.53+03	3.04+06	1.12+06	2.71+00	8.64-06	2.98-06	5.61+02	3.16-04
33	8.02-01	1.91+04	2.86+06	1.12+06	2.53+00	8.06-06	2.98-06	1.49+03	7.58-04
34	5.04-01	4.20+04	2.68+06	1.12+06	2.35+00	7.48-06	2.98-06	3.24+03	1.57-03
35	3.05-01	8.51+04	2.43+06	1.12+06	2.09+00	6.67-06	2.98-06	6.29+03	2.85-03
36	2.19-01	1.34+05	2.28+06	1.12+06	1.92+00	6.20-06	2.98-06	9.91+03	4.63-03
37	9.15-02	3.42+05	1.79+06	1.12+06	1.46+00	4.72-06	2.98-06	2.33+04	8.68-03
38	5.61-02	5.56+05	1.50+06	1.12+06	1.23+00	3.86-06	2.98-06	3.72+04	7.78-03
39	4.17-02	9.20+05	1.19+06	1.12+06	1.03+00	2.98-06	2.98-06	7.86+04	-8.03-03
40	3.98-02	1.56+06	9.10+05	1.12+06	9.22-01	2.22-06	2.98-06	2.30+05	-1.23-01
41	4.07-02	2.66+06	7.62+05	1.12+06	9.05-01	1.82-06	2.98-06	7.13+05	-6.26-01
42	4.00-02	4.03+06	7.18+05	1.12+06	9.22-01	1.71-06	2.98-06	1.64+06	-1.71+00
43	3.69-02	7.69+06	7.54+05	1.12+06	9.58-01	1.80-06	3.00-06	5.40+06	-5.77+00
44	3.15-02	1.94+07	9.48+05	1.15+06	9.90-01	2.32-06	3.06-06	2.72+07	-1.94+01
45	2.78-02	4.50+07	1.24+06	1.24+06	1.00+00	3.12-06	3.32-06	1.21+08	-2.37+01
46	2.64-02	9.58+07	1.68+06	1.53+06	1.00+00	4.39-06	4.17-06	4.78+08	1.04+02
47	2.79-02	1.34+08	2.04+06	1.85+06	1.00+00	5.45-06	5.10-06	9.34+08	3.18+02
48	3.60-02	1.78+08	2.61+06	2.40+06	1.00+00	7.20-06	6.75-06	2.02+09	8.98+02
49	7.17-02	2.18+08	3.65+06	3.50+06	1.00+00	1.05-05	1.01-05	5.89+09	1.98+03
50	1.40-01	2.22+08	4.68+06	4.55+06	1.00+00	1.39-05	1.36-05	1.24+10	4.30+03
51	3.41-01	1.97+08	6.40+06	6.30+06	1.00+00	1.99-05	1.96-05	3.00+10	8.46+03
52	7.45-01	1.60+08	8.46+06	8.46+06	1.00+00	2.76-05	2.76-05	6.35+10	1.20+01

models are lower than observed. Ayres and Linsky (1976) used instead the observed Ca II and Mg II intensities to determine the temperature distribution plotted in Figure 37 for comparison. Basri *et al.* (1979) adopted the Ayres and Linsky model in the temperature-minimum region but have proposed a substantial reduction of the temperature in the low chromosphere.

In Figures 38 and 39 we show the observed profiles of the Ca II K and Mg II  $k$  lines (as given in similar figures by Ayres and Linsky 1976), the profiles calculated by Ayres and Linsky, and the ones we calculate from model C. (The profiles from our five other models appear in Figs. 23 and 24.) These results indicate that our temperature values should be higher at the temperature minimum and on the photospheric side of the minimum in order to match the Ca II and Mg II observations. The microwave observations of Rast, Kneubühl, and Müller (1978) shown in Figure 22 also indicate higher minimum temperatures, but see also the earlier observations plotted in Figure 11 of Paper II. Unless something is wrong with the way we calculate the UV continuum in the

range 135–168 nm, such higher temperatures are not consistent with these UV observations. We discuss this problem in § VIII.

Figure 40 shows the continuation of Figure 37 to greater heights in the chromosphere. The rapid rise of the HSRA temperature relative to models A–F in the upper chromosphere is partly due to the lack of a turbulent-pressure contribution to the total pressure in the HSRA calculations, as was assumed in the other models plotted in Figure 40, and thus the HSRA model is less extended when plotted as a function of height. The HSRA model is generally bounded by our models A and F when plotted on a column mass scale.

Figure 27 of § IV shows the profile of the L $\beta$  line observed by Gouttebroze *et al.* (1978) and the poor fit to the observed line shape that we are able to obtain with our calculated profile. Nevertheless, we obtain reasonable agreement with the integrated L $\beta$  intensities as shown in Figure 28. Gouttebroze *et al.* investigated the effect of various changes in the upper chromospheric temperature distribution on the computed L $\beta$  profiles in

TABLE 26  
MODEL C MEAN INTENSITIES USED IN THE H<sup>-</sup> CALCULATION

$\lambda$	$a$	$J_\lambda$ ( $10^{-5}$ ergs cm $^{-2}$ s $^{-1}$ Hz $^{-1}$ )											
	(nm)	( $10^{-17}$ cm $^2$ )	18	19	20	21	22	23	24	25	26	27	
1	1642	0.000	1.43	1.43	1.43	1.43	1.43	1.43	1.43	1.43	1.43	1.43	1.43
2	1550	0.295	1.51	1.51	1.51	1.51	1.51	1.51	1.51	1.51	1.51	1.51	1.51
3	1450	0.839	1.54	1.54	1.54	1.54	1.54	1.54	1.54	1.54	1.54	1.54	1.54
4	1350	1.526	1.57	1.57	1.57	1.57	1.57	1.57	1.57	1.57	1.57	1.57	1.57
5	1200	2.620	1.59	1.59	1.59	1.59	1.59	1.59	1.59	1.59	1.59	1.59	1.59
6	1050	3.549	1.61	1.61	1.61	1.61	1.61	1.61	1.61	1.61	1.61	1.61	1.61
7	850	4.135	1.58	1.58	1.58	1.58	1.58	1.58	1.58	1.58	1.58	1.58	1.58
8	700	3.892	1.46	1.46	1.46	1.46	1.46	1.46	1.46	1.46	1.46	1.46	1.46
9	550	3.149	1.16	1.16	1.16	1.16	1.16	1.16	1.16	1.16	1.16	1.16	1.16
10	450	2.530	7.58-01	7.58-01	7.58-01	7.58-01	7.58-01	7.58-01	7.58-01	7.58-01	7.58-01	7.58-01	7.58-01
11	350	1.917	2.34-01	2.34-01	2.34-01	2.34-01	2.34-01	2.34-01	2.34-01	2.34-01	2.34-01	2.34-01	2.34-01
12	250	1.299	7.79-03	7.79-03	7.79-03	7.79-03	7.79-03	7.79-03	7.79-03	7.79-03	7.79-03	7.79-03	7.79-03
13	200	0.972	7.27-04	7.27-04	7.27-04	7.27-04	7.27-04	7.27-04	7.27-04	7.27-04	7.27-04	7.27-04	7.27-04
14	150	0.664	2.49-06	2.49-06	2.49-06	2.49-06	2.49-06	2.49-06	2.49-06	2.49-06	2.49-06	2.49-06	2.49-06
15	100	0.390	7.94-08	7.88-08	7.88-08	7.88-08	7.88-08	7.88-08	7.88-08	7.88-08	7.88-08	7.88-08	7.88-08
28	29	30	31	32	33	34	35	36	37	38	39	40	
1	1.43	1.43	1.43	1.43	1.43	1.43	1.43	1.43	1.43	1.43	1.43	1.43	
2	1.51	1.51	1.51	1.51	1.51	1.51	1.51	1.51	1.51	1.51	1.51	1.51	
3	1.54	1.54	1.54	1.54	1.54	1.54	1.54	1.54	1.54	1.54	1.54	1.54	
4	1.57	1.57	1.57	1.57	1.57	1.57	1.57	1.57	1.57	1.57	1.57	1.57	
5	1.59	1.59	1.59	1.59	1.59	1.59	1.59	1.59	1.59	1.59	1.59	1.59	
6	1.61	1.61	1.61	1.61	1.61	1.61	1.61	1.61	1.61	1.61	1.61	1.61	
7	1.58	1.58	1.58	1.58	1.58	1.58	1.58	1.58	1.58	1.58	1.58	1.58	
8	1.46	1.46	1.46	1.46	1.46	1.46	1.46	1.46	1.46	1.46	1.46	1.46	
9	1.16	1.16	1.16	1.16	1.16	1.16	1.16	1.16	1.16	1.16	1.16	1.16	
10	7.58-01	7.58-01	7.58-01	7.58-01	7.58-01	7.58-01	7.58-01	7.58-01	7.58-01	7.58-01	7.58-01	7.58-01	
11	2.34-01	2.34-01	2.34-01	2.34-01	2.34-01	2.34-01	2.34-01	2.34-01	2.34-01	2.34-01	2.34-01	2.34-01	
12	7.79-03	7.79-03	7.79-03	7.79-03	7.79-03	7.79-03	7.79-03	7.79-03	7.79-03	7.79-03	7.79-03	7.79-03	
13	7.27-04	7.27-04	7.27-04	7.27-04	7.27-04	7.27-04	7.27-04	7.27-04	7.27-04	7.27-04	7.27-04	7.27-04	
14	2.50-06	2.51-06	2.54-06	2.57-06	2.63-06	2.76-06	2.93-06	3.13-06	3.30-06	3.54-06	3.76-06	3.84-06	
15	7.91-08	8.11-08	8.55-08	8.96-08	9.29-08	8.90-08	7.47-08	4.98-08	3.31-08	1.04-08	5.19-09	9.44-10	
41	42	43	44	45	46	47	48	49	50	51	52		
1	1.43	1.43	1.43	1.44	1.46	1.56	1.69	1.95	2.56	3.15	4.03	4.81	
2	1.51	1.51	1.51	1.51	1.55	1.67	1.82	2.12	2.77	3.40	4.33	5.20	
3	1.54	1.54	1.55	1.56	1.60	1.77	1.97	2.32	3.05	3.74	4.74	5.68	
4	1.57	1.57	1.57	1.59	1.65	1.88	2.12	2.55	3.38	4.11	5.17	6.21	
5	1.59	1.59	1.60	1.62	1.72	2.03	2.36	2.90	3.88	4.71	5.89	7.13	
6	1.61	1.61	1.62	1.65	1.77	2.16	2.56	3.20	4.35	5.30	6.69	8.19	
7	1.58	1.58	1.59	1.62	1.76	2.19	2.65	3.40	4.76	5.95	7.73	9.73	
8	1.46	1.46	1.46	1.49	1.62	2.03	2.47	3.23	4.71	6.06	8.20	1.07+01	
9	1.16	1.16	1.16	1.17	1.19	1.27	1.58	1.94	2.59	3.38	7.77	1.08+01	
10	7.59-01	7.60-01	7.63-01	7.79-01	8.43-01	1.07	1.33	1.82	2.96	4.19	6.47	9.55	
11	2.36-01	2.40-01	2.54-01	3.00-01	4.48-01	6.03-01	8.84-01	1.56	2.36	4.17	6.67		
12	7.95-03	8.12-03	8.70-03	1.10-02	1.85-02	4.42-02	7.61-02	1.48-01	3.49-01	6.39-01	1.32	2.52	
13	7.49-04	7.66-04	8.25-04	1.08-03	2.00-03	5.66-03	1.11-02	2.54-02	7.24-02	1.55-01	3.90-01	8.73-01	
14	3.80-06	4.06-06	5.60-06	1.23-05	3.34-05	1.23	1.29	0.4	9.17-04	3.96-03	1.12-02	3.96-02	
15	3.71-10	2.69-10	3.32-10	1.11-09	5.32-09	1.56-07	8.41-07	7.45-06	3.60-05	2.44-04	1.23-03		

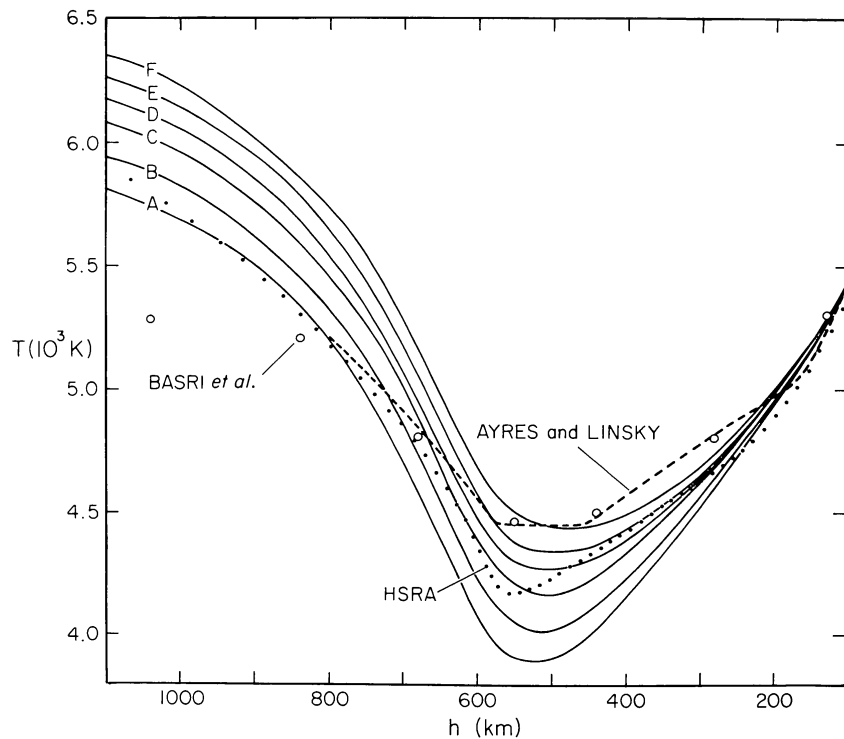


FIG. 37.—Temperature as a function of height for models A–F, the HSRA model of Gingerich *et al.* (1971), and the models of Ayres and Linsky (1976) and Basri *et al.* (1979) in the temperature-minimum region.

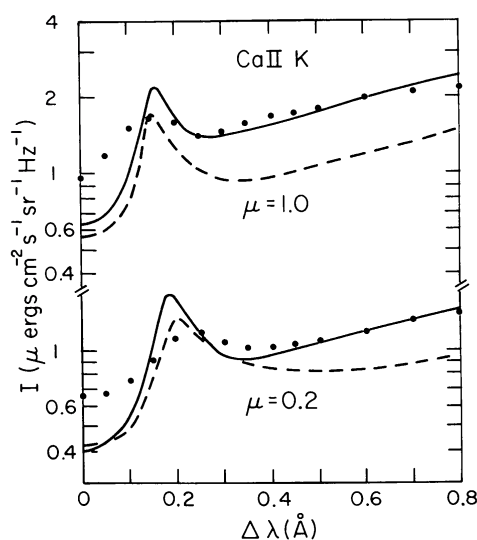


FIG. 38.—Ca II K-line profiles computed from model C (*broken curves*) compared with the ones computed by Ayres and Linsky (*solid curves*) and with the observed average profiles (*dots*).

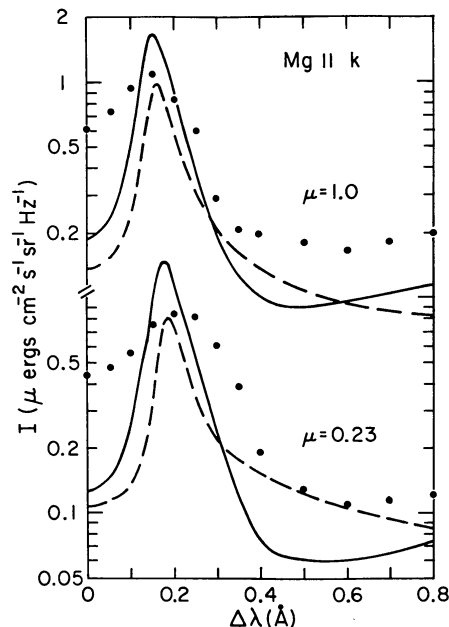


FIG. 39.—Mg II k-line profiles computed from model C (*broken curves*) compared with the ones computed by Ayres and Linsky (*solid curves*) and with the observed average profiles (*dots*).

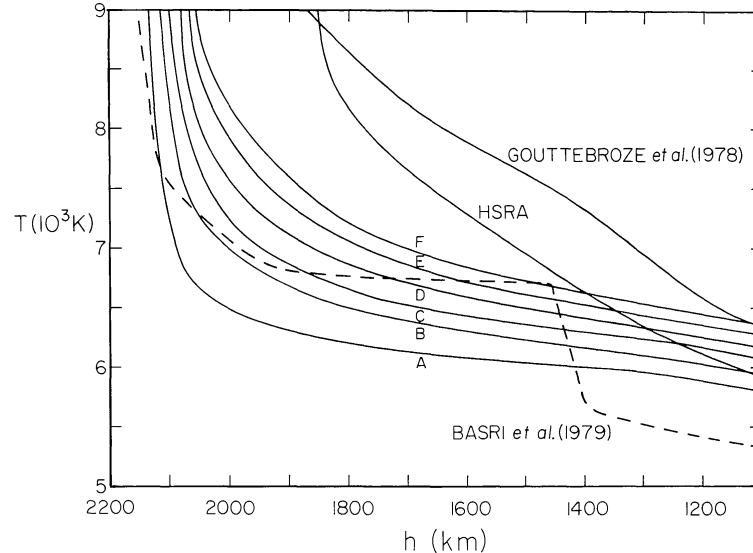


FIG. 40.—Temperature as a function of height in the middle and upper chromosphere for models A–F, the HSRA model, and the models of Gouttebroze *et al.* (1978) and Basri *et al.* (1979).

the search for better agreement with the observed one. However, they did not include a comparison of calculated and observed Lyman continuum intensities. Their temperature distribution, plotted in Figure 40, succeeds in producing a  $L\beta$  computed profile with approximately the observed shape, but implies a Lyman continuum intensity relative to the integrated  $L\beta$  intensity which is more than an order of magnitude larger than observed.

We now turn to the quiet-Sun temperature distribution of Basri *et al.* (1979) shown as a function of height in Figure 40. A comparison of the temperature as a function of column mass for models A, C, and F and the Basri *et al.* model is shown in the lowest portion of Figure 41. The two upper parts of the figure show the  $n_e$  and  $b_1$  distributions for the same models. The temperature reduction in the low chromosphere suggested by Basri *et al.* leads to some difficulties, as these authors admit.

As described in § IV they found that temperatures such as in model C led to much higher intensities in the  $L\alpha$  wing than observed. Thus, they proposed a reduction of the temperature in the low chromosphere where the wing is formed as indicated in Figures 40 and 41.

Basri (private communication) has suggested that the disagreement between their results and ours in the low chromosphere may be due to their use of LTE for the carbon continuum in the wings of  $L\alpha$ . The following results confirm this suggestion.

In Figure 42 we plot the following quantities: the Planck function  $B$  at the center of  $L\alpha$ , the frequency-independent  $L\alpha$  source function  $S$  which is also the monochromatic source function for the central core of the line (see Appendix A), the monochromatic source function  $S_1$  at  $\Delta\lambda=1 \text{ \AA}$  from line center, the corresponding mean intensity  $J_1$ , and the source function  $S_2$

and mean intensity  $J_2$  at  $\Delta\lambda=2 \text{ \AA}$  from line center. Our results from model C and those given by Basri *et al.* are shown in the figure.

The most important difference between the two calculations is that in the middle chromosphere where the line

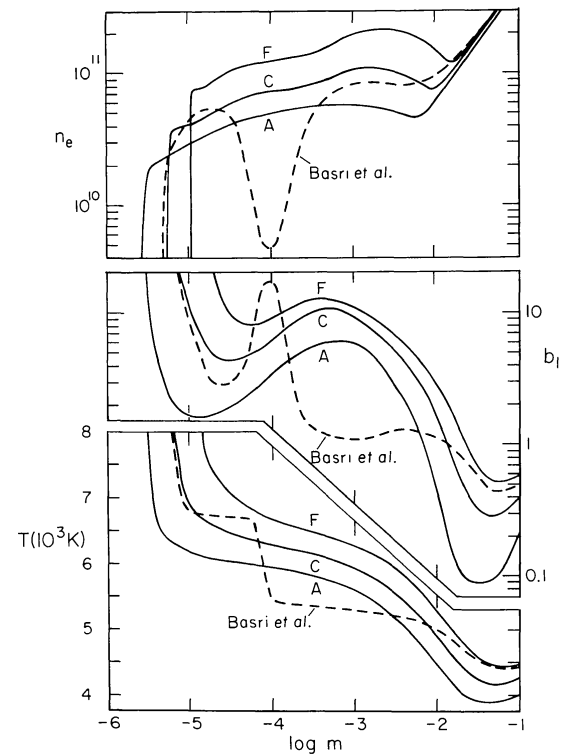


FIG. 41.— $n_e$ ,  $b_1$ , and  $T$  from the Basri *et al.* (1979) average quiet-Sun model compared with our values from models A, C, and F.

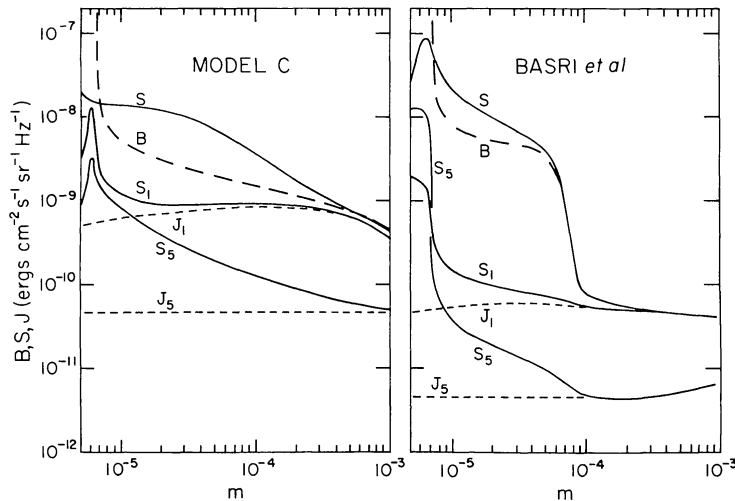


FIG. 42.—Computed source functions and related quantities for  $\text{L}\alpha$ .  $B$  is the Planck function and  $S$  the line-center source function,  $S_1$  is the line source function at  $\Delta\lambda=1 \text{ \AA}$  in the line wing while  $J_1$  is the corresponding mean intensity and  $S_5$  and  $J_5$  are, respectively, the line source function and mean intensity at  $\Delta\lambda=5 \text{ \AA}$ . Our values for model C and those tabulated by Basri *et al.* (1979) are shown.

wing is formed the values of  $S_1$ ,  $J_1$ ,  $S_2$ , and  $J_2$  computed by Basri *et al.* are about a factor of 10 smaller than those we obtain, due to their temperature reduction at  $m=10^{-4}$ . However, the computed  $\text{L}\alpha$  intensities  $I_1$  and  $I_2$  at  $\Delta\lambda=1$  and  $2 \text{ \AA}$  are approximately the same in the two calculations since both computed profiles match the observed profile.

Since the  $\text{L}\alpha$  wing intensity depends not only on the line wing contribution but also on the background carbon continuum, Figure 42 shows that the continuum contribution is much larger than the line contribution in the Basri *et al.* calculation. From the carbon departure

coefficients shown earlier in Figure 33, we expect the carbon continuum when computed in LTE to be at least an order of magnitude higher than the non-LTE continuum.

Figure 43 shows a comparison of the central intensities in the range  $100$ – $121.5 \text{ nm}$  computed with model C and those obtained in a second calculation which is the same except that the non-LTE carbon number densities are replaced by LTE values. The lower solid curve in Figure 43 is in reasonable agreement with the observations (see Fig. 15), while the higher broken curve shows the effect of the incorrect assumption of LTE for carbon.

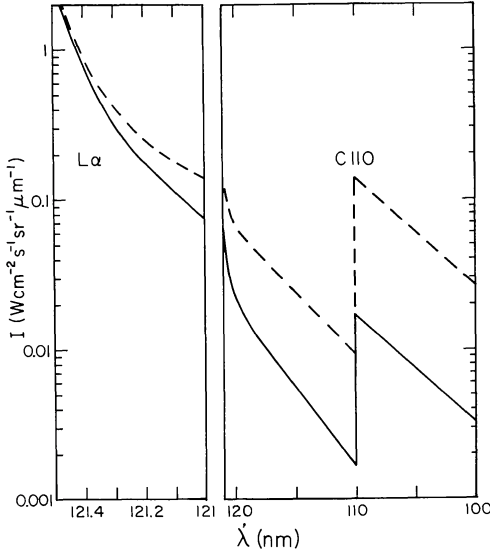


FIG. 43

FIG. 43.—Continuum intensities for  $\mu=1$  in the range  $100$ – $121.5 \text{ nm}$  computed in LTE (broken curve) and by our non-LTE procedure (solid curve).

FIG. 44.—Transition region temperatures as functions of mass column densities. Our models A, C, and F are compared with the dark point, average quiet Sun, bright point, and plage models of Basri *et al.*

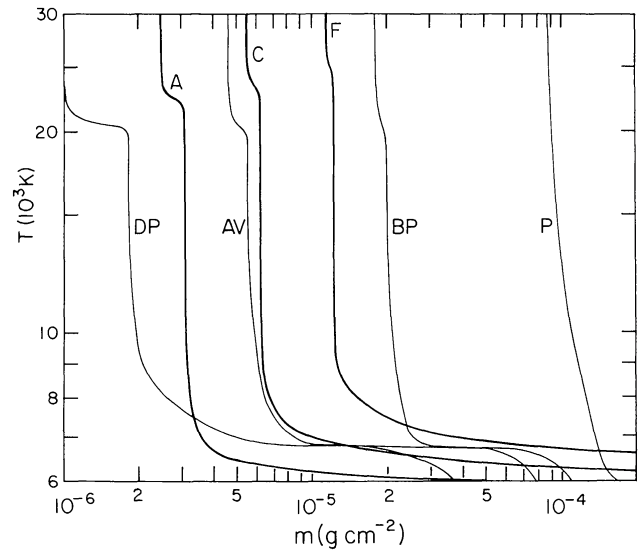


FIG. 44

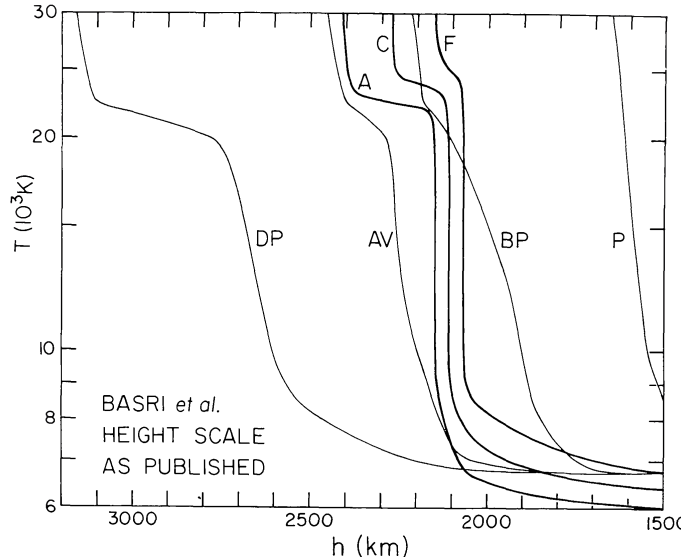


FIG. 45.—The Basri *et al.* temperature distributions as functions of height, as published, compared with our models A, C, and F

Basri *et al.* reduced the temperature in the low chromosphere to bring these higher  $\text{L}\alpha$  wing intensities into agreement with the lower observed intensities.

In the upper chromosphere and transition region our results are completely consistent with those of Basri *et al.* Figure 44 shows the temperature as a function of the column mass for their dark point (DP), average quiet Sun (AV), bright point (BP), and plage (P) models and our models A, C, and F. Their average model is in general agreement with our model C, while their dark point and bright point models are somewhat darker and brighter than our models A and F, respectively.

Basri *et al.* also find it necessary to introduce temperature plateaus above  $2 \times 10^4$  K. Their plateau widths are in good agreement with ours, but we locate the plateaus at somewhat higher temperatures.

In these semiempirical models the temperature stratification has been adjusted to obtain agreement between computed and observed spectra. These plateaus and other features of our one-dimensional temperature stratification may not apply directly to the interpretation of magnetically confined loops and other structures observed with high spatial resolution, but such average computed features may be useful in studying the average characteristics of the atmosphere. In § IX we discuss the possibility that the  $\text{L}\alpha$  line may first absorb energy carried by heat conduction from the corona down to the plateau region, and then deposit part of this energy in the chromosphere by radiative heating.

We conclude our comparison with the Basri *et al.* models by pointing out that the height values in their Tables 5–8 and their Figure 16 have been computed incorrectly, at least in the outer portions of their models. Figure 45 shows their published  $T(h)$  curves and ours plotted for comparison. These results are clearly incon-

sistent with those in Figure 44. This error in the computation of  $h$  does not affect their solution since they used  $m$  as their basic depth variable.

Basri (private communication) reports that it is no longer feasible to redetermine  $h$  from the computational data still available. We have therefore used our computed relationship between  $m$  and  $h$  to obtain  $T(h)$  from the dark point, average, and bright point  $T(m)$  distributions given by Basri *et al.* The results are plotted in Figure 46. Our computed relationship between  $m$  and  $h$  does not extend over a sufficiently wide range to permit a similar transformation of their plage  $T(m)$  distribution. In our comparison of  $T(h)$  curves in Figure 40 we have not corrected the original Basri *et al.* height scale.

Tripp, Athay, and Peterson (1978) compared observed and calculated profiles of the Si II and Si III lines in the EUV spectrum to investigate the distribution of temperature and microvelocity in the upper chromosphere and transition region. They found that the temperature distribution we proposed in Paper I gave calculated profiles in reasonably good agreement with their observed ones but that a modified variation of microvelocity with depth in the upper chromosphere and transition region, namely, 0.7 times the sound speed, gave better results than our values from Paper I. We have shown their microvelocity distribution in Figure 11.

As Tripp, Athay, and Peterson point out in their paper, our temperature distribution in Paper I is constrained to (1) preserve pressure continuity with the corona, (2) produce the observed self-reversals in  $\text{L}\alpha$  and  $\text{L}\beta$ , and (3) produce the observed Lyman continuum intensity. Model C of the present paper satisfies the same constraints and a further one: the integrated  $\text{L}\alpha$  and  $\text{L}\beta$  intensities are in much closer agreement

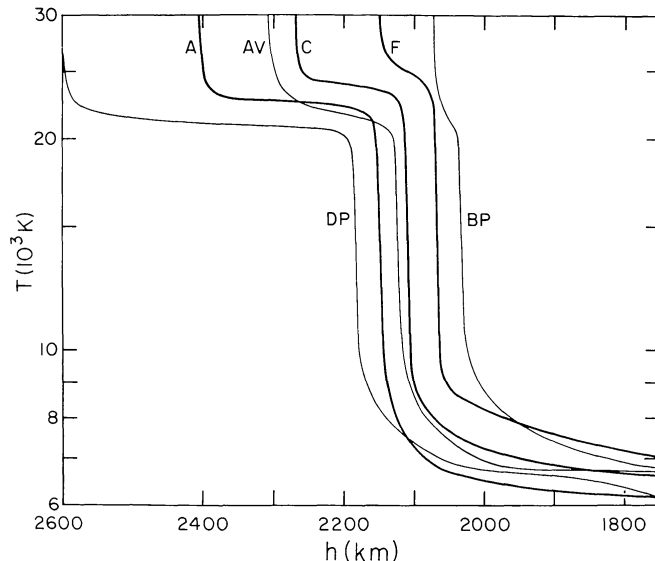


FIG. 46.—The Basri *et al.* quiet-Sun temperature distributions plotted on corrected height scales compared with models A, C, and F

with the observed values than before and are computed according to a more detailed physical theory. We expect model C to give results for the Si II and Si III lines which do not greatly differ from those found by Tripp, Athay, and Peterson with the model from Paper I.

Lites, Shine, and Chipman (1978) investigated the temperature structure of the upper chromosphere using center-to-limb measurements of the C II resonance lines at 133.5 nm. They found that these lines are extremely sensitive to the temperature and thickness of the plateau region and studied various possible choices for these two parameters. They considered not only the computed C II resonance lines in each case but also the computed L $\alpha$  and Lyman continuum intensities.

Lites, Shine, and Chipman found that the use of our model from Paper I led to C II intensities about a factor of 2 larger than observed. They noted that agreement with the observations could be obtained by reducing the plateau width by a factor of 2, but this led to a reduction of both the Lyman line and Lyman continuum intensities by the same factor. They also noted that the computed Lyman line and continuum intensities remain the same when the temperature of the plateau is lowered and its width is suitably increased but that the corresponding C II line intensities are reduced since they are more sensitive to the temperature than to the width of the plateau. In this way they found the best correspondence with their C II line observations, without changing the Lyman line and Lyman continuum intensities, by lowering the plateau temperature to 16,500 K and increasing its width by  $\sim 25\%$ .

Lites, Shine, and Chipman used a result found earlier by Milkey and Mihalas (1973a), that a detailed treatment of the L $\alpha$  partial redistribution problem gives hydrogen populations, L $\alpha$  core intensities, and Lyman

continuum intensities very close to those obtained when the wing transfer in L $\alpha$  is ignored and complete frequency redistribution is used in the L $\alpha$  Doppler core.

On the contrary, as shown in Figure 28, we have found that in the case of model C this approximation is less accurate than assuming the Lyman lines to be in detailed balance. If our results are correct, Lites, Shine, and Chipman may have calculated different L $\alpha$  and Lyman continuum intensities than they would have with a more accurate treatment of the L $\alpha$  line. A difficulty with this interpretation is that their calculated Lyman continuum intensities would be too large, whereas their computed values are in good agreement with the observed ones.

Another difference between our calculation and that of Lites, Shine, and Chipman is in the photoionization rates used in the two calculations. In § IV we explained how we obtained these rates, and listed the chromospheric radiation temperatures  $T_n$  defined by equations (10) and (12) corresponding to these rates, namely 4940, 4810, 4716, and 4738 K for  $n=2, 3, 4$ , and 5, respectively. Lites, Shine, and Chipman give 5060, 4770, 4550, and 4330 K for the same four continua. Effectively, we use a smaller radiation temperature for  $n=2$  but larger values for  $n=3, 4$ , and 5; we have not determined whether the computed Lyman continuum intensities increase or decrease as a result.

The C II calculations of Lites, Shine, and Chipman, as well as the Si II and Si III calculations of Tripp, Athay, and Peterson should be repeated with the models given here to determine whether the results are sensitive to changes in the models and whether the new models give better results. The C II and Si II calculations that we have carried out so far have been only schematic ones for the purpose of seeking all possible contributions to

the total radiative cooling rate plotted in Figure 49 of § IX.

### VIII. THE TEMPERATURE MINIMUM

In Figures 20 and 21 of § IV we found that in the case of wavelengths where the continuum intensity originates on the photospheric side of the temperature minimum our models predict less limb darkening than observed, while at wavelengths where the continuum intensity originates on the chromospheric side, less limb brightening than observed. Thus, our continuum source functions appear to be too flat on both sides of the temperature minimum. Note that any inhomogeneities would be expected to flatten the computed source function even more so that we must examine other possible causes of this discrepancy.

The flat nature of the continuum source function in this region is apparent in the panels of Figure 36 for  $\lambda = 168.1, 160.5, 157.5$ , and  $152.4$  nm. Note that in all cases the Planck function decreases more rapidly than the source function on the photospheric side of the temperature minimum and increases more rapidly on the chromospheric side. If each  $S$  were closer to  $B$  to a sufficient extent, we would match the observed center-to-limb behavior on both sides of the temperature minimum, but our computed values of the intensity and flux would fall below the observed ones. We would then choose higher temperatures in this region to raise the computed intensity and flux accordingly.

Thus, we could reconcile all three determinations of the minimum temperature, i.e., from (1) the Ca II and Mg II resonance lines, (2) the  $33-500\text{ }\mu\text{m}$  microwave continuum, and (3) the  $135-168$  nm UV continuum, using the higher temperature values indicated in the first two cases, if we could identify a mechanism leading to departure coefficients for Si and Fe which are closer to unity in the temperature-minimum region. These departure coefficients were shown in Figures 34 and 35.

One way to achieve this result is to increase the electron number density in the temperature-minimum region. The present  $n_e$  differs from that in Paper II in that we now solve the detailed non-LTE equations for Fe and Mg to obtain their contributions to  $n_e$ , while we assumed LTE in Paper II. As a result,  $n_e$  is somewhat larger at the temperature minimum, but not large enough in our present calculations to solve the problem stated above.

In Figure 47 we show the electron and proton number density distributions in the temperature-minimum region and the relative contributions to  $n_e$  from Fe, Mg, Si, and H. This figure should be considered a replacement of Figure 21 and the upper section of Figure 22 in Paper II.

A second way to drive Si and Fe populations closer to their LTE values is to increase the collision cross sections used for these two ions. However, the departure coefficients in question depend more on the photoionization

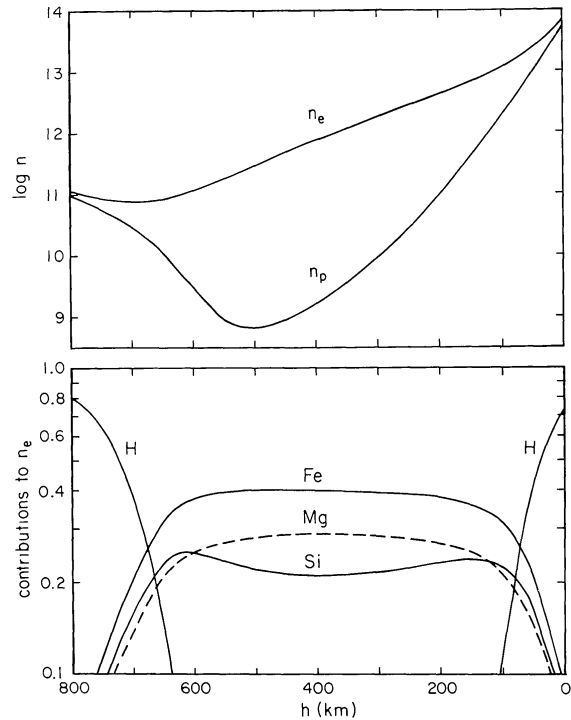


FIG. 47.—Electron density, proton density, and contributions to the electron density in the temperature-minimum region.

zation and recombination rates than on the collision rates. Thus, it seems unlikely that even order of magnitude increases in the collision cross sections would substantially change the results.

A third possibility is that we have to take account of the effect of the many spectral lines in the Si and Fe continua when we evaluate the photoionization rates, which are given by

$$R_{n\kappa} = 4\pi \int_{\nu_n}^{\infty} (h\nu)^{-1} \alpha_{\nu} J_{\nu} d\nu. \quad (20)$$

Here  $\alpha_{\nu}$  is the smoothly varying photoionization cross section, but the mean intensity  $J_{\nu}$  deviates from the continuum distribution in every spectral line. There seems to be a well-defined continuum between the various lines in the  $135-168$  nm range, but it may be inappropriate to use a continuum  $J_{\nu}$  in equation (20), as we have done, because of the possible line contributions. Suppose that, over a substantial fraction of the spectrum, line opacities exceed the continuous opacity and that, due to either scattering or conditions close to LTE, the source function associated with the lines is generally less than the line-free continuum source function that we have calculated. Then the photoionization rate will be reduced, and our continuum source function, which depends on this rate, will be reduced in turn. However, the emission lines which are also present could produce the opposite effect. The influence of the spectral lines in this region will be investigated in a subsequent paper.

Ayres (1978) studied the center-to-limb behavior of the first-overtone vibration-rotation bands of carbon monoxide and concluded that the observed properties of the solar CO spectrum suggests a temperature minimum value no higher than 4200 K. Thus, the way in which the cooler and hotter components of the temperature-minimum region affect different features of the observed spectrum continues to be an unresolved problem.

### IX. ENERGY BALANCE

If there were no heating or cooling of the solar atmosphere by various types of wave motions or other nonradiative mechanisms, then the sum of all net radiative gains and losses from the atmosphere would be zero. Conversely, in a steady state, the total net radiative loss as a function of depth for a given atmospheric model indicates the amount of nonradiative heating necessary to sustain the prescribed temperature structure. In this section we evaluate the net radiative losses from the chromosphere in the lines and continua that are important in cooling (and heating) the atmosphere.

In a line transition between upper and lower levels  $u$  and  $l$  the net radiative cooling rate is

$$h\nu[n_u(A_{ul}+B_{ul}\bar{J})-n_lB_{lu}\bar{J}]\equiv\Phi_{ul}, \quad (21)$$

where  $n_u$  and  $n_l$  are the upper and lower level number densities,  $A_{ul}$ ,  $B_{ul}$ , and  $B_{lu}$  are the Einstein emission and absorption coefficients, and

$$\bar{J}=\int\phi_\nu J_\nu d\nu, \quad (22)$$

where  $\phi_\nu$  is the line absorption coefficient normalized so that  $\int\phi_\nu d\nu=1$  and  $J_\nu$  is the mean intensity at the frequency  $\nu$  within the line. Equation (21) also can be written as

$$\Phi_{ul}=h\nu n_u A_{ul}\rho, \quad (23)$$

where  $\rho$  is the net radiative bracket (Thomas 1960), given by

$$\rho=1-\frac{\bar{J}}{S^L}. \quad (24)$$

The frequency-independent line source function  $S^L$  depends on the number densities and the statistical weights  $g_u$  and  $g_l$  according to

$$S^L=\frac{2h\nu^3}{c^2}\left[\frac{n_l}{n_u}\frac{g_u}{g_l}-1\right]^{-1}. \quad (25)$$

In Appendices A and B (eqs. [A28], [A29], [B42], and [B43]) we show that  $S^L$  is related to  $\bar{J}$  and the statistical-equilibrium parameters  $\epsilon$  and  $B^S$  by the equation

$$S^L=\frac{\bar{J}+\epsilon B^S}{1+\epsilon}. \quad (26)$$

Then we can write

$$\rho=\epsilon\left(\frac{B^S}{S^L}-1\right). \quad (27)$$

We use this equation for the calculation of each  $\rho$  (because it has better numerical properties than eq. [24]). The monochromatic line source function  $S_\nu^L$  is equal to  $S^L$  only if we assume complete frequency redistribution throughout the line. Equations (23) and (27) for  $\Phi_{ul}$  and  $\rho$  are general ones and are not restricted to this special case. For the L $\alpha$  and L $\beta$  lines and the resonance lines of Ca II and Mg II we use the partial-redistribution method described in Appendix A to compute  $S_\nu^L$ ,  $J_\nu$ , and  $S^L$ . Then we determine  $\rho$  and  $\Phi_{ul}$  as indicated above.

The net radiative cooling rate for the bound-free transition from continuum  $m$ , using notation from Appendix B, is

$$\begin{aligned} & n_\kappa(n_m^*/n_\kappa^*)4\pi\int_{\nu_m}^\infty a_m(\nu)\beta_\nu(\alpha_\nu+J_\nu)d\nu \\ & -n_m4\pi\int_{\nu_m}^\infty a_m(\nu)J_\nu d\nu \\ & =4\pi n_m\left[b_m^{-1}\int_{\nu_m}^\infty a_m(\nu)\beta_\nu(\alpha_\nu+J_\nu)d\nu\right. \\ & \left.-\int_{\nu_m}^\infty a_m(\nu)J_\nu d\nu\right]\equiv\Phi_m \end{aligned} \quad (28)$$

(here  $\alpha_\nu=2h\nu^3/c^2$  and  $\beta_\nu=\exp[-h\nu/kT]$ ). The photoionization rate is

$$R_{mk}=4\pi\int_{\nu_m}^\infty(h\nu)^{-1}a_m(\nu)J_\nu d\nu, \quad (29)$$

and in Appendix B we define the corresponding recombination parameter

$$R_{mk}^\dagger=4\pi\int_{\nu_m}^\infty(h\nu)^{-1}a_m(\nu)\beta_\nu(\alpha_\nu+J_\nu)d\nu. \quad (30)$$

When the above integrals are determined mostly by contributions close to the ionization limit  $\nu_m$ , we can write

$$\Phi_m\sim h\nu_m n_m(b_m^{-1}R_{mk}^\dagger-R_{mk}), \quad (31)$$

which is the same as

$$\Phi_m\sim h\nu_m(n_\kappa R_{km}-n_m R_{mk}). \quad (32)$$

We use equation (28) rather than these approximations in our calculations of  $\Phi_m$ .

In Figure 48 we plot the net radiative cooling rates per unit volume due to the lines and continua of hydrogen, computed from model C. Three general conclusions are apparent from these results: (1) the L $\alpha$  line gives the most important hydrogen cooling rate in the temperature range  $T>10^4$  K; (2) the L $\alpha$  cooling rate is substantial throughout the plateau region where  $2\times10^4<T<3\times10^4$  K; and (3) the total contribution due to all

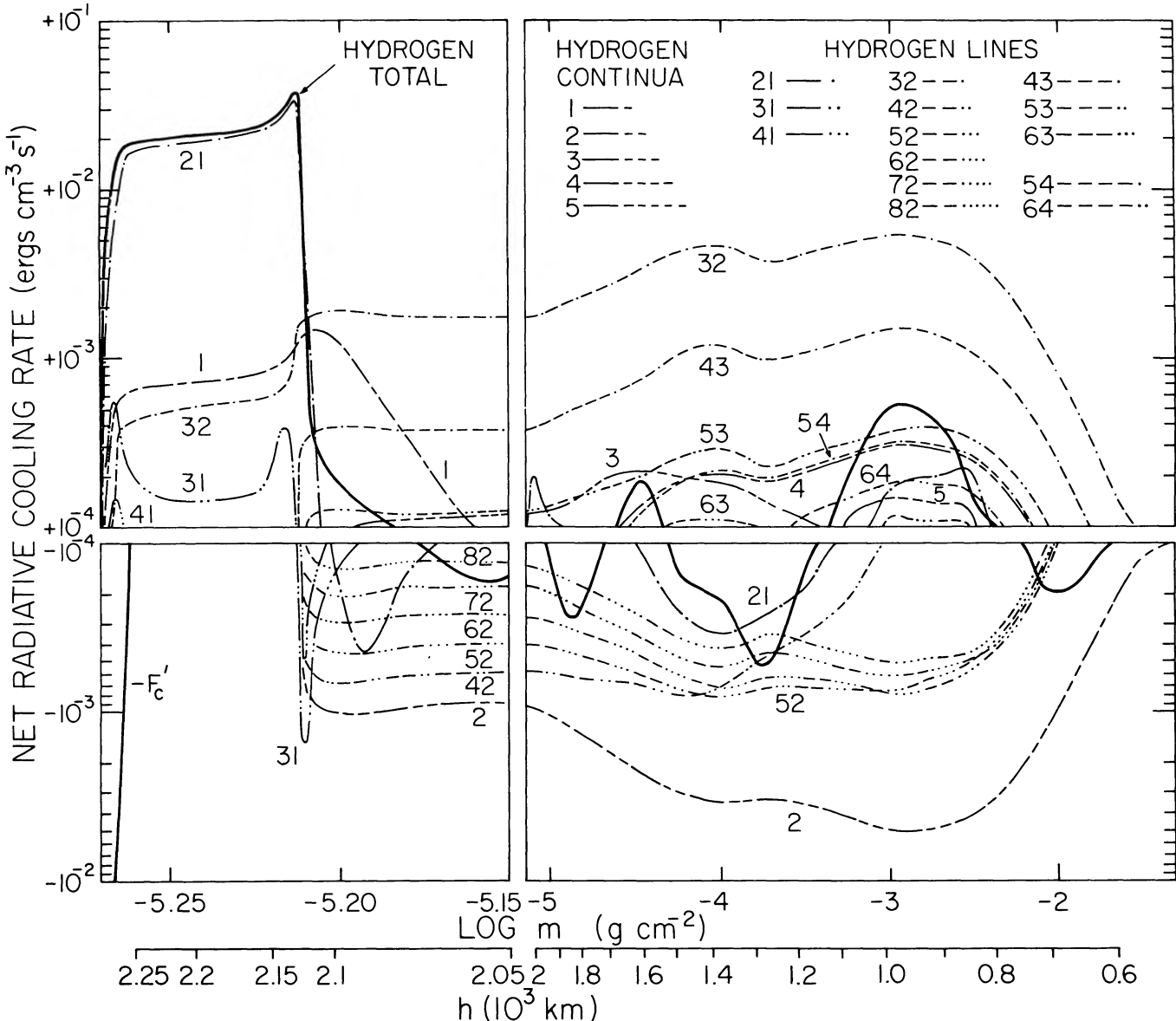


FIG. 48.—Net radiative cooling rates for hydrogen transitions calculated from model C. The negative of the conductive flux gradient is shown in the lower left panel.

hydrogen transitions, plotted as a heavy line in the figure, is small throughout the chromosphere.

This last result arises because net heating in the Balmer continuum approximately cancels the cooling due to H $\alpha$ . The negative values of  $\Phi_2$  for the Balmer continuum can be understood as follows. The statistical equilibrium equation for level 2 is

$$\begin{aligned} n_2(A_{21}\rho_{21} + C_{21} + C_{23} + C_{24} + \dots + R_{2\kappa} + C_{2\kappa}) \\ = n_1C_{12} + n_3(A_{32}\rho_{32} + C_{32}) + n_4(A_{42}\rho_{42} + C_{42}) \\ + \dots + n_\kappa(R_{\kappa 2} + C_{\kappa 2}). \end{aligned} \quad (33)$$

In the chromosphere the optical thickness of the L $\alpha$  line is so great that

$$n_2(A_{21}\rho_{21} + C_{21}) \sim n_1C_{12}, \quad (34)$$

as can be seen from the values listed in Table 27 for a representative depth in the chromosphere. This table also shows that the predominant terms on the left side of equation (33) are  $n_2(C_{23} + R_{2\kappa})$  and that the right side is essentially  $n_3(A_{32}\rho_{32} + C_{32}) + \delta + n_\kappa R_{\kappa 2}$ , where

$$\delta = \sum_{i=4}^8 n_i(A_{i2}\rho_{i2} + C_{i2}). \quad (35)$$

TABLE 27  
PARAMETERS IN THE  $n=2$  STATISTICAL EQUILIBRIUM EQUATION AT  
 $h=1065$  km ( $T=6040$  K) FOR MODEL C

$A_{21} \rho_{21} = 8.83$
$C_{21} = 516$
$C_{23} = 1420$
$C_{24} = 70.6$
$R_{2\kappa} = 8083$
$C_{2\kappa} = 8.47$
$n_2 (A_{21} \rho_{21} + C_{21}) = 1.072(8)$
$n_1 C_{12} = 1.076(8)$
$n_2 (C_{23} + R_{2\kappa}) = 1.96(9)$
$A_{32} \rho_{32} = 5.05(5)$
$C_{32} = 2.38(4)$
$n_3 (A_{32} \rho_{32} + C_{32}) = 1.65(9)$
$n_4 (A_{42} \rho_{42} + C_{42}) = -3.80(7)$
$n_5 (A_{52} \rho_{52} + C_{52}) = -1.56(8)$
$n_6 (A_{62} \rho_{62} + C_{62}) = -1.45(8)$
$n_7 (A_{72} \rho_{72} + C_{72}) = -1.13(8)$
$n_8 (A_{82} \rho_{82} + C_{82}) = -9.07(7)$
$R_{\kappa 2} = 9.75(-3)$
$C_{\kappa 2} = 1.96(-6)$
$n_{\kappa} R_{\kappa 2} = 8.66(8)$
$\sum n (A \rho + C) + n_{\kappa} R_{\kappa 2} = 1.97(9)$

It then follows that

$$n_{\kappa} R_{\kappa 2} - n_2 R_{2\kappa} \sim -n_3 A_{32} \rho_{32} + \delta', \quad (36)$$

where

$$\delta' = n_2 C_{23} - n_3 C_{32} - \delta. \quad (37)$$

From equations (23) and (32) the net radiative rates for the Balmer continuum and the H $\alpha$  line have approximately the same absolute value but opposite sign. Thus, the cooling of the gas due to net emission in H $\alpha$  is effectively canceled by net absorption of photospheric radiation in the Balmer continuum. This result is contrary to the generally held view that H $\alpha$  is one of the largest contributors to the net cooling rate in the chromosphere and that the Balmer continuum provides additional cooling. See Athay (1976, Table IX-1).

In § V we discussed the radiative heating due to L $\alpha$  in the upper chromosphere near  $\tau_{LyC}=10^2$ . This is the region in Figure 48 where the 21 curve reaches maximum negative values near  $\log m=-4$ . In this quiet-Sun model the L $\alpha$  heating does not appear to be important. Note, however, the dominant role of L $\alpha$  in removing

energy from the transition region, and the possibility that some of this energy could reappear at chromospheric heights in other hydrogen transitions, either to heat the gas radiatively or to offset, at least in part, other radiative cooling losses.

Part of the energy in the transition region that the L $\alpha$  line could absorb is that carried by thermal conduction from the corona to the lower portions of the transition region. The conductive flux gradient  $F'_c$ , in ergs cm $^{-3}$  s $^{-1}$ , is given by

$$F'_c = 10^{-6} \frac{d}{dx} \left( T^{5/2} \frac{dT}{dx} \right) \\ = \frac{2}{7} \times 10^{-6} \frac{d^2}{dx^2} (T^{7/2}), \quad (38)$$

where  $x$  is height in cm. The values of  $F'_c$  that correspond to the temperature distribution of model C are given in Table 28. In Figure 48 we plot the negative of  $F'_c$  (since this is a heating rate). In this model the conductive heating is clearly insufficient to match the L $\alpha$  cooling except in the narrow layer where  $T>3\times 10^4$  K. However, in the brighter components of the quiet Sun the regions  $T>3\times 10^4$  K are located deeper in the atmosphere, so that the effective  $F'_c$  distribution could be much more extended if interactions between the brightness components were taken into account.

We now consider the cooling rates due to constituents other than hydrogen. In Figure 49 we plot the total hydrogen contribution along with the net radiative cooling rates due to the Ca II K, H, and infrared triplet lines, the Mg II  $h$  and  $k$  lines, the H $^-$  ion, the Mg I  $b$  and Na I D lines, the lines Si II  $\lambda 181.6$  nm and He I  $\lambda 58.4$  nm, and the continua of Si I at 152.4 nm and 168.1 nm, Fe I at 157.5 nm and 176.8 nm, Mg I at 162.2 nm, and He I

TABLE 28  
CONDUCTIVE FLUX GRADIENT IN THE  
TRANSITION REGION OF MODEL C

$\log m$	$h$ (km)	$T(10^3$ K)	$F'_c$ (ergs cm $^{-3}$ s $^{-1}$ )
-5.268	2280	50	5.4(-2)
-5.267	2274	37	1.1(-2)
-5.266	2271	32	6.0(-3)
-5.265	2267	28	2.1(-3)
-5.264	2263	25.5	1.1(-3)
-5.262	2255	24.5	4.6(-5)
-5.253	2230	24.2	1.9(-6)
-5.243	2200	24	-1.3(-6)

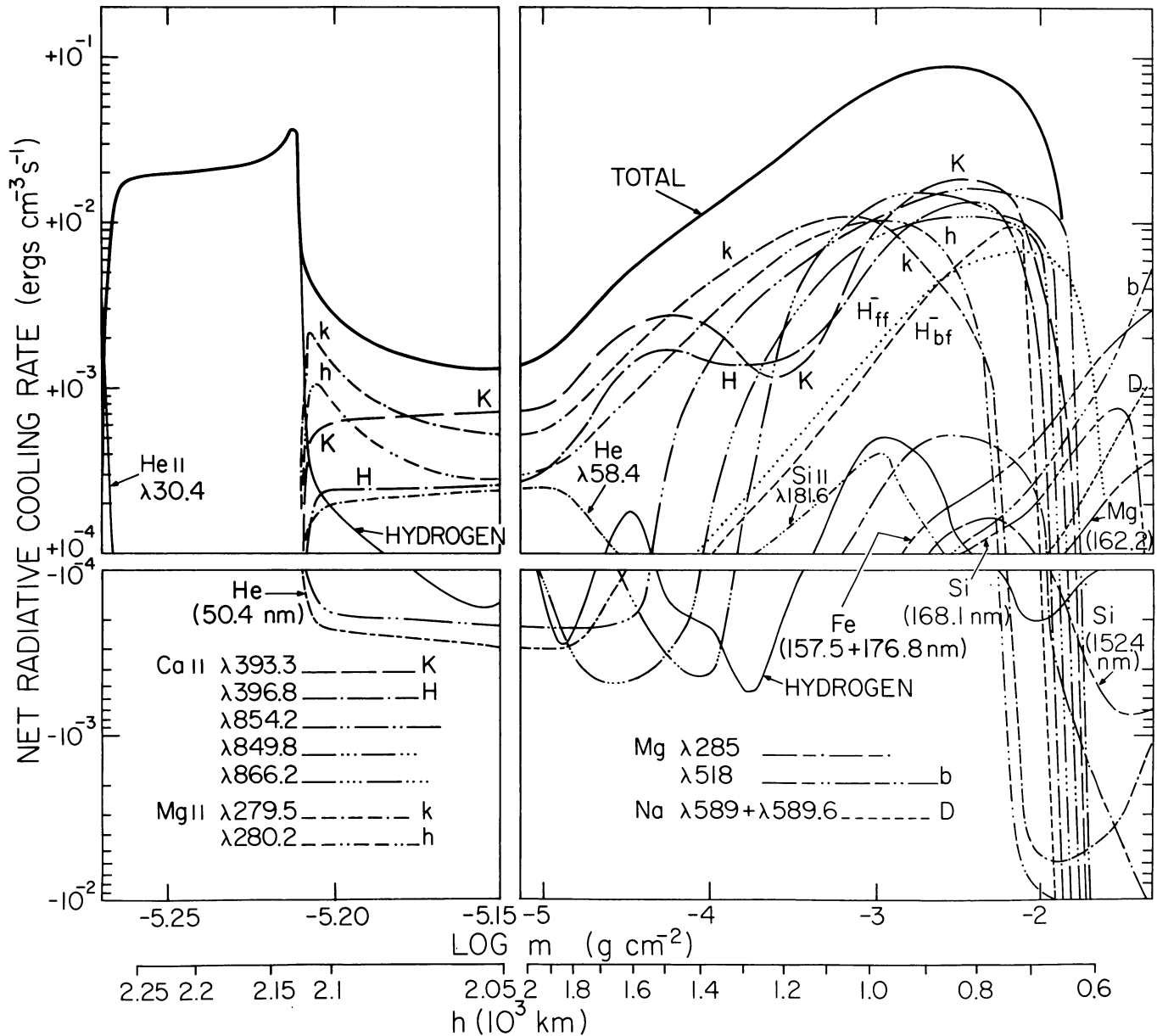


FIG. 49.—Net radiative cooling rates for Ca II, Mg II, H<sup>-</sup>, H, and other constituents calculated from model C

at 50.4 nm, all calculated from model C. In all the calculations we have carried out for various atoms and ions, namely, H, H<sup>-</sup>, neutral and ionized He, C, Si, Mg, Ca, and O, and neutral Fe, Al, Na, and B, these are the only line and continuum rates that appear to exceed  $10^{-4}$  ergs  $\text{cm}^{-3}$   $\text{s}^{-1}$  in absolute value.

The calculated net radiative cooling rates for the Ca II and Mg II resonance lines are quite sensitive to the convergence and internal consistency of our numerical solution. Some of our preliminary solutions gave maximum rates for these lines 2 to 3 times larger than those shown in Figure 49.

In Table 29 we list the integrated net cooling rates  $\int \Phi dh$  for the Ca II and Mg II lines, L $\alpha$ , and H<sup>-</sup>, i.e., the area under each  $\Phi$  as a function of  $h$  in Figure 49. Negative values of  $\Phi$  in the temperature-minimum region are assumed to be zero in each integral. Athay (1976, Table IX-1) estimates that the contributions to  $\int \Phi dh$  have the following order of importance: Balmer continuum, H $\alpha$ , Ca II IR triplet, Mg II, Ca II K and H, Fe I lines, and Na I D. Athay states, however, that these estimates are not based on detailed computations of the net energy loss or gain in the bound-free continua. The order we determine is listed in Table 29.

TABLE 29

INTEGRATED NET RADIATIVE COOLING  
RATES IN UNITS OF  $10^5$  ergs  $\text{cm}^{-2}$   $\text{s}^{-1}$

Ca II K .....	7
$\lambda$ 854.2 .....	7
$\lambda$ 849.8 .....	6
$\lambda$ 866.2 .....	5
H .....	5
Mg II $k$ .....	5
$h$ .....	4
L $\alpha$ .....	3
$\text{H}^-_{\text{bf}}$ .....	2
$\text{H}^-_{\text{ff}}$ .....	2
Total.....	46

Linsky and Ayres (1978) estimated that the observed quiet-Sun emission components of the Mg II  $k$  and Ca II K flux profiles imply integrated net cooling rates of  $6 \times 10^5$  and  $2.4 \times 10^5$  ergs  $\text{cm}^{-2}$   $\text{s}^{-1}$ , respectively, while the corresponding values we obtain are  $5 \times 10^5$  and  $7 \times 10^5$  ergs  $\text{cm}^{-2}$   $\text{s}^{-1}$  for these two lines. It should be emphasized that there can be significant differences between the rates obtained from observed emission fluxes and those calculated from an atmospheric model. In determining the integrated cooling rates from the observed emission components, the emission is measured relative to the hypothetical central flux profile that would be produced in the absence of a chromospheric temperature rise. When the emission features are weak, as in the case of the Ca II K line, this underlying flux profile is uncertain. Note also that the Ca II and Mg II profiles computed from model C are not in close agreement with the observed ones, as shown in Figures 23 and 24. Thus, further calculations are needed to verify the rates listed in Table 29.

In the low chromosphere we find that (1) the  $\text{H}^-$  cooling rate is much less than the contributions due to the Ca II lines, (2) the  $\text{H}^-$  bound-free cooling rate never exceeds  $0.01$  ergs  $\text{cm}^{-3}$   $\text{s}^{-1}$ , and (3) this bound-free rate is comparable to the  $\text{H}^-$  free-free cooling rate. Contrary to this result, Ulmschneider and Kalkofen (1978) find a maximum value of  $\sim 0.12$  ergs  $\text{cm}^{-3}$   $\text{s}^{-1}$  for the  $\text{H}^-$  bound-free rate.

In view of this discrepancy we give the explicit equations for the bound-free  $\text{H}^-$  cooling rate. Let

$$\int J = 4\pi \int a(\nu) J_\nu d\nu, \quad (39)$$

and

$$\int L = 4\pi \int a(\nu) L_\nu d\nu, \quad (40)$$

where

$$L_\nu = \beta_\nu (\alpha_\nu + J_\nu). \quad (41)$$

Equation (28) for  $\text{H}^-$  then can be written as

$$\Phi_{\text{H}^-} = n_{\text{H}^-}^* \int L - n_{\text{H}^-} \int J. \quad (42)$$

This expression is identical to that given by Kalkofen and Ulmschneider (1979) in their Appendix I. Equation (42) also is given by

$$\Phi_{\text{H}^-} = n_{\text{H}^-}^* (\int L - b_{\text{H}^-} \int J), \quad (43)$$

since

$$b_{\text{H}^-} = n_{\text{H}^-} / n_{\text{H}^-}^*. \quad (44)$$

Now let

$$\int J / \nu = 4\pi \int (h\nu)^{-1} a(\nu) J_\nu d\nu, \quad (45)$$

and

$$\int L / \nu = 4\pi \int (h\nu)^{-1} a(\nu) L_\nu d\nu. \quad (46)$$

Using equation (108) of Paper I (see also Gebbie and Thomas 1970 and Jordan 1977)  $b_{\text{H}^-}$  is calculated from

$$b_{\text{H}^-} = \frac{\int L / \nu + r}{\int J / \nu + r}, \quad (47)$$

where

$$r = 2 \times 10^{-9} \left( \frac{n_{\text{H}_1}}{1 + \delta} + \theta^{-3/2} n_e \right), \quad (48)$$

$$\delta = 38\theta^{1/2} e^{1.736\theta} n_e / n_{\text{H}_1}, \quad (49)$$

and

$$\theta = 5040/T. \quad (50)$$

We substitute equation (47) into equation (43) to obtain an expression for  $\Phi_{\text{H}^-}$  which depends on the  $J$  and  $L$  integrals and on  $T$ ,  $n_e$ , and  $n_{\text{H}_1}$ . The final result is

$$\Phi_{\text{H}^-} = \frac{n_{\text{H}^-}^* (X + rY)}{\int J / \nu + r}, \quad (51)$$

where

$$X = \int L \int J / \nu - \int L / \nu \int J, \quad (52)$$

and

$$Y = \int L - \int J. \quad (53)$$

Here,

$$n_{\text{H}^-}^* = 2.89 \times 10^{-22} n_{\text{H}_1} n_e \theta^{3/2} e^{1.736\theta}. \quad (54)$$

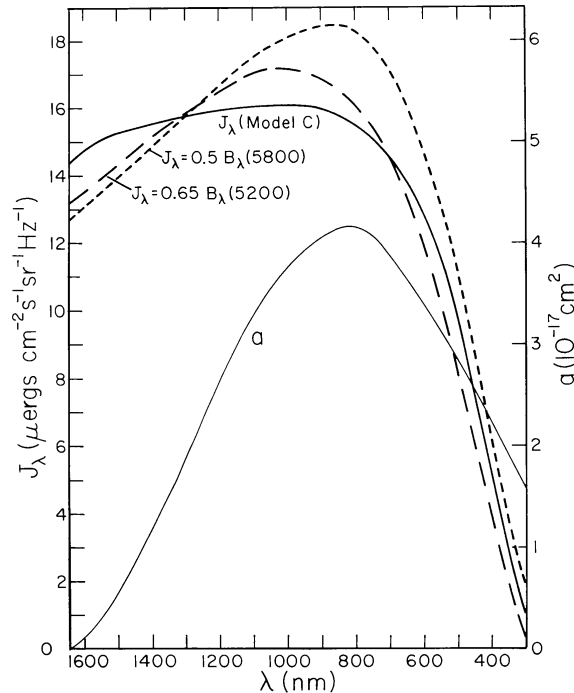


FIG. 50.—The mean intensity as a function of wavelength used in the  $H^-$  calculations for model C compared with the values obtained by two analytic expressions of the form  $J_\nu = WB_\nu(T)$ . The bound-free cross section  $\alpha$  also is plotted.

The heavy curve in Figure 50 shows the mean intensity  $J$ , for model C, as a function of wavelength which was used to obtain the  $H^-$  cooling rate in Figure 49. The short-dash and long-dash curves in Figure 50 correspond to the analytical expressions  $J_\nu = 0.5B_\nu(5800)$  and  $J_\nu = 0.65B_\nu(5200)$ , where  $B_\nu(T)$  is the Planck function. The first of these expressions is the one adopted by Ulmschneider and Kalkofen (1978), and the second is a somewhat better fit to the solid curve. The cross section  $\alpha(\nu)$  also is plotted in Figure 50 as a light solid line.

Equation (51) can be evaluated unambiguously given  $T$ ,  $n_e$ ,  $n_{H1}$ , and one of these analytical expressions for  $J_\nu$ . In Table 30 we list the temperature and density parameters for model C at various heights from  $h = 515$  km (the temperature minimum) to  $h = 1065$  km, as well as the computed values of  $\Phi_{H^-}$  from equation (51), and  $b_{H^-}$  from equation (47). The values obtained using  $J_\nu = 0.65B_\nu(5200)$  are close to those shown in Figure 49, while the values obtained with  $J_\nu = 0.5B_\nu(5800)$  are considerably smaller. In neither case do we find a maximum as large as the value  $0.12 \text{ ergs cm}^{-2} \text{ s}^{-1}$  of Ulmschneider and Kalkofen. It should be noted that these authors assume that  $H^-$  is in radiative equilibrium at the temperature minimum, a condition we have not imposed. The parameters that we used to determine  $\Phi_{H^-}$  shown in Figure 49 are listed in Tables 25 and 26 of § VI.

Larger values of  $\Phi_{H^-}$  are determined from models having higher temperatures. Table 31 shows the values

computed from model F. For  $J_\nu = 0.65B_\nu(5200)$ ,  $\Phi_{H^-}$  reaches a maximum of  $0.049 \text{ ergs cm}^{-3} \text{ s}^{-1}$  which is still smaller than the maximum value obtained by Ulmschneider and Kalkofen.

In the temperature minimum region where  $T$  is less than  $\sim 5000$  K our calculations indicate net radiative heating by  $H^-$  and the Ca II and Mg II lines, resulting in a total  $\Phi$  that is strongly negative. Ayres (1980) also has found that  $\Phi_{H^-}$  is negative in the temperature-minimum region. Such net heating in the temperature-minimum region may be due to our omission of radiative cooling by numerous weak atomic and molecular lines. The adoption of higher minimum temperatures causes the total  $\Phi$  to be less negative, but in test cases we have found that the total rate remains negative for minimum temperatures as high as 4800 K.

Ulmschneider and Kalkofen assumed that (1) the net radiative cooling is due to  $H^-$  alone, and (2) the atmosphere is in radiative equilibrium at the temperature minimum. Thus, they normalized the  $H^-$  cooling rate so that  $\Phi_{H^-} = 0$  at the temperature minimum. Their  $\Phi_{H^-}$  calculation can be viewed as an attempt to use the  $H^-$  equations alone to estimate the total net radiative cooling rate.

The bound-free and free-free  $H^-$  cooling rates can be compared as follows. We can write equation (42) as

$$\Phi_{H^-_{bf}} = 4\pi \int \kappa(\nu)_{bf} \left( \frac{L_\nu}{b_{H^-}} - J_\nu \right) d\nu, \quad (55)$$

while

$$\Phi_{H^-_{ff}} = 4\pi \int \kappa(\nu)_{ff} (B_\nu - J_\nu) d\nu. \quad (56)$$

The term  $L_\nu/b_{H^-} - J_\nu$  is about an order of magnitude smaller than  $B_\nu - J_\nu$  because of the dependence of  $b_{H^-}$  on  $L_\nu$  and  $J_\nu$  in equation (47). The free-free opacity  $\kappa(\nu)_{ff}$  is about an order of magnitude smaller than the bound-free opacity  $\kappa(\nu)_{bf}$ . Thus  $\Phi_{H^-_{bf}}$  is comparable to  $\Phi_{H^-_{ff}}$  as shown in Figure 49.

In a subsequent paper we will give detailed descriptions of the other contributing curves in Figure 49, present corresponding results for our five other models, show the sensitivity of the results to the parameters in our partial-redistribution equations, and discuss the implications of the results for theories of nonradiative heating.

We are grateful to the referee and Dimitri Mihalas for their helpful comments. This research was supported by NASA grant NSG-7054 and NASA contract NAS-5-3949.

TABLE 30  
H<sup>-</sup> PARAMETERS FOR MODEL C

<i>h</i>	<i>T</i>	<i>n<sub>e</sub></i>	<i>n<sub>H1</sub></i>	<i>b<sub>H<sup>-</sup></sub></i>	<i>Φ<sub>H<sup>-</sup></sub></i>	<i>b<sub>H<sup>-</sup></sub></i>	<i>Φ<sub>H<sup>-</sup></sub></i>
515	4170	2.49(11)	2.10(15)	0.894	-2.353	0.923	-1.614
555	4230	1.73(11)	1.38(15)	0.868	-0.874	0.906	-0.584
605	4420	1.11(11)	8.12(14)	0.869	-0.193	0.923	-0.109
655	4730	8.11(10)	4.79(14)	0.957	-0.030	1.034	-0.003
705	5030	7.69(10)	2.93(14)	1.118	-0.002	1.227	0.011
755	5280	8.86(10)	1.86(14)	1.313	.003	1.460	0.011
855	5650	1.06(11)	8.13(13)	1.703	.002	1.926	0.006
905	5755	1.05(11)	5.54(13)	1.838	.001	2.088	0.004
980	5925	1.04(11)	3.14(13)	2.058	.001	2.349	0.002
1065	6040	9.34(10)	1.70(13)	2.215	.000	2.535	0.001

TABLE 31  
H<sup>-</sup> PARAMETERS FOR MODEL F

<i>h</i>	<i>T</i>	<i>n<sub>e</sub></i>	<i>n<sub>H1</sub></i>	<i>b<sub>H<sup>-</sup></sub></i>	<i>Φ<sub>H<sup>-</sup></sub></i>	<i>b<sub>H<sup>-</sup></sub></i>	<i>Φ<sub>H<sup>-</sup></sub></i>
500	4440	3.18(11)	2.48(16)	0.941	-2.073	0.968	-1.113
550	4500	2.08(11)	1.53(15)	0.923	-0.657	0.965	-0.319
600	4690	1.43(11)	9.26(14)	0.957	-0.135	1.011	-0.021
650	4975	1.24(11)	5.65(14)	1.066	-0.006	1.146	0.042
700	5280	1.41(11)	3.53(14)	1.262	0.020	1.379	0.049
750	5540	1.74(11)	2.29(14)	1.500	0.023	1.661	0.043
855	5890	2.09(11)	9.98(13)	1.940	0.010	2.190	0.019
905	6020	2.13(11)	6.88(13)	2.125	0.007	2.413	0.013
980	6190	2.10(11)	3.99(13)	2.375	0.004	2.710	0.007
1065	6315	1.89(11)	2.21(13)	2.566	0.002	2.935	0.003

## APPENDIX A

THE LYMAN- $\alpha$  LINE WITH PARTIAL REDISTRIBUTION

## I. LINE BROADENING AND LINE OPACITY

We assume that the line absorption coefficient is given by

$$\kappa_{\nu}^L = n_1 \frac{h\nu_0}{4\pi} B_{12} \frac{1}{\Delta\nu_D} \phi(a, y), \quad (\text{A1})$$

where  $\phi(a, y)$  is the Voigt function

$$\phi(a, y) = \frac{a}{\pi^{3/2}} \int_{-\infty}^{+\infty} \frac{e^{-z^2} dz}{a^2 + (z-y)^2}. \quad (\text{A2})$$

Here  $y = \Delta\nu / \Delta\nu_D$  and  $a = \delta / \Delta\nu_D$ , where  $\delta$  is the damping parameter given below and  $\Delta\nu_D$  is the Doppler width

$$\Delta\nu_D = \frac{\nu_0}{c} \left( \frac{2kT}{M} + V^2 \right)^{1/2}. \quad (\text{A3})$$

In the line wings where  $\Delta\nu \gg \Delta\nu_D$ , equation (A1) reduces to

$$\kappa_\nu^L = n_1 \frac{h\nu_0}{4\pi} B_{12} \frac{\delta}{\pi(\Delta\nu)^2}. \quad (\text{A4})$$

The damping parameter  $\delta$  for the L $\alpha$  line is given by the sum

$$\delta = \frac{1}{4\pi} (\Gamma_{\text{rad}} + \Gamma_{\text{Stark}} + \Gamma_{\text{res}}), \quad (\text{A5})$$

where the radiative damping coefficient is

$$\Gamma_{\text{rad}} = A_{21} = 4.70 \times 10^8. \quad (\text{A6})$$

In the case of resonance broadening we use the formula of Lortet and Roueff (1969),

$$\Gamma_{\text{res}} = \frac{2}{\sqrt{3}} \frac{e^2 f_{12}}{m\nu_0} n_1 = 4.93 \times 10^5 \bar{n}_1, \quad (\text{A7})$$

where

$$\bar{n}_1 = n_1 / 10^{13}.$$

Stark broadening has contributions from both electrons and protons,

$$\Gamma_{\text{Stark}} = \Gamma_e + \Gamma_p, \quad (\text{A8})$$

and we adopt the expressions for  $\Gamma_e$  and  $\Gamma_p$  derived by Roussel-Dupré (1980) based on the theoretical work of Vidal, Cooper, and Smith (1970), Omont, Smith, and Cooper (1972), and Cooper (1979). Also see Appendix A of Basri *et al.* (1979).

It is convenient to express  $\Gamma_e$  in terms of  $\bar{n}_e = n_e / 5 \times 10^{10}$ ,  $\bar{T} = T / 6500$ ,  $\xi_1 = 0.0014 \bar{n}_e^{1/2}$ , and  $\xi_2 = 44.5 \bar{T}$ . In the impact regime  $\Delta\lambda(\text{\AA}) < \xi_1$ , which is well within the L $\alpha$  Doppler core,  $\Gamma_e$  is given by

$$\Gamma_e^{\text{impact}} = 1.26 \times 10^6 \bar{n}_e \bar{T}^{-1/2} \left[ 1 - 0.051 \ln \left( \bar{n}_e / \bar{T}^2 \right) \right]. \quad (\text{A9})$$

In the Holtzman limit  $\Delta\lambda(\text{\AA}) > \xi_2$ , which is far in the line wings,  $\Gamma_e$  is given by

$$\Gamma_e^{\text{Holtz}} = \Gamma_e^{\text{impact}} \eta \left( \xi_2 / \Delta\lambda \right)^{1/2}, \quad (\text{A10})$$

where

$$\eta = \frac{0.071}{1 - 0.051 \ln \left( \bar{n}_e / \bar{T}^2 \right)}. \quad (\text{A11})$$

TABLE 32  
L $\alpha$  BROADENING PARAMETERS

$\Delta\lambda_I$	0.5	1	2	5	10
$h$ .....	1605	1380	1180	1065	905
$T$ .....	6440	6280	6150	6040	5755
$n_e$ .....	6.0(10)	7.6(10)	8.1(10)	9.3(10)	1.0(11)
$n_1$ .....	5.8(11)	2.2(12)	7.8(12)	1.7(13)	5.5(13)
$\Gamma_e^{\text{impact}}$ ...	1.5(6)	1.9(6)	2.0(6)	2.3(6)	2.6(6)
$\Gamma_e$ .....	7.2(5)	7.9(5)	7.2(5)	6.3(5)	5.2(5)
$\Gamma_p$ .....	1.0(6)	9.0(5)	6.8(5)	4.9(5)	3.7(5)
$\Gamma_{\text{Stark}}$ ....	1.7(6)	1.7(6)	1.4(6)	1.1(6)	8.9(5)
$\Gamma_{\text{res}}$ .....	2.9(4)	1.1(5)	3.9(5)	8.4(5)	2.7(6)
$\Gamma_E$ .....	1.8(6)	1.8(6)	1.8(6)	2.0(6)	3.6(6)
$\Gamma_{\text{rad}}$ .....	4.7(8)	4.7(8)	4.7(8)	4.7(8)	4.7(8)
$\gamma_s$ .....	0.9963	0.9962	0.9962	0.9958	0.9924

In the intermediate regime  $\xi_1 \leq \Delta\lambda \leq \xi_2$ , where the wavelengths of interest occur,  $\Gamma_e$  is assumed to vary linearly with  $\log(\Delta\lambda/\xi_1)$  between the value  $\Gamma_e^{\text{impact}}$  at  $\Delta\lambda = \xi_1$  and  $\Gamma_e^{\text{Holtz}}$  at  $\Delta\lambda = \xi_2$ ; i.e.,

$$\Gamma_e = \Gamma_e^{\text{impact}} \left[ 1 + (\eta - 1) \frac{\log(\Delta\lambda/\xi_1)}{\log(\xi_2/\xi_1)} \right]. \quad (\text{A12})$$

For protons, the Holtzman limit equation is valid for wavelengths  $\Delta\lambda(\text{\AA}) > 0.024\bar{T}$  (i.e.,  $\xi_2 m_e/m_p$ ), and

$$\Gamma_p = 5.90 \times 10^5 \bar{n}_e (\Delta\lambda)^{-1/2}. \quad (\text{A13})$$

(In this equation we use  $n_e$  since  $n_p \approx n_e$  in the atmospheric region of interest.)

We now give representative values for  $\Gamma_e$  and  $\Gamma_p$  to assess the relative importance of  $\Gamma_{\text{rad}}$ ,  $\Gamma_{\text{Stark}}$ , and  $\Gamma_{\text{res}}$ . In our model C the largest contributions to the disk-center L $\alpha$  intensity at  $\Delta\lambda = 0.5, 1, 2, 5$ , and  $10 \text{\AA}$  occur at heights 1605, 1380, 1180, 1065, and 905 km, respectively. The values of  $T$ ,  $n_e$ , and  $n_1$  at these heights are given in Table 32 with the corresponding values of  $\Gamma_e^{\text{impact}}$ ,  $\Gamma_e$ ,  $\Gamma_p$ ,  $\Gamma_{\text{Stark}}$ , and  $\Gamma_{\text{res}}$ . We also list  $\Gamma_E = \Gamma_{\text{Stark}} + \Gamma_{\text{res}}$  and the scattering ratio

$$\gamma_s = \frac{\Gamma_{\text{rad}}}{\Gamma_{\text{rad}} + \Gamma_E} \quad (\text{A14})$$

which will be discussed later.

Since  $\Gamma_{\text{Stark}} \ll \Gamma_{\text{rad}}$ , the line absorption coefficient is unaffected by the value and wavelength dependence of  $\Gamma_{\text{Stark}}$ . This parameter is an important component of the scattering ratio, but  $\Gamma_E$  is practically constant throughout the region in which  $\Gamma_{\text{Stark}}$  exceeds  $\Gamma_{\text{res}}$ .

Table 32 indicates that  $1.5 \times 10^6$  is a representative value for  $\Gamma_{\text{Stark}}$ . From equations (A8) through (A13) we define the function  $s(n_e, T, \Delta\lambda)$  such that

$$\Gamma_{\text{Stark}} = 1.5 \times 10^6 s(n_e, T, \Delta\lambda). \quad (\text{A15})$$

Equation (A4) then becomes

$$\kappa_{\nu}^L = \kappa_{\nu}^{\text{rad}} + \kappa_{\nu}^{\text{Stark}} + \kappa_{\nu}^{\text{res}}, \quad (\text{A16})$$

where

$$\kappa_{\nu}^{\text{rad}} = 1.32 \times 10^{-12} \bar{n}_1 y^{-2}, \quad (\text{A17})$$

$$\kappa_{\nu}^{\text{Stark}} = 4.22 \times 10^{-15} s \bar{n}_1 y^{-2}, \quad (\text{A18})$$

$$\kappa_{\nu}^{\text{res}} = 1.40 \times 10^{-15} \bar{n}_1^2 y^{-2}, \quad (\text{A19})$$

and where we have defined  $y = \Delta\nu/10^{15}$ .

According to Sando, Doyle, and Dalgarno (1969), equation (A19) does not properly describe the resonance-broadening absorption in the  $\text{L}\alpha$  wing at wavelengths greater than  $\sim 130$  nm (see also Dalgarno and Sando 1973). Sando and Wormhoudt (1973) have carried out quantum-mechanical calculations to determine  $\kappa_{\nu}^{\text{res}}$ , and we represent their results by the approximate formula

$$\kappa_{\nu}^{\text{res}} = \left( \frac{0.14}{y^2} + 3.0 \right) m_{\lambda} \times 10^{-14} \bar{n}_1^2, \quad (\text{A20})$$

where

$$m_{\lambda} = \begin{cases} 1 & \lambda \leq 162 \text{ nm}, \\ e^{-0.05(\lambda - 162)} & \lambda > 162 \text{ nm}. \end{cases} \quad (\text{A21})$$

We use equation (A20) in place of equation (A19). The line absorption coefficient for  $\Delta\nu \gg \Delta\nu_D$  then may be written as

$$\kappa_{\nu}^L = \left[ \frac{132}{y^2} + \left( \frac{0.14}{y^2} + 3.0 \right) m_{\lambda} \bar{n}_1 + \frac{0.42}{y^2} s \right] 10^{-14} \bar{n}_1, \quad (\text{A22})$$

or effectively,

$$\kappa_{\nu}^L = (132 y^{-2} + 3.0 m_{\lambda} \bar{n}_1) 10^{-14} \bar{n}_1. \quad (\text{A23})$$

The resonance-broadening term in this equation never becomes a primary opacity contribution to the quiet-Sun spectrum: at those wavelengths, e.g., 160 nm, where  $\bar{n}_1 > 44 y^{-2}$  at the depth of formation, other opacities such as the bound-free opacity of Si I greatly exceed  $\kappa_{\nu}^L$ .

## II. THE LINE SOURCE FUNCTION

The line source function  $S_{\nu}^L$  and the line absorption coefficient  $\kappa_{\nu}^L$  appear in the transfer equation as follows:

$$\mu \frac{dI_{\nu}}{dz} = \kappa_{\nu}^L (I_{\nu} - S_{\nu}^L) + \sigma (I_{\nu} - J_{\nu}) + \kappa^c (I_{\nu} - S^c). \quad (\text{A24})$$

This equation is a general one which applies to any line, not just to  $\text{L}\alpha$ . Here  $\kappa^c$  is the continuum absorption coefficient,  $S^c$  is the continuum source function,  $\sigma$  is the continuum scattering coefficient, and  $J_{\nu}$  is the mean intensity. We write  $\kappa_{\nu}^L = \kappa^L \phi_{\nu}$ , where  $\int \phi_{\nu} d\nu = 1$ . Thus,  $\phi_{\nu} = \phi(a, y)/\Delta\nu_D$  (cf. eq. [A2]).

As discussed by Heasley and Kneer (1976), the line source function can be written as

$$S_{\nu}^L = S^L + \frac{F(\nu)}{1 + \epsilon}, \quad (\text{A25})$$

where  $S^L$  is the frequency-independent line source function given by

$$S^L = \frac{2h\nu^3}{c^2} \left[ \frac{n_1}{n_2} \frac{g_2}{g_1} - 1 \right]^{-1}, \quad (\text{A26})$$

and

$$F(\nu) = \frac{1}{\phi_{\nu}} \int [R(\nu', \nu) - \phi_{\nu'} \phi_{\nu}] J_{\nu'} d\nu'. \quad (\text{A27})$$

Here  $R(\nu', \nu)$  is the angle-averaged redistribution function obtained with an assumed isotropic radiation field.

The parameter  $\epsilon$  in equation (A25) is defined as follows. As we show in Appendix B, the statistical equilibrium equations can be used to derive the following relationship between  $S^L$  and  $\bar{J} = \int \phi_\nu J_\nu d\nu$ :

$$S^L = \frac{\bar{J} + [R_p(1-\beta)/A]B}{1 + (R_d - \beta R_p)/A}. \quad (\text{A28})$$

Here  $B$  is the Planck function,  $A$  is the Einstein coefficient for spontaneous emission, and  $\beta = \exp(-h\nu/kT)$ . The parameters  $R_p$  and  $R_d$  represent the rates of photon production and destruction, respectively. In the simplest case of a two-level atom without a continuum,  $R_p$  and  $R_d$  both reduce to  $C_{21}$ , the collision rate between levels 2 and 1. In general, these two parameters depend on ionization and recombination rates and on other bound-bound radiative and collisional rates. We express equation (A28) as

$$S^L = \frac{\bar{J} + \epsilon B^S}{1 + \epsilon}, \quad (\text{A29})$$

where

$$\epsilon = (R_d - \beta R_p)/A, \quad (\text{A30})$$

and

$$B^S = B \left[ \frac{R_p(1-\beta)}{R_d - \beta R_p} \right]. \quad (\text{A31})$$

Our treatment of stimulated emission is approximate; Heasley and Kneer (1976) give a more detailed formulation based on the fact that stimulated emission is coherent in both the atom's and the observer's frame of reference.

Following Omont, Smith, and Cooper (1972) and Milkey and Mihalas (1973a) we write

$$R(\nu', \nu) = \gamma_s R^{\text{II}}(\nu', \nu) + (1 - \gamma_s) \phi_{\nu'} \phi_\nu, \quad (\text{A32})$$

where  $\gamma_s$  is the frequency-independent probability for coherent scattering in the atom's frame (eq. [A14]) and  $R^{\text{II}}(\nu', \nu)$  is the redistribution function for radiation damping with coherence in the atom's rest frame. Then equation (A27) becomes

$$F(\nu) = \frac{\gamma_s}{\phi_\nu} \int [R^{\text{II}}(\nu', \nu) - \phi_{\nu'} \phi_\nu] J_{\nu'} d\nu'. \quad (\text{A33})$$

We adopt the approximation for  $R^{\text{II}}(\nu', \nu)$  given by Kneer (1975):

$$R^{\text{II}}(\nu', \nu) = \langle a \rangle_\nu \phi_{\nu'} \delta(\nu' - \nu) + (1 - a_{\nu', \nu}) \phi_{\nu'} \phi_\nu, \quad (\text{A34})$$

where

$$\langle a \rangle_\nu = \int a_{\nu', \nu} \phi_{\nu'} d\nu'. \quad (\text{A35})$$

This relationship between  $a_{\nu', \nu}$  and  $\langle a \rangle_\nu$  insures that  $\int R^{\text{II}}(\nu', \nu) d\nu' = \phi_\nu$ . The function  $a_{\nu', \nu}$  is defined as follows. Let  $x$  be the larger of  $|\nu - \nu_0|/\Delta\nu_D$  and  $|\nu' - \nu_0|/\Delta\nu_D$ , where  $\nu_0$  is the line-center frequency and  $\Delta\nu_D$  is the Doppler width. Then  $a_{\nu', \nu} = f(x)$ , where  $f$  is zero within the Doppler core, rising to unity in the far wings. Kneer (1975) found that  $f(x) = 1 - \exp[-(x-2)^2/2]$  for  $x \geq 2$  gave a computed profile for the Ca II K line in reasonable agreement with the observed profile. We have found that the computed L $\alpha$  profile is sensitive to the choice of  $f(x)$  but that the computed Ca II K and Mg II k profiles are relatively insensitive to  $f(x)$ . We obtain best agreement with the L $\alpha$  line and retain good agreement with the Ca II K and Mg II k lines, when the Doppler core region, where  $f=0$ , extends to about  $x=6$ . We have determined tabular values for  $f(x)$  which give a computed L $\alpha$  profile in reasonable agreement with the observed one. These values are listed in Table 33 and are used in all of the partial-redistribution calculations in this paper.

TABLE 33  
TABULAR VALUES FOR  $f(x)$

$x$	$f$
$\leq 5.5 \dots$	0
6.5 ....	0.1
7.0 ....	0.35
8.0 ....	0.75
10.0 ....	0.9
$\geq 15.0 \dots$	1.0

Equation (A33) then reduces to

$$F(\nu) = \gamma_s (\langle a \rangle_\nu J_\nu - \langle aJ \rangle_\nu), \quad (\text{A36})$$

where

$$\langle aJ \rangle_\nu = \int a_{\nu'} \phi_{\nu'} d\nu'. \quad (\text{A37})$$

Equation (A25) for the line source function finally becomes

$$S_\nu^L = S^L + \frac{\gamma_s}{1+\epsilon} (\langle a \rangle_\nu J_\nu - \langle aJ \rangle_\nu). \quad (\text{A38})$$

In the Doppler core,  $\langle a \rangle_\nu$  and  $\langle aJ \rangle_\nu$  are small so that  $S_\nu^L \sim S^L$ . We obtain this result throughout the line if  $\gamma_s$  is small. In the line wings  $\langle a \rangle_\nu \rightarrow 1$ ,  $\langle aJ \rangle_\nu \rightarrow \bar{J}$ , and from equation (A29) it follows that

$$S_\nu^L \rightarrow \frac{\gamma_s J_\nu + (1-\gamma_s) \bar{J} + \epsilon B^S}{1+\epsilon}. \quad (\text{A39})$$

This equation shows that  $S_\nu^L \sim J_\nu$  in the wings when  $\gamma_s$  is close to unity and  $\epsilon \ll 1$ .

In our calculations we modify equation (A14) for  $\gamma_s$  so that

$$\gamma_s = \left[ \text{smaller of } \frac{\Gamma_{\text{rad}}}{\Gamma_{\text{rad}} + \Gamma_E} \text{ and } \gamma_{\max} \right]. \quad (\text{A40})$$

This upper limit is introduced to account for multilevel processes in addition to those in the derivation of Omont, Smith, and Cooper (1972) which is based on a two level atom. Yelnik and Voslamber (1979) show that inelastic collisions can enhance the amount of redistribution estimated by Omont, Smith, and Cooper. See also Cooper and Ballagh (1978). Vardavas and Cram (1974) suggest that  $\gamma_{\max}$  could be 0.99 (Zanstra 1941) or 0.8 (Edmonds 1955).

In the final two sections of this appendix we describe the method we use to solve the radiative transfer and statistical equilibrium equations when the partial-redistribution parameters given above are included.

### III. CALCULATION OF $J_\nu$

According to equation (A38), the line source function  $S_\nu^L$  depends on both  $S^L$  (equation A29) and  $J_\nu$ . Given  $S^L$ , we need to solve the transfer equation (A24) to obtain  $J_\nu$ . For this purpose we write equation (A38) as

$$S_\nu^L = Q_\nu + v_\nu J_\nu, \quad (\text{A41})$$

where

$$v_\nu = \frac{\gamma_s \langle a \rangle_\nu}{1+\epsilon}. \quad (\text{A42})$$

We express  $Q_\nu$  in the form

$$Q_\nu = (1 - \langle a \rangle_\nu) Q_\nu^{\text{core}} + \langle a \rangle_\nu Q_\nu^{\text{wing}}, \quad (\text{A43})$$

where

$$Q_\nu^{\text{core}} = S^L - \frac{\gamma_s \langle aJ \rangle_\nu}{1 + \epsilon}, \quad (\text{A44})$$

and

$$Q_\nu^{\text{wing}} = \frac{\tilde{J}_\nu + \epsilon B^S}{1 + \epsilon}, \quad (\text{A45})$$

where

$$\tilde{J}_\nu = \int (1 - \gamma_s a_{\nu', \nu}) J_{\nu'} \phi_{\nu'} d\nu'. \quad (\text{A46})$$

Note that  $Q_\nu^{\text{core}}$  and  $Q_\nu^{\text{wing}}$  are equivalent expressions for  $Q_\nu$ , having different numerical properties with regard to the core and wing of the line, respectively. Equation (A41) indicates explicitly the primary dependence of  $S_\nu^L$  on  $J_\nu$ . The  $J_\nu$  terms in  $Q_\nu$  are of secondary importance, and we evaluate  $Q_\nu$  from  $S^L$  and the values of  $J_\nu$  from a previous stage in our iterative solution.

The transfer equation is then

$$\mu \frac{dI_\nu}{dz} = \kappa_\nu^L (I_\nu - Q_\nu - v_\nu J_\nu) + \sigma (I_\nu - J_\nu) + \kappa^c (I_\nu - S^c), \quad (\text{A47})$$

where only  $I_\nu$  and  $J_\nu$  are unknown. We let

$$d\tau_\nu = (\kappa_\nu^L + \sigma + \kappa^c) dz, \quad (\text{A48})$$

and

$$S_\nu = \frac{(\kappa_\nu^L v_\nu + \sigma) J_\nu + \kappa_\nu^L Q_\nu + \kappa^c S^c}{\kappa_\nu^L + \sigma + \kappa^c}. \quad (\text{A49})$$

The transfer equation then has the standard form

$$\mu \frac{dI_\nu}{d\tau_\nu} = I_\nu - S_\nu. \quad (\text{A50})$$

We select  $L$  discrete depths in the atmosphere and use this equation to express  $J_\nu$  at depth  $i$  in terms of the values of  $S_\nu$  at all of the discrete depths  $j$ . Using  $k$  as a frequency subscript we can write

$$J_{ik} = S_{ik} + \sum_{j=1}^L W_{ijk}^{-1} S_{jk}, \quad (\text{A51})$$

where the  $\Lambda - 1$  weighting coefficients depend only on the optical depths  $\tau_{ik}$ ; see Avrett and Loeser (1969).

Equation (A49) can be expressed as

$$S_\nu - r_\nu (J_\nu - S_\nu) = B_\nu^\dagger, \quad (\text{A52})$$

where

$$r_\nu = \frac{\kappa_\nu^L v_\nu + \sigma}{\kappa_\nu^L (1 - v_\nu) + \kappa^c}, \quad (\text{A53})$$

and

$$B_\nu^\dagger = \frac{\kappa_\nu^L Q_\nu + \kappa^c S^c}{\kappa_\nu^L (1 - v_\nu) + \kappa^c}. \quad (\text{A54})$$

We obtain  $S_{ik}$ ,  $i=1,2,\dots,L$  from the set of equations

$$S_{ik} - r_{ik} \sum_{j=1}^L W_{ijk}^{-1} S_{jk} = B_{ik}^\dagger, \quad (\text{A55})$$

and  $J_{ik}$  follows from equation (A51) or (A52).

#### IV. CALCULATION OF $S^L$

The line source function  $S_\nu^L$  depends on  $S^L$  and  $J_\nu$  according to equation (A38), and in equation (A41) we expressed  $S_\nu^L$  as

$$S_\nu^L = Q_\nu + v_\nu J_\nu. \quad (\text{A56})$$

Since we are now dealing with the explicit evaluation of  $S^L$ , we write equation (A38) in the form

$$S_\nu^L = S^L + z_\nu J_\nu, \quad (\text{A57})$$

where

$$z_\nu = v_\nu \left( 1 - \frac{\langle aJ \rangle_\nu}{\langle a \rangle_\nu J_\nu} \right). \quad (\text{A58})$$

Now  $z_\nu$  is assumed to be a given function of frequency and depth based on the values of  $J_\nu$  obtained in a previous iterative step of the calculation.

In direct analogy with equation (A49) we obtain

$$S_\nu = \frac{(\kappa_\nu^L z_\nu + \sigma) J_\nu + \kappa_\nu^L S^L + \kappa^c S^c}{\kappa_\nu^L + \sigma + \kappa^c}. \quad (\text{A59})$$

From the transfer equation we again have

$$J_{ik} = S_{ik} + \sum_{j=1}^L W_{ijk}^{-1} S_{jk}. \quad (\text{A60})$$

We replace the first term on the right side of this equation by  $S_{ik}$  from equation (A59), and then combine the two  $J_{ik}$  terms. As a result,

$$J_{ik} = S_i^L (1 - f_{ik}^\alpha) + f_{ik}^\beta S_i^c + f_{ik}^\gamma \sum_{j=1}^N W_{ijk}^{-1} S_{jk}, \quad (\text{A61})$$

where

$$f_{ik}^\alpha = \frac{\kappa_i^c - \kappa_{ik}^L z_{ik}}{\kappa_{ik}^L (1 - z_{ik}) + \kappa_i^c}, \quad (\text{A62})$$

$$f_{ik}^\beta = \frac{\kappa_i^c}{\kappa_{ik}^L (1 - z_{ik}) + \kappa_i^c}, \quad (\text{A63})$$

and

$$f_{ik}^\gamma = \frac{\kappa_{ik}^L + \sigma_i + \kappa_i^c}{\kappa_{ik}^L (1 - z_{ik}) + \kappa_i^c}. \quad (\text{A64})$$

We write  $\bar{J} = \int \phi_\nu J_\nu d\nu$  as  $\bar{J}_i = \sum_{k=1}^K A_k \phi_{ik} J_{ik}$  where  $\sum_{k=1}^K A_k \phi_{ik} = 1$ . Then

$$\bar{J}_i = S_i^L (1 - \delta'_i) + \delta_i S_i^c + H_i, \quad (\text{A65})$$

where

$$\delta'_i = \sum_{k=1}^K A_k \phi_{ik} f_{ik}^\alpha, \quad (\text{A66})$$

$$\delta_i = \sum_{k=1}^K A_k \phi_{ik} f_{ik}^8, \quad (\text{A67})$$

and

$$H_i = \sum_{j=1}^L \sum_{k=1}^K A_k \phi_{ik} f_{ik}^\gamma W_{ijk}^{-1} S_{jk}. \quad (\text{A68})$$

The above expression for  $\bar{J}_i$  is combined with the statistical equilibrium equation

$$S_i^L = \frac{\bar{J}_i + \epsilon_i B_i^S}{1 + \epsilon_i}, \quad (\text{A69})$$

giving the result

$$(\epsilon_i + \delta'_i) S_i^L - H_i = \epsilon_i B_i^S + \delta_i S_i^c. \quad (\text{A70})$$

The function  $H_i$  depends on the values of  $S_j^L$  according to

$$H_i = \sum_{j=1}^L M_{ij} S_j^L + L_i, \quad (\text{A71})$$

where

$$M_{ij} = \sum_{k=1}^K \frac{A_k \phi_{ik} f_{ik}^\gamma \kappa_{jk}^L W_{ijk}^{-1}}{\kappa_{jk}^L + \sigma_j + \kappa_j^c}, \quad (\text{A72})$$

and

$$L_i = \sum_{j=1}^L \sum_{k=1}^K \frac{A_k \phi_{ik} f_{ik}^\gamma p_{jk} W_{ijk}^{-1}}{\kappa_{jk}^L + \sigma_j + \kappa_j^c}. \quad (\text{A73})$$

In this last equation,

$$p_{jk} = (\kappa_{jk}^L z_{jk} + \sigma_j) J_{jk} + \kappa_j^c S_j^c. \quad (\text{A74})$$

The values of  $S_i^L$  are then obtained from the set of linear equations

$$S_i^L - \frac{1}{\epsilon_i + \delta'_i} \sum_{j=1}^L M_{ij} S_j^L = \tilde{B}_i, \quad i = 1, 2, \dots, L, \quad (\text{A75})$$

where

$$\tilde{B}_i = \frac{\epsilon_i B_i^S + \delta_i S_i^c + L_i}{\epsilon_i + \delta'_i}. \quad (\text{A76})$$

TABLE 34

L $\alpha$  PARTIAL-REDISTRIBUTION PARAMETERS  
 $S_\nu^L = Q_\nu + v_\nu J_\nu$

$\Delta\lambda_I$	0	0.2	0.5	1	2	5	10
$h$	2267	2160	1605	1380	1180	1065	905
$m$	5.43(-6)	5.90(-6)	3.41(-5)	1.01(-4)	3.11(-4)	6.30(-4)	1.84(-3)
$T$	28000	23500	6440	6280	6150	6040	5755
$\epsilon$	1.66(-5)	1.08(-5)	9.56(-6)	1.00(-5)	1.04(-5)	1.08(-5)	1.12(-5)
$\delta'$	2.83(-6)	5.87(-6)	4.84(-7)	2.99(-7)	2.04(-7)	1.97(-7)	2.11(-7)
$\gamma_s$	9.80(-1)	9.80(-1)	9.80(-1)	9.80(-1)	9.80(-1)	9.80(-1)	9.80(-1)
$\Delta\lambda = 0$							
$v_\nu$	1.60(-5)	1.69(-5)	3.23(-5)	3.42(-5)	3.58(-5)	3.71(-5)	3.93(-5)
0.45	1.60(-5)	1.69(-5)	8.37(-1)	8.81(-1)	8.91(-1)	8.97(-1)	9.06(-1)
0.58	5.54(-2)	1.45(-1)	9.23(-1)	9.38(-1)	9.49(-1)	9.57(-1)	9.69(-1)
0.77	7.41(-1)	7.93(-1)	9.80(-1)	9.80(-1)	9.80(-1)	9.80(-1)	9.80(-1)
1.10	9.11(-1)	9.30(-1)	9.80(-1)	9.80(-1)	9.80(-1)	9.80(-1)	9.80(-1)
3.87	9.80(-1)	9.80(-1)	9.80(-1)	9.80(-1)	9.80(-1)	9.80(-1)	9.80(-1)
5.91	9.80(-1)	9.80(-1)	9.80(-1)	9.80(-1)	9.80(-1)	9.80(-1)	9.80(-1)
$\Delta\lambda = 0$							
$J_\nu$	1.76(-8)	1.51(-7)	9.43(-9)	3.84(-9)	1.15(-9)	6.71(-10)	2.41(-10)
0.45	7.55(-9)	7.68(-9)	8.02(-9)	4.10(-9)	1.16(-9)	6.65(-10)	2.37(-10)
0.58	3.14(-9)	3.19(-9)	4.25(-9)	3.50(-9)	1.21(-9)	6.54(-10)	2.25(-10)
0.77	8.23(-10)	8.30(-10)	1.09(-9)	1.29(-9)	1.02(-9)	6.18(-10)	2.05(-10)
1.10	4.04(-10)	4.06(-10)	5.45(-10)	6.61(-10)	6.50(-10)	5.09(-10)	1.85(-10)
3.87	6.32(-11)	6.32(-11)	6.66(-11)	6.70(-11)	6.47(-11)	6.22(-11)	4.82(-11)
5.91	3.30(-11)	3.30(-11)	3.40(-11)	3.36(-11)	3.17(-11)	3.02(-11)	2.44(-11)
$S^L$							
	1.85(-8)	1.51(-7)	9.68(-9)	3.81(-9)	1.15(-9)	6.70(-10)	2.40(-10)
$\Delta\lambda = 0$							
$Q_\nu$	1.85(-8)	1.51(-7)	9.43(-9)	3.84(-9)	1.15(-9)	6.71(-10)	2.41(-10)
0.45	1.85(-8)	1.51(-7)	1.54(-9)	4.55(-10)	1.26(-10)	6.93(-11)	2.25(-11)
0.58	1.75(-8)	1.29(-7)	7.30(-10)	2.39(-10)	5.88(-11)	2.89(-11)	7.36(-12)
0.77	5.29(-9)	3.16(-8)	1.89(-10)	7.68(-11)	2.31(-11)	1.34(-11)	4.81(-12)
1.10	2.28(-9)	1.09(-8)	1.89(-10)	7.68(-11)	2.31(-11)	1.34(-11)	4.81(-12)
3.87	1.05(-9)	3.42(-9)	1.89(-10)	7.68(-11)	2.31(-11)	1.34(-11)	4.81(-12)
5.91	1.05(-9)	3.42(-9)	1.89(-10)	7.68(-11)	2.31(-11)	1.34(-11)	4.81(-12)
$\Delta\lambda = 0$							
$S_\nu^L$	1.85(-8)	1.51(-7)	9.43(-9)	3.84(-9)	1.15(-9)	6.71(-10)	2.41(-10)
0.45	1.85(-8)	1.51(-7)	8.25(-9)	4.07(-9)	1.16(-9)	6.66(-10)	2.38(-10)
0.58	1.77(-8)	1.30(-7)	4.65(-9)	3.52(-9)	1.20(-9)	6.55(-10)	2.26(-10)
0.77	5.90(-9)	3.22(-8)	1.25(-9)	1.34(-9)	1.03(-9)	6.19(-10)	2.06(-10)
1.10	2.65(-9)	1.13(-8)	7.23(-10)	7.24(-10)	6.60(-10)	5.12(-10)	1.86(-10)
3.87	1.11(-9)	3.48(-9)	2.54(-10)	1.42(-10)	8.64(-11)	7.44(-11)	5.21(-11)
5.91	1.08(-9)	3.45(-9)	2.22(-10)	1.10(-10)	5.41(-11)	4.30(-11)	2.87(-11)
$B^S$							
	4.19(-5)	3.68(-5)	9.61(-9)	3.69(-9)	1.13(-9)	6.71(-10)	2.42(-10)
$\tilde{B}$							
	3.58(-5)	2.38(-5)	8.61(-9)	3.41(-9)	1.03(-9)	6.34(-10)	2.33(-10)
$B$							
	3.28(-3)	1.45(-3)	2.31(-9)	1.44(-9)	9.70(-10)	6.83(-10)	2.59(-10)
$(1 - \gamma_s)J$							
	6.96(-10)	3.97(-10)	9.19(-14)	3.69(-14)	1.18(-14)	7.25(-15)	2.71(-15)
sum							
	1.05(-9)	3.42(-9)	1.94(-10)	7.62(-11)	2.30(-11)	1.34(-11)	4.80(-12)

The values of  $J_{ik}$  enter the solution in the expressions for  $L_i$  and  $z_{ik}$  and are obtained by the equations given in the preceding section, which in turn depend upon  $S_i^L$ . We find that these iterative steps converge rapidly. In deriving equation (A75) we have incorporated the effects of partial redistribution into the integral equation method of solution formulated originally by Athay and Skumanich (1967); see also Avrett (1971).

For reference we include a table listing parameters that enter our determination of the L $\alpha$  source function  $S_\nu^L$  at selected depths and frequencies. In Table 34 the columns under the values of  $\Delta\lambda_I = 0$  to 10 give various atmospheric parameters at the depth producing the largest contribution to the intensity at  $\Delta\lambda_I$  Å from the line center. The functions  $v_\nu$ ,  $J_\nu$ ,  $Q_\nu$ , and  $S_\nu^L$  listed in the table depend on frequency as well as depth, and we give the calculated values at  $\Delta\lambda = 0, 0.45, \dots, 5.91$ , also in Å measured from the line center.

The function  $v_\nu$  from equation (A42) is a measure of the amount of coherent scattering at any depth and frequency. In the core of the line  $v_\nu \ll 1$ , while  $v_\nu \sim \gamma_s$  in the line wings (when  $\epsilon \ll 1$ ).

In the line core the function  $Q_\nu$  from equation (A43) is approximately equal to the frequency-independent line source function  $S^L$ , and in the wings  $Q_\nu$  is approximately  $(1 - \gamma_s)\bar{J} + \epsilon B^S$  as indicated in the last three rows of the table. The mean intensity  $J_\nu$  is calculated as we have described above. Then  $S_\nu^L = Q_\nu + v_\nu J_\nu$ .

## APPENDIX B

### SUPPLEMENTARY LEVELS IN THE EQUATIONS OF STATISTICAL EQUILIBRIUM

#### I. THE LYMAN CONTINUUM PARAMETERS $\epsilon_1$ AND $\epsilon_2$

We write the statistical equilibrium equation for the continuum as

$$n_\kappa \left( \sum_{l=1}^N P_{\kappa l} + Q_s \right) = \sum_{l=1}^N n_l P_{l\kappa}, \quad (\text{B1})$$

where

$$Q_s = \sum_{l=N+1}^{N'} \left( P_{\kappa l} - \frac{n_l}{n_\kappa} P_{l\kappa} \right), \quad (\text{B2})$$

and where each  $P$  is the sum of a radiative rate  $R$  and a collisional rate  $C$ . We deal with levels 1 through  $N$  explicitly and treat levels  $N+1$  through  $N'$  as supplementary levels. The supplementary levels are assumed to be in equilibrium with the continuum. The collisional terms then drop out of the equation for  $Q_s$ , and

$$Q_s = \sum_{l=N+1}^{N'} \left( R_{\kappa l} - \frac{n_l^*}{n_\kappa^*} R_{l\kappa} \right). \quad (\text{B3})$$

We write the bound level equations as

$$n_m \left( \sum_{\substack{l=1 \\ l \neq m}}^N P_{ml} + P_{mk} \right) = \sum_{\substack{l=1 \\ l \neq m}}^N n_l P_{lm} + n_k (P_{km} + f_m Q_s). \quad (\text{B4})$$

The fractions  $f_m$  are such that

$$\sum_{m=1}^N f_m = 1. \quad (\text{B5})$$

Thus, we retain the property that the sum of equations (B4) for  $l=1$  to  $N$  reduces to the continuum equation (B1).

We select the values of  $f_m$  as follows. The net radiative rates from levels  $>2$  to levels 1 and 2 tend to be negative or very small at depths near  $\tau=1$  in the Lyman continuum. The additional radiative recombination is thus unlikely to affect the two lowest levels directly, and we set  $f_1=f_2=0$ . We choose  $f_m$ ,  $m>2$  in proportion to the values  $\sum_{l=N+1}^{12} A_{lm}$ ,  $m=3, 4, \dots, N$ . Then for a three level atom  $f_3=1$ , for a five level atom  $f_3=0.33$ ,  $f_4=0.31$ ,  $f_5=0.36$ , and for eight levels the values of  $f_3$  to  $f_8$  are 0.19, 0.16, 0.14, 0.14, 0.16, and 0.21. The effect of choosing model atoms with different numbers of levels is discussed in § V.

The photoionization and radiative recombination rates are given by

$$R_{l\kappa} = 4\pi \int_{v_l}^{\infty} \frac{d\nu}{h\nu} a_l(\nu) J_\nu, \quad (\text{B6})$$

and

$$R_{\kappa l} = (n_l^*/n_\kappa^*) R_{l\kappa}^\dagger, \quad (\text{B7})$$

where

$$R_{lk}^\dagger = 4\pi \int_{\nu_l}^{\infty} \frac{d\nu}{h\nu} a_l(\nu) \beta_\nu (\alpha_\nu + J_\nu). \quad (B8)$$

Here  $\alpha_\nu = 2h\nu^3/c^2$ ,  $\beta_\nu = \exp(-h\nu/kT)$ , and

$$\frac{n_l^*}{n_k^*} = n_e \left( \frac{h^2}{2\pi mkT} \right)^{3/2} \frac{g_l}{2U_k} \exp(h\nu_{kl}/kT). \quad (B9)$$

Equation (B1) for  $l=1$  then may be written as

$$n_k \left[ P_{k1} + \frac{n_1^*}{n_k^*} (P_{kL} + \sigma) \right] = n_1 P_{1k} + P_{Lk}, \quad (B10)$$

where

$$P_{kL} = \sum_{l=2}^N \frac{n_l^*}{n_1^*} (R_{lk}^\dagger + C_{lk}), \quad (B11)$$

$$\sigma = \sum_{l=N+1}^{N'} \frac{n_l^*}{n_1^*} (R_{lk}^\dagger - R_{lk}), \quad (B12)$$

and

$$P_{Lk} = \sum_{l=2}^N n_l (R_{lk}^\dagger + C_{lk}). \quad (B13)$$

Here,  $n_l^*/n_m^* = (g_l/g_m) \exp(-h\nu_{lm}/kT)$ .

We now introduce net radiative rates into the bound level statistical equilibrium equations (B4). For  $l > m$  we write

$$P_{ml} - \frac{n_l}{n_m} P_{lm} = C_{ml} - \frac{n_l}{n_m} (A_{lm} \rho_{lm} + C_{lm}), \quad (B14)$$

using the notation from Paper I, § II. For  $m=1$  equation (B4) (with  $f_1=0$ ) becomes

$$n_1 (P_{1L} + P_{1k}) = P_{L1} + n_k P_{k1}, \quad (B15)$$

where

$$P_{1L} = \sum_{l=2}^N C_{1l}, \quad (B16)$$

and

$$P_{L1} = \sum_{l=2}^N n_l (A_{l1} \rho_{l1} + C_{l1}). \quad (B17)$$

This equation for level 1 is combined with the continuum equation by multiplying equations (B10) and (B15) by  $P_{L1}$  and  $P_{Lk}$ , respectively, and subtracting one equation from the other. As a result we obtain

$$n_1 [P_{1k}(P_{L1} + P_{Lk}) + P_{1L}P_{Lk}] = n_k \left[ P_{k1}(P_{L1} + P_{Lk}) + \frac{n_1^*}{n_k^*} (P_{kL} + \sigma) P_{L1} \right]. \quad (B18)$$

Finally,

$$b_1(R_{1\kappa} + T_{1\kappa}) = R_{1\kappa}^* + T_{\kappa 1}, \quad (\text{B19})$$

where

$$b_1 = \frac{n_1}{n_\kappa} \frac{n_\kappa^*}{n_1^*}, \quad (\text{B20})$$

$$T_{1\kappa} = C_{1\kappa} + \frac{P_{1L} P_{L\kappa}}{P_{L1} + P_{L\kappa}}, \quad (\text{B21})$$

and

$$T_{\kappa 1} = C_{1\kappa} + \frac{(P_{\kappa L} + \sigma) P_{L1}}{P_{L1} + P_{L\kappa}}. \quad (\text{B22})$$

Equation (B19) is the statistical equilibrium equation which we have obtained by combining the level 1 and continuum equations. The supplementary levels affect the parameter  $T_{\kappa 1}$ . Note that apart from the collisional ionization rate (which is essentially negligible in the present application)  $T_{1\kappa}$  is given by  $P_{1L}$  times the branching ratio  $P_{L\kappa}/(P_{L1} + P_{L\kappa})$ , while  $T_{\kappa 1}$  is determined by  $P_{\kappa L} + \sigma$  times the ratio  $P_{L1}/(P_{L1} + P_{L\kappa})$ . The parameters  $T_{1\kappa}$  and  $T_{\kappa 1}$  specify the transition rates between level 1 and the continuum apart from direct photoionization and radiative recombination.

It is convenient to define two additional radiative rates to substitute for  $R_{1\kappa}$  and  $R_{1\kappa}^*$  in equation (B19). We let

$$R_{1\kappa}^* = 4\pi \int_{\nu_1}^{\infty} \frac{d\nu}{h\nu} \alpha_1(\nu) \beta_\nu \alpha_\nu, \quad (\text{B23})$$

and

$$R'_{1\kappa} = 4\pi \int_{\nu_1}^{\infty} \frac{d\nu}{h\nu} \alpha_1(\nu) \gamma_\nu J_\nu, \quad (\text{B24})$$

where

$$\gamma_\nu = 1 - \frac{\beta_\nu}{b_1}. \quad (\text{B25})$$

Then equation (B19) can be rewritten as

$$b_1(R'_{1\kappa} + T_{1\kappa}) = R_{1\kappa}^* + T_{\kappa 1}. \quad (\text{B26})$$

Finally we obtain

$$\frac{1}{b_1} = \frac{U + \epsilon_2}{1 + \epsilon_1}, \quad (\text{B27})$$

where

$$U = R'_{1\kappa} / R_{1\kappa}^*, \quad (\text{B28})$$

$$\epsilon_1 = T_{\kappa 1} / R_{1\kappa}^*, \quad (\text{B29})$$

and

$$\epsilon_2 = T_{1\kappa} / R_{1\kappa}^*. \quad (\text{B30})$$

The statistical equilibrium equation (B27) will be combined with the radiative transfer equation in Appendix C.

II. THE PARAMETERS  $\epsilon$  AND  $B^s$  FOR LINE TRANSITIONS

Here we derive the equations for the photon production and destruction rates  $R_p$  and  $R_d$  which appear in equation (A28) for  $S^L$  and equations (A30) and (A31) for  $\epsilon$  and  $B^s$ .

We combine equations (B1) and (B4) to eliminate  $n_\kappa$ , and obtain

$$n_m \sum_{\substack{l=1 \\ l \neq m}}^N (P_{ml} + p_{ml}) = \sum_{\substack{l=1 \\ l \neq m}}^N n_l (P_{lm} + p_{lm}), \quad (\text{B31})$$

where

$$p_{ij} = \frac{P_{ik}(P_{kj} + f_j Q_s)}{\sum_{l=1}^N P_{kl} + Q_s}. \quad (\text{B32})$$

Introducing net radiative rates (eq. [B14]) gives

$$n_m \left( \sum_{l=1}^{m-1} A_{ml} \rho_{ml} + \sum_{l=1}^N Z_{ml} \right) = \sum_{l=m+1}^N n_l A_{lm} \rho_{lm} + \sum_{l=1}^N n_l Z_{lm}, \quad (\text{B33})$$

where

$$Z_{ij} = C_{ij} + p_{ij}. \quad (\text{B34})$$

The statistical equilibrium equations for levels  $U$  and  $L$ ,  $U > L$ , can be written as

$$n_U (A_{UL} \rho_{UL} + Z_{UL} + X_U) = n_L Z_{LU} + n_1 V_U, \quad (\text{B35})$$

and

$$n_L (Z_{LU} + X_L) = n_U (A_{UL} \rho_{UL} + Z_{UL}) + n_1 V_L, \quad (\text{B36})$$

where

$$X_U = \sum_{\substack{l=1 \\ l \neq L}}^{U-1} A_{Ul} \rho_{Ul} + \sum_{\substack{l=1 \\ l \neq U, L}}^N Z_{Ul}, \quad (\text{B37})$$

$$X_L = \sum_{l=1}^{L-1} A_{Ll} \rho_{Ll} + \sum_{\substack{l=1 \\ l \neq U, L}}^N Z_{Ll}, \quad (\text{B38})$$

$$V_U = \sum_{l=U+1}^N A_{lU} \rho_{lU} \frac{n_l}{n_1} + \sum_{\substack{l=1 \\ l \neq U, L}}^N Z_{lU} \frac{n_l}{n_1}, \quad (\text{B39})$$

and

$$V_L = \sum_{\substack{l=L+1 \\ l \neq U}}^N A_{lL} \rho_{lL} \frac{n_l}{n_1} + \sum_{\substack{l=1 \\ l \neq U, L}}^N Z_{lL} \frac{n_l}{n_1}. \quad (\text{B40})$$

We combine equations (B35) and (B36) by multiplying the first by  $V_L / (V_U + V_L)$  and the second by  $V_U / (V_U + V_L)$  and subtracting one from the other. The result is

$$\frac{n_U}{n_L} (A_{UL} \rho_{UL} + R_d) = \frac{n_U^*}{n_L^*} R_p, \quad (\text{B41})$$

where the photon destruction rate is given by

$$R_d = Z_{UL} + \frac{X_U V_L}{V_U + V_L}, \quad (\text{B42})$$

and the production rate is

$$R_p = \frac{n_L^*}{n_U^*} \left( Z_{LU} + \frac{X_L V_U}{V_U + V_L} \right). \quad (\text{B43})$$

It can be shown that equation (B41) is algebraically equivalent to equation (A28) where  $S^L$ ,  $B$ , and  $A$  correspond to the  $U$  to  $L$  transition.

The supplementary levels affect these rate coefficients only through equation (B32) for  $p_{ij}$ , which can be rewritten as

$$p_{ij} = \frac{(R_{ik} + C_{ik})(x_j + f_j \sigma)}{\sum_{l=1}^N x_l + \sigma}, \quad (\text{B44})$$

where

$$x_i = (n_i^* / n_1^*) (R_{ik}^\dagger + C_{ik}), \quad (\text{B45})$$

and where  $\sigma$  is defined by equation (B12).

## APPENDIX C

### SOLUTION OF THE LYMAN CONTINUUM TRANSFER EQUATION

The continuum transfer equation for  $\nu \geq \nu_1$  is

$$\mu \frac{dI_\nu}{dz} = \kappa_\nu^{\text{Ly}} (I_\nu - S_\nu^{\text{Ly}}) + \kappa'_\nu (I_\nu - S'_\nu). \quad (\text{C1})$$

The Lyman continuum opacity and source function are given by  $\kappa_\nu^{\text{Ly}} = n_1 a_1(\nu) \gamma_\nu$  and

$$S_\nu^{\text{Ly}} = \frac{\alpha_\nu}{b_1 \beta_\nu^{-1} - 1} = \frac{\alpha_\nu \beta_\nu}{b_1 \gamma_\nu}, \quad (\text{C2})$$

using notation from Appendix B. We write  $a_1(\nu) = \bar{a}_1(\nu_1/\nu)^3 G_\nu$ , where  $\bar{a}_1 = 7.906 \times 10^{-18} \text{ cm}^2$  and  $G_\nu$  is the bound-free Gaunt factor. The opacity  $\kappa'_\nu$  and source function  $S'_\nu$  include all continuous opacity sources other than the ground state of hydrogen.

We define

$$d\tau_\nu = (\kappa_\nu^{\text{Ly}} + \kappa'_\nu) dz, \quad (\text{C3})$$

and

$$I_\nu = \kappa'_\nu / (\kappa_\nu^{\text{Ly}} + \kappa'_\nu), \quad (\text{C4})$$

and evaluate the transfer equation at discrete depths  $i$  and frequencies  $k$  so that

$$\frac{\mu dI_{ik}}{d\tau_{ik}} = I_{ik} - S_{ik}, \quad (\text{C5})$$

where

$$S_{ik} = (1 - l_{ik}) \frac{\alpha_k \beta_{ik}}{b_{1i} \gamma_{ik}} + l_{ik} S'_{ik}. \quad (\text{C6})$$

The departure coefficient  $b_1$  is related to the mean intensity  $J_\nu$  by equation (B27), i.e.,

$$\frac{1}{b_1} = \frac{U + \epsilon_2}{1 + \epsilon_1}. \quad (\text{C7})$$

The function  $U = R'_{1k}/R^*_{1k}$  can be written as

$$U = \frac{1}{V} \int_1^\infty \frac{dx}{x} G_x \frac{\gamma_x J_x}{\alpha_x}, \quad (\text{C8})$$

where

$$V = \int_1^\infty \frac{dx}{x} G_x \beta_x, \quad (\text{C9})$$

and where we have defined  $x = \nu/\nu_1$ .

Frequency integrations over the Lyman continuum are expressed as

$$\int_1^\infty f(x) dx = \sum_k A_k f_k, \quad (\text{C10})$$

so that the above equations become

$$U_i = \frac{1}{V_i} \sum_k \frac{A_k G_k \gamma_{ik} J_{ik}}{x_k \alpha_k}, \quad (\text{C11})$$

where

$$V_i = \sum_k \frac{A_k G_k \beta_{ik}}{x_k}. \quad (\text{C12})$$

From the transfer equation we have

$$J_{ik} = \sum_{j=1}^L W_{ijk}^\Lambda S_{jk}. \quad (\text{C13})$$

Then

$$U_i = \frac{1}{V_i} \left( \sum_{j=1}^L \frac{P_{ij}}{b_{1j}} + L_i \right), \quad (\text{C14})$$

where

$$P_{ij} = \sum_k \frac{A_k G_k \gamma_{ik} (1 - l_{jk}) \beta_{jk} W_{ijk}^\Lambda}{x_k \gamma_{jk}}, \quad (\text{C15})$$

and

$$L_i = \sum_{j=1}^L \sum_k \frac{A_k G_k \gamma_{ik} l_{jk} W_{ijk}^\Lambda S'_{jk}}{x_k \alpha_k}. \quad (\text{C16})$$

We define the source function  $S_i^L = V_i/b_{1i}$  and the matrix array  $M_{ij} = P_{ij}/V_j$ . Then from equations (C7) and (C14) we obtain a set of linear equations for  $S_i^L$ :

$$S_i^L = \frac{\sum_{j=1}^L M_{ij} S_j^L + \epsilon_{2i} V_i + L_i}{1 + \epsilon_{1i}}. \quad (\text{C17})$$

These equations for  $i=1,2,\dots,L$  are used to obtain  $S^L$  and thus  $b_1$  at each depth. Given  $b_1$  we can determine the Lyman continuum source function from equation (C2) or the total source function from equation (C6). In this formulation of the equations, the slight dependence of  $\gamma_\nu$  on  $b_1$  is treated iteratively, i.e.,  $\gamma_\nu$  is obtained from a previously calculated  $b_1$ . The Lyman continuum opacity also is treated iteratively, since  $n_1$  depends on  $b_1$ .

It is of interest to consider the asymptotic form of equation (C17) at large optical depths where  $W_{ijk}^\Lambda$  approaches unity for  $j=i$  and zero for  $j \neq i$ . In this case  $\sum M_{ij} S_j^L$  reduces to  $(1-d_i)S_i^L$ , where

$$d_i = \frac{\sum_k A_k G_k \beta_{ik} x_k^{-1} l_{ik}}{\sum_k A_k G_k \beta_{ik} x_k^{-1}}. \quad (\text{C18})$$

Then from equation (C17),

$$S_i^L \rightarrow \frac{\epsilon_{2i} V_i + L_i}{\epsilon_{1i} + d_i}. \quad (\text{C19})$$

We find that  $d$  is at most a few percent of  $\epsilon_1$  and, therefore, we replace  $\epsilon_1 + d$  by  $\epsilon_1$  in the denominator. Then since  $S^L = V/b_1$  this equation is equivalent to

$$b_1 \rightarrow \frac{\epsilon_1/\epsilon_2}{1+\xi}, \quad (\text{C20})$$

where  $\xi = L/\epsilon_2 V$ .

The parameters  $\epsilon_1$  and  $\epsilon_2$  are given by equations (B21), (B22), (B29), and (B30). The collisional ionization rate  $C_{1k}$  is negligible compared with comparable radiative rates throughout the atmosphere. Hence, the ratio of  $\epsilon_1$  and  $\epsilon_2$  is

$$\frac{\epsilon_1}{\epsilon_2} = \frac{(P_{\kappa L} + \sigma) P_{L1}}{P_{1L} P_{L\kappa}}. \quad (\text{C21})$$

This equation can be simplified by using only the  $l=2$  term in each of the equations for  $P_{\kappa L}$ ,  $P_{L1}$ ,  $P_{1L}$ , and  $P_{L\kappa}$  and by neglecting  $C_{2\kappa}$  which is small compared with  $R_{2\kappa}$  and  $R_{2\kappa}^\dagger$  in the chromosphere. Then  $\epsilon_1/\epsilon_2 \sim \langle \epsilon_1/\epsilon_2 \rangle$ , where

$$\langle \epsilon_1/\epsilon_2 \rangle = \frac{R_{2\kappa}^\dagger}{R_{2\kappa}} \left( 1 + \frac{\sigma'}{R_{2\kappa}^\dagger} \right) \left( 1 + \frac{A_{21} \rho_{21}}{C_{21}} \right), \quad (\text{C22})$$

and where

$$\sigma' = \sum_{l=N+1}^{N'} \frac{n_l^*}{n_2^*} (R_{l\kappa}^\dagger - R_{l\kappa}). \quad (\text{C23})$$

Equation (C22) shows that at large optical depths  $b_1$  depends on temperature and on the Balmer continuum intensity through  $R_{2\kappa}^\dagger/R_{2\kappa}$  and that  $b_1$  is sensitive to the  $\mathrm{Ly}\alpha$  net radiative rate except when  $\rho_{21} \ll C_{21}/A_{21}$ . The term  $\sigma'/R_{2\kappa}^\dagger$  represents the contribution due to supplementary levels.

We list in Table 35 the values of the various contributions to  $b_1$  at six representative depths in the atmosphere. In addition to  $h$ ,  $T$ , and  $n_e$ , we give the optical depth  $\tau_1$  at the head of the Lyman continuum and the parameter  $\epsilon_1$  in equation (C17). The other terms are those which appear in equations (C20) through (C23). The values in the table are from our model C calculation based on an eight level atom with supplementary levels 9–12.

TABLE 35

## LYMAN-CONTINUUM PARAMETERS

<i>h</i>	2160	2107	2050	1605	1180
<i>T</i>	23500	10700	7660	6440	6150
<i>n<sub>e</sub></i>	2.1(10)	3.5(10)	3.8(10)	6.0(10)	8.1(10)
$\tau_1$	0.021	0.062	1.08	60.6	782
$\epsilon_1$	1.16	0.304	0.041	0.013	0.041
$R_{2\kappa}^{\dagger}/R_{2\kappa}$	2.1(3)	1.5(2)	26	8.3	6.0
$\sigma'/R_{2\kappa}^{\dagger}$	0.19	0.22	0.22	0.20	0.20
$A_{21\rho_{21}}/C_{21}$	1.1(4)	26	0.53	-0.23	-0.18
$\langle \epsilon_1/\epsilon_2 \rangle$	2.8(7)	4.9(3)	48	7.7	5.9
$\epsilon_1/\epsilon_2$	5.4(6)	5.0(3)	90	6.3	9.9
$\frac{\epsilon_1/\epsilon_2}{1+\xi}$	5.4(6)	4.9(3)	63	6.0	9.8
<i>b<sub>1</sub></i>	9.5(6)	1.1(4)	52	5.9	10

From the results in Table 35 we conclude the following:

1. For  $\tau_1$  of order unity and larger,  $b_1 \sim R_{2\kappa}^{\dagger}/R_{2\kappa}$  within a factor of  $\sim 2$ .
2. The comparison of  $\langle \epsilon_1/\epsilon_2 \rangle$  and  $\epsilon_1/\epsilon_2$  shows that the  $l=2$  approximation also is accurate only to a factor of  $\sim 2$ .
3. The large increase in  $b_1$  at small  $\tau_1$  is due to the variations of both  $\rho_{21}$  and  $T$ .
4. The supplementary levels 9–12 tend to increase  $b_1$  by a factor of order 20%.
5. At large  $\tau_1$  the negative values of  $\rho_{21}$  decrease  $b_1$  by a similar factor.
6. The parameter  $\xi$  is small except near  $\tau_1=1$  where it has the value 0.43. This value arises from the depth and frequency integrations over  $S'_{jk}$  in equation (C16) and represents the effect of the helium continua on the hydrogen Lyman continuum.

## REFERENCES

- Athay, R. G. 1976, *The Solar Chromosphere and Corona: Quiet Sun* (Dordrecht: Reidel).
- Athay, R. G., and Lites, B. W. 1972, *Ap. J.*, **176**, 809.
- Athay, R. G., and Skumanich, A. 1967, *Ann. d'Ap.*, **30**, 669.
- Avrett, E. H. 1971, *J. Quant. Spectrosc. Rad. Transf.*, **11**, 511. — 1977, in *The Solar Output and Its Variation*, ed. O. R. White (Boulder: Colorado Associated University Press), pp. 327–348.
- Avrett, E. H., and Loeser, R. 1969, *Smithsonian Ap. Obs. Spec. Rept.*, No. 303.
- Avrett, E. H., Vernazza, J. E., and Linsky, J. L. 1976, *Ap. J. (Letters)*, **207**, L199.
- Ayres, T. R. 1978, *Ap. J.*, **225**, 665. — 1980, *Solar Phys.*, submitted.
- Ayres, T. R., and Linsky, J. L. 1976, *Ap. J.*, **205**, 874.
- Basri, G. S., Linsky, J. L., Bartoe, J.-D. F., Brueckner, G., and Van Hoosier, M. E. 1979, *Ap. J.*, **230**, 924.
- Bastin, J. A., Gear, A. E., Jones, G. O., Smith, H. J. T., and Wright, P. J. 1964, *Proc. Roy. Soc. London, A*, **278**, 543.
- Bonnet, R. M., Bruner, E. C., Jr., Acton, L. W., Brown, W. A., and Decaudin, M. 1980, *Ap. J. (Letters)*, **237**, L47.
- Brault, J., and Testerman, L. 1972, *Preliminary Edition of the Kitt Peak Solar Atlas* (Tucson: Kitt Peak National Observatory).
- Brueckner, G. E., Bartoe, J.-D. F., and Van Hoosier, M. E. 1977, *Proc. OSO 8 Workshop* (Boulder: University of Colorado, Laboratory for Atmospheric and Space Physics).
- Brueckner, G. E., and Nicolas, K. 1972, *Bull. AAS*, **4**, 378.
- Buhl, D., and Tlamicha, A. 1968, *Ap. J.*, **153**, L189.
- Canfield, R. C., and Beckers, J. M. 1976, in *Physique des Mouvements dans les Atmosphères Stellaires*, ed. R. Cayrel and M. Steinberg (Colloques Internationaux du CNRS No. 250), pp. 291–330.
- Cooper, J. 1979, *Ap. J.*, **228**, 339.
- Cooper, J., and Ballagh, R. J. 1978, *Phys. Rev. A*, **18**, 1302.
- Dalgarno, A., and Sando, K. M. 1973, *Comments Atomic Molec. Phys.*, **4**, 29.
- Doughty, N. A., Fraser, P. A., and McEachran, R. P. 1966, *M.N.R.A.S.*, **132**, 255.
- Dupree, A. K., Huber, M. C. E., Noyes, R. W., Parkinson, W. H., Reeves, E. M., and Withbroe, G. W. 1973, *Ap. J.*, **182**, 321.
- Dupree, A. K., and Reeves, E. M. 1971, *Ap. J.*, **165**, 599.
- Eddy, J. A., Lee, R. H., MacQueen, R. M., and Mankin, W. G. 1973, *Bull. AAS*, **5**, 271.
- Edmonds, F. N. 1955, *Ap. J.*, **121**, 418.
- Epstein, E. E., Oliver, J. P., Soter, S. L., Schom, R. A., and Wilson, W. J. 1968, *A.J.*, **73**, 271.
- Fedoseev, L. I. 1963, *Radiofizika*, **6**, 655.
- Fite, W. L., and Brackman, R. T. 1958, *Phys. Rev.*, **112**, 1141.
- Fite, W. L., Stebbings, R. F., and Brackman, R. T. 1960, *Phys. Rev.*, **119**, 1939.
- Gebbie, K. B., and Thomas, R. N. 1970, *Ap. J.*, **161**, 229.
- Gezari, D. Y., Joyce, R. R., and Simon, M. 1973, *Astr. Ap.*, **26**, 409.

- Gingerich, O. J., Noyes, R. W., Kalkofen, W., and Cuny, Y. 1971, *Solar Phys.*, **18**, 347.
- Gouttebroze, P., Lemaire, P., Vial, J. C., and Artzner, G. 1978, *Ap. J.*, **225**, 655.
- Griem, H. R. 1964, *Plasma Spectroscopy* (New York: McGraw Hill).
- Hall, L. A., and Hinteregger, H. E. 1970, *J. Geophys. Res.*, **75**, 6959.
- Heasley, J. N., and Kneer, F. 1976, *Ap. J.*, **203**, 660.
- Heroux, L., Cohen, M., and Higgins, J. E. 1974, *J. Geophys. Res.*, **79**, 5237.
- Heroux, L., and Swirbalus, R. A. 1976, *J. Geophys. Res.*, **81**, 436.
- Higgins, J. E. 1976, *J. Geophys. Res.*, **81**, 1301.
- Holweger, H., and Müller, E. A. 1974, *Solar Phys.*, **39**, 19.
- Houtgast, J. 1970, *Solar Phys.*, **15**, 273.
- Johnson, L. C. 1972, *Ap. J.*, **174**, 227.
- Jordan, S. D. 1977, *Solar Phys.*, **51**, 51.
- Kalaghan, P. M., and Telford, L. E. 1970, *Air Force Cambridge Res. Lab. Rept.*, No. 408.
- Kalkofen, W., and Ulmschneider, P. 1979, *Ap. J.*, **227**, 655.
- Karzas, W. J., and Latter, R. 1961, *Ap. J. Suppl.*, **6**, 167.
- Kneer, F. 1975, *Ap. J.*, **200**, 367.
- Kohl, J. L., and Parkinson, W. H. 1976, *Ap. J.*, **205**, 599.
- Kohl, J. L., Parkinson, W. H., and Reeves, E. M. 1975, private communication.
- Kuseski, R. A., and Swanson, P. N. 1976, *Solar Phys.*, **48**, 41.
- Labs, D., and Neckel, H. 1970, *Solar Phys.*, **15**, 79.
- Laurence, G. M., and Savage, B. D. 1966, *Phys. Rev.*, **141**, 67.
- Linsky, J. L. 1973, *Solar Phys.*, **28**, 409.
- Linsky, J. L., and Ayres, T. R. 1978, *Ap. J.*, **220**, 619.
- Lites, B. W., Shine, R. A., and Chipman, E. G. 1978, *Ap. J.*, **222**, 333.
- Lortet, M., and Roueff, E. 1969, *Astr. Ap.*, **3**, 462.
- Low, F. J., and Davidson, A. W. 1965, *Ap. J.*, **142**, 1278.
- Machado, M. E., Avrett, E. H., Vernazza, J. E., and Noyes, R. W. 1980, *Ap. J.*, **242**, 336.
- McGowan, J. W., Williams, J. F., and Curley, E. K. 1969, *Phys. Rev.*, **180**, 132.
- Menzel, D. H., and Pekeris, C. L. 1935, *M.N.R.A.S.*, **96**, 77.
- Mihalas, D. 1967, *Ap. J.*, **149**, 169.
- Milkey, R. W., and Mihalas, D. 1973a, *Ap. J.*, **185**, 709.
- . 1973b, *Solar Phys.*, **32**, 361.
- . 1974, *Ap. J.*, **192**, 769.
- Naumov, A. I. 1963, *Radiofizika*, **6**, 848.
- Noyes, R. W., and Kalkofen, W. 1970, *Solar Phys.*, **15**, 120.
- Omont, A., Smith, E., and Cooper, J. 1972, *Ap. J.*, **175**, 185.
- Osterbrock, D. E. 1974, *Astrophysics of Gaseous Nebulae* (San Francisco: Freeman).
- Parkinson, W. H., and Reeves, E. M. 1969, *Solar Phys.*, **10**, 342.
- Peach, G. 1968, *J. Phys. B.*, **1**, 1088.
- Rast, J., Kneubühl, F. K., and Müller, E. A. 1978, *Astr. Ap.*, **68**, 229.
- Reber, E. E. 1971, *Solar Phys.*, **16**, 75.
- Reeves, E. M. 1976, *Solar Phys.*, **46**, 53.
- Reeves, E. M., Foukal, P. V., Huber, M. C. E., Noyes, R. W., Schmahl, E. J., Timothy, J. G., Vernazza, J. E., and Withbroe, G. L. 1974, *Ap. J. (Letters)*, **188**, L27.
- Reeves, E. M., Huber, M. C. E., and Timothy, J. G. 1977, *Appl. Optics*, **16**, 837.
- Reeves, E. M., and Parkinson, W. H. 1970, *Ap. J. Suppl.*, **21**, 1.
- Reeves, E. M., Timothy, J. G., Huber, M. C. E., and Withbroe, G. L. 1977, *Appl. Optics*, **16**, 849.
- Rottman, G. J. 1974, *EOS Trans. AGU*, **55**, 1157.
- Roussel-Dupré, D. 1980, Ph.D. thesis, University of Colorado.
- Rutten, R. J., and Milkey, R. W. 1979, *Ap. J.*, **231**, 277.
- Salomonovich, A. E. 1958, *Soviet Astr.—AJ*, **2**, 112.
- Salomonovich, A. E., Koschenko, F. N., and Noskova, R. I. 1959, *Solechnye Dannye*, No. 9, 83.
- Samain, D. 1978, Ph.D. thesis, University of Paris (see Samain 1979).
- . 1979, *Astr. Ap.*, **74**, 225.
- . 1980, *Ap. J. Suppl.*, **44**, 273.
- Samain, D., Bonnet, R. M., Gayet, R., and Lizambert, C. 1975, *Astr. Ap.*, **39**, 71.
- Sampson, D. H., and Golden, L. B. 1970, *Ap. J.*, **161**, 321.
- . 1971, *Ap. J.*, **170**, 169.
- Sando, K., Doyle, R. O., and Dalgarno, A. 1969, *Ap. J. (Letters)*, **157**, L143.
- Sando, K. M., and Wormhoudt, J. C. 1973, *Phys. Rev. A.*, **7**, 1889.
- Schmidtke, G., Rawer, K., Botzek, H., Norbert, D., and Holzer, K. 1977, *J. Geophys. Res.*, **82**, 2423.
- Seaton, M. J. 1962, in *Atomic and Molecular Processes*, ed. D. R. Bates (New York: Academic), pp. 375–420.
- Shine, R. A., Milkey, R. W., and Mihalas, D. 1975, *Ap. J.*, **199**, 724.
- Smith, K., Henry, R. J. W., and Burke, P. G. 1967, *Phys. Rev.*, **157**, 51.
- Staelin, D. H., Gant, N. E., Law, S. E., and Sullivan, W. T. 1968, *Solar Phys.*, **3**, 26.
- Stettler, P., Rast, J., Kneubühl, F. K., and Müller, E. A. 1975, *Solar Phys.*, **40**, 337.
- Swanson, P. N., and Kuseski, R. A. 1975, *Nature*, **253**, 513.
- Thomas, R. N. 1960, *Ap. J.*, **131**, 429.
- Timothy, J. G. 1977, in *The Solar Output and Its Variation*, ed. O. R. White (Boulder: Colorado Associated University Press), pp. 237–259.
- Tolbert, C. W., and Coats, G. T. 1962, *Univ. Texas Elect. Eng. Rept.*, Nos. 7–24.
- Tolbert, C. W., and Straiton, A. W. 1961, *Ap. J.*, **134**, 91.
- Tripp, D. A., Athay, R. G., and Peterson, V. L. 1978, *Ap. J.*, **220**, 314.
- Ulich, B. L., Cogdell, J. R., and Davis, J. H. 1973, *Icarus*, **19**, 59.
- Ulmschneider, P., and Kalkofen, W. 1978, *Astr. Ap.*, **69**, 407.
- Van Regemorter, H. 1962, *Ap. J.*, **136**, 906.
- Vardavas, I. M., and Cram, L. E. 1974, *Solar Phys.*, **38**, 367.
- Vernazza, J. E., Avrett, E. H., and Loeser, R. 1973, *Ap. J.*, **184**, 605 (Paper I).
- . 1976, *Ap. J. Suppl.*, **30**, 1 (Paper II).
- Vernazza, J. E., and Reeves, E. M. 1978, *Ap. J. Suppl.*, **37**, 485.
- Vidal, C., Cooper, J., and Smith, E. 1970, *J. Quant. Spectrosc. Rad. Transf.*, **10**, 1011.
- White, O. R. 1964, *Ap. J.*, **139**, 1340.
- White, O. R., and Suemoto, Z. 1968, *Solar Phys.*, **3**, 523.
- Wiese, W. L., Glennon, B. M., and Smith, M. W. 1969, *Atomic Transition Probabilities* (Washington: U.S. Government Printing Office), NSRDS-NBS 4.
- Withbroe, G. L. 1971, in *The Menzel Symposium on Solar Physics, Atomic Spectra, and Gaseous Nebulae*, ed. K. B. Gebbie (NBS Spec. Pub. 353), pp. 127–148.
- Wrixton, G. T., and Hogg, D. C. 1971, *Astr. Ap.*, **10**, 193.
- Wrixton, G. T., and Schneider, M. V. 1974, *Nature*, **250**, 314.
- Wulfsberg, K. N., and Short, J. A. 1965, *Air Force Cambridge Res. Lab. Rept.*, No. 77.
- Yelnik, J.-B., and Voslamber, D. 1979, *Ap. J.*, **230**, 184.
- Zanstra, H. 1941, *M.N.R.A.S.*, **101**, 273.

EUGENE H. AVRETT and RUDOLF LOESER: Harvard-Smithsonian Center for Astrophysics, 60 Garden Street, Cambridge, MA 02138

JORGE E. VERNAZZA: L481 Lawrence Livermore Laboratory, P.O. Box 5508, Livermore, CA 94550